Computational Studies of the Water Splitting Reaction on Ceria-Based Catalysts

Wu, Tiantian

Publication date:
2019

Document Version
Publisher's PDF, also known as Version of record

Tiantian Wu

Computational Studies of the Water Splitting Reaction on Ceria-Based Catalysts

PhD Thesis

July 2019

Department of Energy Conversion and Storage
Technical University of Denmark

Computational Studies of the Water Splitting Reaction on Ceria-Based Catalysts

Author:

Tiantian Wu
E-mail: tianwu@dtu.dk

Supervisors:

Tejs Vegge
Professor, Head of Section
Section for Atomic Scale Materials Modelling
Department of Energy Conversion and Storage
Technical University of Denmark
E-mail: teve@dtu.dk

Heine Anton Hansen
Associate Professor
Section for Atomic Scale Materials Modelling
Department of Energy Conversion and Storage
Technical University of Denmark
E-mail: heih@dtu.dk

Department of Energy Conversion and Storage
Section for Atomic Scale Materials Modelling
Technical University of Denmark
Fysikvej, Building 309
2800 Kgs. Lyngby
Denmark
www.energy.dtu.dk
Tel: +45 46 77 58 00
E-mail: info@energy.dtu.dk

不積跬步，無以至千里，不積小流，無以成江海

《荀子-勸學》

Preface

This thesis is submitted in candidacy for a PhD degree from Technical University of Denmark (DTU). The work has been conducted between August 2016 and July 2019 supervised by Prof. Dr. Tejs Vegge and Assoc. Prof. Dr. Heine Anton Hansen in the Section for Atomic Scale Materials Modelling, at the Department of Energy Conversion and Storage.

This work has been financially supported by the Velux Foundations through the research center V-Sustain (grant number 9455).

Tiantian Wu
July 2019

Acknowledgements

I am thankful to many people who I met during my PhD studies, especially to whom have helped me during my PhD journey, and contributed to the work in this thesis.

Firstly, I would like to express my sincere gratitude to my supervisors, Prof. Dr. Tejs Vegge and Assoc. Prof. Dr. Heine Anton Hansen. Without their excellent guidance, fruitful discussions, and constructive suggestions during such a three-year journey, my PhD studies would not end up with great fulfills.

I am very thankful to the wonderful working environment provided by the section of Atomic Scale Materials Modelling. I really enjoyed working with my nice colleagues: Steen Lysgaard, Jaysree Pan, Qingming Deng, Arghya Bhowmik, Vladimir Tripkovic, Rune Christensen, Murat Mesta, Henrik Høgh Kristoffersen, Jin hyun Chang, Nicolai Rask Mathiesen, Alexander Sougaard Tygesen, Zhenyun Lan and others. Specially, I would like to thank to Karina Ulvskov Frederiksen who help me on how to fill in and submit important documents to the PhD board. I am also very thankful to Katrine Louise Svane for her help on translating the abstract of this thesis to Danish. In addition, I enjoyed collaborating with Pei Liu at Center for Electron Nanoscopy in DTU Physics, by sharing theoretical and experimental findings.

It is my great honor to meet and work with Prof. Dr. Núria López at Institute of Chemical Research of Catalonia (ICIQ). I am grateful to her for giving me the opportunity for working in her group and learning useful computational skills during the external stay of three months.

In addition, I feel thankful to people from DTU Energy (Peter Vang Hendriksen's group), DTU Physics (Ib Chorkendorff's group, Jens Kehlet Nørskov's group), University of Copenhagen (Jan Rossmeisl's group), Stanford University (Thomas Francisco Jaramillo's group), working together on the challenging project of "Water Electrolysis and the Oxygen Evolution Reaction" founded by the Velux foundations. I received many significant suggestions from our monthly-held skype meetings.

Last, but not least, many thanks to my friends and family for their support and love, especially my husband Ming Ma, who gives me many understandings and accompanies in my life. I also would like to thank him for many suggestions in the academic writing.

Tiantian Wu
July 2019

Abstract

Ceria-based catalysts have attracted considerable interest for the electrocatalytic water splitting reaction (WSR) in solid oxide electrolysis cells (SOECs), due to the high efficiency and high stability for sustainable hydrogen production. Traditional SOECs suffer from instabilities, owing to cracking and polarization at gas/catalyst/electrolyte triple-phase boundaries (TPBs). Ceria-based catalysts as hydrogen electrodes in SOECs can be accessible to both ionic and electronic carriers, and gas molecules, which enables a wider surface area for electrocatalysis in comparison with the TPBs, significantly enhancing the efficiency of hydrogen production in the SOECs. However, the fundamental understanding of the WSR on ceria-based catalysts remains unclear. By using density functional theory corrected for on-site Coulomb interactions (DFT+*U*), the reaction mechanism for the WSR on low index facets of ceria, as well as the effect of strain and doping are systemically investigated in this thesis, providing a platform for understanding of the electrocatalytic WSR on ceria-based catalysts.

Initially the effect of Gd doping in ceria (GDC) on the WSR is explored because of the highly increased ionic conductivity of ceria by the incorporation of gadolinium. It is found that the rate-determining step (RDS) of the WSR on both ceria and GDC is hydroxyl decomposition into H_2. At the RDS, H_2 evolution is more likely to proceed via the Ce-H and Gd-H moiety on the hydroxylated pure ceria and GDC, respectively. Notably, the formation of such Gd-H is more facile compared to that of Ce-H, which gives rise to the improved electrocatalytic activity of the WSR on ceria by the incorporation of Gd.

In addition, doping ceria or creating oxygen vacancies in ceria generally leads to lattice strain. Thereby, the effect of strain on the WSR on the pure CeO_2(111) is investigated. It is found that the RDS of the WSR on CeO_2(111) remains unchanged under different lattice strains. However, the formation of intermediates as well as the reaction efficiency of the WSR could be effectively tuned by tailoring the lattice strain. The WSR activity on CeO_2(111) is predicted to be strongly enhanced when CeO_2(111) is compressed by more than 3.0%.

Finally, a comparison of the catalytic activity of the WSR on the (110), (100) and (111) facets of ceria is presented. The WSR for H_2 production on the (111) and (110) facets of ceria is 10~100 times faster in comparison with that on the (100) facet of ceria at temperature (T) < 950 K, which reveals that the WSR on ceria is strongly facet-dependent at low and intermediate temperature. Interestingly, this facet-dependence is found to diminish at high temperature, suggesting the temperature sensitivity in the facet-dependence of the WSR on ceria.

Resume

Cerium oxid har tiltrukket stor opmærsomhed som katalysator for den elektrokatalytiske spaltning af vand (Water splitting reaction, WSR) i keramiske elektrolyseceller til bæredygtig produktion af brint på grund af den høje effektivitet og stabilitet. Traditionelle keramiske elektrolyseceller kan blive ustabile på grund af revner og polarisation på trefase-grænsen mellem gas, katalysator og elektrolyt. Når cerium oxid baserede katalysatorer bruges som hydrogen elektroder i keramiske elektrolyseceller kan de være tilgængelige for både ioniske og elektroniske ladningsbærere og gas molekyler. Dette giver adgang til et større overfladeareal for elektrokatalyse i sammenligning med trefase-grænsen, og medfører en betydeligt højere effektivitet af elektrolysecellen. Den fundamentelle forståelse af WSR på cerium oxid baserede katalysatorer er dog utilstrækkelig. I denne afhandling studeres reaktionsmekanismen for WSR på cerium-oxid-overflader med lave index, samt effekten af gitterkonstant og doping, ved brug af tæthedsfunktionalteori korrigeret for on-site Coulomb vekselvirkninger (DFT+*U*), for at skabe en bedre forståelse af den elektrokatalytiske WSR på cerium oxid baserede katalysatorer.

Først undersøges effekten af Gd-doping i cerium oxid (GDC) da dette leder til en øget ionisk ledningsevne i materialet. Vi finder at det hastighedsbestemmende reaktionstrin af WSR for både cerium oxid og GDC er omdannelsen af hydroxyl til H_2. I dette trin vil H_2 overvejende blive dannet via Ce-H intermediatet på cerium oxid og via Gd-H intermediatet på GDC. Dannelsen af Gd-H er mere favorabel end dannelsen af Ce-H, hvilket forklarer den forbedrede aktivitet af WSR ved doping med Gd.

Doping eller dannelse af ilt vakancer i cerium oxid leder til tøjning i materialet. Derfor undersøger vi også effekten af ændringer i gitterkonstanten for den rene CeO_2(111) overflade. Vores resultater viser at det hastighedsbestemmende skridt for WSR på CeO_2(111) forbliver uændret når gitterkonstanten ændres, men dannelsen af de forskellige intermediater og reaktionens effektivitet varierer. Vi beregner at effektiviteten af WSR er betydeligt forbedret når CeO_2(111) komprimeres med mere end 3%.

Til sidst sammenlignes den katalytiske aktivitet af WSR på (110), (100) og (111) facetterne af cerium oxid. Dannelsen af H_2 på (111) og (110) facetterne er 10-100 gange hurtigere end på (100) overfladen for temperaturer under 950 K. Dette viser at WSR er stærkt afhængig af den tilgængelige overflade ved lave og middelhøje temperaturer, men denne overflade-afhængighed forsvinder ved høje temperaturer.

List of Papers

- **Publications (found in Appendix B) included in the PhD thesis.**

Paper 1

Mechanism of Water Splitting on Gadolinium Doped CeO_2(111): A DFT+*U* Study

Tiantian Wu, Qingming Deng, Heine Anton Hansen, Tejs Vegge

The Journal of Physical Chemistry C 2019, 123, 5507−5517

Paper 2

Improved Electrocatalytic Water Splitting Reaction on CeO_2(111) by Strain Engineering: A DFT+*U* Study

Tiantian Wu, Tejs Vegge, Heine Anton Hansen

ACS Catalysis 2019, 9, 4853−4861

Paper 3

Facet-Dependent Electrocatalytic Water Splitting Reaction on CeO_2: A DFT+*U* Study

Tiantian Wu, Núria López, Tejs Vegge, Heine Anton Hansen

Submitted

➢ Publications out of the scope of this thesis

Paper 4

Transformations of Supported Gold Nanoparticles Observed by *In Situ* Electron Microscopy

Pei Liu, Tiantian Wu, Jacob Madsen, Jakob Schiøtz, Jakob Birkedal Wagner, Thomas Willum Hansen

Nanoscale 2019, 11, 11885-11891

Paper 5

2D Transition Metal–TCNQ Sheets as Bifunctional Single-Atom Catalysts for Oxygen Reduction and Evolution Reaction (ORR/OER)

Qingming Deng, Jiong Zhao, Tiantian Wu, Guibin Chen, Heine Anton Hansen, Tejs Vegge

Journal of Catalysis 2019, 370, 378-384

Paper 6

Combinatorial Selection of a Two-Dimensional 3d-TM-Tetracyanoquinodimethane (TM-TCNQ) Monolayer as a High-Activity Nanocatalyst for CO Oxidation

Qingming Deng, Tiantian Wu, Guibin Chen, Heine Anton Hansen, Tejs Vegge

Physical Chemistry Chemical Physics 2018, 20, 5173-5179

Contents

List of Figures

List of Tables

Chapter 1. Introduction

1.1 Sustainable Hydrogen Production via WSR

Generation of hydrogen through the electrocatalytic water splitting reaction (WSR) powered by renewable energy like wind, solar and hydro energy is a sustainable way for hydrogen fuel production without carbon emission,[1,2] where the produced hydrogen is also crucial as a reducing reactant in many chemical processes.[3,4]

The renewable energy has been widely used nowadays. However, the supply of electricity converted from renewable energy usually mismatches electricity demands of our life, leading to an increasing desire for developing efficient and cheap storage of the surplus renewable electricity.[5] Thus, the conversion of electricity to chemical energy by using the electrocatalytic WSR also provides an alternative way for indirect storage of such excess renewable energy.

Through the net reaction of the WSR, H_2 and O_2 is generated from H_2O. Hydrogen is generated from water via the hydrogen evolution reaction (HER) in equation (1-1).

$$H_2O+2e^-\rightarrow H_2+O^{2-} \quad (1\text{-}1)$$

which is a half reaction at cathodes in WSR technologies such as commercial alkaline water electrolysis and newly developed solid oxide electrolysis cells (SOECs),[4] as shown in **Figure 1-1.** Alkaline water electrolysis is a low-temperature technology, operating below 400 K, while SOECs operate at high temperature above 500 K.[4] In alkaline water electrolysis, a diaphragm is set in liquid electrolytes to separate gas production but enable OH^- transport as shown in **Figure 1-1**. The alkaline water electrolysis has been utilized in industrial applications because of its long-term stability and low cost by using non-precious metals as catalysts. However, OH^- transport through the diaphragm is slow, leading to low current densities in alkaline. In addition, traditional alkaline water electrolysis has slow dynamics at anodes, which limits the efficiency of the WSR.

By contrast, the newly developed SOECs have great potential for the sustainable hydrogen production, which can operate with high efficiency up to 100 %.[4] Compared to aqueous solution in alkaline, electrolytes in SOECs are solid oxides that have high ionic conductivity, providing high efficiency for hydrogen production. Although the WSR by using SOECs technology is an alternative promising approach for hydrogen

production, the practical applications of this technology is still limited at laboratory scale due to the mechanical instabilities of hydrogen electrodes in SOECs. Thus, to address the mechanical instabilities is the key step for achieving the industrial utilization of SOECs for sustainable hydrogen production, which requires a better understanding of the mechanism of the WSR in SOECs.

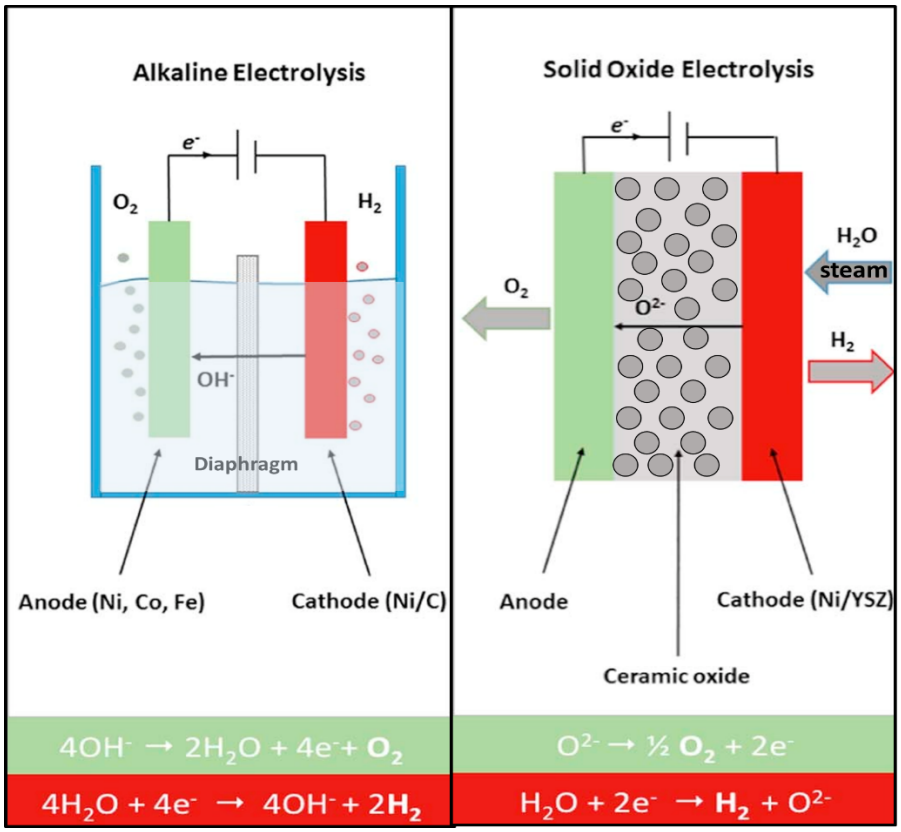

Figure 1-1. Operation principle of alkaline water electrolysis and SOEC for the WSR. The figure is redrawn from reference 4.

1.2 Solid Oxide Electrolysis Cells

At the anode in a SOEC, producing oxygen vacancies proceeds via oxygen evolution reaction driven by an external power source. Then the produced oxygen vacancies diffuse easily through the solid electrolyte to the cathode, owing to the high ionic conductivity of the solid electrolyte. At the cathode, the created oxygen vacancies react with water to produce H_2 through the WSR.

Compared to alkaline water electrolysis, SOECs are capable of efficiently dissociating H_2O into H_2 with lower electrical consumptions by utilization of heat under high temperature.[4,6,7] The total energy demands for the WSR in a SOEC include electricity energy and thermal energy. The total energy cost for the WSR is stable

although it increase slightly at high operating temperature as reported by Sapountzi et al.[4] By contrast, the heat demands increase largely at high temperature. The increased heat consumptions at high temperature significantly reduce the contributions from electricity energy for generating hydrogen, leading to a lower cost of hydrogen production in SOECs in comparison with alkaline water electrolysis. By using the required heat supplied renewably from sun, nuclear and waste heat, SOECs can operate with high efficiency up to 100 %.[4] Thus, SOECs offer a sustainable technology for the hydrogen production through the WSR powered by the electricity converted from renewable energy, and the heat generated renewably from nature and industry.

Nickel employed in yttrium-stabilized zirconia (YSZ) is typically used as hydrogen electrodes in SOECs due to its high activity, fast electronic and ionic conductivity, and low cost.[7–9] However, it is accessible for oxygen ions transport via YSZ into deeper electrode layers, leading to terrible degradations and cracks at the triple-phase boundaries (TPBs) between the gas channels, the solid electrolyte and the electrode.[7,10] Because of such cracks at the TPBs, the hydrogen electrodes in SOECs are mechanically unstable. In addition, the oxidation of nickel results in terrible loss of activity of the electrodes. For developing SOECs towards hydrogen production via the WSR, the main scientific challenge is to develop an efficient catalyst that can block the TPBs by enabling large reaction surface, and show high catalytic activity.

1.3 State of the Art in Ceria-Based Catalysts

Being high-efficient and economically attractive solid oxide catalysts among the identified materials, ceria-based catalysts have been widely used in many catalytic processes such as oxygen storage in three-way catalysts,[11–13] CO oxidation,[14,15] water-gas shift reaction,[16–18] and production of fossil fuels [19,20] because of the easy redox cycle between Ce^{4+} and Ce^{3+} states.[6,21,22] Recently, ceria has also been proposed for the electrocatalytic WSR in SOECs due to the fast mobility of oxygen ions and the highly improved efficiency for sustainable hydrogen production.[6,21,22] In addition, the ceria/gas interface in a SOEC is accessible to electrons, ions and molecules, which can extend the WSR from the limiting TPBs to a wider surface area, a two-phase (ceria/gas) boundary[23,24] as presented in **Figure 1-2**. The high ionic conductivity and the extended reaction surface further promote catalytic reactions on ceria.

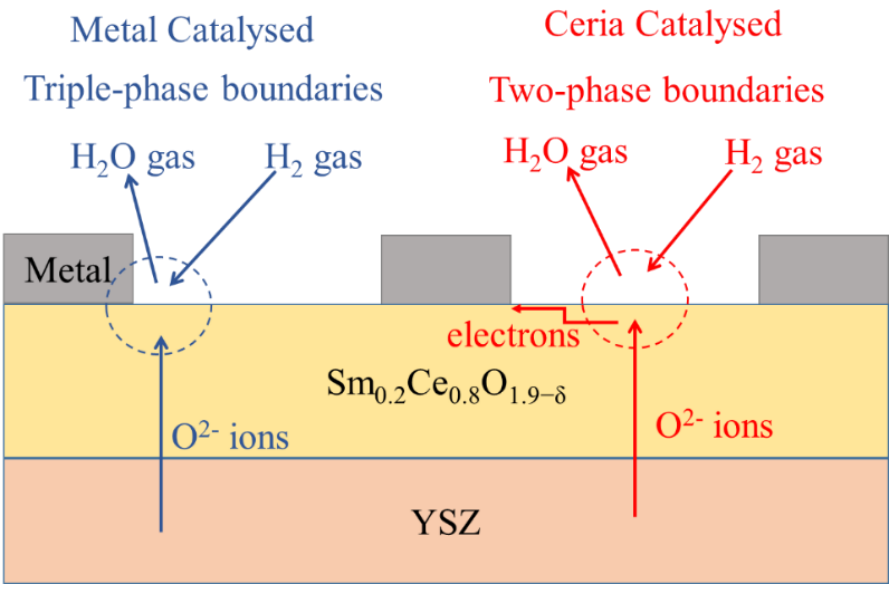

Figure 1-2. The illustration of reactions at the triple-phase boundaries and two-phase boundaries in a SOEC. The figure is redrawn from reference 23.

The electrocatalytic WSR on ceria usually includes reaction steps as follows.[6,21]

$$2Ce^{4+} \rightarrow 2Ce^{3+} + V_O + O^{2-} \quad (1\text{-}2)$$

$$H_2O_{ads} + 2Ce^{3+} + V_O + O^{2-} \rightarrow 2OH^- + 2Ce^{3+} \quad (1\text{-}3)$$

$$2OH^- + 2Ce^{3+} \rightarrow H_2 + 2Ce^{4+} + 2O^{2-} \quad (1\text{-}4)$$

During reaction (1-2), an oxygen vacancy (V_O) is created by removing one lattice oxygen, where two excess electrons localize on two cerium atoms somewhere in the cerium layers, leading to the reduction of $2Ce^{4+}$ to $2Ce^{3+}$. Water adsorbs near V_O and easily dissociates into hydroxyls via reaction (1-3), where OH of H_2O accommodates the vacant site on ceria, while H binds with one lattice O neighbor to the vacant site, leading to the formation of two hydroxyls on ceria. At reaction (1-3), the surface is partially hydroxylated and has low hydrogen coverage. H_2 then forms via the hydroxyl decomposition via reaction (1-4), where $2OH^-$ release two lattice O^{2-} and $2Ce^{3+}$ are oxidized to $2Ce^{4+}$. From reaction (1-2) to reaction (1-4), the WSR on ceria undergoes a $Ce^{4+} \rightarrow Ce^{3+} \rightarrow Ce^{4+}$ redox cycle. In addition, two more hydroxyls can form on the partially hydroxylated ceria via reaction (1-2) and (1-3). H_2 could form on the ceria surface having more hydroxyls via reaction (1-4), undergoing the same reaction as that on the surface having two hydroxyl groups. After CeO_2 is fully hydroxylated and there is no more lattice oxygen available for binding with one more H, reaction (1-3) and (1-4) compete strongly with the reaction of

$$2Ce^{3+} + V_O + H_2O_{ads} \rightarrow OH^- + Ce^{4+} + Ce^{4+}H^- \rightarrow H_2 + 2Ce^{4+} + O^{2-} \quad (1\text{-}5)$$

where one lattice Ce^{4+} binds with the adsorbed H, forming $Ce^{4+}H^{-}$ (Ce-H). The ceria surface is excessively hydroxylated because of the formation of the Ce-H. The WSR on ceria is associated with the reactions among water, oxygen vacancies, hydroxyls and ceria. In this thesis, the WSR including the above reaction steps is investigated on the partially, fully and excessively hydroxylated CeO_2.

The calculated formation energy of one V_O in ceria by using computational simulations is determined by $2Ce^{3+}$ distributions due to the localization of two excess electrons on ceria after removing one lattice oxygen. Identifying the preference distribution of $2Ce^{3+}$ polarons of one V_O is correlated to the method for describing 4*f* orbitals of cerium atoms, and the created oxygen vacancy position.[25–27] Density functional theory corrected for on-site Coulomb interactions (DFT+*U*) is a popular method for describing the 4*f* orbitals of cerium and predicting the strong localization of electrons on ceria-based catalysts, seeing Chapter 2 for more details. Generally, creating one oxygen vacancy in the sub-layer of ceria (V_O^{sub}) is much more favored than that in the top layer (V_O^{sur}).[21,25,26] However, it is facile for the hopping of Ce^{3+} polarons between different distributions,[25,28,29] and for diffusions of oxygen vacancies from deep to top layers of ceria surface.[21,25]

The experimental [30] and theoretical [31,32] investigations of water adsorption on ceria have been widely reported, showing both dissociated water and molecularly adsorbed water on ceria. In presence of oxygen vacancies, water is more likely to dissociate into hydroxyls than adsorb as molecules near ceria surface.[31,32] Hydroxyls formed on the oxidized (111) facet of ceria is observed to be less stable than that formed on the oxidized (100) facet of ceria,[30] suggesting that the stability of hydroxyls has large dependence on the exposed facets of ceria. Generally, the dissociated adsorption of water by forming hydroxyls via reaction (1-3) on ceria is barrierless.[31,32]

As for the formation of hydroxyls on ceria, both theoretical and experimental studies have demonstrated that the rich OH^{-} species[17,20] formed on ceria surface during the WSR are important intermediates at the rate-determining step (RDS), where hydroxyl decomposes into H_2 combined with oxidation of Ce^{3+} to Ce^{4+}.[6,21] At 400-600 K, surface hydroxyls on ceria are very stable as observed by experiments.[30,34] Furthermore, the formation of highly stable hydroxyls on ceria facilities the further surface reduction via reaction (1-2) and (1-3) in the presence of water, promoting the formation of fully and excessively hydroxylated CeO_2.[21,35] Therefore, more investigations are desired for understanding the formation of hydroxyls on ceria-based catalysts.

The reaction steps of oxygen vacancy formation and diffusion, and water dissociation into hydroxyls on CeO_2(111) are reported to be much more facile than

hydroxyl decompositions on the partially and fully hydroxylated CeO_2(111) (having an about 3.0 eV activation barrier).[21] In addition, the activation barrier for H_2 production on the excessively hydroxylated ceria surface via a Ce-H intermediate is found to be lower than that on the partially and fully hydroxylated CeO_2(111). However, the formation of more than one monolayer hydroxyls on ceria via water dissociation becomes more difficult than the formation of the fully hydroxylated ceria in the presence of water.[21] **Figure 1-3** shows that the most stable intermediate is 6H (one monolayer coverage of H). Compared to the fully hydroxylated ceria (6H), oxygen vacancies and vacancy-hydroxyl mixed intermediates like $5H+V_O^{sub}$ at water atmosphere are unstable, which easily react with an adsorbed H_2O to form 6H. The activation barrier for H_2 production on the 7H covered CeO_2(111) is 1.6 eV, while a twice-higher barrier is found on the 2H covered surface as shown in **Figure 1-3**, indicating that the formation of more than one monolayer hydroxyls on ceria enhances the reactivity for H_2 production. However, the formation of 7H is 1.31 and 1.60 eV unstable than that of 6H, at 800 K at 1200 K, respectively. Therefore, one important challenge for the WSR on ceria is to stabilize the reaction intermediates like hydroxylated ceria especially the fully and excessively hydroxylated ceria. In addition, reducing the reaction barrier for hydrogen production by stabilizing the transition state during the hydroxyl decomposition on the hydroxylated ceria is also critical for improving the reaction kinetics of the WSR on ceria.

Tuning the formation of reaction intermediates like hydroxyls and Ce-H moiety by doping or using strain technology may provide an effective way for improving the reaction efficiency of the WSR on ceria, because of the fact that the catalytic activity is linked to the electronic structure of catalysts which could be significantly affected by doping and strain.[36–39] In addition, the varied stability of the hydroxyls on the different facets of ceria[30] also indicates that the activity of ceria for the WSR is affected by the exposed facets. Therefore, by using DFT method that has been successfully used for describing the electronic structure and reaction activity of catalysts,[40–43] the fundamental reaction mechanism for the WSR on low index facets of ceria as well as the effect of strain and doping are investigated in this thesis.

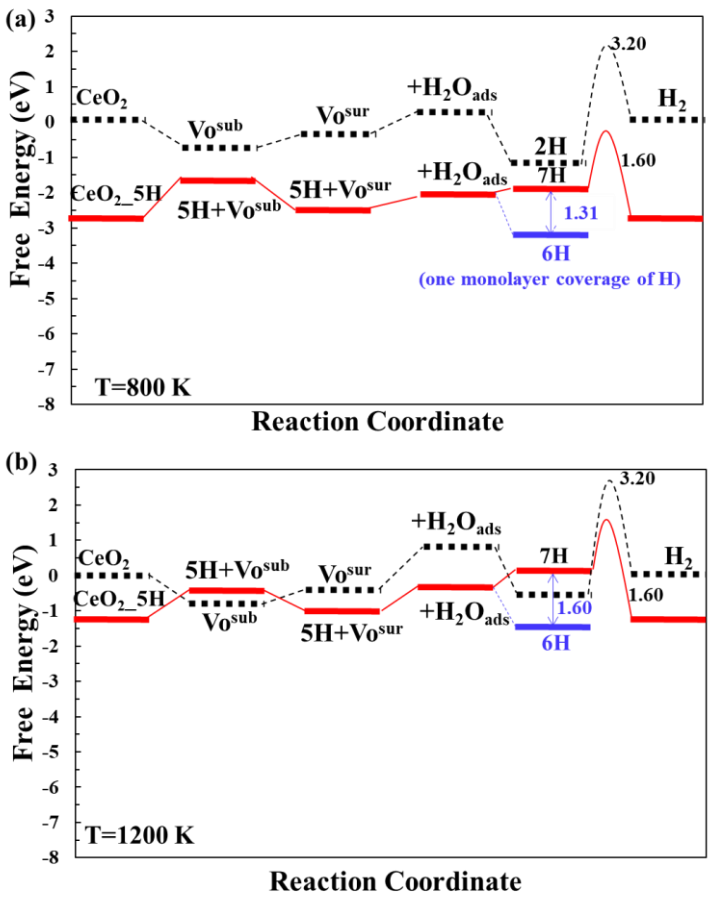

Figure 1-3. Reaction pathways of the WSR on CeO_2(111) at 800 and 1200 K. Data is taken from Paper 1.

1.4 Outline of Thesis

This thesis includes six chapters. The remaining chapters are outlined as follows:

Chapter 2 introduces the computational methods used for investigating the WSR on ceria-based catalysts, including the introduction of density-functional theory, and computational parameters used in this thesis, followed with methods for identifying the transition states (obtaining reaction barriers) and calculating the free energy of reaction intermediates on ceria.

Chapter 3 presents how Gd doping affects the stability of the reduced ceria surface by creating oxygen vacancies and formation of hydroxyls, and the impact of Gd doping on the reaction pathways for the WSR.

Chapter 4 focuses on the effect of strain on the formation of oxygen vacancies, hydroxyls and vacancy-hydroxyl mixed phases on CeO_2(111), as well as the strain effect on the activation barriers for oxygen vacancy diffusion, water dissociation into hydroxyls and the following hydroxyl decomposition. A direct mapping between the most efficient WSR pathway and strain at different operating temperature is also investigated, providing insights into the strain effect on the thermodynamics and reaction kinetics of the WSR on CeO_2(111).

Chapter 5 explores the formation of reaction intermediates and their preferred Ce^{3+} distributions on the CeO_2(110) and CeO_2(100) surface. Then, the reaction pathways on CeO_2(110) and CeO_2(100) at different operating temperature are compared to the WSR on the most often observed CeO_2(111) surface. In addition, a mapping of the most efficient reaction pathway on the (110), (100) and (111) facets of ceria at different operating temperature reveals how the WSR is facet-dependent on ceria and how this fact sensitivity is affected by operating temperature.

Chapter 6 draws the conclusions of the main findings in this thesis and gives brief outlook on the further enhancements of the electrocatalytic WSR on ceria-based catalysts that can be achieved by combing strain effect and doping strategy, followed with outlook on applications of ceria-based catalysts in other catalytic processes.

Chapter 2. Computational Theory and Method

2.1 Density Functional Theory

As a developed computational electronic structure theory by utilizing quantum mechanical theories, DFT has been a popular tool for investigating electronic structure in solid-state physics. Using the descriptions of the electronic structure of a catalyst obtained by using DFT, the activity of chemical reactions on the catalyst can be predicted. Thus, DFT has been widely used in catalysis-related studies during the last two decades, giving insights into mechanism of chemical reactions on catalysts.[40–43] In this thesis, the DFT method is applied to understand the electrocatalytic WSR on ceria-based catalysts.

2.1.1 Schrödinger equation

Erwin Schrödinger derived the famous time-independent Schrödinger equation for describing wave functions or state functions of a quantum-mechanical system containing electrons and nuclei.[44] The time-independent Schrödinger equation is

$$\hat{H}\,\psi = E\,\psi \tag{2-1}$$

where $\hat{H}$ is the Hamiltonian operator, ψ is the wave function of the quantum system, and E is the total energy of the quantum system. This equation is valid whenever the Hamiltonian is time independent.

In equation (2-1), $\hat{H}$ consists of the kinetic energies of electrons ($\hat{T}_{el}$) and nuclei ($\hat{T}_{nuc}$), and columbic interactions between electron-electron ($\hat{V}_{el\text{-}el}(r)$), electron-nucleus ($\hat{V}_{el\text{-}nuc}(r, R)$), and nucleus-nucleus ($\hat{V}_{nuc\text{-}nuc}(R)$):

$$\begin{aligned}\hat{H} &= \hat{T}_{el}+\hat{T}_{nuc}+\hat{V}_{el\text{-}el}(r)+\hat{V}_{el\text{-}nuc}(r, R)+\hat{V}_{nuc\text{-}nuc}(R)\\ &= -\sum_{i}\frac{1}{2}\nabla_i^2-\sum_{A}\frac{1}{2M_A}\nabla_A^2+\frac{1}{2}\sum_{i>j}\frac{1}{r_{ij}}-\frac{1}{2}\sum_{i,A}\frac{Z_A}{r_{iA}}+\frac{1}{2}\sum_{B>A}\frac{Z_A Z_B}{R_{AB}}\end{aligned} \tag{2-2}$$

where i, j present two different electrons, and A, B are two different nuclei. r_{ij}, r_{iA}, R_{AB}, are distances of electron-electron, electron-nucleus, and nucleus-nucleus, respectively.

Because of complex interactions among electrons and nuclei, the Schrödinger equation is unsolvable even for a system containing a modest number of electrons and nuclei.

2.1.2 Born-Oppenheimer approximation

Usually, the mass of one nucleus is much larger than an electron in a molecule. Correspondingly, nuclei move more slowly than electrons in the quantum-mechanical system.[45] The Born-Oppenheimer approximation is developed based on the assumption that the electrons move speedily and quickly response to an external potential set by the nuclei of the system at a fixed position.[46] Thus, the wave function of the system in equation (2-1) can be separated into electronic wave function, ψ_{el}, and the nuclear wave function, ψ_{nuc}, as shown in equation (2-3).

$$\psi(\{r_i\}, \{R_j\}) = \psi_{el}(\{r_i\}, \{R_j\})\psi_{nuc}(\{R_j\}) \tag{2-3}$$

where $\{r_i\}$ and $\{R_j\}$ are the positions of electrons and nuclei, respectively. Then the Schrödinger equation for the electrons is

$$\hat{H}_{el}(\{r_i\}, \{R_j\})\psi_{el}(\{r_i\}, \{R_j\}) = E_{el}(\{R_j\})\psi_{el}(\{r_i\}, \{R_j\}) \tag{2-4}$$

where the Hamiltonian for the electrons, $\hat{H}_{el}$, is

$$\begin{aligned}\hat{H}_{el} &= \hat{T}_{el}+\hat{V}_{el\text{-}el}(r)+\hat{V}_{el\text{-}nuc}(r, R)+\hat{V}_{nuc\text{-}nuc}(R) \\ &= -\sum_i \frac{1}{2}\nabla_i^2+\frac{1}{2}\sum_{i>j}\frac{1}{r_{ij}}+\frac{1}{2}\sum_{B>A}\frac{Z_A Z_B}{R_{AB}}-\frac{1}{2}\sum_{i,A}\frac{Z_A}{r_{iA}}\end{aligned} \tag{2-5}$$

By using the Born-Oppenheimer approximation, the total Hamiltonian of the system in equation (2-2) is reduced to $\hat{H}_{el}$.

2.1.3 The many-body problem

In the Born-Oppenheimer approximation, all spatial coordinates of electrons determine the electronic wave function of the system. Each electron has three spatial degrees of freedom. Thus, for a quantum-mechanical system containing N electrons, solving the Schrödinger equation for the electrons in equation (2-4) is a 3N dimensional problem, which is a many-body problem. The computational cost to solve the Schrödinger equation increases exponentially with the number of particles.[47] More approximations

are needed for solving the many-particle Schrödinger equation. Instead of using wave functions to describe the electronic energy, the total electronic energy can be written as a functional of electronic density as shown in equation (2-6).

$$n(r) = 2\sum_{i}^{N} \psi_i^*(r)\psi_i(r) \tag{2-6}$$

which is a function of electron position (r). The factor of 2 means that the electrons have two spins in the occupation of the orbital (i), indicating that the total system can be described after knowing the distribution of electrons.

2.1.4 The Hohenberg-Kohn theorems

To obtain a better approximation of the Schrödinger equation, Hohenberg and Kohn[48] provided an assumption that the electrons of the quantum system move under an external potential, $\upsilon(r)$, which can be described by using the electronic density functional in equation (2-6).

In the Theorem 1, the electronic ground-state density uniquely determines the external potential. The corresponding terms like the Hamiltonian and ground state properties are described by using the electronic density. So the total system energy is written as the sum of an existent universal functional of density ($F_{HK}[n(r)]$) and external potential energy ($V_{ext}[n(r)]$), as shown in equation (2-7).

$$\begin{aligned} E_{tot} &= F_{HK}[n(r)] + V_{ext}[n(r)] \\ &= T[n] + U[n] + V_{ext}[n(r)] \\ &= T[n] + U[n] + \int \upsilon(r) n(r)\, dr \end{aligned} \tag{2-7}$$

In equation (2-7), $T[n]$ is the classic kinetic energy and $U[n]$ is the classic columbic interaction energy. However, the Theorem 1 does not provide information about the exact universal functional of density.

In the Theorem 2, the total system energy in equation (2-8) yields an energy minimum only when the electronic density is the exact ground-state energy (E_0). Therefore, for all trial electronic densities, $n(r)$, the corresponding total energy ($E_v[n(r)]$) satisfies an equation of

$$E_v[n(r)] \geq E_0 \tag{2-8}$$

Solving the Schrödinger equation then is approximated into a problem of minimizing the functional $E_v[n(r)]$.

2.1.5 The Kohn-Sham equations

Compared to the approximations introduced above, the Kohn-Sham scheme[49] provides an exact solution to the calculation of the ground-state density. Instead of using the concept of an external potential, the Kohn-Sham system applies an effective potential (v_r), where there are no interactions between electrons. The corresponding energy from electron-electron interactions consists of the Hartree energy and exchange-correlation energy. The effective Hamiltonian of a system containing N non-interacting electrons is written as

$$\hat{H}_r = \sum_{i=1}^{N} \left[-\frac{1}{2}\nabla_i^2 + v_r(r_i) \right] \tag{2-9}$$

where the effective potential includes the external potential ($v_{ext}(r)$), the exchange-correlation potential ($v_{xc}(r)$) and the Hartree potential (v_H), as shown in equation (2-10).

$$v_r(r) = v_{ext}(r) + v_{xc}(r) + v_H \tag{2-10}$$

where
$$v_H(r) = \int dr'[p(r')/|r-r'|] \tag{2-11}$$

The potential of each individual electron (r') generated from the other electron, where the electron interacts with itself, leading to a self-interaction error and an increase of the total energy. The Kohn-Sham equation is written as

$$\left[-\frac{1}{2}\nabla_i^2 + v_r(r_i) \right] \phi_i(r) = \varepsilon_i \phi_i(r) \tag{2-12}$$

By using a trial electronic density in equation (2-10), the Kohn-Sham equation can be solved iteratively. The new generated $p(r)$ then acts as new input of the Kohn-Sham equation. The iteration finishes when reaching a self-consistency with a given convergence criteria. Finally, in the Kohn-Sham equation the total energy is calculated by

$$E[p] = T_r[p] + V_H[p] + V_{ext}[p] + E_{xc}[p] \tag{2-13}$$

where the main contributions come from the Hartree energy, $V_H[p]$, and the term of $E_{xc}[p]$. However, the exchange-correlation functional giving $E_{xc}[p]$ is unknown in equation (2-13). Therefore, many approximations of the exchange-correlation term have been developed for realizing the application of the Kohn-Sham equation.

2.1.6 Exchange-correlation functional

The exchange-correlation energy includes contributions from the exchange energy and correlation energy. The first one comes from the repelling interaction among electrons with the identical spins because they cannot localize in one quantum state. The correlation term is determined by the interaction among individual electrons. The Jacob's ladder of DFT divides exchange-correlation functional into different levels and shows how the functional at each level satisfies research interests.[50] At the bottom of the ladder is the simplest approximation of the exchange-correlation term, the local-density approximation (LDA). LDA is developed by using the assumption that electrons in any system are the same, known as a homogeneous gas.[45,49] The exchange-correlation energy is then written as

$$E_{xc}^{LDA} = \int dr\, p(r)\varepsilon_{xc}^{LDA}[p(r)] \tag{2-14}$$

where ε_{xc}^{LDA} is the exchange-correlation functional of LDA. Considering the spins of electrons, LDA has local spin density appropriation. LDA is applied successfully in systems of small variation in density, but usually over-estimates the energy for more complicated system. LDA is then further expanded into generalized-gradient approximation (GGA) by using the gradient of the electronic density (∇p) and an enhancement factor (F_{xc}), which is expressed as

$$E_{xc}^{GGA} = \int dr\, p(r)\varepsilon_{xc}^{LDA}[p(r)]\, F_{xc}[p(r),\nabla p(r)] \tag{2-15}$$

Among the developed GGA functional, Perdew-Burke-Ernzerhof (PBE) functional[51] is widely used in both molecules and solids systems. However, GGA tends to delocalize electrons, especially for transition metals and rare-earth elements which have a strong localization of the *d* and *f* orbital electrons, leading to the calculated DFT results largely deviating from experimental results.[52] This shortcoming can be reduced by using hybrid functionals, where the self-interaction error can be partially cancelled by using a fraction of Hartree exchange.[53,54]

2.1.7 The Hubbard-*U* correction

Although the developed hybrid functionals can reduce the self-interaction error,[54] its computational cost is high. By contrast, using Hubbard-*U* correction to the electron correlation is much cheaper. The Hubbard parameter U_{eff}=*U*-*J* (*U* is on-site repulsion term and *J* is on-site exchange term) gives corrections to the strong electrostatic interaction. Then the total energy calculated by adding the Hubbard-*U* correction to the normal DFT is

$$E_{DFT+U} = E_{DFT} + \sum_{\sigma} \frac{U_{eff}}{2} (T_r p^{\sigma} - T_r p^{\sigma} p^{\sigma}) \quad (2\text{-}16)$$

where $T_r p^{\sigma}$ traces a density matrix of described electrons with a given projection of spin σ.[55] In this thesis, *U* correction to Ce 4*f* orbitals is used to describe the strong localization of the 4*f* orbital electrons of ceria, which has been widely used for computational studies of electrocatalysis on ceria-based catalysts (more details are given in section 2.2.3).

2.2 DFT Study on Ceria

To simulate the electrocatalytic WSR on ceria, spin-polarized DFT calculations are performed by using the Vienna ab initio simulation package (VASP) software[56,57] with the PBE functional[51] corrected with Hubbard *U* term. In VASP, the wave functions are described by plane wave basis functions, of which the most computationally efficient one is the projector augmented wave (PAW). [58] In PAW method, the DFT calculations are performed for a periodic cell with core electrons of atoms frozen. An energy cutoff controls how many plane waves are applied to reach the accuracy to describe the system. In this thesis, the interactions between the ions and the electrons are described by expanding wave functions in plane waves with an energy cutoff of 550 eV. The Ce (4*f*, 5*s*, 5*p*, 5*d*, 6*s*) and O (2*s*, 2*p*) electrons are treated as valence states. In addition, corrections from sampling Brillouin zone with wave vectors using Γ-centered k-points are added to the PAW. A 15 Å vacuum is introduced to reduce interactions between the periodic cells. The lattice constant of ceria used in the thesis is 5.497 Å, which is calculated by using a dense *Γ*-centered 8×8×8 k-point mesh. The calculated lattice constant is well consistent with both theoretical (5.497 Å[25,59–61]) and experimental values (5.411 Å[62]).

2.2.1 Nudged elastic band method

Searching the transition state (TS) between the stable initial state (IS) and the final state (FS) is to find a saddle point on the potential energy landscape, which is a local minimum only at one direction. Thus, the TS can be further verified with only one imaginary vibrational mode. For the identifications of transition states as well as activation energies for oxygen vacancy diffusion, water dissociation into hydroxyls and hydroxyl decomposition releasing H_2 in this thesis, the climbing image nudged-elastic band method (CI-NEB) as implemented in VASP [63] with a force tolerance of 0.03 eV /Å is applied.

Some guessed images are created between the IS and FS in a NEB calculation and kept evenly distributed by using spring forces (setting SPRING parameter in VASP) during the search of the minimum reaction path. While for CI-NEB, only the image having the highest energy is not under control of the spring forces, the energy of which is minimized from all directions until reaching the saddle point. However, it is computationally expensive if the highest energy image is far from the saddle point. Thus, a better solution is to start from a regular NEB guess then shift to CI-NEB to search the TS.

2.2.2 The Brønsted−Evans−Polanyi (BEP) relation

The Brønsted−Evans−Polanyi (BEP) relation states that a number of similar reactions at different metal surfaces in homogeneous systems show a linear relation between the activation energy (E_a) and the reaction energy ($E_f = E_{FS}-E_{IS}$).[40,64] The BEP relation indicates that the activation energy is strongly dependent on bindings of reactants to the metal surfaces, etc. Strong adsorption of reacts on metals leads to higher activation barriers, which has been widely used in DFT calculations to get insights in homogeneous catalysis. This thesis also investigates the BEP relation for hydrogen production via the WSR on ceria-based catalysts.

2.2.3 Choice of U_{eff} parameter

This section is based on the discussion of U_{eff} in Paper 1. Readers do not need to refer to Paper 1 for more information.

The optimal value of the Hubbard U parameter for cerium varies in the range of $0 < U_{eff} < 10$ eV depending on the quantity of interest.[27,52,65,66] The reduction energy of ceria is well described already at $U_{eff} \approx 2.0$ eV[65] while the calculated band gap is consistent with experiments at $U_{eff} > 5.5$ eV.[27] Initially, this thesis investigates the formation of

oxygen vacancies as well as the reaction kinetics of the hydroxyl decomposition on a $CeO_2(111)$ surface built as a 2×2 repeated surface unit cell with three atomic layers at the bottom fixed, aiming at finding out the best choice of U_{eff} for the WSR on ceria-based surface. The candidate U_{eff} is expected to appropriately describe the strong localization of the 4*f* electrons of reduced ceria, and the hydrogen adsorption on ceria during the hydroxyl decomposition into H_2.

It is found that the oxygen vacancy formation energy (E_{Vo}) and the barrier for the hydroxyl decomposition over $CeO_2(111)$ are strongly correlated with the values of U_{eff}, as shown in **Figures 2-1 and 2-2**. As noted from **Figure 2-1**, E_{Vo} linearly decreases with increasing U_{eff} when U_{eff} is larger than 3.5 eV. Electrons delocalize on the 4*f* orbitals of ceria at U_{eff} < 3.5 eV, consistent with the findings reported by Castleton *et al.* that charge starts to localize at U_{eff} ≈3.0 eV.[27] The degree of localization was reported to reach a maximum at U_{eff} ≈5.5 eV for the GGA+*U* method.[27] Thus, 3.5 < U_{eff} < 5.5 eV is proper for the description of the V_O in the ceria system investigated in this thesis. However, the stability of the hydroxylated $CeO_2(111)$ is overestimated largely when using a large U_{eff}, leading to an increase of the calculated barrier for the hydroxyl decomposition into H_2 on $CeO_2(111)$, as shown in **Figure 2-2**. In addition, it was reported that U_{eff} > 4.0 eV tends to overestimate the binding energy of CO to ceria surfaces.[59] Herein, a medium value of U_{eff} = 4.5 eV is used in this thesis, which is large enough to describe the strong localization of Ce 4*f* electrons but slightly overestimates the hydrogen adsorption during the hydroxyl decomposition. U_{eff} =4.5 eV has often been used for investigations on vacancy diffusion and related reactions on ceria.[25,67–69] In addition, the vacancy formation energy and the activation barrier for the hydroxyl decomposition on $CeO_2(111)$ calculated in this thesis agree well with previously reported DFT results.[25,26,70] Thus, U_{eff} =4.5 eV used in this thesis is appropriate to describe the electrochemical properties of ceria during the WSR.

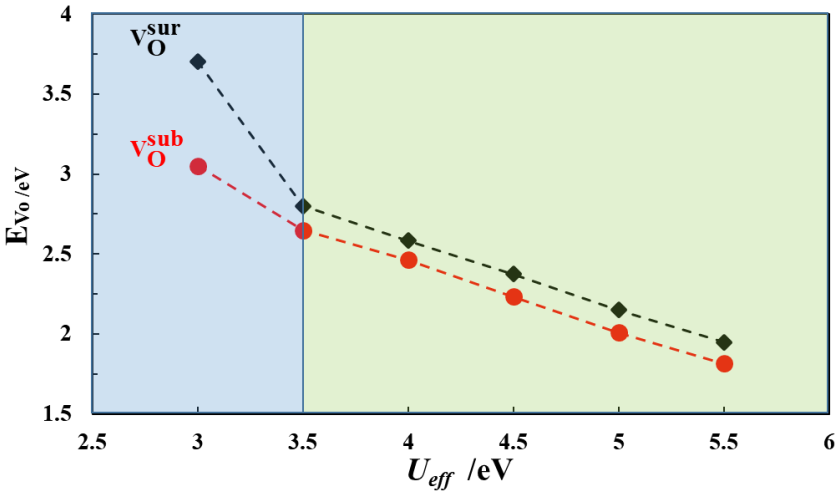

Figure 2-1. Vacancy formation energy (E_{Vo}) in $CeO_2(111)$ as a function of values of U_{eff}=*U*-*J* (*J*=0).

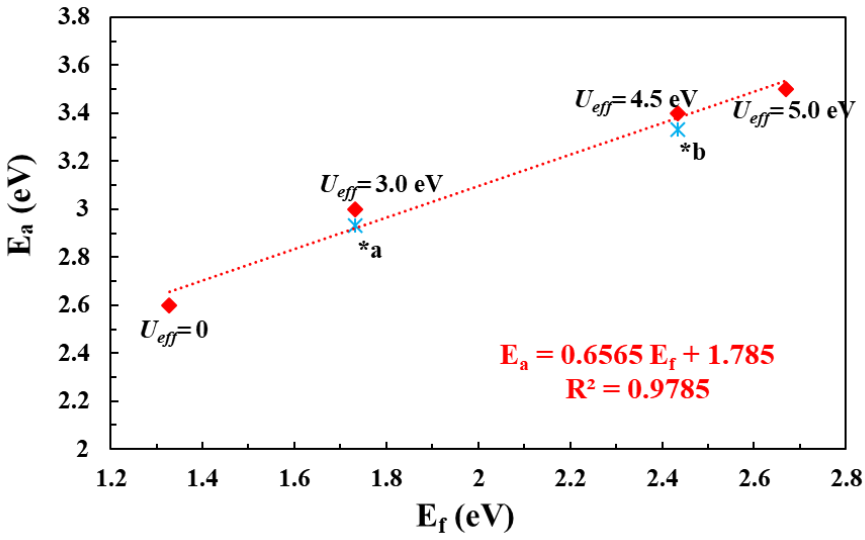

Figure 2-2. Activation barriers (E_a) of the hydroxyl decomposition into H_2 on $CeO_2(111)$ as a function of the reaction energy ($E_f = E_{FS}-E_{IS}$): *a[21] and *b[70].

2.2.4 From DFT energy to Gibbs free energy

This section is based on the discussion of how to calculate the free energy of the reduced ceria in the supporting information of Paper 1. Readers do not need to refer to Paper 1 for more information.

In order to calculate the free energy of surfaces with different coverages of oxygen vacancies and hydrogen, the surface is assumed in equilibrium with reservoirs of water and oxygen molecules. A "slab(N_H, N_{V_O})" ceria surface with N_H excess H atoms and N_{V_O} excess oxygen vacancies can be formed via the reaction between water and vacancies at a reference surface "slab(0, 0)", as shown in equation (2-17).[21]

$$\text{slab}(0,0)+\frac{N_H}{2}H_2O \leftrightarrow \text{slab}(N_H, N_{V_O})+(\frac{N_H}{4}+\frac{N_{V_O}}{2})O_2 \qquad (2\text{-}17)$$

The total free energy of the reduced ceria adsorbed with two hydrogen (2H) is written as

$$\Delta G(2H) = E(2H)-E(0,0)+\frac{1}{2}E(O_2)-E(H_2O)+\Delta\Delta G(2H) \qquad (2\text{-}18)$$

where $E(2H)$, $E(0, 0)$, $E(O_2)$ and $E(H_2O)$ are the calculated DFT energies of the 2H covered surface, the reference surface, an oxygen molecule, and a water molecule,

respectively. $\Delta\Delta G(2H)$ is a temperature and pressure dependent correction to the free energy as expressed by

$$\Delta\Delta G(2H) = F_{vib}(2, 0)-F_{vib}(0, 0) + \frac{1}{2}(\mu_{O_2}(\rho^0, T) + K_B T \ln (\rho_{O_2}/\rho^0) + ZPE_{O_2}) -(\mu_{H_2O}(\rho^0, T) + K_B T \ln (\rho_{H_2O}/\rho^0) + ZPE_{H_2O} \quad (2\text{-}19)$$

where $F_{vib}=\sum_i {}^1/_2 hv_i+\sum_i K_B T \ln(1-\exp(hv_i/(K_B T))$ is the vibrational free energy of the surface. It is approximated from the harmonic vibrational frequencies, v_i. $F_{vib}(2, 0)$ is the vibrational free energy of the ceria surface adsorbed with 2H. ZPE is the zero point energy of the surface.$\mu_{O_2}(\rho^0, T)$ and $\mu_{H_2O}(\rho^0, T)$ represent the chemical potential of O_2 and H_2O at temperature (T) and standard pressure (ρ^0), respectively, which can be taken from the online NIST-JANAF thermodynamic tables.[71]

The free energy of the reduced ceria having one oxygen vacancy is expressed by using the equation of

$$\Delta G(V_O) = E(V_O)-E(0, 0)+\frac{1}{2}E(O_2)+\Delta\Delta G(V_O) \quad (2\text{-}20)$$

$$\Delta\Delta G(V_O) = F_{vib}(0, 1)-F_{vib}(0, 0)+\frac{1}{2}\left(\mu_{O_2}(\rho^0, T)+ K_B T \ln (\rho_{O_2}/\rho^0) + ZPE_{O_2}\right) \quad (2\text{-}21)$$

For any slab(N_H, N_{V_O})surface, the formation free energy $\Delta G(N_H, N_{V_O})$ includes contributions from DFT energies, $\Delta E(N_H, N_{V_O})$ and thermodynamic corrections, $\Delta\Delta G(N_H, N_{V_O})$, as shown in equation (2-22).

$$\Delta G(N_H, N_{V_O}) = \Delta E(N_H, N_{V_O})+\Delta\Delta G(N_H, N_{V_O}) \quad (2\text{-}22)$$

where $$\Delta\Delta G(N_H, N_{V_O}) = F_{vib}\left(N_H, N_{V_O}\right)-F_{vib}(0, 0) + \frac{1}{2}\left(N_{V_O}+\frac{1}{2}N_H\right)\left(\mu_{O_2}(p^0, T)+K_B T \ln\left(\frac{p_{O_2}}{p^0}\right)+ZPE_{O_2}\right) -\frac{1}{2}N_H\left(\mu_{H_2O}(p^0, T)+K_B T \ln\left(\frac{p_{H_2O}}{p^0}\right)+ZPE_{H_2O}\right) \quad (2\text{-}23)$$

By using an assumption that the interaction between vacancies and hydroxyls do not contribute to the vibrational free energy, $F_{vib}(N_H, N_{V_O})$ in equation (2-23) is approximated as

$$F_{vib}(N_H, N_{V_O}) = \frac{1}{2}N_H(F_{vib}(2, 0)-F_{vib}(0, 0)) + N_{V_O}(F_{vib}(0, 1)-F_{vib}(0, 0))+F_{vib}(0, 0) \quad (2\text{-}24)$$

By using the expression of $F_{vib}(N_H, N_{V_O})$ in equation (2-24), $\Delta\Delta G(N_H, N_{V_O})$ in equation (2-23) can be written as

$$\Delta\Delta G(N_H, N_{V_O}) = \frac{1}{2}N_H\left(F_{vib}(2, 0)- F_{vib}(0, 0)\right) + N_{V_O}\left[F_{vib}(0, 1)- F_{vib}(0, 0)\right]+ F_{vib}(0, 0)-F_{vib}(0, 0) + \frac{1}{2}\left(N_{V_O}+\frac{1}{2}N_H\right)\left(\mu_{O_2}(\rho^0, T)+ K_B T \ln(\rho_{O_2}/\rho^0\right) - \frac{1}{2}N_H(\mu_{H_2O}(\rho^0, T) + K_B T \ln(\rho_{H_2O}/\rho^0) + ZPE_{H_2O}) \quad (2\text{-}25)$$

Based on equation (2-25), $\Delta\Delta G(N_H, N_{V_O})$ can be further written as the sum of contributions from $\Delta\Delta G(2H)$ and $\Delta\Delta G(V_O)$ as shown in equation (2-26).

$$\Delta\Delta G(N_H, N_{V_O}) = \frac{1}{2}N_H\left[F_{vib}(2, 0)-F_{vib}(0, 0)+\frac{1}{2}\left(\mu_{O_2}(\rho^0, T) + K_B T \ln(\rho_{O_2}/\rho^0\right) - \left(\mu_{H_2O}(\rho^0, T) + K_B T \ln(\rho_{H_2O}/\rho^0\right)\right] + N_{V_O}\left[F_{vib}(V_O)-F_{vib}(0, 0)+\frac{1}{2}\left(\mu_{O_2}(\rho^0, T) + K_B T \ln(\rho_{O_2}/\rho^0)\right)\right]$$

$$= \frac{1}{2}N_H\Delta\Delta G(2H)+N_{V_O}\Delta\Delta G(V_O) \quad (2\text{-}26)$$

Finally, $\Delta G(N_H, N_{V_O})$ of any reduced ceria can be calculated by using equation (2-27) after knowing $\Delta\Delta G(2H)$ in equation (2-19) and $\Delta\Delta G(V_O)$ in equation (2-21).

$$\Delta G(N_H, N_{V_O}) = \Delta E(N_H, N_{V_O})+\Delta\Delta G(N_H, N_{V_O}) = \Delta E(N_H, N_{V_O})+\frac{1}{2}N_H\Delta\Delta G(2H)+N_{V_O}\Delta\Delta G(V_O) \quad (2\text{-}27)$$

Chapter 3. The WSR on Gadolinium Doped CeO_2(111)

This chapter is based on Paper1, which has been included in Appendix B.1. The supplemental information of Paper 1 that has also been included in Appendix B.1.

3.1 Introduction

Computational studies have shown that hydrogen production through the WSR at the ceria/gas interface would be facile once oxygen vacancies can diffuse from bulk to the top surface.[21] Improved ionic conductivity increases the reaction efficiency of ceria, and doping ceria is a promising approach for improving the ionic conductivity and the electrochemical activity of ceria for hydrogen production. Gadolinium doped ceria (GDC) has been demonstrated to have the highest ionic conductivity among ceria-based materials,[72] which allows the electrochemical reactions at intermediate temperature (773-1073 K).[73,74] Therefore, GDC holds great potentials for hydrogen production, through H_2O electrolysis in SOECs. So far, computational studies on GDC have been limited to electronic structures and properties related to oxygen diffusions.[61,75,76] Therefore, the fundamental understanding of the reaction mechanism for the WSR on the pure ceria and especially the doped ceria in SOECs remains elusive.

By using DFT+*U*, this chapter investigates the formation and diffusion of oxygen vacancies, as well as hydroxyl formation and decomposition on ceria and GDC, respectively. The effect of Gd doping on the stability of the reduced ceria surface by creating oxygen vacancies and formation of hydroxyls, and the effect of Gd doping on the reaction pathways for the WSR are discussed to obtain a more clear understanding of the WSR on the doped ceria.

3.2 Simulation Details

The CeO_2(111) surface is built as a 2×3 repeated surface unit cell consisting of nine atomic layers ($Ce_{18}O_{36}$). Three atomic layers at the bottom are fixed as shown in **Figure 3-1**. The calculated equilibrium lattice constant of bulk ceria is 5.497 Å, which is well consistent with the reported DFT result[25,61] but overestimates the experimental lattice constant of 5.411 Å[62] by 1.6 %. The lattice constant has a 1.4% mismatch with the experimental lattice constant of $Ce_{0.8}Gd_{0.2}O_{1.9}$ (5.423 Å)[36]. The lattice with the same mismatch has been used by Aparicio-Anglès et al. for investigations of dopant clustering near the GDC(111) surface.[61] The previous studies have shown that the

highest ionic conductivity is obtained in ceria with 10% Gd concentration.[61,77] In this chapter, two cerium atoms in $Ce_{18}O_{36}$ (111) are replaced with two gadolinium atoms to reach a Gd concentration of 11%. The selected system size allows for investigations of compensating oxygen vacancies near the optimal doping level, because two Gd^{3+} dopants are expected to induce the formation of an oxygen vacancy. The $Gd_2Ce_{16}O_{35}$(111) surface is investigated as the GDC model in this chapter. A Γ-centered 3×2×1 k-point mesh is used for optimization of all surfaces. Other parameters used for the DFT calculations refer to the section 2.2 of Chapter 2.

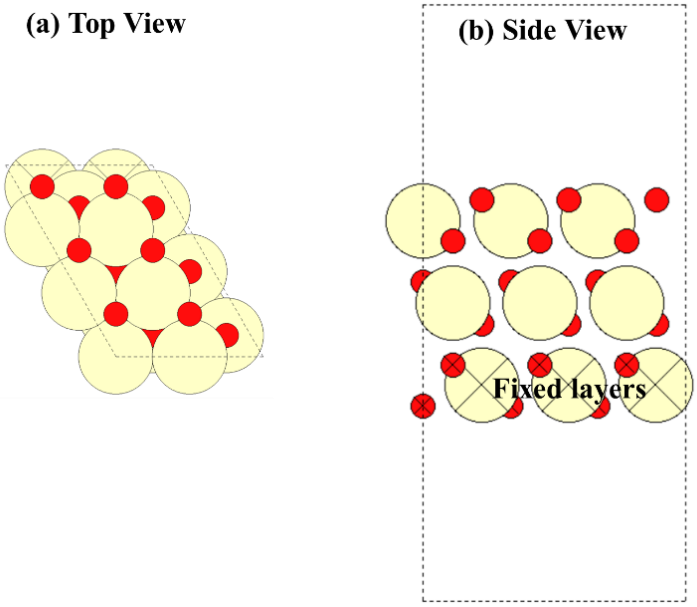

Figure 3-1. CeO_2(111) surface model ($Ce_{18}O_{36}$): (a) top and (b) side views. Yellow and red balls stand for cerium and oxygen atoms, respectively. The balls with crosses represent fixed atoms.

3.3 Results and Discussions

3.3.1 Distribution of Gd and oxygen vacancies in $Gd_2Ce_{16}O_{35}$(111)

Firstly, GDC without a compensating oxygen vacancy is created by substituting one Gd atom into the surface layer and another Gd atom into either the surface or subsurface layer. The distribution of the two Gd atoms is labelled from Type1 to Type4 with increasing Gd-Gd distance as shown in **Figure 3-2(a)**. The uncompensated situation was normally investigated for aliovalent dopants in CeO_2.[61,78] Based on the four uncompensated configurations of the $Gd_2Ce_{16}O_{36}$(111), a compensating oxygen vacancy (V_O) is then introduced into one oxygen atomic layer, leading to the formation of $Gd_2Ce_{16}O_{35}$(111). The V_O formation energy in GDC is defined as:

$$E_{V_O}=E_{Gd_2Ce_{16}O_{35}}-E_{Gd_2Ce_{16}O_{36}}+\frac{1}{2}E_{O_2} \quad (3\text{-}1)$$

where $E_{Gd_2Ce_{16}O_{35}}$ is the total energy of the GDC after creating an oxygen vacancy, $E_{Gd_2Ce_{16}O_{36}}$is the total energy of the uncompensated system, and E_{O_2} is the energy of an oxygen molecule.

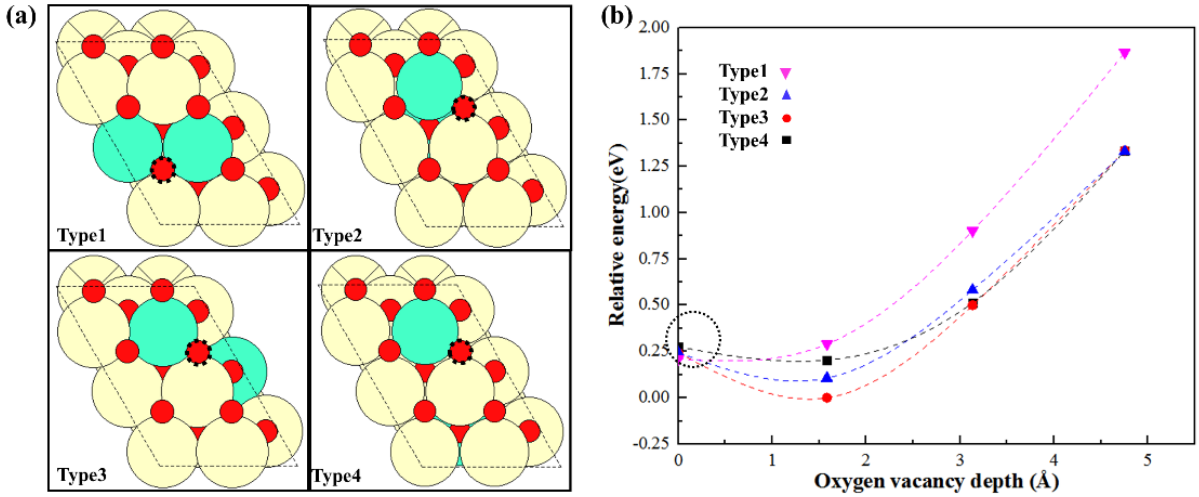

Figure 3-2: (a) Configurations of the most stable vacancy in the top surface (depth = 0.0 Å) of the $Gd_2Ce_{16}O_{35}$(111) with Type1, Type2, Type3 and Type4 Gd distribution. Color legend: yellow for cerium, green for gadolinium and red for oxygen atoms. The balls with crosses represent the fixed atoms, whereas red balls with a dashed perimeter mark the oxygen vacancy. (b) Relative energy of creating an oxygen vacancy at different depths in the $Gd_2Ce_{16}O_{35}$(111) with four types of Gd distribution. The depth is measured from the top of the surface.

The formation energy of an oxygen vacancy in the subsurface (V_O^{sub}) and top surface (V_O^{sur}) in the uncompensated system to form $Gd_2Ce_{16}O_{35}$ (111) is list in **Table 3-1**. Creating one V_O^{sub} in Type3 is more facile than that in GDC with other types of Gd distribution. Taking the energy of the V_O^{sub} in Type3 as a reference, the relative energy of creating one Vo in each oxygen atomic layer in $Gd_2Ce_{16}O_{35}$(111) with four types of Gd distribution as a function of the distance from the top oxygen layer to the Vo location (depth) is given in **Figure 3-2(b)**. For Type 1 GDC, the V_O favors to be created in the top surface, in comparison with creating one V_O in the subsurface and deeper layers. However, for Type2, Type3 and Type4 with two gadolinium atoms sitting in two different atomic layers, the most favorable oxygen vacancy location is in the subsurface oxygen layer. The relative energy of creating one V_O in these GDC model increases when the vacancy is created in the deeper oxygen layers (depth > 1.5 Å) and the two excess electrons remain localized on the two gadolinium atoms. The energy difference

between the V_O^{sur} with four types of Gd distribution is lower than 0.006 eV, as displayed in **Table 3-1**. Compared to the V_O^{sur}, a slightly larger energy difference (within 0.23 eV) between the V_O^{sub} with four types of Gd distribution is found, consistent with Aparicio-Anglès's findings that the V_O formation difference between Gd distribution is within 0.25 eV.[61] However, the energy difference between the four different types of Gd distribution in $Gd_2Ce_{16}O_{36}$ is within 0.065 eV as presented in **Table 3-1**. In addition, It is found that the calculated energy difference between the formation energy of $Gd_2Ce_{16}O_{35}$ having one oxygen vacancy in the top surface with four types of Gd distributions is < 0.066 eV. For oxygen vacancy in the subsurface, the energy difference is < 0.291 eV as shown in **Table 3-2**. Thus, the above DFT+*U* results suggest that Gd can distribute freely in the top surface or subsurface of the $Gd_2Ce_{16}O_{35}$(111) at 11% Gd concentration. These results are in line with the previously reported findings.[61]

In addition, the calculated formation energy of an oxygen vacancy in the top surface of the clean $Ce_{18}O_{36}$(111) is 2.18 eV, which is closed to 2.15 eV calculated for a p(3×3) unit cell by using U_{eff} =4.5 eV.[25] The calculated formation energy for a slightly larger p(3×4) unit cell is only 0.16 eV smaller than that calculated by using p(2×3) unit cell, agreeing well with the findings reported by Hui-Ying et al[79] that the interaction between oxygen vacancy in neighbored supercells could be neglected. Because introducing a compensating oxygen vacancy into the uncompensated $Gd_2Ce_{16}O_{36}$ system is preferred, the V_O formation energies in $Gd_2Ce_{16}O_{36}$ with four types of Gd distribution are negative values.

Table 3-1. Minimum Gd-Gd distance in the four types of Gd distribution in $Gd_2Ce_{16}O_{36}$ (111) and the relative energy between them. The formation energy of one oxygen vacancy (V_O) in the uncompensated system to form $Gd_2Ce_{16}O_{35}$ (111). V_O in the subsurface and in the top surface layer is abbreviated as V_O^{sub} and V_O^{sur}, respectively.

Gd distribution type	Gd-Gd Distance /Å	Relative Energy/eV	V_O^{sub}/eV	V_O^{sur}/eV
Type1	3.982	0	-0.725	-0.783
Type2	4.014	0.040	-0.927	-0.789
Type3	5.489	0.039	-0.957	-0.787
Type4	6.717	0.065	-0.855	-0.783
$Ce_{18}O_{36}$(111)	/	/	1.808	2.184

Table 3-2. The formation energy of $Gd_2Ce_{16}O_{35}$ with an oxygen vacancy created in the top surface or subsurface is calculated by the reaction of Gd_2O_3 + $Ce_{18}O_{36}$ –> $Gd_2Ce_{16}O_{35}$ + $2CeO_2$. The four different types of Gd distribution are considered.

Gd distribution type	Type4	Type3	Type2	Type1
$E_f(Gd_2Ce_{16}O_{35}, V_O^{sur})$/eV	-1.712	-1.745	-1.743	-1.778
ΔE/eV	< 0.066			
Gd distribution type	Type4	Type3	Type2	Type1
$E_f(Gd_2Ce_{16}O_{35}, V_O^{sub})$/eV	-1.784	-1.988	-1.881	-1.697
ΔE/eV	< 0.291			

3.3.2 Reduced GDC and ceria

Increased surface reduction has been observed to improve the activity of ceria for H_2 production.[21,35] Herein, the reduced ceria and GDC having oxygen vacancies (V_O) and hydroxyls via reaction (1-2) and (1-3) are investigated. The magnetizations of the reduced cerium or gadolinium atoms refer to Figures S5-S7 in the supplemental information of Paper 1. It is found that the V_O^{sub} in Type1 is 0.202 eV less stable than the V_O^{sub} in Type2. However, the difference in the formation energy of one V_O in the top surface of Type1 and Type2 is very small (6 meV), which indicates a similar formation of the top surface vacancy in GDC regardless of the Gd distribution. In addition, among the four considered types of Gd distribution, the V_O formation energies in Type2 and Type3 are the lowest and closed to each other. Therefore, Type2 is chosen as a model of 2Gd distributing on the two different layers. Then, V_O and hydroxyl formation in Type2 GDC, Type1 GDC where 2Gd distribute in the top layer, and the pure CeO_2 are investigated.

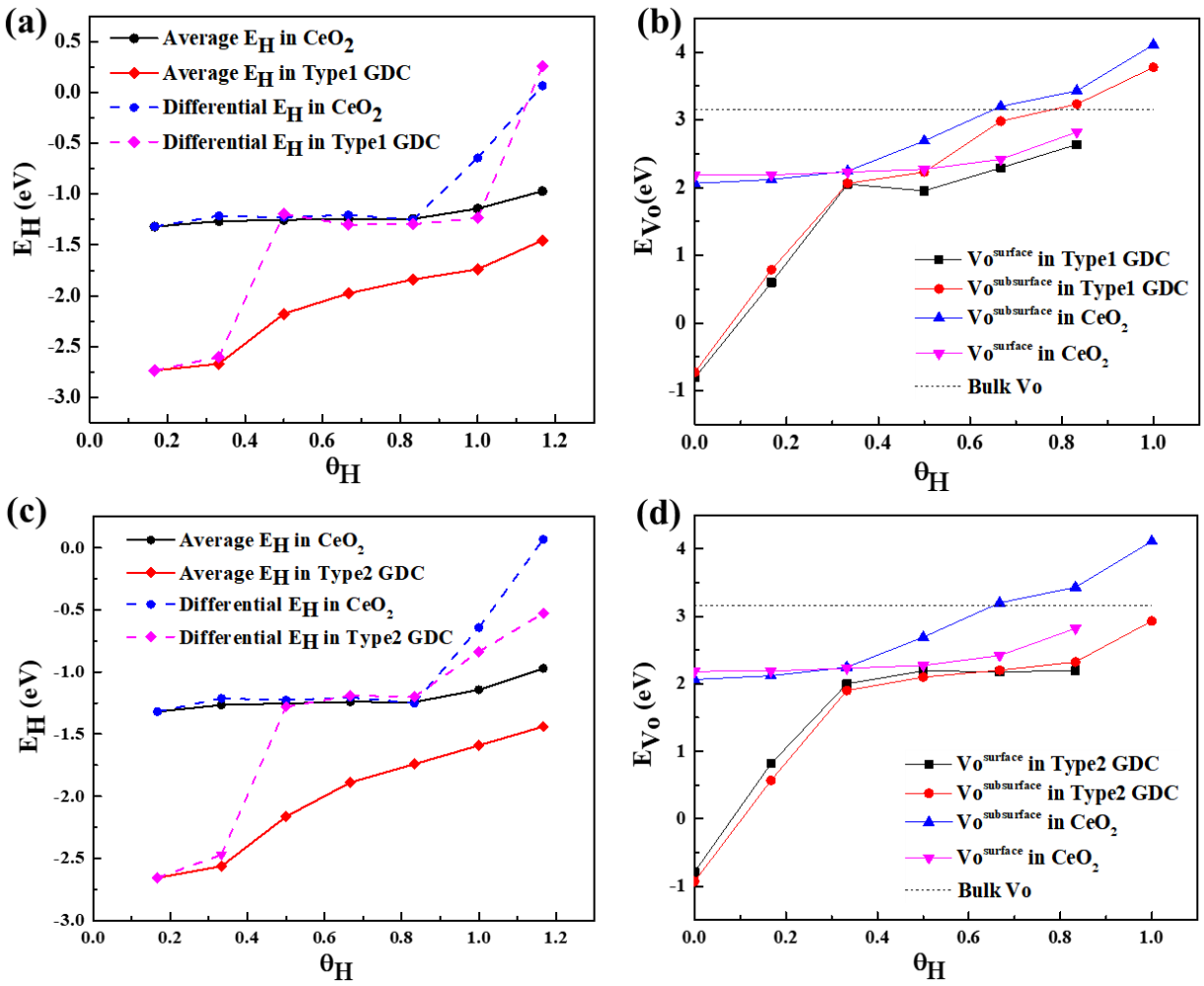

Figure 3-3. The formation energy of hydroxyls (E_H) as a function of hydrogen coverage (Θ_H) on Type1 GDC (a) and Type2 GDC (c) as compared to the E_H on the pure CeO_2; The formation energy of an oxygen vacancy (E_{V_O}) as a function of Θ_H in Type1 GDC (b) and Type2 GDC (d) as compared to E_{V_O} calculated in the pure CeO_2.

Figure 3-3 shows the average and differential formation energy of hydroxyls, E_H, and formation energies of creating one oxygen vacancy, E_{V_O}, as a function of hydrogen coverage in Type1 and Type2 GDC as compared to the pure ceria. Here, the hydrogen coverage $\Theta_H = N_H/N$ is used to distinguish surfaces with different degrees of reduction by hydrogen adsorption, which is defined as the number of the adsorbed hydrogen (N_H) divided by the total number of oxygen (N=6 in this chapter) in the top layer. As noted from **Figure 3-3**, the average E_H increases with the increasing Θ_H. When the GDC surface has one or two hydroxyls, the differential E_H on GDC is about 1.4 eV more negative than that on ceria, which again is due to the strong driving force to create Gd^{3+}

rather than Ce^{3+}. After two hydroxyls form on GDC, Ce^{4+} ions are reduced to Ce^{3+} near the surface hydroxyls because of the further reduction, leading to the differential E_H in Type1 and Type2 closed to that in ceria when hydrogen coverage ranges from 0.5 to 0.83. Forming one more hydroxyl at Θ_H=0.83, the differential E_H increases dramatically, which indicates the repulsive interaction between the hydroxyls and the reduced surface. When the hydrogen coverage increases beyond one monolayer, the additional hydrogen reacts with one lattice oxygen ion in the subsurface, forming one subsurface hydroxyl (subO-H), which is unfavorable compared to other surface hydroxyls. The differential energy required for the formation of the subO-H in Type2 GDC is much more negative than that in ceria and Type1 GDC, which means that the formation of the subO-H is relatively favorable in Type2 GDC. Overall, the average E_H in both Type1 and Type2 GDC is much more negative than that in ceria. Therefore, the formation of the reduced ceria via forming hydroxyls is significantly favorable by the incorporation of Gd.

At the hydroxylated surfaces, E_{Vo} increases with increasing hydrogen coverage. However, E_{Vo} in GDC is more negative than that in ceria, which reveals that creating a V_O^{sub} or V_O^{sur} in the hydoxylated GDC is much easier than in the hydroxylated ceria. As for creating one V_O in the hydroxylated ceria surface, V_O^{sub} is more favorable than V_O^{sur} at $\Theta_H < 0.4$. In Type2 GDC, forming a V_O^{sub} can be favored until the hydrogen coverage reaches 0.8. By contrast, the V_O^{sur} is always more favorable than the V_O^{sub} in Type1 GDC at all hydrogen coverages. For comparison. the Vo formation energy in the bulk (a 2×2×2 cubic cell) is 3.16 eV, which is closed to the value of 3.10 eV calculated by Tang et al.[80] The V_O in the Type2 GDC surface is more stable than the bulk V_O when the surface is fully hydroxylated. While the V_O is unstable in the Type1 GDC surface and in ceria at $\Theta_H > 0.67$. Therefore, GDC especially Type2 GDC can easily be reduced by forming hydroxyls and creating V_O. Thus, Type2 GDC is used as the GDC model for the following kinetic studies of the V_O diffusion, water dissociation and hydroxyl decomposition.

In addition, the relative stability of subsurface and surface oxygen vacancies in CeO_2 with and without Gd doping at different H coverages can be attributed to the relative repulsion between vacancies and hydroxyls based on the charge distributions on the reduced surface, referring to Page S10 in the supporting information of Paper 1.

3.3.3 The reaction barriers at each reaction step of the WSR on reduced GDC and reduced ceria

3.3.3.1 Barriers for V_O diffusion

When forming one V_O^{sur} in ceria, $2Ce^{4+}$ are reduced to $2Ce^{3+}$, where one Ce^{3+} ion locates in the nearest neighbored site relative to the oxygen vacancy and the other Ce^{3+} sits in the next nearest neighbored (NN-NNN) position. The same Ce^{3+} distribution on the most stable V_O^{sur} has been reported by Su et al.[25] and Ganduglia-Pirovano et al.[26] calculated by using U_{eff} =4.5 eV. In addition, the calculated formation energy of the V_O^{sur} (2.18 eV) is closed to the formation energy of 2.15 and 2.34 eV calculated by Su et al. and by Ganduglia-Pirovano et al, respectively. Although the same configuration of the V_O is reported by using PBE+U (U_{eff} =3.0 eV),[21] the total formation energy of the V_O^{sur} (2.78 eV) is about 0.6 eV larger than the values calculated by using U_{eff} =4.5 eV in this chapter, arising from the electrons delocalization on the 4*f* orbitals of ceria using U_{eff} =3.0 eV.

The most stable V_O in GDC has electrons localized on two gadolinium atoms. Creating one more V_O in GDC, the most favorable configuration has the second V_O in the subsurface, where the two more compensating electrons localized on $2Ce^{3+}$ in the NN positions relative to the V_O. The formation energy of creating two V_O in the top surface is very closed to that of creating one V_O in the top surface and the other V_O near the Gd in the subsurface. The most stable configuration of the GDC with the second V_O in the top surface has two electrons localized on two cerium atoms next to the V_O. By using the NEB method, the barriers for the oxygen vacancy diffusion from the subsurface to the top surface in ceria having one V_O, and in GDC having one and two oxygen vacancies are identified. In one vacancy system, the diffusion barrier is 0.15 eV in GDC and 0.65 eV in ceria, as shown in **Figure 3-4(a)**. The ionic conductivity in ceria is improved significantly by the incorporation of gadolinium in the "one-vacancy" system. A 0.64 activation barrier for oxygen vacancy diffusion at the same Vo concentration in ceria has been reported by Chen et al.[81] However, the barrier for the vacancy diffusion from the subsurface to the surface increases to 1.5 eV when two vacancies are created in GDC, referring to Figure S8 in the supporting information of Paper 1. Although the mobility of oxygen decreases when two vacancies exit in GDC, it is still a facile reaction as compared to the hydroxyl decomposition where breaking the strong O-H bond has a 2.93 eV activation barrier.[21]

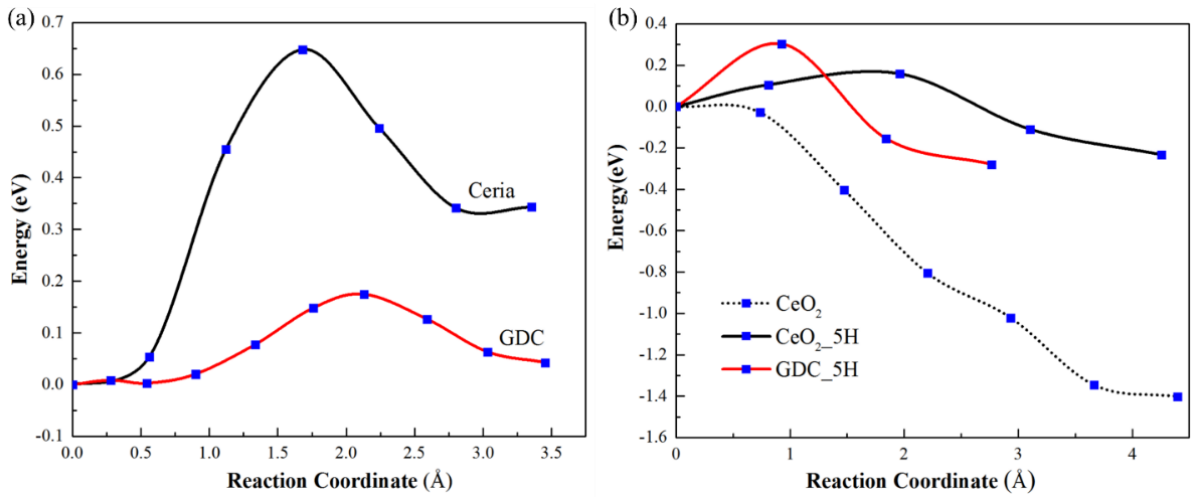

Figure 3-4. (a) Oxygen vacancy diffusion from the subsurface to the surface in ceria and GDC. (b) Water dissociation into hydroxyls on the ceria, the 5H covered ceria, and the 5H covered GDC, respectively.

3.3.3.2 Barriers for water dissociation

It is easy for water to adsorb on the ceria or GDC surface after creating oxygen vacancies on them. The most stable configuration for adsorption of one water molecule on the $CeO_2(111)$ surface is where water adsorbs at next nearest neighbored position relative to the oxygen vacancy. On a highly reduced surface where having five hydroxyls and an oxygen vacancy, the most stable site for one water adsorption is near a cerium or gadolinium atom next to the V_O^{sur}, referring to Figure S9 in the supporting information of Paper 1. The reaction barriers for the water dissociation into hydroxyls are calculated and presented in **Figure 3-4(b)**. On the ceria surface having one V_O^{sur} (the dotted line), the water dissociates into two hydroxyls via the reaction in equation (1-3). The migration of the V_O from the subsurface to the surface provides a vacant site in the surface, which can accommodate one OH coming from H_2O. The other H from H_2O binds with the nearest neighbored lattice O in the surface, forming a second OH. The reaction barrier for water dissociation into 2OH is closed to zero and thus it is facile to perform water dissociation at the ceria surface. A similar reaction pathway and barrier for water dissociation has been demonstrated previously.[21] No reaction path for water dissociation via the reaction of

$$H_2O_{ads} + 2Gd^{3+} + V_O + O^{2-} \rightarrow 2OH^- + 2Gd^{3+} \qquad (3\text{-}2)$$

on the GDC having one V_O^{sur} is presented because the activation energy is negligible.

Because of the low barrier for water dissociation into hydroxyls, it is possible to form more hydroxyls on the ceria and GDC surface. When the ceria and GDC surface are covered by five hydroxyls, one oxygen vacancy is created in the surface in order to form seven hydroxyls (excessively hydroxylated surface) via water dissociation. The water dissociates into such highly reduced ceria surface via the reaction of

$$H_2O_{ads} + 7Ce^{3+} + 5OH^- + V_0 + O^{2-} \rightarrow 7OH^- + 7Ce^{3+} \quad (3\text{-}3)$$

where one OH from H_2O takes the place of the Vo while the H of H_2O reacts with one subsurface oxygen ion of the ceria to form one subsurface hydroxyl (subO-H). This subO-H is unfavorable compared to other surface hydroxyls as discussed in **Figure 3-2**. On the 5OH covered GDC surface, water dissociates into 7OH via the reaction of

$$H_2O_{ads} + 2Gd^{3+} + 5Ce^{3+} + 5OH^- + V_0 + O^{2-} \rightarrow 7OH^- + 2Gd^{3+} + 5Ce^{3+} \quad (3\text{-}4)$$

where one OH from water takes the place of the Vo while the H of water reacts with the subsurface oxygen that is nearest neighbor to Gd. In Comparison with the facile formation of the 2OH on the surface, the kinetic barriers for the water dissociation to form the 7OH on the 5H covered ceria and 5H covered GDC increase slightly to 0.2 and 0.3 eV, respectively. Thus, it is easy to form fully and excessively hydroxylated ceria and GDC via reactions between water and oxygen vacancies.

3.3.3.3 Barriers for hydroxyl decomposition

After oxygen vacancies have diffused to the surface and reacted with the adsorbed water to form hydroxyls on ceria, the last step of the WSR is the hydroxyl decomposition into H_2, which is widely reported as the RDS during many hydroxyl-associated reactions.[6,21,69,80] The reaction barriers for the hydroxyl decomposition on ceria ($Ce_{18}O_{36}$), GDC ($Gd_2Ce_{16}O_{36}$) and GDC having a compensating subsurface V_O (GDC_subVo, $Gd_2Ce_{16}O_{35}$) are presented in **Figure 3-5**. The hydroxyl decomposition on the ceria surface proceeds via the reaction as given in equation (1-4). While the reaction of the hydroxyl decomposition on the GDC is

$$2OH^- + 2Gd^{3+} \rightarrow H_2 + 2Gd^{3+} + 2O^{2-} + 2h^+ \quad (3\text{-}5)$$

on the GDC_subVo surface, the hydroxyl decomposition proceeds via the reaction of

$$2OH^- + 2Gd^{3+} + V_0 \rightarrow H_2 + 2Gd^{3+} + V_O + 2O^{2-} \quad (3\text{-}6)$$

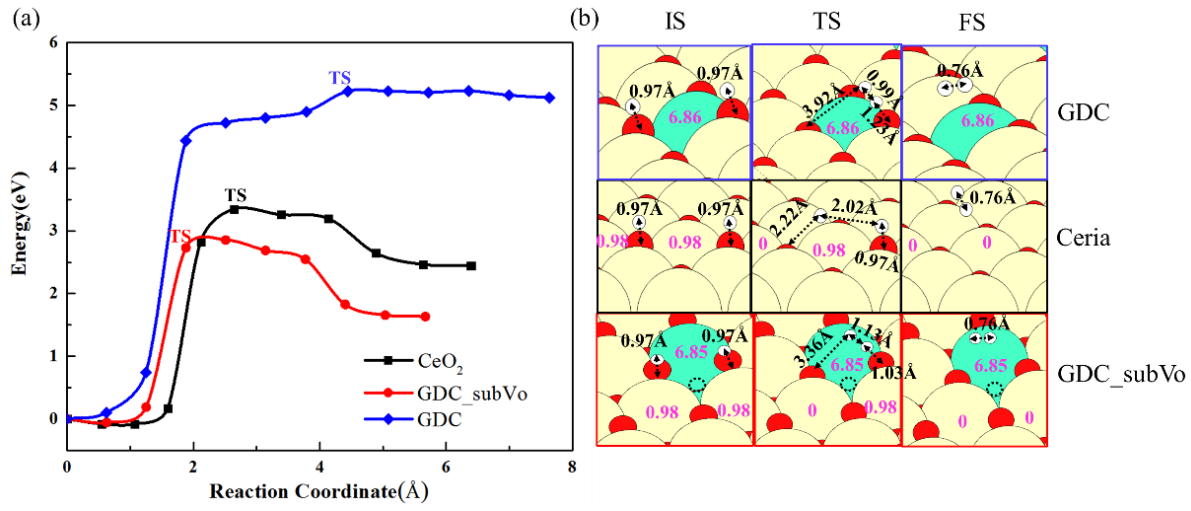

Figure 3-5. (a) Right panel: reaction pathways of the hydroxyl decomposition on ceria, GDC and GDC_subVo surfaces. (b) Left panel: configurations of the initial state (IS), transition state (TS) and final state (FS) along each reaction pathway. Bond lengths of the surface hydroxyls and H_2, as well as the magnetization (μB) of the each reaction states are labelled. The color for each atom refers to **Figure 3-1**. The dashed circle indicates the oxygen vacancy in the subsurface of GDC.

The reaction pathway for the hydroxyl decomposition on ceria is asymmetric and the transition state appears early when breaking the first O-H bond.[21,70] A vibrational analysis of each transition state for hydroxyl decompositions on these hydroxylated surfaces reveals a single mode with an imaginary frequency. The mode corresponds to one H moving over a Gd/Ce ion while shortening the H-H bond. At the TS for the hydroxyl decomposition on ceria, one O-H bond is broken and one Ce^{3+} is oxidized to Ce^{4+}, where the total magnetization of the ceria decreases from 1.96 to 0.98 μB, as shown in **Figure 3-5(b)**. The breaking of an O-H bond with a bond length of 2.02 Å at the TS agrees with previous literature reports.[21,82] After the TS, breaking the second O-H bond is downhill in energy as shown in **Figure 3-5(a)**, which finally leads to the formation of one hydrogen molecule. This asymmetric reaction pathway totally leads to a 3.4 eV barrier for the hydroxyl decomposition over the ceria surface.

Similarly, the asymmetric reaction pathway is found for the H_2 production on the GDC and GDC_subVo, which respectively leads to a 5.2 eV and a 2.8 eV activation barrier. The barrier decreases dramatically for the H_2 production over the GDC reduced by creating one V_O^{sub} and forming two hydroxyls, compared with the partially hydroxylated (2H) GDC. This is because the formation of the final state, GDC_subVo ($Gd_2Ce_{16}O_{35}$) is more favored than that of $Gd_2Ce_{16}O_{36}$ (an uncompensated GDC surface) as discussed in the section **3.3.1**. Therefore, the hydroxyl decomposition may proceed more easily over the highly hydroxylated GDC surface by creating oxygen vacancies

and formation of hydroxyls. For 2H adsorption on ceria and GDC, it has not been possible to identify Ce (Gd)-H as a stable intermediate structure because it easily relaxes into H_2 or 2OH.

The reaction barriers for the H_2 production on the excessively hydroxylated ceria and excessively hydroxylated GDC are presented in **Figure 3-6**. As discussed in the section 3.3.3.2, the water dissociates into hydroxyls on the 5OH covered ceria surface via reaction (3-3) where the H of H_2O reacts with one subsurface oxygen ion of the ceria to form one subsurface hydroxyl (subO-H). This reaction is highly competed by

$$H_2O_{ads} + 5OH^- + 7Ce^{3+} + V_0 \rightarrow 6OH^- + Ce^{4+} + Ce^{4+}H^- + 5Ce^{3+} \quad (3\text{-}7)$$

Where the H from H_2O binds to the metal ions and thus forms a Ce-H moiety ($Ce^{4+}H^-$) on the surface. Two electrons from the 4*f* shell of $2Ce^{3+}$ contribute to the formation of the $Ce^{4+}H^-$ and one Ce^{4+} (i.e. oxidation of ceria). In this Ce-H system, there are total $5Ce^{3+}$ and the total magnetization of the system is 5.0 μB as presented in **Figure 3-6(c)**. For the water dissociation on the GDC surface, the Gd-H moiety forms via the reaction of

$$H_2O_{ads} + 5OH^- + 5Ce^{3+} + 2Gd^{3+} + V_0 \rightarrow 6OH^- + 2Ce^{4+} + Gd^{3+}H^- + 3Ce^{3+} + Gd^{3+} \quad (3\text{-}8)$$

The $4f^1$ of $2Ce^{3+}$ donates two electrons, which contributes to the formation of the $Gd^{3+}H^-$. In the Gd-H system, the magnetization of each Gd^{3+} is 7.0 μB and there are $3Ce^{3+}$ with the magnetization of 1.0 μB for each, as shown in **Figure 3-6(c)**.

The binding of H to Ce in the surface is about 0.9 eV weaker than the binding to an oxygen in the subsurface as shown in **Figure 3-6(a)**. The Ce-H bond is 0.28 and 1.15 eV weaker than the subO-H bond calculated by using a U_{eff} value of 3.0 and 5.0 eV, respectively, which indicates these bindings are strongly dependent on the values of U_{eff} corrections. The sensitivity to the choice of U_{eff} arises from the fact that there are $5Ce^{3+}$ ions on the surface when one Ce-H and six O-H form, while the surface that forms seven O-H has $7Ce^{3+}$ ions. On the excessively hydroxylated GDC, the binding between H and one lattice oxygen next to the Gd in the subsurface is 1.9 eV stronger than the binding between H and Gd in the surface as presented in **Figure 3-6(b)**. Because of the strong binding between H and one lattice O in the subsurface, the direct breaking of the O-H bond for the H_2 production is difficult. Herein, for the hydroxyl decomposition on such excessively hydroxylated ceria and GDC surfaces, the reaction pathways are split into two independent paths via Ce-H and Gd-H moieties, respectively. Path I involves the breaking of the O-H bond in the subsurface to form Me-H (Gd-H or Ce-H). Path II

involves the reaction between the Me-H and the nearby O-H, finally leading to the formation of one H_2. The reaction along Path I is

$$OH^-_{subsurface}+2Ce^{3+}+Gd^{3+}\rightarrow 2Ce^{4+}+Gd^{3+}H^-+O^{2-}_{subsurface} \quad (3\text{-}9)$$

on the GDC surface and is

$$OH^-_{subsurface}+2Ce^{3+}\rightarrow Ce^{4+}+Ce^{4+}H^-+O^{2-}_{subsurface} \quad (3\text{-}10)$$

on the ceria surface. The reaction along Path II is

$$OH^-_{surface}+Gd^{3+}H^-\rightarrow Gd^{3+}+ H_2+O^{2-}_{surface} \quad (3\text{-}11)$$

on the GDC surface and is

$$OH^-_{surface}+Ce^{4+}H^-\rightarrow Ce^{4+}+ H_2+O^{2-}_{surface} \quad (3\text{-}12)$$

on the ceria surface.

For the reaction along Path I on ceria, breaking the O-H bond in the subsurface of the excessively hydroxylated ceria is difficult, leading to a 2.0 eV activation barrier. At the TS1, the Ce^{3+} in the subsurface is oxidized to Ce^{4+}, which is followed by the oxidation of the second Ce^{3+} in the top surface to form the Ce-H. For the reaction along path I on the excessively hydroxylated GDC, the activation barrier is 2.5 eV, where the O-H bond of the TS1 is broken but the total magnetization remains unchanged (i.e., no Ce^{3+} or Gd^{3+} is oxidized). The higher barrier in GDC system arises from the higher stability of the excessively hydroxylated GDC as discussed for E_H (presented in **Figure 3-3**). However, the hydrogen production proceeds easily along Path II, having 0.7 eV and 0.05 eV barriers on the excessively hydroxylated ceria and GDC, respectively. By comparing Path I and Path II, it is noted that breaking the O-H bond in the subsurface along Path I is the most difficult step. This indicates that if the formation of Me-H moiety becomes more favorable by adding a substitutional dopant, the reaction along Path I can proceed with a lower activation barrier for H_2 production.

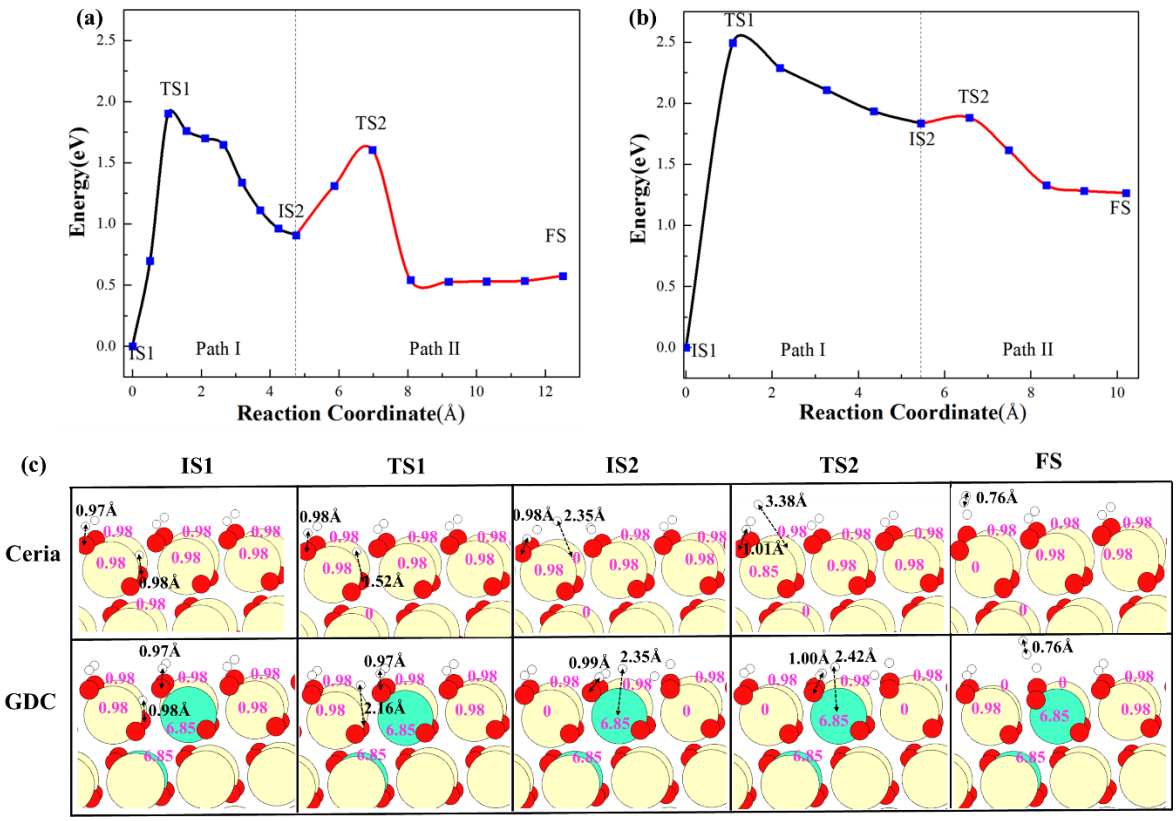

Figure 3-6. Energy diagrams for the hydroxyl decomposition into H_2 on the excessively hydroxylated CeO_2 (7H) surface (a) and on the excessively hydroxylated GDC (7H) surface (b). (c) Side views of the optimized structures for each intermediate and transition state. The bond lengths of the O-H, Ce-H, and Gd-H involved in the reactions are labelled. In addition, the magnetization (μB) of the each reaction state is marked with pink.

3.3.4 The reaction pathways for hydrogen production on reduced GDC and ceria

Based on the previous discussions on the configurations of the reduced surface and the kinetic barriers of each reaction step at the reduced surface, the free energy of the intermediates at each reaction step during the WSR is calculated. Because the electrochemical reactions over GDC operates at temperature of 773-1073 K,[73,74] the free energy diagram at T=800 K is investigated and at a higher temperature (T=1200 K) is investigated for comparison. The simplified free energy diagram of the HER on the ceria and GDC are shown in **Figure 3-7**. To calculate the relative free energy of the reduced surfaces at each reaction step, a ceria and GDC surface without any vacancies

or hydroxyl groups is chosen as a reference surface, respectively for ceria and GDC system. The reduced surfaces form via the reaction between vacancies, oxygen and water at the reference surface. On the bias of this reaction, the free energies for each reduced surface are calculated by using method discussed in chapter 2. The formation of the fully hydroxylated (covered by 6H) GDC and fully hydroxylated ceria is more favorable than the formation of other H coverage at $400 \leq T \leq 1200$ K, as presented in **Figure 3-8**. Besides, it is easier to form the excessively hydroxylated (7H) GDC than that to from the excessively hydroxylated ceria at $400 \leq T \leq 1200$ K.

At 800 K, 3.20 and 2.60 eV enthalpy barriers are required for the H_2 production on the partially hydroxylated ceria and GDC surface, respectively as shown in **Figure 3-7**. Here, the TS occurs with the first O-H bond broken, coupled with electron transferring from Ce^{3+} as discussed in the section **3.3.3.3**. Compared to the reaction on the partially hydroxylated surfaces, the HER proceeds more efficiently via the Ce-H and Gd-H moieties on the excessively hydroxylated ceria and the excessively hydroxylated GDC surfaces, respectively, leading to a 1.60 and 2.20 eV kinetic barrier for the H_2 formation, respectively. However, the reaction energy required to form the Ce-H intermediate on fully hydroxylated ceria is 1.31 eV, whereas only 0.46 eV is required for the formation of the Gd-H on the fully hydroxylated GDC because of the stabilization of the reduced states by the incorporation of Gd. Thus, it is more difficult to form excessively hydroxylated ceria and the overall free energy barrier for the HER on the excessively hydroxylated ceria surface is 2.91 eV. By contrast, 2.67 eV is required for the hydrogen production on the excessively hydroxylated GDC. The DFT+*U* results indicate that the reaction activity of the HER on ceria is significantly improved by the incorporation of gadolinium. In addition, if the formation of 7H is favored and the Metal-H is stabilized by adding a substitutional dopant in ceria, the total free energy required for the H_2 formation will decrease.

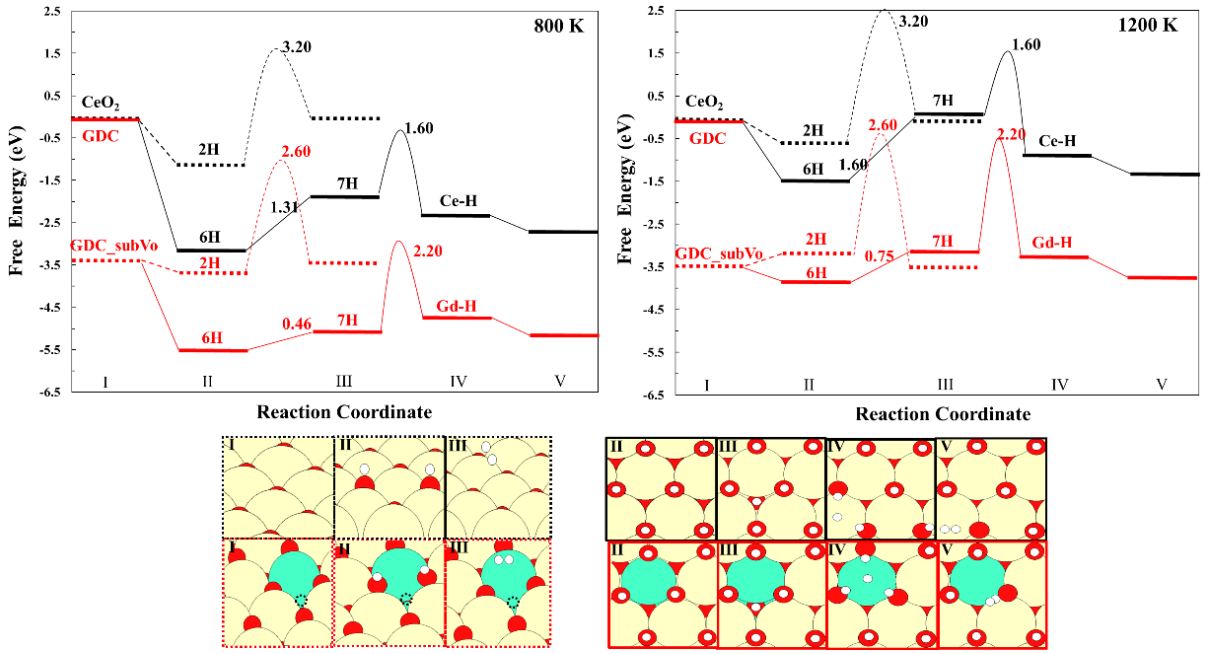

Figure 3-7. Top panel: Free energy of the intermediates during H_2 production on the partially (2H) and excessively (7H) hydroxylated GDC and CeO_2, at 800 and 1200 K, respectively. Bottom panel: Atomic configurations of reaction intermediates. The color for each kind of atom refers to **Figure 3-1**. The dashed circle stands for an oxygen vacancy.

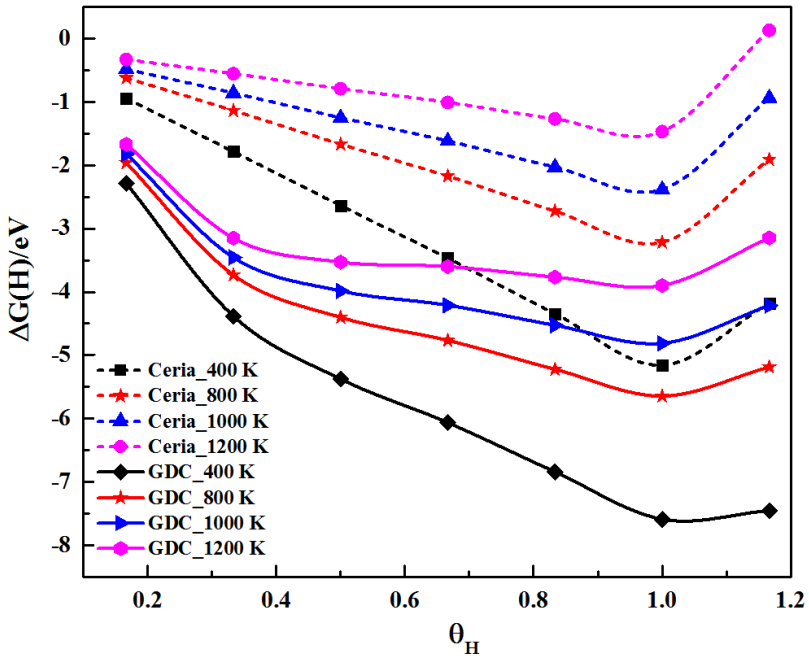

Figure 3-8. Free energy of the hydroxylated ceria and GDC as a function of H coverage (Θ_H), at 400, 800, 1000 and 1200 K, respectively.

As temperature increases to 1200 K, the free energies of all intermediates increase mainly due to the loss of gas phase entropy upon adsorption.[21] A significant increase is found for the reaction free energy to form the excessively hydroxylated surfaces, which increases to 1.60 and 0.75 eV in ceria and GDC, respectively. The formation of the overly reduced ceria competes heavily with the water adsorption/desorption at such high temperature (referring to Figure S12 in the supporting information of paper 1 for more details), which prevents the formation the highly reduced states. However, the hydroxyl decomposition remains to be the RDS. At 1200 K, the reaction proceeding via the Gd-H intermediate on the excessively hydroxylated GDC has the lowest energy cost. The operating temperature for the HER on GDC should be higher than 800 K to reach the same rate as on Pt(111) at 400 K[21] as shown in **Figure 3-9**. The predicted operating temperature is consistent with the experimental operating temperature range (773-1073 K).[73,74] However, temperature higher than 900 K is required for the HER on ceria. Therefore, the H_2 production is allowed to proceed at lower temperature on GDC, compared with the reaction on pure ceria. The reactivity of the WSR on ceria is improved by the incorporation of gadolinium.

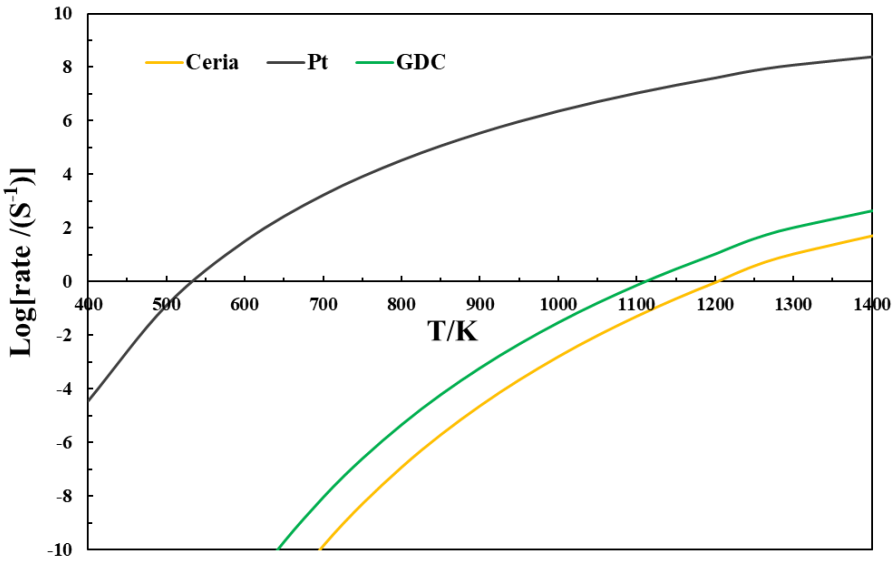

Figure 3-9. Reaction rates of H_2 production on GDC and ceria as compared to the reaction on Pt (111).

3.4 Chapter Conclusions

Using the DFT+*U* method, the configurations of the reduced ceria and reduced GDC via creating vacancies and forming hydroxyls have been studied. It is found that Gd can distribute freely in the top surface or subsurface of the $Gd_2Ce_{16}O_{35}(111)$ surface at 11% Gd concentration. The vacancy and hydroxyl formation energy in GDC are more negative than in pure ceria. Thus, it is much easier to form the highly reduced GDC than to form the highly reduced ceria via creating vacancies and forming hydroxyls. Then, the mechanism of the WSR on the GDC surface compared to the WSR on the pure ceria is revealed. One vacancy diffusion in the GDC surface is observed to be faster than that in the ceria surface. The following step for the water dissociation on both GDC and ceria surface is facile even the surface has high hydrogen coverage. However, there is a large barrier for the hydroxyl decomposition on the partially hydroxylated ceria and partially hydroxylated GDC. The reaction activity for the HER is improved via the Gd-H intermediate on the excessively hydroxylated GDC surface at 800 and 1200 K, which is attributed to the much more favorable formation of the Gd-H than the formation of Ce-H intermediate.

In conclusion, the incorporation of Gd plays an important role in stabilizing the intermediates and transition states for hydroxyl decompositions into H_2 and further enhancing performance of ceria for the WSR. Therefore, a dopant that stabilizes the reduced ceria surface and has strong binding to hydrogen is capable of effectively improving the reaction activity of ceria for renewable hydrogen production in SOECs. The findings in Chapter 3 give insight in the mechanism of the WSR on the doped ceria.

Chapter 4. Improved WSR on CeO_2(111) by Strain Engineering

This chapter is based on Paper 2, which has been included in Appendix B.2. The supplemental information has also been included in Appendix B.2.

4.1 Introduction

To overcome the limitations of hydroxyl decompositions into H_2 during the WSR, strain engineering is a promising approach due to its significant influence on the local atomic structure and chemical reactivity.[39,60,83–86] Because the variation of strain is an unavoidable consequence during the fabrication of nanostructured ceria and ionic incorporation into ceria, the strain effect on ceria has been widely reported,[37,39,59,60,87–91]although the focus has mostly been on oxygen formation and oxygen ionic transport.[37,59,87–91] Even though impressive progress has been made on understanding reaction pathways and reaction mechanism for the WSR on ceria,[21,33,92] the fundamental understanding of the effect of strain on the reaction kinetics and the formation of intermediates (such as oxygen vacancies, hydroxyls and their mixed phase) that, determines the reaction pathways remains unclear. Here, the effect of strain on the formation of oxygen vacancies, hydroxyls and vacancy-hydroxyl mixed phases on CeO_2(111), as well as the effect on the activation barriers for oxygen vacancy diffusion, water dissociation into hydroxyls and the following hydroxyl decomposition is systematically investigated by performing DFT+*U* calculations. In addition, a direct mapping between the most efficient WSR pathway and strain at different operating temperature is investigated.

4.2 Simulation Details

A dense Γ-centered 8×8×8 k-point mesh is used to calculate lattice constants of doped ceria, Ce_3MO_8, where M=Al, Ga, Ni, Pb, Pr, Gd and La. The CeO_2(111) surface ($Ce_{12}O_{24}$) is built as a 2×2 repeated surface unit cell consisting of three O-Ce-O atomic layers as shown in **Figure 4-1**. The O-Ce-O atomic layer at the bottom is kept fixed in the bulk geometry. Both compressive (-) and tensile (+) lattice strain is applied in the CeO_2(111) plane. The Ce-O bond lengths of strained and unstrained CeO_2(111) agree well with values reported by Capdevila-Cortada et al,[60] referring to Table S1 in the supporting information of Paper 2 that has been included in Appendix B.2. A Γ-centered 3×3×1 k-point mesh is used for optimization of all surfaces. Density of states are recalculated

using a Γ-centered 13×13×1 k-point mesh. Other parameters in VASP used for the DFT calculations in this chapter are the same as that introduced in the section 2.2 of Chapter 2.

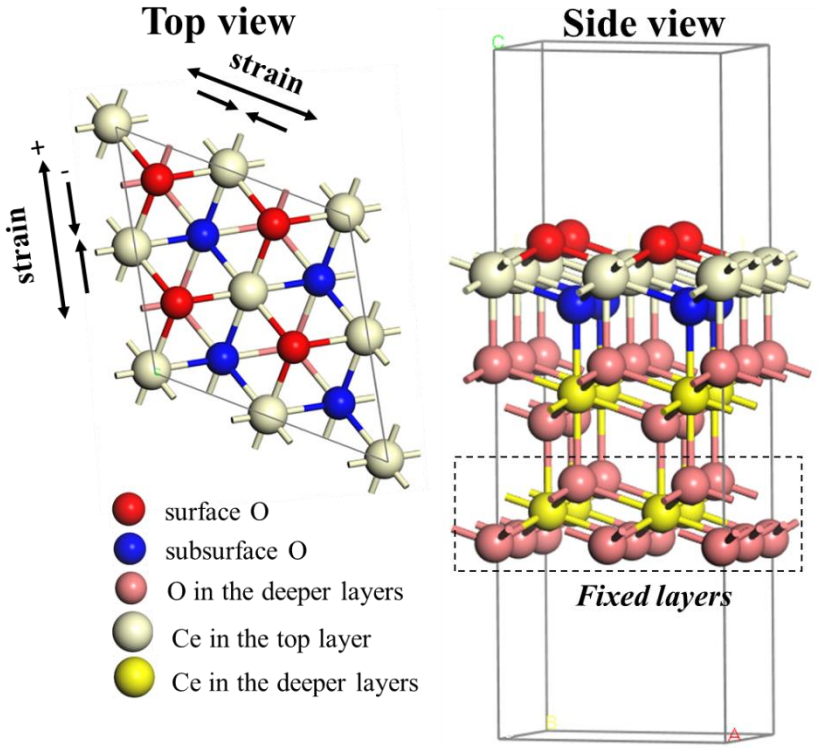

Figure 4-1. Simulation model of CeO_2(111).

4.3 Results and Discussions

4.3.1 Strain effect on the formation of reduced CeO_2(111)

This Chapter focuses the WSR on partially ($2H^*$), fully ($4H^*$, 1 monolayer H^*) and excessively ($5H^*$, above 1 monolayer H*) hydroxylated CeO_2(111) under strain in the following. The most likely reaction pathways via $2H^*$, $4H^*$ or $5H^*$ surface structures include creating one oxygen vacancy in the subsurface (V_O^{sub}), which then moves to the surface (V_O^{sur}), followed by water adsorption, hydroxyl formation and hydrogen desorption through pathways presented in **Figure 4-2**. Along these reaction pathways, the ability to create an oxygen vacancy plays an important role in the formation of the reduced CeO_2(111) for the electrocatalytic WSR.

For creating an oxygen vacancy in the unstrained ceria, the distribution of $2Ce^{3+}$ in ceria has been investigated. The most stable configuration of V_O^{sub} has $2Ce^{3+}$ next

nearest neighbor to it, which is about 0.5 eV more stable than that $2Ce^{3+}$ locate nearest neighbor to the V_O^{sub}, as shown in **Table 4-1**. For creating one V_O^{sur}, the next nearest neighbored locations of $2Ce^{3+}$ is 0.18 eV more favored over the nearest neighbored locations as shown in **Table 4-2**. These findings agree well with the results reported by Ganduglia-Pirovano et al.[26] By comparison, the different Ce^{3+} locations at -4%, -3% -2%, 2%, and 4% strain have also been investigated as shown in **Tables 4-1 and 4-2**. The preference of Ce^{3+} distribution for both V_O^{sub} and V_O^{sur} is not affected by strain, which is consistent with Ma's findings.[3] For each vacancy formation, the energy difference between different Ce^{3+} locations is below 0.5 eV and the reported polaron hopping between different Ce^{3+} distribution is facile.[25,28] In addition, vacancy formation and diffusion is not a fundamental step to the discussions on the efficient reaction pathway.[21] In chapter 4, Ce^{3+} sitting nearest neighbor to an oxygen vacancy or hydroxyls is investigated.

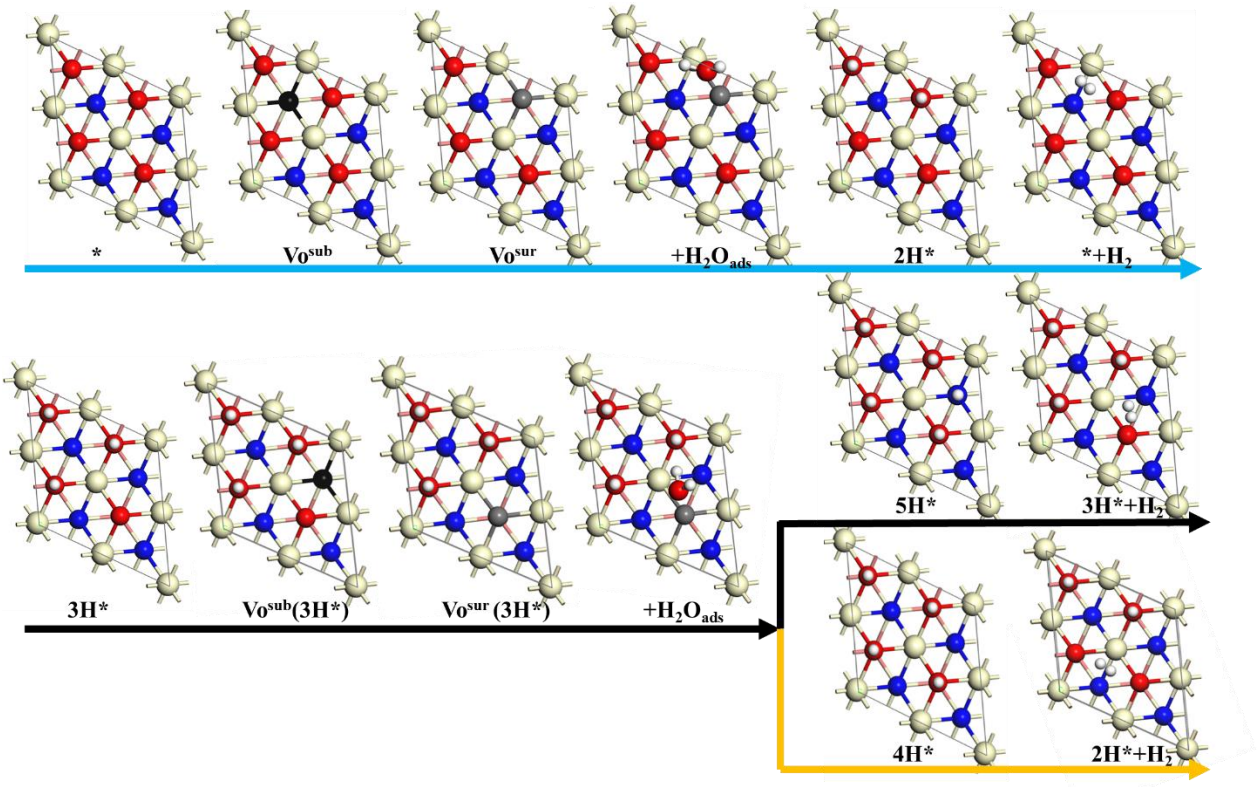

Figure 4-2. Schematic illustration of the hydrogen formation on the partially ($2H^*$), fully ($4H^*$) and excessively ($5H^*$) hydroxylated $CeO_2(111)$. $3H^*$ represents that the surface is reduced by three hydroxyls (3/4 monolayer hydroxyl). V_O^{sub} ($3H^*$) and V_O^{sur}($3H^*$) represent one oxygen vacancy in the subsurface and in the top surface of the $3H^*$ surface, respectively. Black and grey spheres show the oxygen vacancy in the subsurface and top surface, respectively.

Table 4-1. Formation energy of one oxygen vacancy in the subsurface $E(V_O^{sub})$ of $CeO_2(111)$, at -4%, -3%, -2%, 0, 2%, and 4% strain with different Ce^{3+} locations. Atom numbering refers to **Figure A-1**. NNN and NN represent Ce^{3+} locating next nearest neighbor and nearest neighbor to the V_O, respectively. The subscripts of "sur" and "sub" represent Ce^{3+} sitting in the top surface and subsurface, respectively.

Ce^{3+} locations to the V_O^{sub}	Atomic number of Ce^{3+}	-4%	-3%	-2%	0	2%	4%
NNN_{sur}-NNN_{sub}	(2,6)	2.51	2.32	2.14	1.75	1.41	1.01
NNN_{sur}-NN_{sur}	(1,2)	2.71	2.48	2.25	1.90	1.49	1.08
NNN_{sur}-NN_{sub}	(2,5)	2.84	2.62	2.42	1.95	1.56	1.05
NN_{sur}-NNN_{sub}	(1,6)	2.75	2.33	2.40	2.20	1.69	1.25
NN_{sur}-NN_{sur}	(1,3)	2.73	2.70	2.53	2.23	1.97	1.56
NN_{sur}-NN_{sub}	(1,5)	3.04	2.88	2.68	2.29	2.10	

Table 4-2. Formation energy of one oxygen vacancy in the top surface $E(V_O^{sur})$ of $CeO_2(111)$, at -4%, -3%, -2%, 0, 2%, and 4% strain with different Ce^{3+} locations. Atom numbering refers to **Figure A-1**.

Ce^{3+} locations to the V_O^{sur}	Atomic number of Ce^{3+}	-4%	-3%	-2%	0	2%	4%
NNN_{sub}-NNN_{sub}	(5,7)	3.22	2.94	2.64	2.11	1.60	
NN_{sur}-NNN_{sur}	(1,2)	3.19	2.95	2.70	2.19	1.68	1.15
NN_{sur}-NN_{sur}	(2,4)	3.22	3.03	2.84	2.37	1.88	1.37
NN_{sur}-NNN_{sub}	(2,7)	3.49	3.19	2.94	2.46	1.93	1.46

In **Figure 4-3**, creating an oxygen vacancy in the top surface and in the subsurface of the pure $CeO_2(111)$ is facile compared to creating vacancies in hydroxylated $CeO_2(111)$. When the surface is covered by 3 hydroxyls (3/4 monolayer hydroxyl), the oxygen vacancy in the subsurface of the expansively strained $CeO_2(111)$ is very unstable compared to the oxygen vacancy created in bulk ceria. The formation energy of an oxygen vacancy in the unstrained or compressively strained $CeO_2(111)$ follows the order: $V_O^{sub} < V_O^{sur} < V_O^{sur}(3H^*) < V_O^{sub}(3H^*)$. In addition, the formation energy of these oxygen vacancies decrease gradually as increasing of the lattice strain, well

consistent with Ma et al.'s findings.[87] Under tensile strain, creating one oxygen vacancy becomes much easier in the hydroxylated CeO_2(111) than that under compressive strain. These findings indicate that, due to the difficult formation of the oxygen vacancy-hydroxyl mixed phases, the formation of fully and excessively hydroxylated CeO_2(111) require more energy than the formation of partially hydroxylated CeO_2(111).

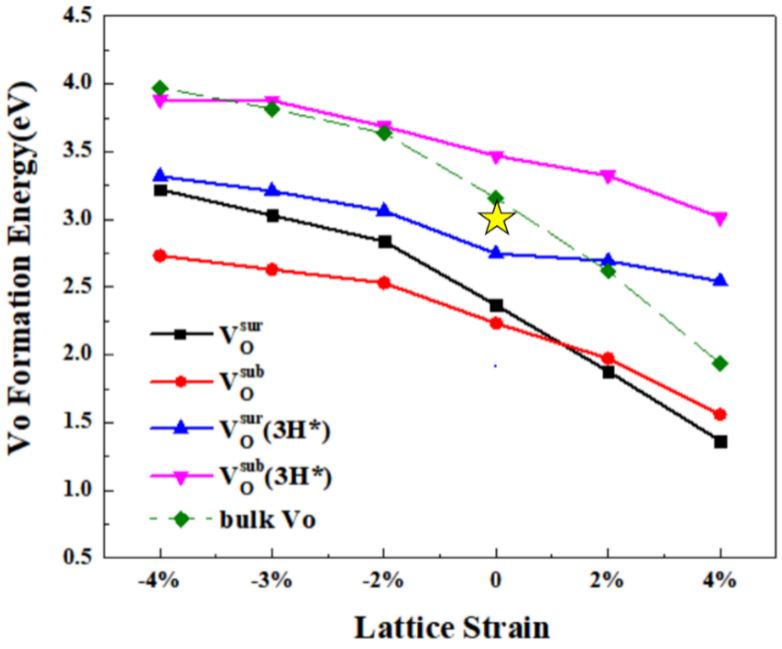

Figure 4-3. Formation energy of an oxygen vacancy as a function of lattice strain compared to the vacancy formation in bulk ceria. Yellow star represents the vacancy formation energy for the unstrained bulk ceria reported by Gopal et al. [59]

Figure 4-4(a) shows the average hydrogen adsorption energy (E_H) at different hydrogen coverages (Θ_H) on the strained CeO_2(111). For the hydrogen coverage below one monolayer, hydrogen adsorption results in the formation of surface hydroxyls and is exothermic. However, the hydrogen adsorption energy on CeO_2(111) increases dramatically as the hydrogen coverage increases from 1.0 to 1.25, where the surface now either has five hydroxyls in total by forming an unstable subsurface hydroxyl or a Ce-H moiety in the surface. In addition, E_H at each hydrogen coverage decreases as the lattice strain increase. When the lattice is expanded by 4.0%, E_H decreases significantly, and the formation of the excessively hydroxylated CeO_2(111) becomes as facile as the partially hydroxylated CeO_2(111) under no strain. Analysis of the projected density of states shows a downshift of the Ce 4f band center of CeO_2(111) under tensile strain, as shown in Figure S3 in the supporting information of Paper 2, which in turn leads to higher stability of electrons localized on Ce 4*f* orbitals in expansively strained ceria. Thus, it is easier to form the reduced CeO_2(111) by creating oxygen vacancies or

formation of hydroxyls as the lattice expands. The facile formation of the reduced $CeO_2(111)$ under tensile strain also agrees with the larger size of the Ce^{3+} ion than the Ce^{4+} ion.

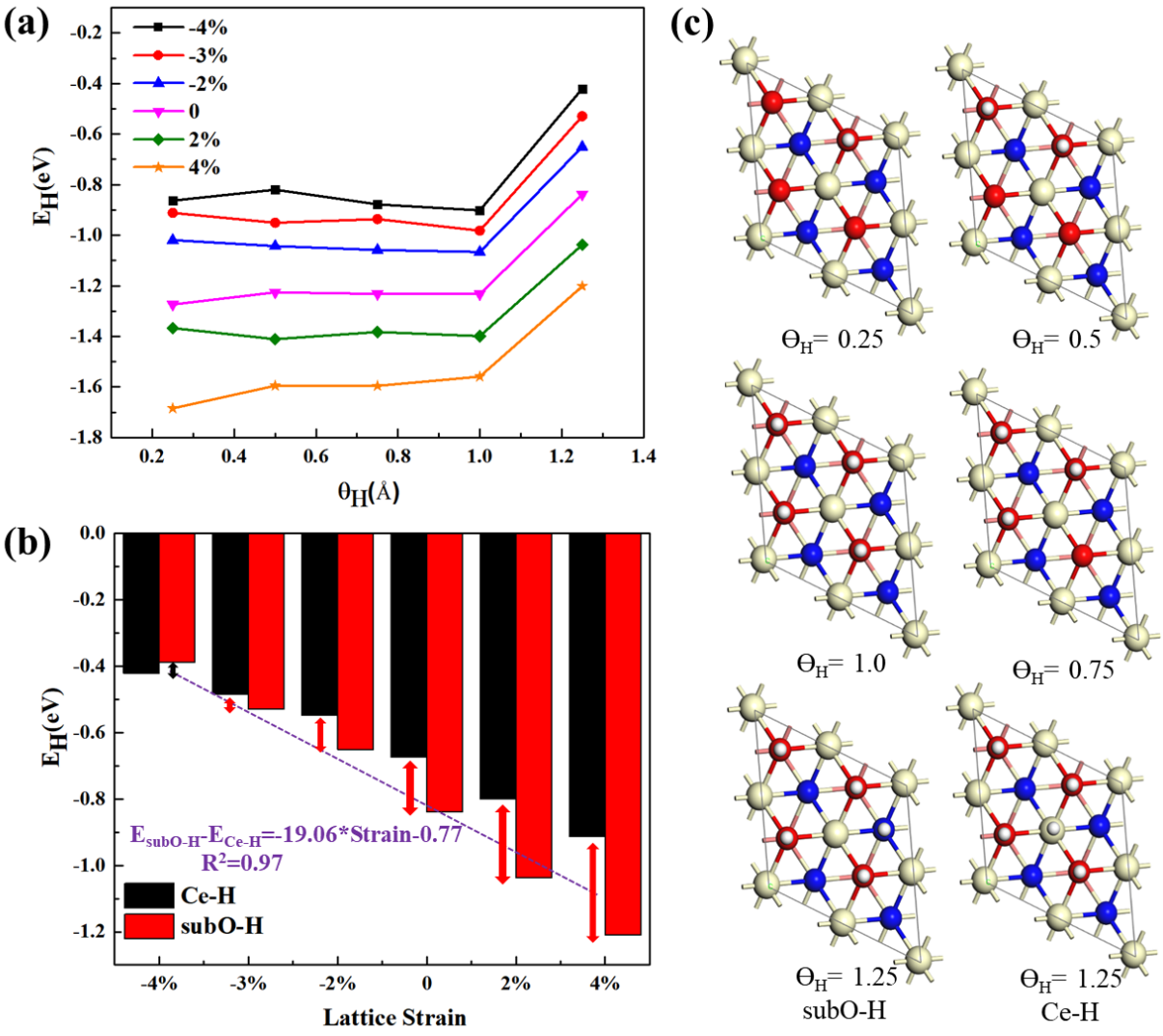

Figure 4-4. (a) Average hydrogen adsorption energy (E_H) on the strained $CeO_2(111)$ as a function of hydrogen coverage Θ_H. (b) Comparison between the E_H of Ce-H and subsurface hydroxyl (subO-H) at Θ_H=1.25 under different lattice strains. (c) Top views of the hydroxyls on $CeO_2(111)$ under different hydrogen coverage.

In addition, lattice strain effectively modifies the most stable configuration of the excessively hydroxylated $CeO_2(111)$ as shown in **Figure 4-4(b)**. Being an important intermediate in the hydrogen production along the 5H* pathway, the excessively hydroxylated $CeO_2(111)$ has two possible configurations: (i) H binding to a Ce atom in the top surface (Ce-H),[21,93] (ii) H binding to an oxygen atom (lattice oxygen) in the subsurface (subO-H), as shown in **Figure 4-4(c)**. For the unstrained $CeO_2(111)$, the

average hydrogen adsorption energy of the subO-H is about 0.16 eV more negative than that of the Ce-H. The energy difference between the two configurations increases with the increasing tensile strain. By contrast, the energy difference between the Ce-H and subO-H gets smaller with increasing compressive strain. As the surface is compressed by 4.0%, Ce-H becomes the most stable configuration of the excessively hydroxylated CeO_2(111), which indicates that the Ce-H is a likely intermediate for the hydroxyl decomposition on the excessively hydroxylated CeO_2(111). The strain effects on the formation of the most stable $5H^*$ may further adjust the hydroxyl decomposition on the Ce-H. Hydrogen formation via a Ce-H intermediate has been reported to have a low reaction barrier and might provide an efficient reaction pathway for the WSR on ceria surfaces.[21] The choice of the *U* value affects H chemisorption energy on ceria.[70] Chapter 3 has shown that reducing the *U* value from 4.5 to 3.0 eV could stabilize Ce-H by about 0.6 eV relative to subO-H on the unstrained CeO_2(111), which indicates that **Figure 4-4(b)** possibly overestimates the strain required for Ce-H to become more stable than subO-H.

Therefore, strain effectively regulates the formation of the reduced CeO_2(111) and the most stable intermediates during the WSR, which may influence the kinetics at each reaction step along partially, fully and excessively H covered pathways.

4.3.2 Strain effect on the reaction barriers at each reaction step of the WSR on reduced CeO_2(111)

Using DFT+*U* based NEB calculations, the activation barriers for oxygen vacancy diffusion, water dissociation, and hydroxyl decomposition along partially, fully and excessively hydroxylated pathways under different lattice strain are identified (referring to Figure S2 in the supporting information of Paper 2 for more information of the Ce^{3+} locations). There is a strong strain dependence of the barriers for oxygen vacancy diffusion from its most stable subsurface position to the most stable top surface position as presented in **Figure 4-5**. The diffusion of one oxygen vacancy becomes more facile as the lattice expands, likely because of the larger space available for diffusing oxygen ions. The efficient strain control of the ionic conductivity in ceria also gives insight into the fast ionic diffusion in doped ceria, where local tensile strain is realized.

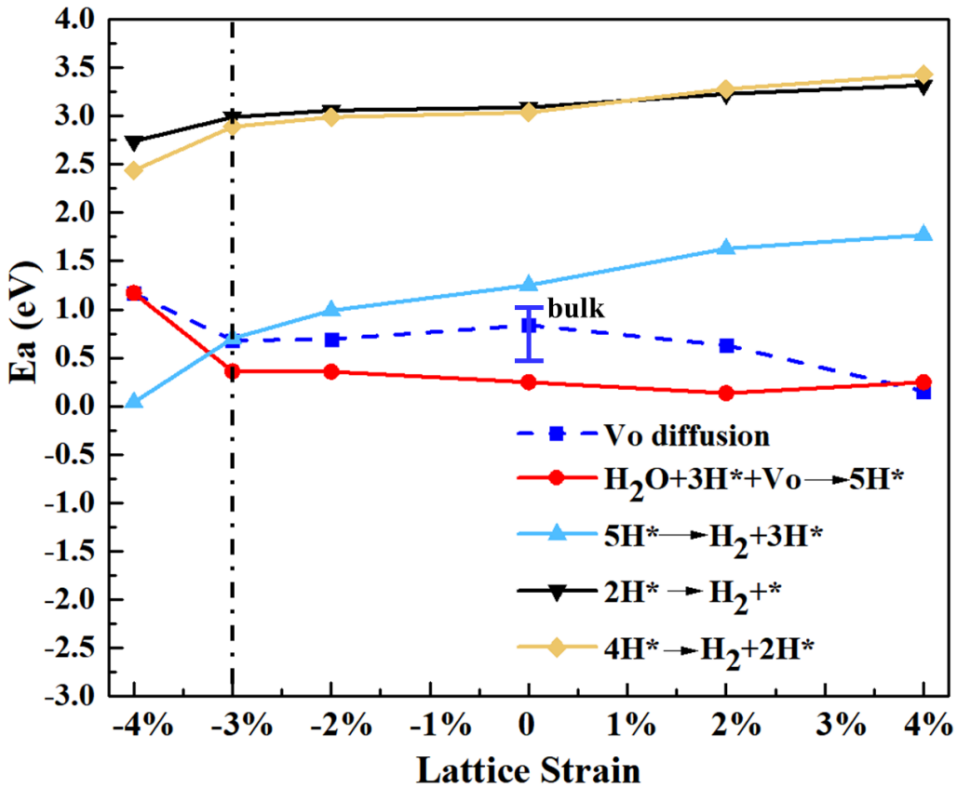

Figure 4-5. Reaction barriers for oxygen vacancy diffusion from the most stable subsurface position to the most stable top surface position, the formation of $5H^*$ via water dissociation ($H_2O_{ads}+3H^*+V_O \rightarrow 5H^*$) as well as the hydroxyl decomposition on the partially ($2H^* \rightarrow H_2+*$), fully ($4H^* \rightarrow H_2+2H^*$), and excessively ($5H^* \rightarrow H_2+3H^*$) hydroxylated $CeO_2(111)$, under different lattice strains. The calculated diffusion barrier of an oxygen vacancy in the unstrained ceria is compared to the reported barrier in bulk ceria (having a range of 0.46-1.08 eV [94]). The water dissociation into the partially and fully hydroxylated $CeO_2(111)$ has negligible activation energy.

The following step of water dissociation on the reduced $CeO_2(111)$ is very facile, with no barrier along the partially[21,95] and fully hydroxylated pathways,[21] while the formation of the excessively hydroxylated $CeO_2(111)$ has an about 0.25 eV barrier at >-3.0% strain. However, the activation barrier for water dissociation is larger than 1.0 eV as the lattice is compressed by larger than 3.0% because the hydrogen binding to subsurface O becomes weak, c.f. **Figure 4-4(b)**. It has been reported that the formation of oxygen vacancies favor the formation of hydridic H species via the H_2 dissociation on ceria, where H occupies the vacant O lattice positions.[96] By comparison, it is found that the presence of oxygen vacancy in ceria favors the formation of hydroxyls, however via the water dissociation where OH from H_2O is easily accommodated in the vacant O position. The previous results have shown that vacancy-hydroxyl mixed configurations like $2H^*$+Vo and $3H^*$+Vo are unstable intermediates during the WSR,[21] which easily

react with adsorbed H_2O to form $4H^*$ or $5H^*$, respectively. H_2O dissociating on oxygen vacancies reacts with either subsurface oxygen or surface cerium when the surface is fully hydroxylated.[21]

Table 4-3. Adsorption energy of 2H with different Ce^{3+} locations (atomic numbers) on the unstrained CeO_2(111). Atom numbering refers to **Figure A-1**

Ce^{3+} locations to the Vo^{sur}	Atomic number of Ce^{3+}	E(2H)
NN_{sur}-NN_{sur}	(2,3)	-2.45
NNN_{sub}-NN_{sub}	(5,7)	-2.15
NN_{sur}-NNN_{sub}	(2,7)	-2.01

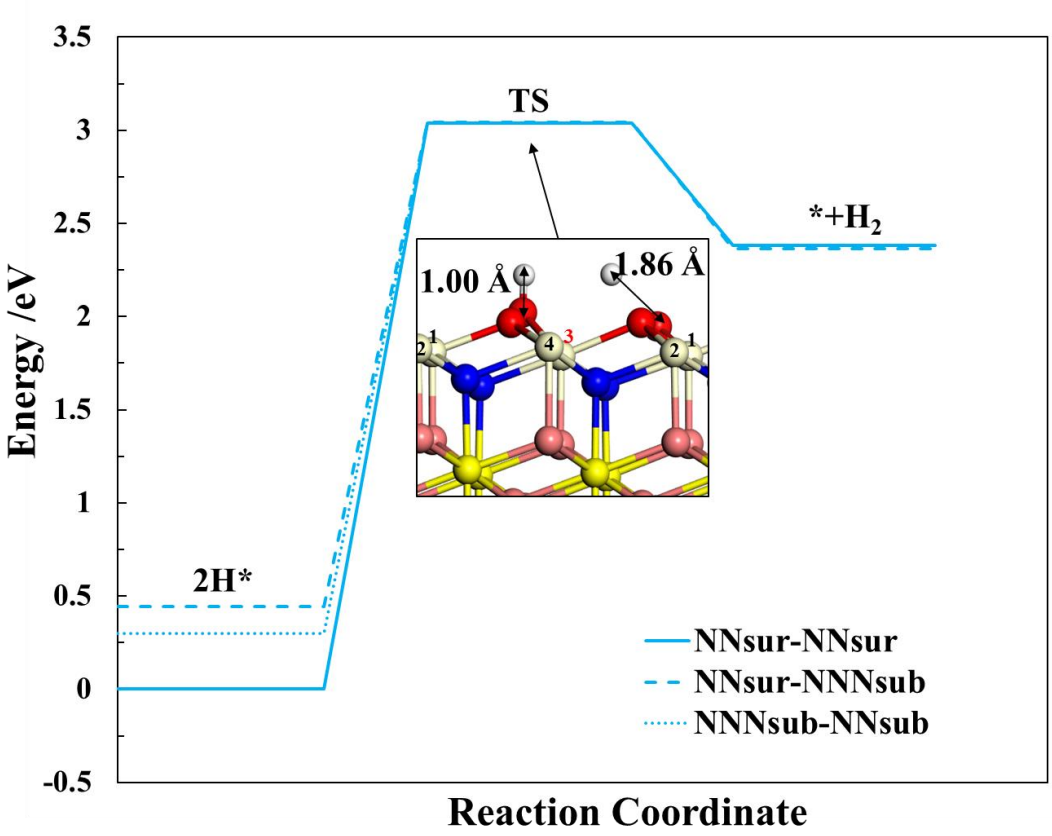

Figure 4-6. Hydroxyl decomposition into H_2 on 2H* with the most favorable Ce^{3+} distribution (NN_{sur}-NN_{sur}), compared to the distribution of NN_{sur}-NNN_{sub} and NNN_{sub}-NN_{sub}. The same transition sate (TS) for H_2 formation on the 2H* with different Ce^{3+} locations is identified, where one H moves close to the other H, leading to the breaking of one O-H. At the TS, only number 3 cerium is reduced to Ce^{3+}. The configurations of 2H* and *+H_2 are given in **Figure 4-2**.

In contrast, the activation barrier for the hydroxyl decomposition into H_2, the RDS during the WSR on ceria,[6,21] is regulated differently by strain. Firstly, the different locations of the Ce^{3+} ions around the hydroxyls like $2H^*$ are compared. It is found that the configuration of $2H^*$ with Ce^{3+} nearest neighbor to the adsorbed H is more stable than other Ce^{3+} distributions as shown in **Table 4-3**. The relative stability of the adsorbed H on ceria strongly dependent on the Ce^{3+} locations agrees well with the reported findings.[70] However, the similar transition sates for the H_2 formation on $2H^*$ with different Ce^{3+} distribution are identified as shown in **Figure 4-6**. The highest and lowest energy along the $2H^*$ pathway is therefore independent of the Ce^{3+} locations immediately before the hydroxyl decomposition into H_2. The activation energy for the hydroxyl decomposition on the partially, fully and excessively hydroxylated $CeO_2(111)$ increases as the lattice expands, which arises from the stabilization of the hydroxylated $CeO_2(111)$ under tensile strain, referring to **Figure 4-4**. As noted from **Figure 4-5**, the WSR over the fully hydroxylated $CeO_2(111)$ has similarities to the reactions on the partially hydroxylated $CeO_2(111)$.[21] A significant drop in the activation energies for the hydroxyl decomposition on the excessively hydroxylated $CeO_2(111)$ when the lattice is compressed by more than 3%, is noted from **Figure 4-5**, because the most stable intermediate for the hydrogen production changes from the subO-H to Ce-H by strain engineering. The observed facile H_2 production via the Ce-H by using DFT+*U* is consistent with the reported finding that the activation energy for breaking the Ce-H bond is much easier than breaking an O-H bond during the hydroxyl decomposition.[21] Because of the strain effects on the formation of the reduced $CeO_2(111)$ by forming oxygen vacancies, vacancy-hydroxyl phases or hydroxyls, the activation barriers at each reaction step during the WSR on the reduced $CeO_2(111)$ are correspondingly regulated by strain. In addition, it shows how to reduce the reaction barrier at the RDS and improve the reaction efficiency of the WSR on ceria by using strain engineering.

In addition, there exists a BEP relation (shown in **Figure 4-7**) between the activation energy of hydrogen formation, E_a, on the different hydroxylated $CeO_2(111)$ surfaces and the reaction energy ($\triangle E=E_{FS}-E_{IS}$, the energy difference between the initial and the final states) because of the similar geometries of the initial and the transition states. The calculated E_a for the strained ceria also correlates with the lattice parameter, as shown in Figures S6 and S7 in the supporting information of Paper 2, which is an experimentally accessible descriptor for the activation energy of the hydroxyl decomposition.

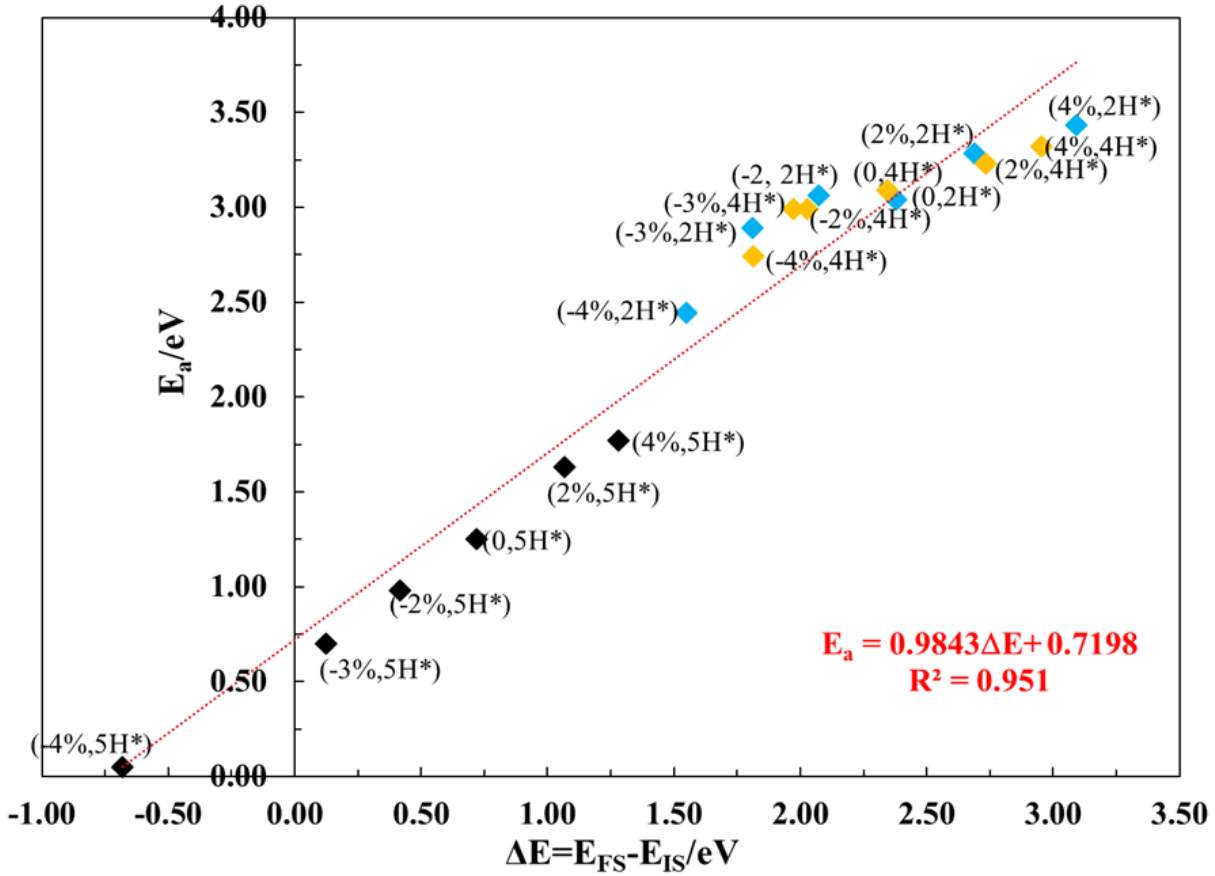

Figure 4-7. The BEP relation for hydroxyl decompositions into H_2 on the different hydroxylated $CeO_2(111)$ surfaces with different strains. The annotation (-4%, 5H*) indicates the activation energy is calculated for a $CeO_2(111)$ surface under -4 % strain and adsorbed with 5H.

4.3.3 Strain engineering of the thermodynamics of the WSR on $CeO_2(111)$

To calculate the relative free energy of the reduced $CeO_2(111)$ along each reaction pathway, a DFT-based thermodynamics approach is applied that has been described in Chapter 2. First, the clean $CeO_2(111)$ is chosen as the reference surface. The reduced $CeO_2(111)$ surfaces then form via reactions between oxygen vacancies and water molecules at the referenced surface. In a SOEC, oxygen vacancies are produced at the anode by evolving oxygen. Oxygen vacancies then diffuse through the solid electrolyte to the cathode, where oxygen vacancies react with water to produce hydrogen through the WSR. The chemical potential of oxygen at the ceria cathode is chosen such that H_2O (1 bar) and oxygen vacancies are in equilibrium with H_2 (1 bar), which corresponds to the SOEC being at the equilibrium potential of the net reaction of the WSR.

Here, the simplified free energy diagrams are drawn to compare the hydroxyl decomposition on the partially ($2H^*$), fully ($4H^*$) and excessively ($5H^*$) hydroxylated CeO_2(111) under different strains, at 800 (**Figure 4-8**), 1000 (**Figure 4-9**) and 1200 K (**Figure 4-10**). The free energy of intermediates and transition states for the full reaction pathways is given in Tables S4- S6 in the supporting information of paper 2. In addition, the free energy of $2H^*$, $4H^*$ and $5H^*$ can be fitted by experimentally measurable descriptors such as temperature (T) and the lattice parameter (a), as shown in Figure S10 in the supporting information of Paper 2.

As noted from **Figure 4-8**, in the unstrained system at 800 K, the activation barrier for the WSR on the partially, fully and excessively hydroxylated CeO_2(111) is, 3.04, 3.09, and 1.25 eV, respectively. This means that under a certain strain, breaking the H bonding to the CeO_2(111) surface becomes easier as more hydroxyls form on the CeO_2(111) surface. The WSR via a Ce-H intermediate on the excessively hydroxylated CeO_2(111) requires a lower activation energy, compared to the reactions on the partially and fully hydroxylated CeO_2(111). At 800 K, the most stable reduced state is the fully hydroxylated CeO_2(111), compared to which the formation of the partially and excessively hydroxylated CeO_2(111) is unfavorable.

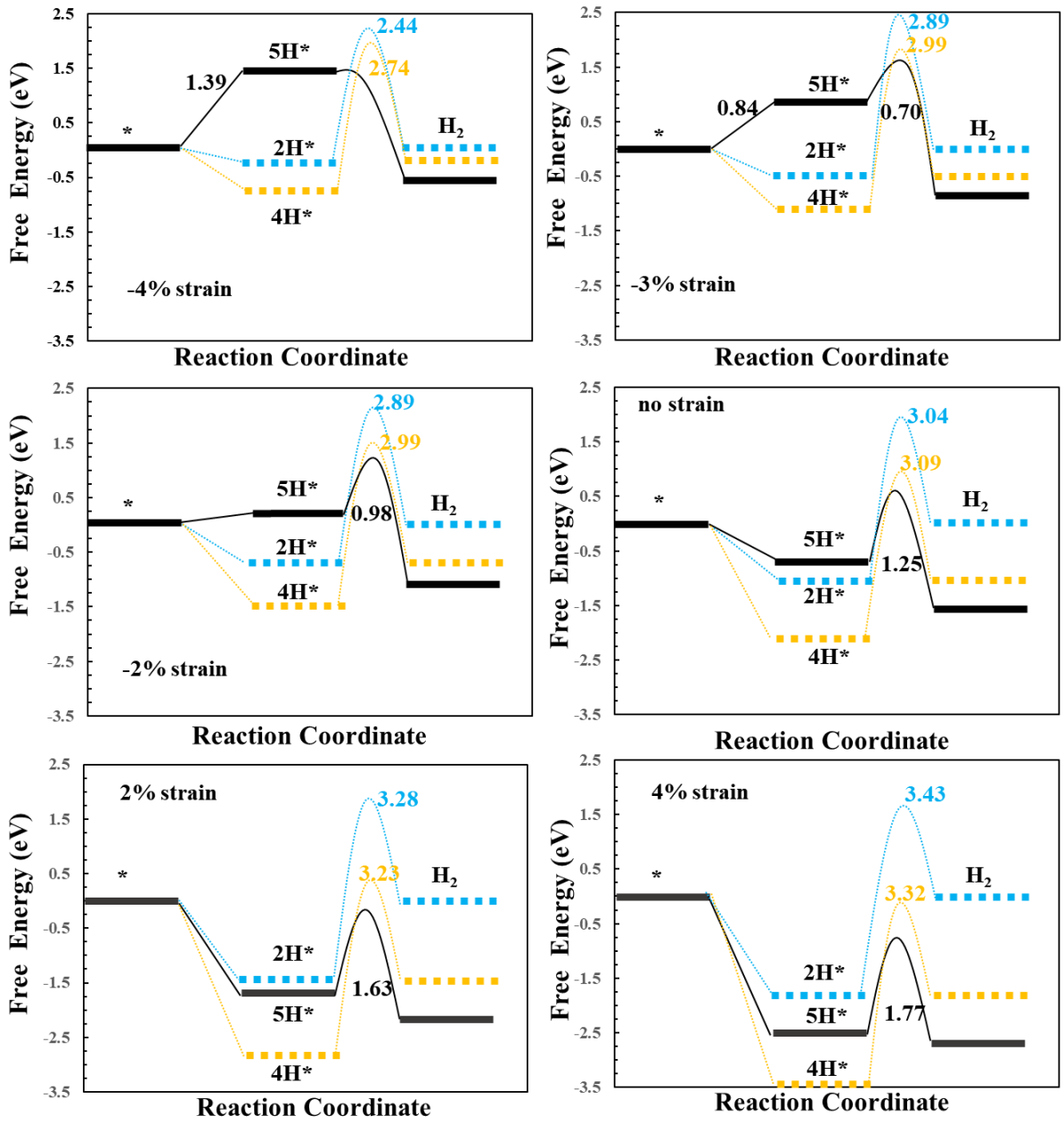

Figure 4-8. Simplified free energy diagrams for hydroxyl decompositions on the partially ($2H^*$), fully ($4H^*$) and excessively ($5H^*$) hydroxylated $CeO_2(111)$ under different strains at 800 K. The most efficient reaction pathway under each strain is highlighted by a solid line.

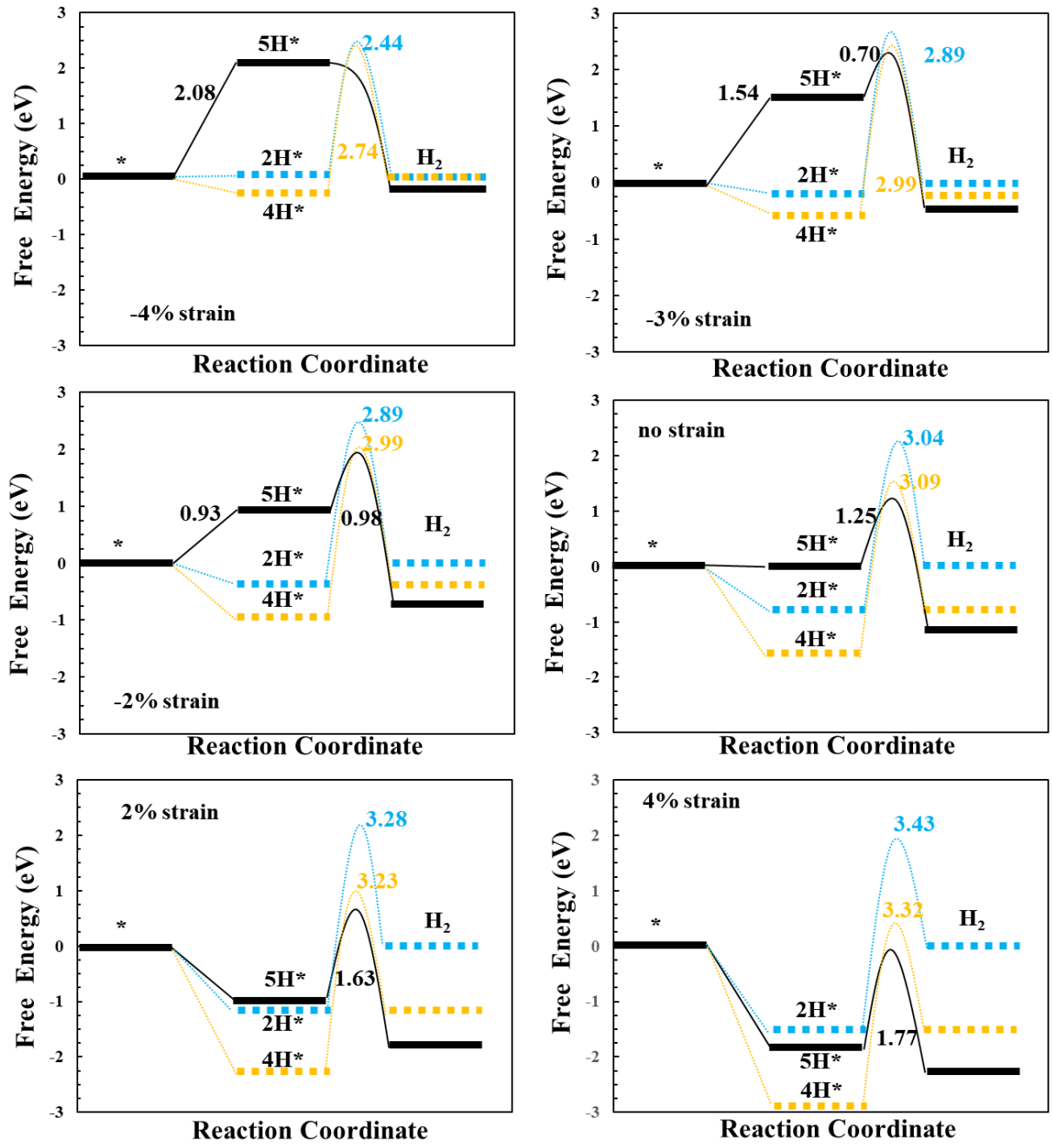

Figure 4-9. Simplified free energy diagrams for hydroxyl decompositions on the partially (2H*), fully (4H*) and excessively (5H*) hydroxylated CeO_2(111) under different strains at 1000 K. A solid line highlights the most efficient reaction pathway under each lattice strain.

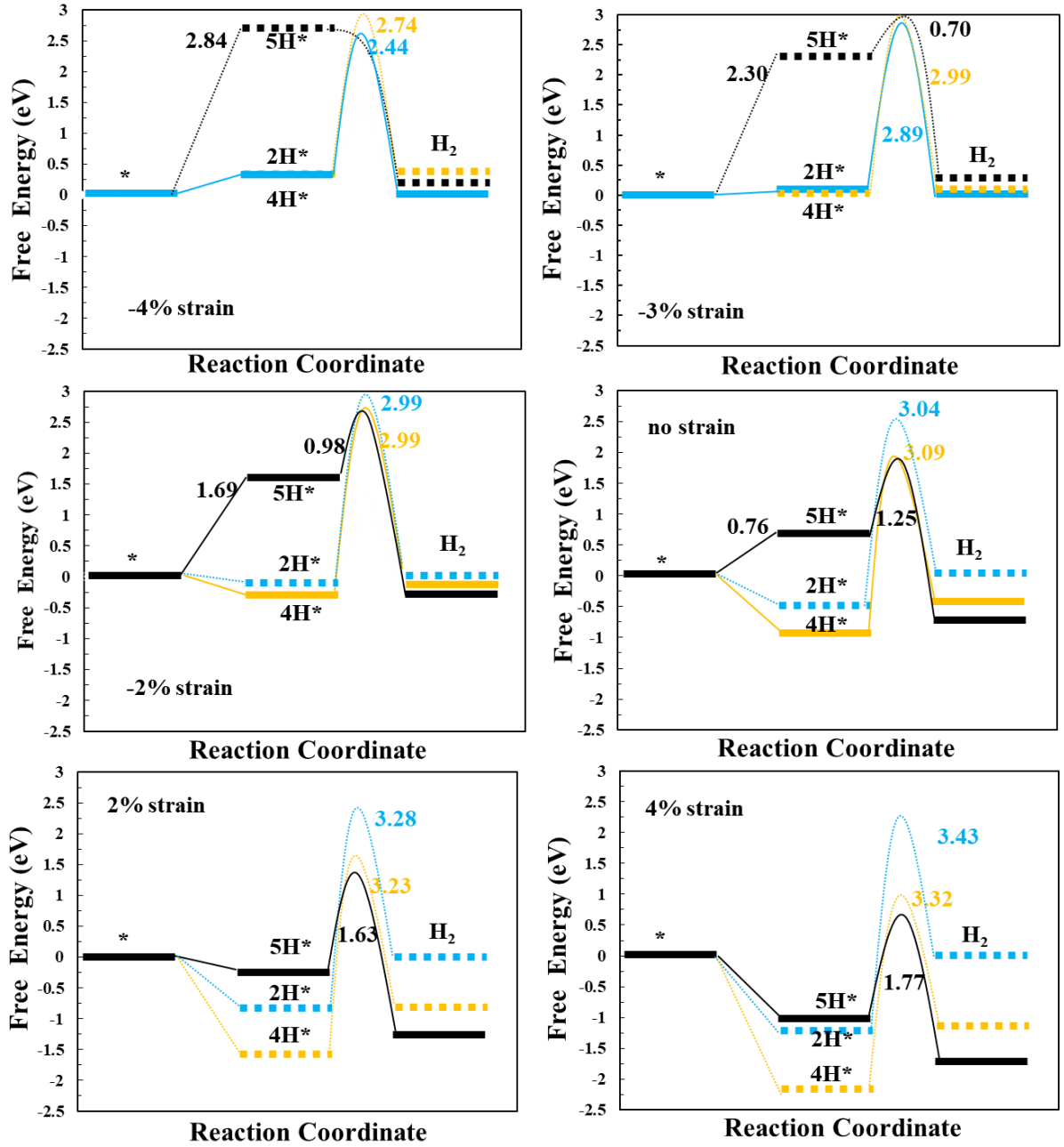

Figure 4-10. Simplified free energy diagrams for hydroxyl decompositions on the partially (2H*), fully (4H*) and highly (5H*) hydroxylated CeO_2(111) under different strains at 1200 K. A solid line highlights the most efficient reaction pathway under each lattice strain.

To evaluate the turnover frequency (TOF) of the WSR, an energetic span model is applied in this thesis.[97,98] For each reaction path over the $2H^*$, $4H^*$ and $5H^*$ surfaces, the TOF determining intermediate (TDI) and the TOF determining transition state (TDTS) are identified, which maximize the energetic span between the TDI and the TDTS.

Consider the unstrained CeO_2(111) at 800 K as an example, where the energy of the TS for the hydroxyl decomposition into H_2 on the $5H^*$ surface is lower than the that of the TSs of the reaction on the $2H^*$ and $4H^*$ surfaces, which makes the TS for the hydroxyl decomposition into H_2 on the $5H^*$ surface the TDTS. On the other hand, the TDI occurs with the $4H^*$ surface. The energetic span can then be approximated by $\delta E = E_a + \Delta G_H$, where E_a is the activation energy for the hydroxyl decomposition and $\Delta G_H = G_H - G^*$, where $G^* = \min(\{G_i\})$ is the free energy of the most stable reduced state of the ceria. In this way, the energetic span model includes the fact, that the excessively hydroxylated surface, which has low activation energy for the H_2 formation, is rather unlikely to form due to the low stability compared to the fully hydroxylated surface. Transition states for e.g. oxygen vacancy diffusion and water dissociation, and reduced states with both oxygen vacancies and hydroxyls are included in the energetic span analysis, seeing Tables S4-S6 in the supporting information of Paper 2, but left out of **Figures 4-8, 4-9 and 4-10** for clarity.

Table 4-4. ΔG_H, E_a and the energetic span required for the WSR on the ***partially (2H*), fully (4H*)*** and ***excessively (5H*)*** hydroxylated CeO_2(111), respectively, at 800, 1000 and 1200 K.

T=800 K	**2H***			**4H***			**5H***		
Strain	ΔG_H	E_a	E_{total}	ΔG_H	E_a	E_{total}	ΔG_H	E_a	E_{total}
-4%	0.57	2.44	3.01	0	2.74	2.74	2.69	0	***2.69***
-3%	0.63	2.89	3.52	0	2.99	2.99	1.98	0.70	***2.68***
-2%	0.78	2.99	3.77	0	2.99	2.99	1.71	0.98	***2.69***
0	1.08	3.04	4.12	0	3.09	3.09	1.44	1.25	***2.69***
2%	1.38	3.28	4.66	0	3.23	3.23	1.11	1.63	***2.74***
4%	1.65	3.43	5.08	0	3.32	3.32	0.94	1.77	***2.71***
T=1000 K	**2H***			**4H***			**5H***		
Strain	ΔG_H	E_a	E_{total}	ΔG_H	E_a	E_{total}	ΔG_H	E_a	E_{total}
-4%	0.29	2.44	***2.73***	0	2.74	2.74	2.84	0	2.84
-3%	0.35	2.89	3.24	0	2.99	2.99	2.12	0.70	***2.82***
-2%	0.50	2.99	3.49	0	2.99	2.99	1.85	0.98	***2.83***
0	0.81	3.04	3.85	0	3.09	3.09	1.58	1.25	***2.83***
2%	1.10	3.28	4.38	0	3.23	3.23	1.25	1.63	***2.88***
4%	1.37	3.43	4.80	0	3.32	3.32	1.07	1.77	***2.84***
T=1200 K	**2H***			**4H***			**5H***		
Strain	ΔG_H	E_a	E_{total}	ΔG_H	E_a	E_{total}	ΔG_H	E_a	E_{total}
-4%	0.13	2.44	***2.57***	0.35	2.74	3.09	3.28	0	3.28
-3%	0.03	2.89	***2.92***	0.03	2.99	***3.02***	2.30	0.70	***3.00***
-2%	0.20	2.99	3.19	0	2.99	2.99	2.00	0.98	***2.98***
0	0.50	3.04	3.54	0	3.09	3.09	1.73	1.25	***2.98***
2%	0.80	3.28	4.08	0	3.23	3.23	1.40	1.63	***3.03***
4%	1.07	3.43	4.50	0	3.32	3.32	1.23	1.77	***3.00***

By strain engineering, the activation barrier (E_a) for the H_2 production along each reaction pathway increases with increasing tensile strain, while E_a decrease with increasing compressive strain. The increase in stability of the reduced ceria with tensile strain explain the trend in the BEP relation for the hydroxyl decomposition into H_2. The variation of ΔG_H for $2H^*$ with strain follows the same trend as E_a, because the formation of the $2H^*$ surface happens through oxidation of more reduced surfaces such as $4H^*$. This oxidation becomes increasingly difficult with increasing tensile strain. However, ΔG_H of $5H^*$ varies with strain in the opposite way, where ΔG_H decreases with increasing tensile strain and increases with increasing compressive strain (**Table 4-4**). The $5H^*$ surface is formed by the reduction of less reduced surfaces such as the $4H^*$ surface, which again is facilitated by tensile strain. Thus, considering the effect of strain on both E_a and ΔG_H, the WSR proceeds preferentially through the $5H^*$ surface at 800 K and 1000 K. At 1200 K, the $5H^*$ surface becomes very unstable, especially under compressive strain, leading to the hydrogen production preferentially proceeding over the $2H^*$ or $4H^*$ structures under < -3% strain. Therefore, the preferred reaction pathway for the WSR on CeO_2(111) can be controlled by engineering the strain on ceria because of the strain effect on the formation of hydroxyls.

Overall, the fastest WSR is found at -4.0% strain, where it preferentially proceeds through the $5H^*$ structure at 800 K. At 1000 and 1200 K, the reaction, however, proceeds faster through the $2H^*$ or $4H^*$ structures, as presented in **Figures 4-9 and 4-10**, respectively. The effect of temperature on the free energies of the reduced CeO_2(111), synergize with the effects of strain on the activation barriers for the WSR contributes to the variations of the best pathway for the WSR on CeO_2(111).

A possible way to achieve compressed ceria surfaces could be through core shell particles where a thin CeO_2 shell covers a suitably doped ceria core. The lattice constant of doped ceria largely decreases by incorporating ions with a smaller radius than Ce^{4+} as shown in **Figure 4-11**, where the dopant ionic radius taken from the database of ionic radii [99] is compared to calculated lattice constants of the doped ceria. A decrease of the lattice constant in the doped ceria with decreasing dopant ionic radius is confirmed by experiments,[100] and the lattice can be further decreased when the dopant concentration is increased.[101] Thus, using dopants with smaller ionic radius than Ce^{4+} is possible to reach < -3% strain (compressive strain), which has great potential to increase the WSR activity on ceria. Doping the particle core with e.g. Ga^{3+} ions might lead to vacancy migration from the core to the particle surface, thereby setting up a dipole layer or space charge region. Although the theoretical model fixes the chemical potential of oxygen vacancies from the H_2-H_2O equilibrium, modifications of intermediate energies in response to the dipole layer are not included in the above treatment. However, vacancy migration from the bulk can be avoided by co-doping with small, high valence ions such

as Nb^{5+}. Migration of dopants to the surface can directly influence catalytic activity,[63] and Chapter 3 previously has shown that Gd dopants facilitate the formation of oxygen vacancies, hydroxyls, and hydridic H species.

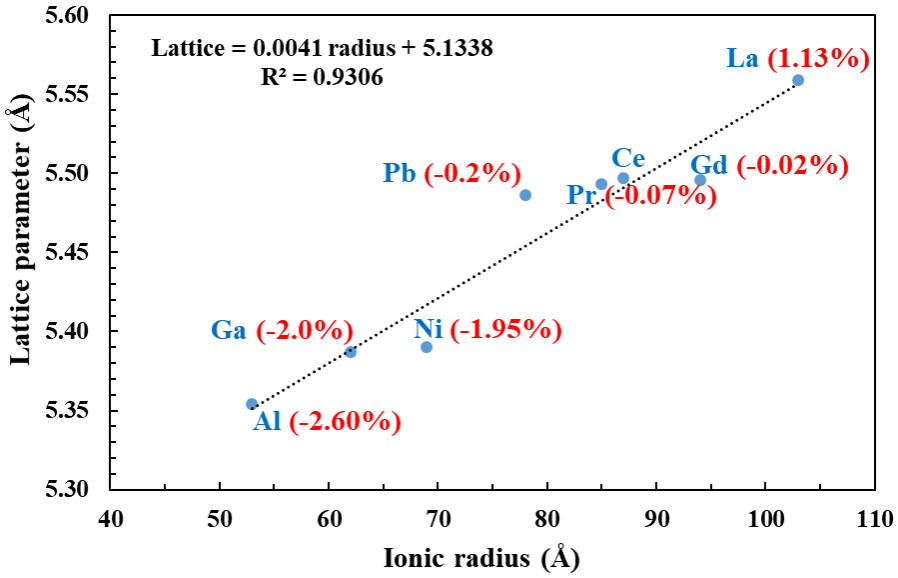

Figure 4-11. Calculated lattice parameter of the doped bulk ceria as a function of the dopant ionic radius. Numbers in parentheses denote the strain of undoped ceria with the same lattice parameter as the doped ceria.

A direct mapping between the total energetic span required for the WSR (ΔG_H+E_a) and strain at different temperature gives insights to evaluate the electrocatalytic WSR by strain engineering, referring to Figure S12 and S13 in the supporting information of Paper 2 with corresponding data listed in **Table 4-4**. The total energetic span for the fastest WSR pathway increases (largely) as the strain increases, which on the other hand shows that compressive strain improves the reaction rate. At 800 and 1000 K, the WSR with the lowest energetic span, proceeds through the excessively hydroxylated CeO_2(111) surface. However, a significant drop in the energetic span under -3% strain at 1200 K, where the most efficient reaction proceeds on the partially hydroxylated CeO_2(111). This arises from a large increase of the required total free energy for the 4H* and 5H* pathways combined with a decrease of the energetic span along the 2H* pathway as noted. In addition, **Figure 4-12** shows the forward TOF of the WSR calculated by the energetic span model ($\delta E=\Delta G_H+E_a$) using equation (4-1)[97] for the best pathway versus lattice strain at 800, 1000, and 1200 K.

$$TOF= K_BT/h\cdot \exp(-\delta E/K_BT) \quad (4\text{-}1)$$

The WSR preferentially proceeds on the excessively hydroxylated CeO_2(111) at 800 and 1000 K, while it proceeds readily on the partially or fully hydroxylated CeO_2(111) under compressive strain at higher temperature (T >1000 K). At high temperature, strain effectively determines the reaction pathway of the WSR. The direct mapping between experimentally accessible descriptors (lattice strain) and kinetic parameters gives insights into the WSR pathway under a given strain and operating temperature.

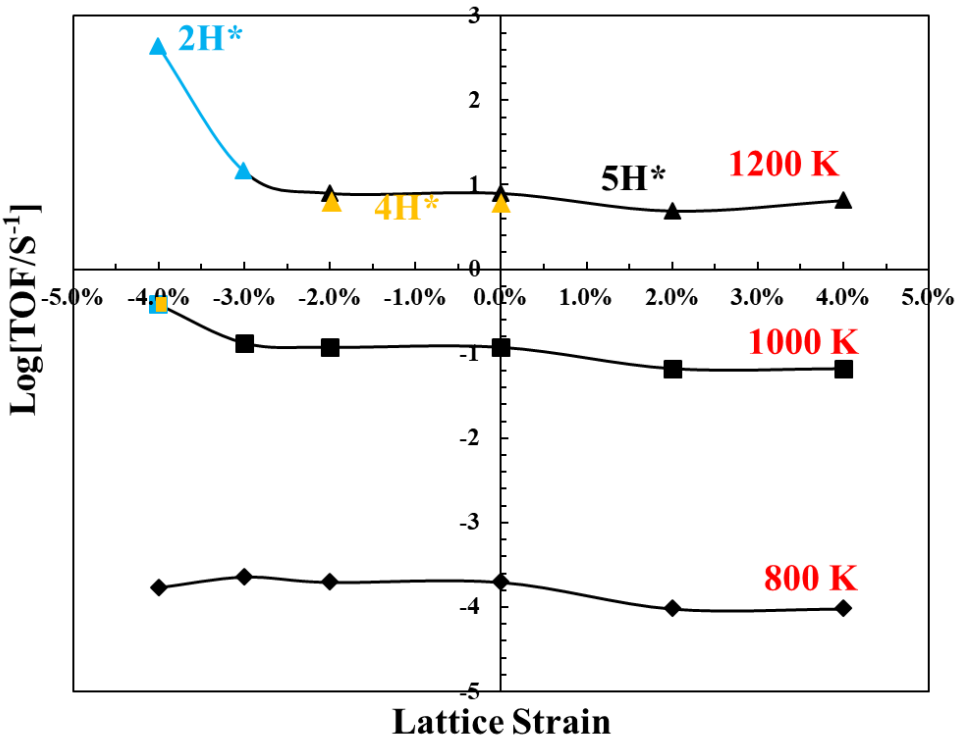

Figure 4-12. TOF of the WSR along the fastest pathway (the 2H*, 4H* or 5H* path) versus lattice strain at 800, 1000 and 1200 K.

4.4 Chapter Conclusions

By using DFT+*U* calculations, the WSR on CeO_2(111) as well as the effect of lattice strain on the formation of the intermediates, reaction barriers and reaction pathways are investigated. It is found that the formation energy of oxygen vacancies, vacancy-hydroxyl phase and hydroxyls decrease gradually as the lattice strain is increased because of downshifts of Ce 4*f* band center, which provides a strong support for the strain engineering on the formation of intermediates during the WSR. Then the activation barriers at each reaction step during the WSR on the reduced CeO_2(111), are correspondingly regulated because of the strain effects on the formation of the reaction intermediates. Strain effectively controls the formation of the Ce-H intermediate along

the excessively hydroxylated pathway, which is proved to have a low reaction barrier for the hydroxyl decomposition.

By studying the thermodynamics of the WSR on the reduced $CeO_2(111)$, it is found that strain effectively adjusts the reaction pathway of the WSR at T >1000 K. The WSR proceeds via a Ce-H intermediate on the excessively hydroxylated $CeO_2(111)$ under tensile strain. While it proceeds preferentially and readily on the partially or fully hydroxylated $CeO_2(111)$ under compressive strain. In addition, the free energy of hydroxyl forming (ΔG_H) prior to the hydroxyl decomposition can act as a thermodynamic barrier. The sum (ΔG_H+E_a) of the hydroxyl formation energy (ΔG_H) and the activation barrier (E_a) for the hydroxyl decomposition at the RDS during the WSR, determines the reaction rate of the hydrogen production on the strained and unstrained $CeO_2(111)$. Chapter 4 shows that compressive strain (< -3.0%) correlates strongly with increased WSR activity on $CeO_2(111)$ because of the reduction of ΔG_H+E_a. $CeO_2(111)$ compressively strained by more than 3.0% has high activity for the WSR along the partially or fully hydroxylated pathways at T=1200 K. Thus, incorporating the ceria with carefully selected metal dopants, which facilitates the formation of excessively hydroxylated ceria (low ΔG_H) and has a stable Metal-H intermediate (low E_a for hydrogen formation via a Metal-H intermediate), is predicted to significantly improve the reaction efficiency of the WSR on the ceria.

Chapter 5. Facet-Dependent WSR on CeO_2

This chapter is based on Paper 3, which has been included in Appendix B.3. The supplemental information has also been included in Appendix B.3.

5.1 Introduction

The most stable low-index terminations of ceria are the (110), (100), and (111) facets. Specific morphologies of ceria nanocrystal can expose these low-index surfaces. The (110) and (100) facets are mostly exposed in ceria nanorods and nanocubes, respectively.[102] However, Yang et al.[103] found that rode-shaped ceria nanoparticles are likely to expose the (111) facet. The ceria particles have more (100) terminations after undergoing a distinct shape evolution with increasing temperature.[104] The (111) facet of ceria is reported to have the lowest free energy under a wide range of oxygen partial pressures up to 1 atm at 300 K and thus becomes the most stable low-index surface of ceria, followed by the (110) and (100) facets.[105] Both experiments[106] and atomistic modelling[107,108] have shown that less energy is required for the oxygen vacancy formation on the (100) and (110) facets than that on the (111) facet of ceria. Therefore, the (100) and (110) facets of ceria are predicted to be more catalytically active than the (111) facet.[105-108]

However, facet dependence of catalytic processes on CeO_2 is widely reported.[30,69,102,109,110] Vilé et al.[109] found that among the (111), (110), and (100) facets, the CeO_2(100) surface is optimal for CO oxidation, whereas the (111) facet of ceria is more active for C_2H_2 hydrogenation. Aneggi et al.[102] reported that ceria exposed with the (100) and (110) terminations are more active in soot oxidation. As for the WSR on ceria, a relatively smaller amount of H_2 is produced from the reduced CeO_2(100) between 450 and 730 K than on CeO_2(111).[30] Recently, a number of computational investigations of water-associated reactions on ceria for H_2 production have been reported, largely focusing on the most often observed (111) terminations.[21,31,32] The rate-determining step for H_2 production via the WSR on CeO_2(111) is found to be hydroxyl decomposition via a Ce-H intermediate.[6,21] The investigations in Chapter 4 have shown that the reaction efficiency of ceria for the WSR can be improved by controlling the formation of Ce-H using strain engineering. In addition, the preference of Ce^{3+} locations on reduced CeO_2(111) like oxygen vacancies, hydroxyls and vacancy-hydroxyl mixed phases have been found to be sensitive to the position of the created oxygen vacancy, and hydrogen adsorption on CeO_2(111).[26,70,87] However, the fundamental understanding of the formation of important intermediates like oxygen

vacancies, hydroxyls and vacancy-hydroxyl mixed phases during the WSR, as well as their preferred Ce^{3+} locations, and the reaction kinetics on $CeO_2(100)$ and $CeO_2(110)$ remain unclear. In addition, more comparisons among $CeO_2(110)$, $CeO_2(100)$, and $CeO_2(111)$ as reaction surfaces for H_2 production via the WSR are desired.

In this chapter, the formation of reaction intermediates during the WSR as well as their preferred Ce^{3+} locations on $CeO_2(110)$ and $CeO_2(100)$ is systematically investigated by performing DFT+*U* calculations. The effect of hydrogen coverage and operating temperature on the WSR on the (110) and (100) facets are compared to the unstrained (111) facet studied in Chapter 4. In addition, the reaction pathways on these facets of ceria at different temperature are investigated, providing a direct mapping of the most efficient WSR pathway on $CeO_2(110)$ and $CeO_2(100)$, as compared to the unstrained $CeO_2(111)$ in Chapter 4.

5.2 Simulation Details

The $CeO_2(110)$ surface is built as a 2×2 surface unit cell consisting of five O-Ce-O atomic layers as shown in **Figure 5-1(a)**. The $CeO_2(100)$ surface is built as a 2×2 surface unit cell consisting of seven atomic layers as shown in **Figure 5-1(b)**. The $CeO_2(100)$ surface with O terminations is created following suggestions from both experiments[111] and DFT calculations.[69,110,112,113] In addition, half of the oxygen monolayer on the outmost layer of the $CeO_2(100)$ surface is transferred to the bottom in a checkerboard way. Herein, the exposed oxygen and cerium of the $CeO_2(100)$ surface are two-fold and six-fold coordinated, respectively. By contrast, the coordination number of the exposed oxygen and cerium of the $CeO_2(110)$ surface is three and six, respectively. For all DFT calculations in this chapter, the two O-Ce-O atomic layers at the bottom of $CeO_2(110)$ are kept fixed in the bulk geometry, while the four outermost atomic layers of $CeO_2(100)$ are allowed to relax as suggested by Capdevila-Cortada et al.[69,114] In **Figure 5-1**, we have enumerated the relaxed cerium atoms in both $CeO_2(110)$ and $CeO_2(100)$ to distinguish their locations and enable labeling of various distributions of Ce^{3+} ions with reduced phases containing oxygen vacancies or hydroxyls. For DFT+*U* calculations on these ceria surfaces, a Γ-centered 3×3×1 k-point mesh is used for optimizations and other DFT parameters are the same as that introduced in the section 2.2 of Chapter 2.

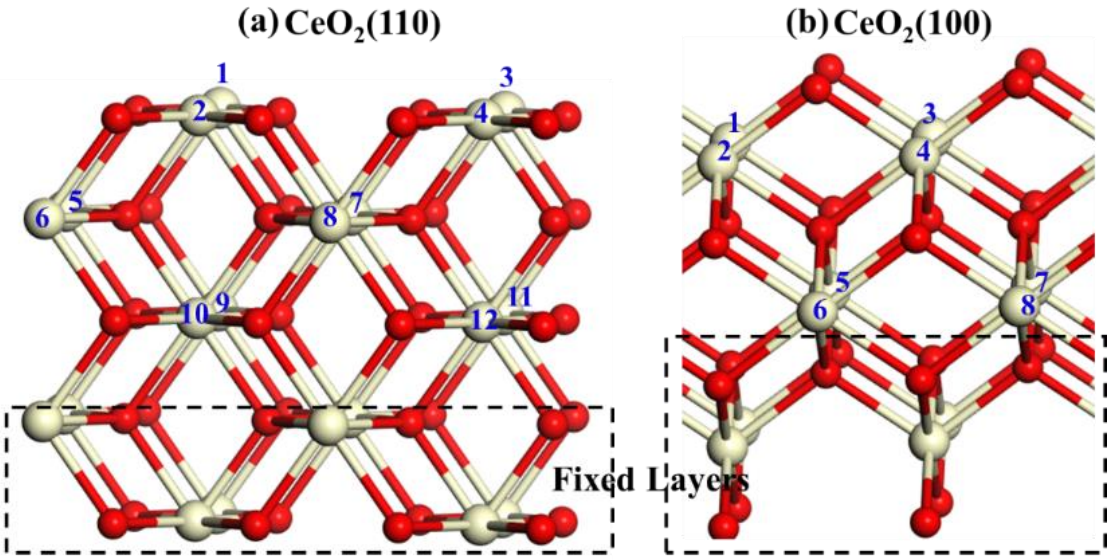

Figure 5-1. Side views of configurations of: (a) $CeO_2(110)$ and (b) $CeO_2(100)$. The relaxed cerium atoms are enumerated for distinguishing their locations. Cerium atoms are light yellow and oxygen atoms red.

5.3 Results and Discussions

In the following studies, the WSR via reaction (1-2), (1-3), (1-4), and (1-5) on the partially, fully and excessively hydroxylated $CeO_2(110)$ and $CeO_2(100)$ are investigated, which is compared with the reactions on $CeO_2(111)$. For the WSR on the partially hydroxylated $CeO_2(110)$, the surfaces covered by 2H, 4H, 5H, and 6H are investigated. The $CeO_2(110)$ surface is covered by 8H when it is fully hydroxylated. Total 9H adsorb on $CeO_2(110)$, forming the excessively hydroxylated $CeO_2(110)$. 2H, 4H, and 5H adsorbed on $CeO_2(100)$ is chosen as the partially, fully, and excessively hydroxylated $CeO_2(100)$ surface, respectively.

5.3.1 Creating one V_O on $CeO_2(110)$ and $CeO_2(100)$

As discussed in Chapter 4, the most stable Ce^{3+} locations after creating one oxygen vacancy in the subsurface (V_O^{sub}) and top surface (V_O^{sur}) of $CeO_2(111)$ is that $2Ce^{3+}$ are next nearest neighbor to the V_O. The oxygen formation energy varies with the Ce^{3+} distribution with a difference below 0.5 eV. However, it is found that the most stable Ce^{3+} locations after creating one oxygen vacancy on $CeO_2(110)$ and $CeO_2(100)$ behave differently from $CeO_2(111)$, referring to Tables S1-S4 in the supporting information of Paper 3.

When creating one subsurface V_O in $CeO_2(110)$, $2Ce^{3+}$ prefers to sit nearest neighbor to the V_O^{sub} and on the deeper cerium atomic layer of $CeO_2(110)$, which is about 0.95 eV more stable than the second most stable Ce^{3+} configurations as shown in Table S1 in the supporting information of Paper 3. However, when creating one surface V_O, an energy difference below 0.63 eV is found among all studied Ce^{3+} distributions in the V_O^{sur}, as shown in Table S2 in the supporting information of paper 3, which is much smaller than the energy difference of Ce^{3+} locations in the V_O^{sub}. The most preferred Ce^{3+} distribution is that $2Ce^{3+}$ locate on the top cerium atomic layer, where one Ce^{3+} is nearest neighbor to the V_O^{sur} while the other Ce^{3+} is next nearest neighbor to the V_O^{sur}. Overall, Ce^{3+} on the (110) facet of ceria is more likely to sit on the deeper cerium layer and next to the V_O^{sub}, while it favors to locate on the top cerium layer and next to the V_O when creating one V_O^{sur} in $CeO_2(110)$.

When creating one subsurface V_O in $CeO_2(100)$, two vacant sites for the formation of one V_O^{sub} on $CeO_2(100)$ have been investigated because there are two different Ce-O bond lengths as presented in **Figure A-2**. The most stable configuration of the V_O^{sub} on $CeO_2(100)$ is that the oxygen vacancy is created nearest neighbor to the cerium atoms, with one Ce^{3+} nearest neighbor to the V_O^{sub} while the second Ce^{3+} next-nearest to the V_O^{sub}, as shown in Table S3 in the supporting information of Paper 3. The most favored Ce^{3+} distribution around the V_O^{sub} is 1.2 eV more stable than the second most stable Ce^{3+} distribution, indicating a highly unfavorable formation of other Ce^{3+} distribution. Overall, when creating one V_O^{sur} on $CeO_2(100)$, the most favorable Ce^{3+} locations are the same as that for V_O^{sub}, see Table S4 in the supporting information of Paper 3. In addition to the similar preference for Ce^{3+} locations, the formation energy of the most stable V_O^{sur} (1.62 eV) is also quite close to that of the V_O^{sub} (1.67 eV) on $CeO_2(100)$. Thus, as compared to $CeO_2(100)$, the preferred Ce^{3+} locations on $CeO_2(110)$ are more sensitive to the position of the created V_O.

Finally, the oxygen formation energy of the most stable V_O^{sub} and V_O^{sur} on the (110), (100), and (111) facets of ceria, is summarized and shown in **Table 5-1,** with their preferred Ce^{3+} locations presented in **Figure 5-2 . Table 5-1** shows that the formation energy of the V_O^{sur} is quite close to that of the V_O^{sub} on $CeO_2(100)$. While the formation energy of the V_O^{sur} on $CeO_2(100)$ is 0.34 eV larger than that of the relaxed $CeO_2(100)$ reported by Kropp et al.[115] Creating one oxygen vacancy on the subsurface of $CeO_2(111)$ is 0.36 eV easier than on the top surface. By contrast, creating one V_O^{sur} on $CeO_2(110)$ becomes 0.34 eV more facile than creating one V_O^{sub}. It shows that creating one V_O^{sur} becomes favorable on $CeO_2(110)$ and $CeO_2(100)$. In addition, the formation energy of one oxygen vacancy is much lower on the (110) or (100) facet than that on the (111) facets, well consistent with reported findings.[106–108] Thus, it is indicated that the (110)

and (100) facets is more reducible than the (111) facet of ceria by creating oxygen vacancies.

Table 5-1. Formation energy of one oxygen vacancy in the subsurface (V_O^{sub}) and top surface (V_O^{sur}) of CeO_2(110) and CeO_2(100), compared with CeO_2(111).

Facets	(110)	(100)	(111)
$E(V_O^{sub})$/eV	1.48	1.67	1.75
$E(V_O^{sur})$/eV	1.14	1.62	2.11

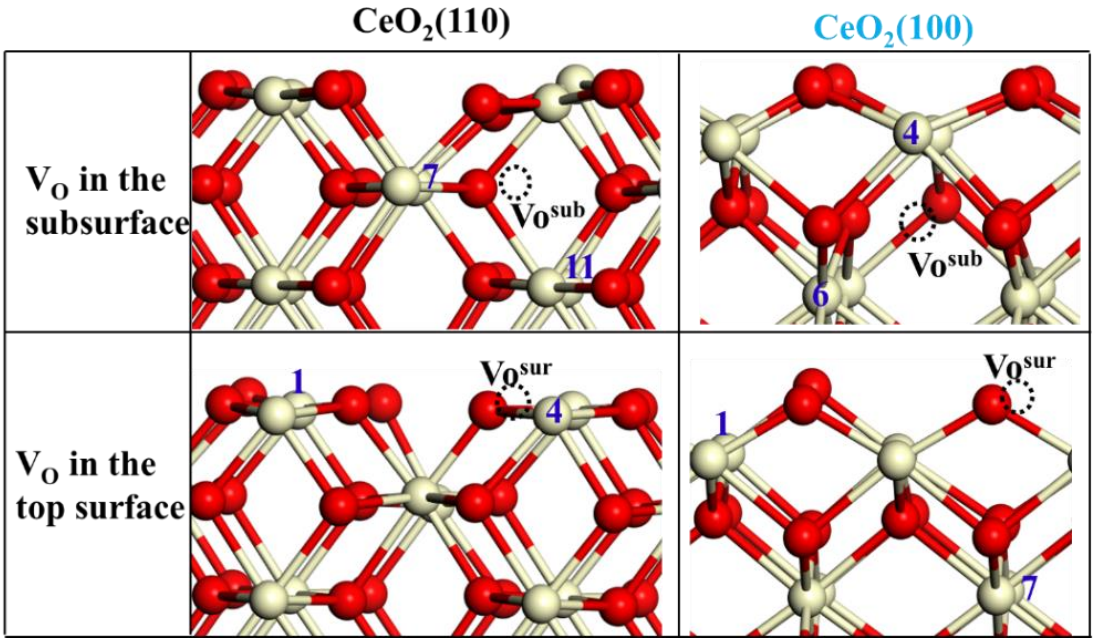

Figure 5-2. The most stable Ce^{3+} positions for the formation of one oxygen vacancy in the subsurface and top surface of CeO_2(110) and CeO_2(100). The numbering of Ce^{3+} locations corresponds to **Figure 5-1**.

5.3.2 Hydroxyl formation on CeO_2(110) and CeO_2(100)

Hydroxyls form via the water dissociation at reaction step (1-3), where hydroxyls locate preferentially nearest to the vacant site. Ce^{3+} sitting next to hydroxyls is always the most favored location on CeO_2(111) with different hydrogen coverages. Here, hydrogen adsorptions on CeO_2(110) and CeO_2(100) are investigated by comparing Ce^{3+} distributions at different hydrogen coverages.

For 1H adsorption on CeO_2(110), the most stable configuration is presented in **Figure 5-3(a)**, where one Ce^{3+} sits in the outmost layer of ceria and is nearest to the adsorbed H. The energy difference between different Ce^{3+} positions for 1H adsorption is below 0.38 eV, as shown in **Table 5-2**. For the formation of two hydroxyls on the (110) facet of ceria, the two hydroxyls can locate in one CeO_2 row (2H) or in the two different rows (2H'), as shown in **Figure 5-3(b)** and **5-3(c)**, respectively. After comparing Ce^{3+} positions in different relaxed cerium layers for the 2H and 2H' structure as list in **Table 5-2**, it is found that the most stable configuration of 2H is that one Ce^{3+} is nearest to hydroxyls, while the other Ce^{3+} sits in other row and far away from the adsorbed H, as shown in **Figure 5-3(b)**. The energy difference among different Ce^{3+} positions is below 0.86 eV. However, $2Ce^{3+}$ are nearest neighbor to 2H' as shown in **Figure 5-3(c)** and the energy difference among different Ce^{3+} positions is smaller than 0.33 eV. Overall, the formation energy of 2H with the most stable Ce^{3+} positions is 0.43 eV much lower than that of 2H' with the most stable Ce^{3+} positions, suggesting that the Ce^{3+} locations on CeO_2(110) is sensitive to the H adsorption site. For the formation of more hydroxyls on CeO_2(110), Ce^{3+} favors sitting nearest neighbor to hydroxyls, as shown in **Figure 5-3(d)** and Table S6 in the supporting information of paper 3. By contrast, the H adsorption sites on the (100) facet of ceria are symmetric. Ce^{3+} always prefers being next to hydroxyls on CeO_2(100) as shown in Table S7 in the supporting information of Paper 3, which is found on the (111) facet.

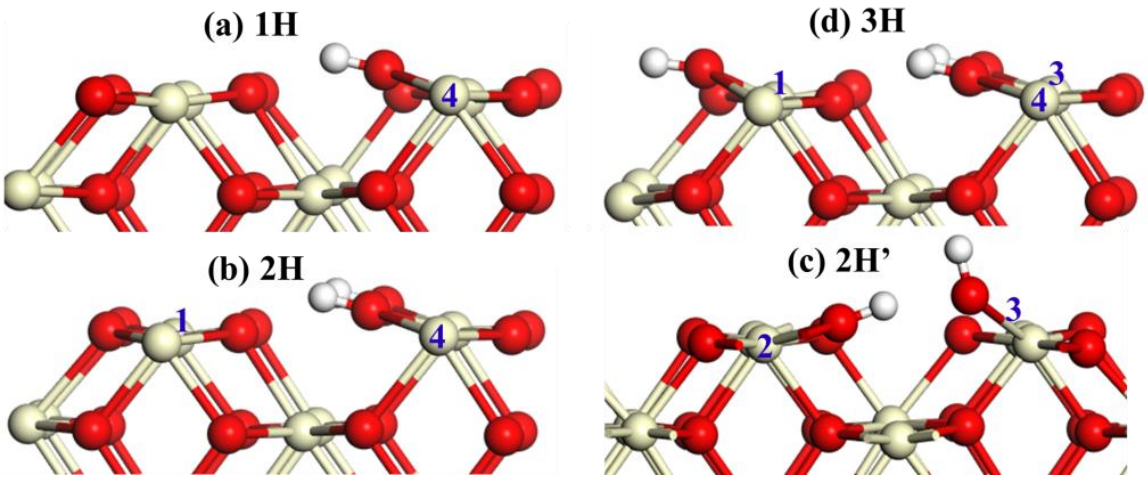

Figure 5-3. Hydrogen adsorption on the (110) facet of ceria with the most stable Ce^{3+} positions at different hydrogen coverages. The numbering of Ce^{3+} positions corresponds to **Figure 5-1.**

Table 5-2. Adsorption energy of one, two, and three H on CeO_2(110). Comparisons between different Ce^{3+} distributions. The numbering of Ce^{3+} positions corresponds to **Figure 5-1.**

1H		2H		2H'		3H	
Ce^{3+} locations	E_H	Ce^{3+} locations	E_2H	Ce^{3+} locations	E_2H'	Ce^{3+} locations	E_3H
(4)	-1.62	(1,4)	-3.14	(2,3)	-2.71	(1,3,4)	-4.76
(2)	-1.54	(2,4)	-3.11	(1,3)	-2.69	(2,3,4)	-4.75
(8)	-1.33	(3,4)	-3.02	(3,4)	-2.33	(1,2,3)	-4.61
(11)	-1.24	(1,2)	-2.62	(2,4)	-2.68	(1,3,11)	-4.45
		(4,8)	-2.99	(3,8)	-2.42	(1,2,8)	-4.29
		(4,6)	-2.80	(3,7)	-2.44	(3,4,8)	-4.21
		(4,12)	-2.80	(3,6)	-2.21	(4,7,6)	-4.20
		(4,11)	-2.76	(3,5)	-2.32	(9,3,11)	-3.86
		(4,9)	-2.74	(4,8)	-2.43	(4,7,10)	-4.08
		(1,12)	-2.73	(4,7)	-2.48	(7,3,11)	-4.58
		(2,12)	-2.70	(4,6)	-2.20	(6,7,8)	-3.76
		(2,11)	-2.68	(4,5)	-2.32	(7,8,10)	-4.28
		(4,11)	-2.75	(7,8)	-2.27	(8,10,11)	-4.45
		(2,10)	-2.80	(7,6)	-2.01	(10,11,12)	-3.90
		(3,10)	-2.75	(7,5)	-1.88		
		(7,8)	-2.58	(8,6)	-1.75		
		(5,8)	-2.64	(8,5)	-1.98		
		(5,6)	-2.36	(3,9)	-2.38		
		(8,12)	-2.48				
		(8,10)	-2.28				
		(11,12)	-2.58				

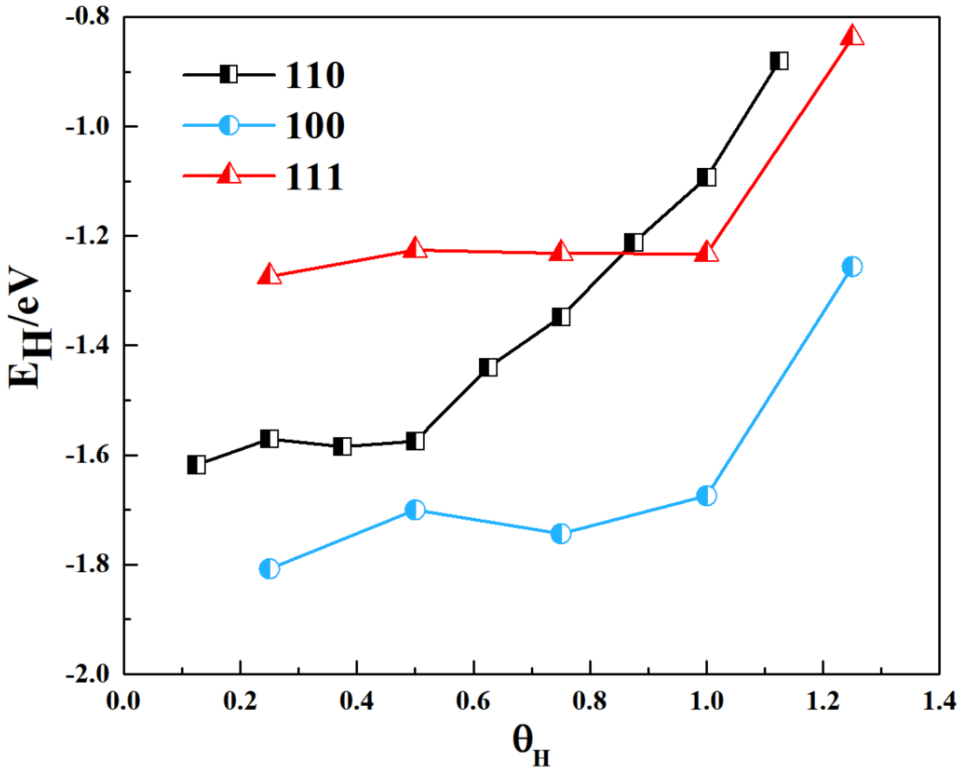

Figure 5-4. Average hydrogen adsorption energy on the (110), (100), and (111) facets of ceria, at different hydrogen coverages (Θ_H).

Average hydrogen adsorption energy (E_H) diagrams of the most stable hydroxylated CeO_2(110) and CeO_2(100) as a function of hydrogen coverage (Θ_H), as compared to CeO_2(111), are presented in **Figure 5-4**. The data for CeO_2(111) is taken from chapter 4. The definition of Θ_H refers to Chapter 3, where it is the number of the adsorbed H (N_H) divided by the total number of oxygen (N) in the outmost layer. The most stable configurations of the hydroxylated ceria exposed with different facets are shown in Figures S2 and S3 in the supporting information of Paper 3. On the CeO_2(100) surface, E_H is around -1.7 eV at Θ_H <1. As hydrogen coverage increases beyond one monolayer, E_H increases dramatically to -1.2 eV, suggesting that more than one monolayer coverage is relatively unstable compared to a lower hydrogen coverage on the CeO_2(100) surface. In contrast, the formation energy of the hydroxylated CeO_2(110) increases significantly above one half monolayer hydrogen coverage. As seen from **Figure 5-4**, hydrogen adsorbs strongest on the (100) facet followed by the (110) and (111) facets at low coverage. The formation of one monolayer hydrogen coverage, is however favored in the order of (100), (111) and (110). **Figure 5-4** reveals that the hydroxylated CeO_2(100) is much more stable than the hydroxylated CeO_2(110). These findings are well consistent with the reported experimental finding that hydroxyls on the (100) facet of ceria are much more stable than on the (111) facet.[30] The more stable formation of

hydroxyls on ceria is predicted to inhibit the hydroxyl decomposition for H_2 production.[21]

5.3.3 Formation of vacancy-hydroxyl mixed phases on CeO_2(110) and CeO_2(100)

Along the reaction pathways of the H_2 production on the partially (i.e. 2H, 4H, 5H, and 6H), fully (8H), and excessively (9H) hydroxylated CeO_2(110), ceria surfaces form vacancy-hydroxyl mixed phases when creating one V_O in the 3H, 4H, 6H, and 7H covered CeO_2(110). During the WSR on the partially (2H), fully (4H), and excessively (5H) hydroxylated CeO_2(100), the vacancy-hydroxyl mixed phase on CeO_2(100) forms when creating one V_O on the 3H covered CeO_2(100). As investigated for oxygen vacancies and hydroxyls, the Ce^{3+} distribution on these vacancy-hydroxyl mixed phases are also investigated, referring to Tables S8 and S9 in the supporting information of Paper 3. The top cerium atomic layer accommodates $3Ce^{3+}$ for the 3H covered CeO_2(110). When creating one V_O on it, Ce^{3+} firstly sits on the top cerium layer (making all cerium atoms in this layer Ce^{3+}) while the other Ce^{3+} locates in the third cerium layer, next to the V_O^{sub}. However, when creating one V_O^{sur}, the other Ce^{3+} sits in the second cerium layer and is next neighbor to it. Creating one V_O on the 4H covered CeO_2(110) where all Ce^{4+} ions on the top cerium layer have been reduced to Ce^{3+} ions because of hydrogen adsorptions, $2Ce^{3+}$ prefer to sit in the second cerium layer and next to the V_O^{sub}. When creating one V_O^{sur} on the 4H covered CeO_2(110), one Ce^{3+} locates in the second cerium layer and next to the vacancy, while the other Ce^{3+} sits in the third cerium layer and next nearest neighbor to the vacancy. When creating one V_O in the 6H or 7H covered CeO_2(110) surface, the next nearest neighbored positions to the V_O become unfavorable, leading to $2Ce^{3+}$ located next to the vacancy. The energy difference between different Ce^{3+} locations in the vacancy-hydroxyl mixed CeO_2(110) is below 0.82 eV, which is lower than creating one oxygen vacancy in CeO_2(110) without hydroxyls. In contrast, the energy difference between different Ce^{3+} locations in vacancy-hydroxyl mixed phases on CeO_2(100) is below 0.16 eV. Therefore, there is no obviously favored Ce^{3+} distributions when creating one V_O in the hydroxylated CeO_2(100), while Ce^{3+} prefers to sit next to V_O on the hydroxylated CeO_2(110).

In addition, the formation energy of one V_O in the CeO_2(110) and CeO_2(111) surfaces increases with increasing Θ_H. Oxygen vacancies in the surface or subsurface becomes unstable compared to the formation of one oxygen vacancy in a cubic bulk ($Ce_{32}O_{64}$), when the surface is covered by more than one monolayer hydrogen, as shown in **Figure 5-5**. In contrast, the formation of one oxygen vacancy in the hydroxylated CeO_2(100) with Θ_H = 0.5 and Θ_H = 0.75 is 1.0 and 0.5 eV, respectively, more stable than creating one V_O in the hydroxylated CeO_2(110) and CeO_2(111).

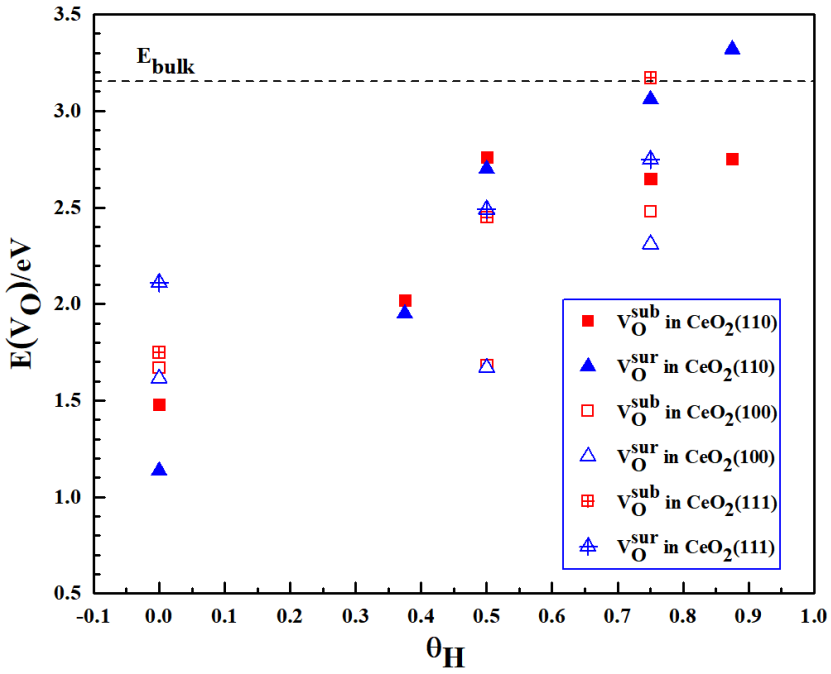

Figure 5-5. Formation energy of one oxygen vacancy in the hydroxylated (110) and (100) facets of ceria, compared with the (111) facet. E_{bulk} refers the oxygen formation energy in a bulk ($Ce_{32}O_{64}$) calculated by using Γ-centered 4×4×4 k-point mesh.

5.3.4 The most efficient reaction pathways on CeO_2(110) and CeO_2(100)

After investigating the formation of oxygen vacancies, hydroxyls and vacancy-hydroxyl mixed phases, the free energies of these reaction intermediates relative to a clean ceria surface are calculated by using the method described in Chapter 2. The free energy diagrams of the H_2 production on the partially, fully, and excessively hydroxylated ceria are presented in **Figures 5-6, 5-7, 5-8, and 5-9**, referring to Tables S10-S16 in the supporting information of Paper 3 for the magnetizations at each reaction step.

The reaction pathways of the WSR on the partially (2H, 4H, 5H, and 6H), fully (8H), excessively (9H) hydroxylated CeO_2(110) at 800 K are shown in **Figure 5-6**, referring to Figure S6 for the reaction pathways at 1200 K. The activation barrier for the formation of H_2 via 2H from one as well as two different rows is investigated on the 2H, 5H, 6H, and 8H covered CeO_2(110), where we use the annotations like 8H and 8H' to represent the H_2 production via 2H from one and two rows of the 8H covered CeO_2(110), respectively. For the H_2 production on the 2H covered CeO_2(110), the reactions including oxygen vacancy formation and diffusion, as well as water adsorption and dissociation are facile compared to hydroxyl decomposition into H_2, referring to Figure S5 in the supporting information of Paper 3. Although 2H is 0.43 eV more stable than 2H', it is found that the energy of the transition state for breaking 2H is close to that for

2H'. Hydroxyl decomposition for H_2 production remains the rate-determining step when more hydroxyls form on CeO_2(110) and the hydrogen coverage is below one monolayer, as seen from **Figure 5-6**. Similar transition states are found during hydroxyl decompositions on the hydroxylated CeO_2(110) with hydrogen coverage below one monolayer as shown in **Figures 5-7** and **5-8**. At these transition states, one hydrogen moves close to the other with one hydroxyl firstly broken and concomitant oxidation of Ce^{3+} to Ce^{4+}, referring to Tables S10-S13 in the supporting information of Paper 3 for the changes of magnetizations. The H_2 production via 2H from two different rows is 0.28 eV more favored over that from one same row when the surface has five hydroxyls, while that transition state for H_2 production via 2H from the same row is 0.26 eV more stable than that from the two different rows when the surface has six hydroxyls. When the surface is fully hydroxylated, the H_2 production via the 8H pathway is 0.18 eV more favorable than the 8H' pathway. The efficient H_2 production via breaking 2H on CeO_2(110) is affected by the hydrogen coverage.

By contrast, the hydroxyl decomposition on the excessively hydroxylated CeO_2(110) has no activation barrier, which has also been found for the WSR on CeO_2(111) in Chapters 3 and 4. However, an 1.0 eV activation barrier is found for forming the excessively hydroxylated CeO_2(110) via reaction (1-5), where one H binds with one lattice Ce to form one Ce-H. The rate-determining step during the WSR on the excessively hydroxylated CeO_2(110) becomes the water dissociation into the Ce-H. Although the free energies of each reaction intermediate increase when temperature increases to 1200 K, the rate-determining step along each reaction pathway remains unchanged.

In summary, the most favorable reaction pathway for the WSR on CeO_2(110) at 800 K is the H_2 production on the fully hydroxylated CeO_2(110). As temperature increases to 1200 K, the formation of the fully and excessively hydroxylated CeO_2(110) becomes less favorable than on the partially hydroxylated CeO_2(110). Therefore, the most efficient hydroxyl decomposition into H_2 at 1200 K proceeds via the partially hydroxylated CeO_2(110) covered by five hydrogens.

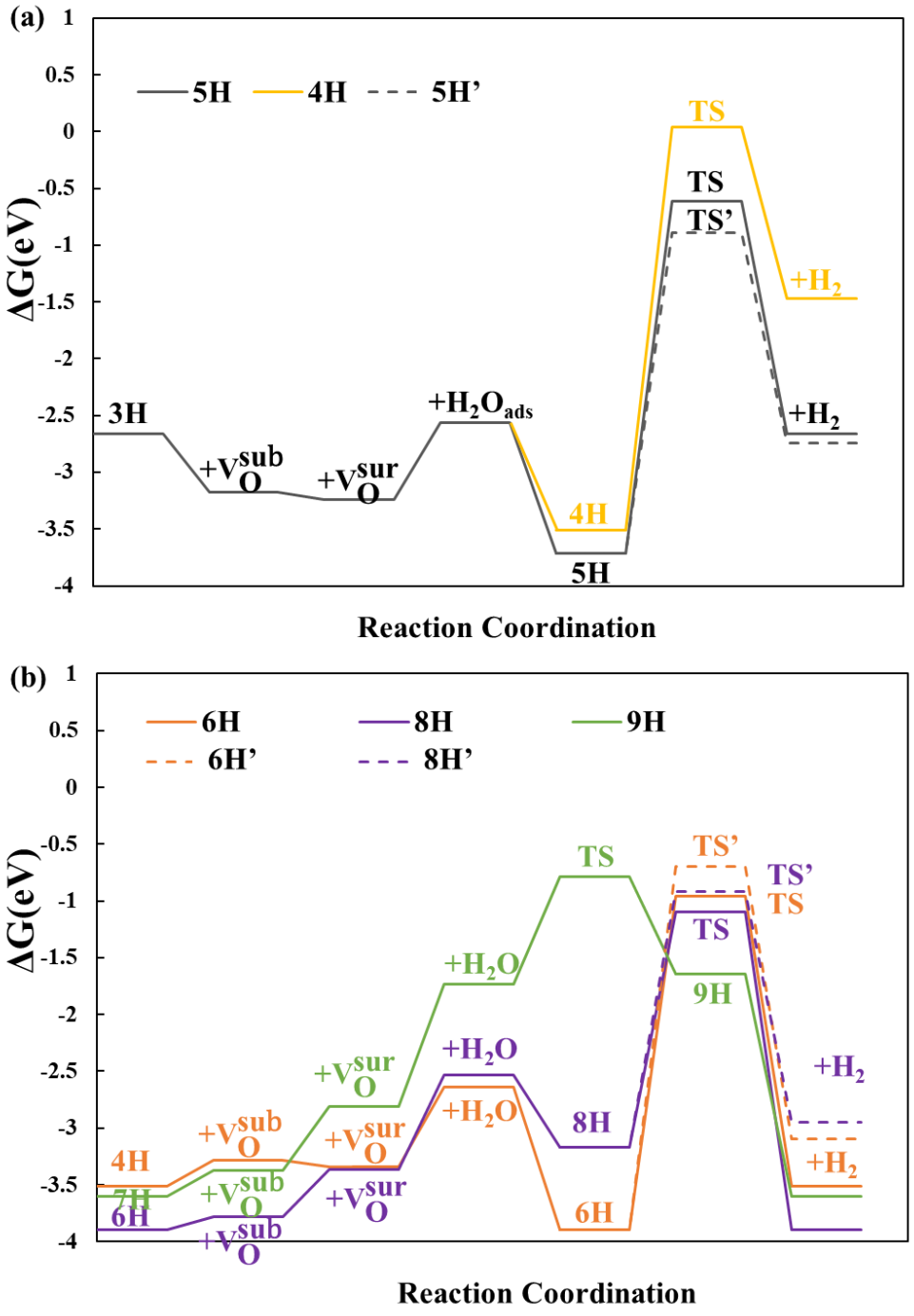

Figure 5-6. Free energy diagrams at 800 K for the WSR on CeO_2(110) with different hydrogen coverages: (a) 4H, 5H, and 5H'; (b) 6H, 6H', 8H, 8H', and 9H. The configurations of intermediates at each reaction step are presented in **Figures 5-7 and 5-8**. The magnetizations of each intermediate are given in Tables S11-S14 in the supporting information of Paper 3.

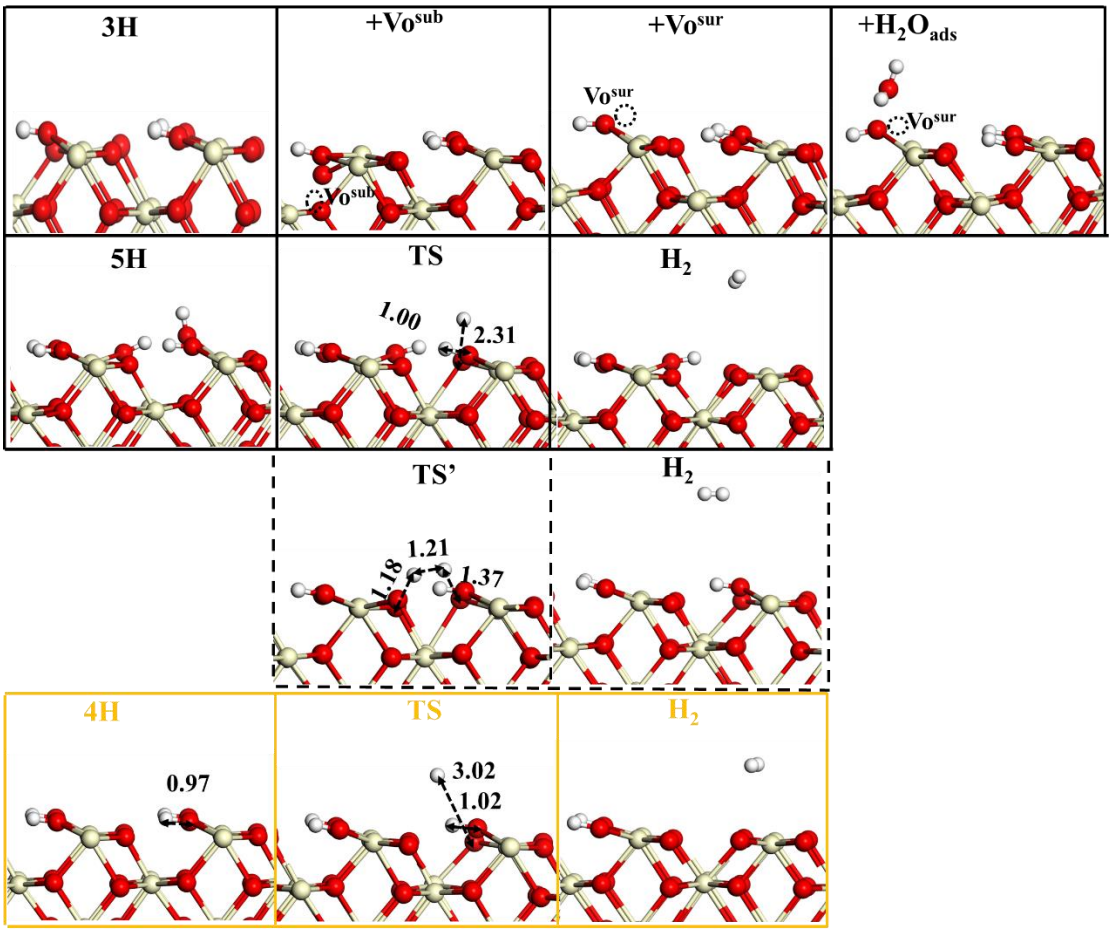

Figure 5-7. The configurations of intermediates at each reaction step along the WSR on the hydroxylated (5H, 4H, and 5H') CeO_2(110). The selected bond lengths are indicated.

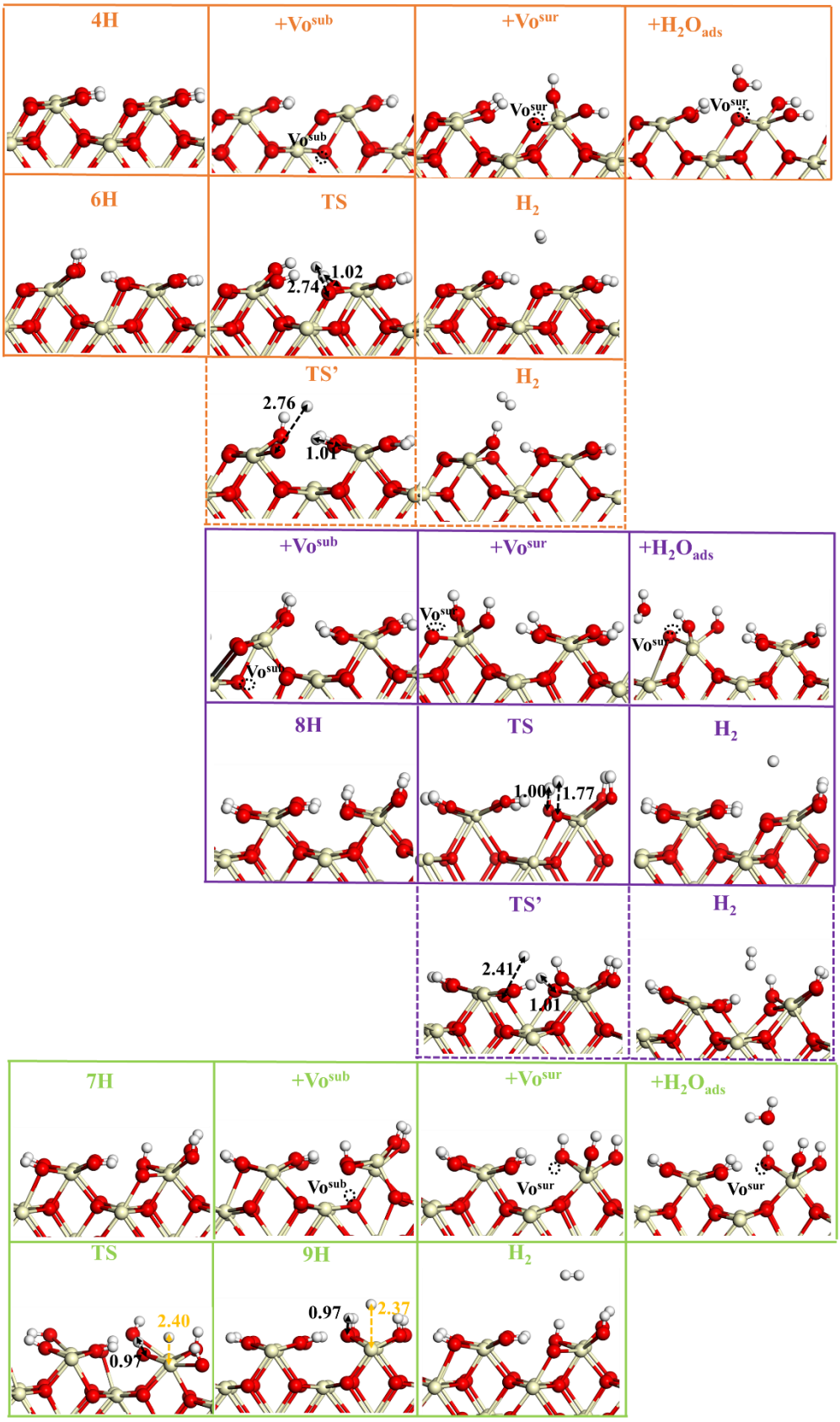

Figure 5-8. The configurations of intermediates at each reaction step along the WSR on the hydroxylated (6H, 6H', 8H, 8H', and 9H) CeO_2(110). The selected bond lengths are indicated.

Figure 5-9 presents the reaction pathways of the WSR on the partially (2H), fully (4H), excessively (5H) hydroxylated CeO_2(100), at 800 K, referring to Figure S9 for the reaction pathways at 1200 K. The fully hydroxylated CeO_2(100) is more stable than other intermediates at both 800 and 1200 K. Similarly with the WSR on CeO_2(110), the hydroxyl decomposition into H_2 is the most difficult step during the WSR on the partially and fully hydroxylated CeO_2(100). The identified transition states for hydroxyl decompositions on the partially and fully hydroxylated CeO_2(100) (having a 3.6 eV activation barrier) are similar to that on the (110) and (111) facets, where one H moves close to the neighbored Ce^{3+}, leading to break apart hydroxyl and oxidize one Ce^{3+} to Ce^{4+}, consistent with findings reported by Capdevila-Cortada et al.[69,82] However, the H_2 production on the excessively hydroxylated CeO_2(100) where one H binds with one lattice oxygen from the subsurface, only has a 1.8 eV activation barrier. Overall, the fastest reaction on CeO_2(100) proceeds on the excessively hydroxylated surfaces at both 800 and 1200 K.

By comparing the reaction pathways on different facets of ceria, the most favorable reaction pathway on ceria is found to be strongly facet-dependent, with the WSR on the CeO_2(100) and CeO_2(111) facets efficiently proceeds on the excessively hydroxylated surfaces. However, the fastest hydrogen production via the WSR on CeO_2(110) facet takes place on the fully hydroxylated surface at 800 K, while it preferentially proceeds on the CeO_2(110) surface with a lower hydrogen coverage at 1200 K.

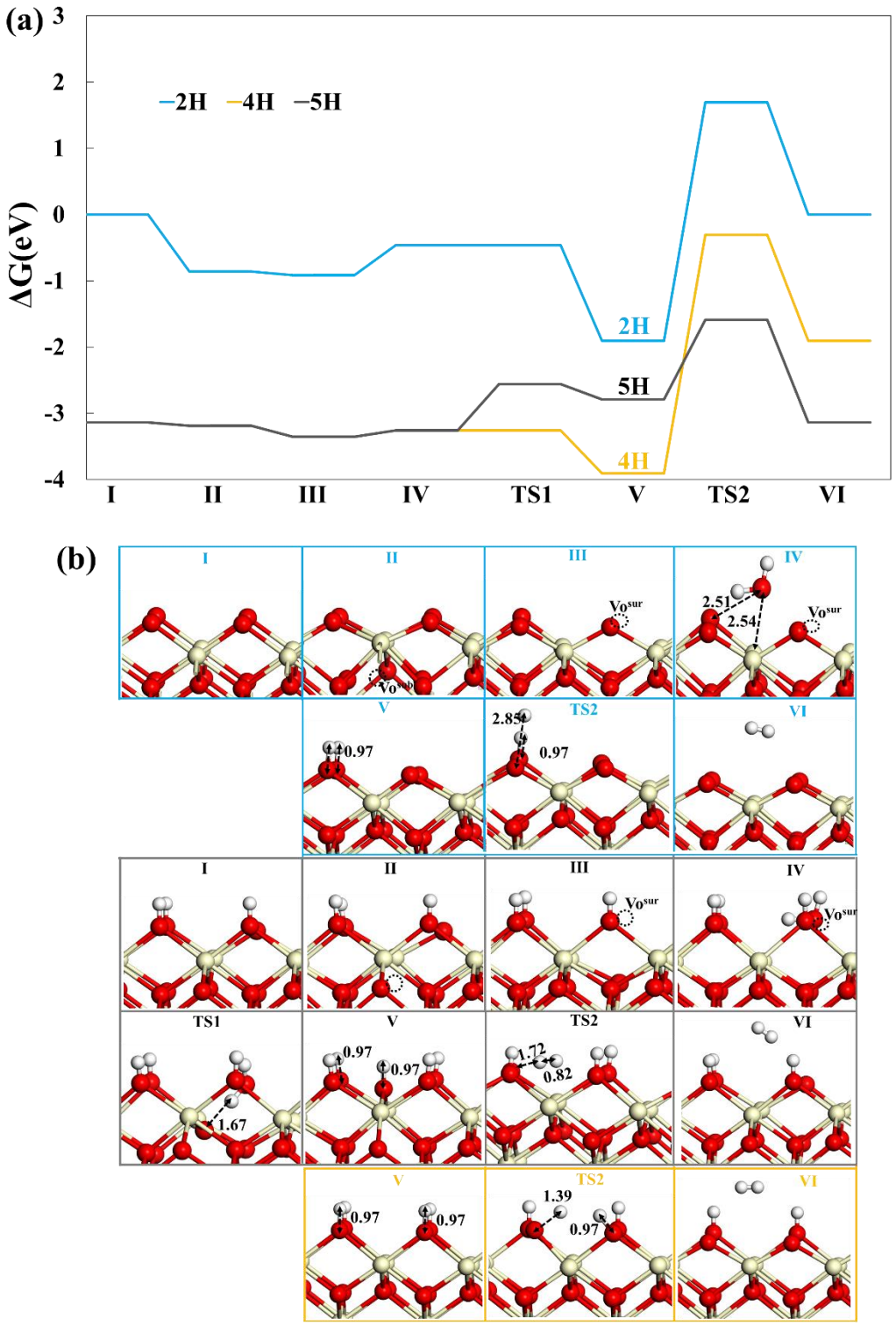

Figure 5-9. (a) Fee energy diagrams at 800 K for the WSR on the hydroxylated CeO_2(100) with different hydrogen coverages. (b) The configurations of intermediates at each reaction step are shown with selected bond lengths indicated. The magnetizations of each intermediate are list in Tables S15 and S16 in the supporting information of Paper 3.

To give a better understanding of the facet-dependence of the electrocatalytic WSR on ceria, the most favored reaction pathways on these facets of ceria at $400 \leq T \leq 1200$ K are presented in **Figure 5-10,** which is divided into three temperature regions. The definition of the TOF and the method to calculate it for the most efficient reaction on the (110) and (100) facets of ceria refer to that for the (111) facet of ceria in Chapter 4. The TOF for the WSR on CeO_2(111) is calculated by using data from Chapter 4. In the low-T region (T< 650 K), the reaction on the hydroxylated ceria with Θ_H=1.25 ML is predicted to be favored on the (110), (111), and (100) facets of ceria. In the intermediate-T region (650 < T < 950 K), the fastest reaction pathway remains on the excessively hydroxylated (111) and (100) facets of ceria, while the reaction on surface with Θ_H =1.0 ML becomes be favored on the (110) facet of ceria. In the high-T region (T > 950 K), the most efficient reaction pathway on the (110) facet of ceria shifts to the reaction on the partially hydroxylated surface with Θ_H=0.63 ML. Thus, the most favored reaction pathway on CeO_2(110) is more sensitive to the operating temperature, as compared to CeO_2(100) and CeO_2(111). This is because the formation of hydroxyls and vacancy-hydroxyl mixed phase on CeO_2(110) is very dependent on the hydrogen adsorption coverages and hydrogen adsorption sites as discussed in section **5.3.2** and **5.3.3.** The most active hydroxylated surface is affected by the operating temperature, as shown in **Figure 5-10**. The formation of more than 2H coverage on each facet improves the activity by orders of magnitude for the WSR for each facet at any operating temperature, as seen from Figure S10 in the supporting information of paper 3.

In summary, the WSR on the (110) facet is much more efficient, followed by the (111) and (100) facets in low-T region. However, the reaction on the (111) facet is fastest at 650 < T < 950 K. At a higher T, the TOF of the WSR on CeO_2(110) is very closed to that on CeO_2(111), but 10~100 times higher than that on CeO_2(100). Overall, the WSR for H_2 production on the (111) and (110) facets of ceria is 10~100 times faster in comparison with that on the (100) facet of ceria at T < 950 K. Thus, the WSR on ceria is strongly facet-dependent at low and intermediate temperature. The BEP relation for hydroxyl decomposition on different facets of ceria is estimated and shown in **Figure 5-11**. The BEP relation clearly shows that the H_2 production via hydroxyl decompositions on the hydroxylated CeO_2(100) is more difficult than that on the hydroxylated CeO_2(111) and CeO_2(110), which is consistent with the finding that the higher stability of the hydroxyls on the CeO_2(100) surface leads to more difficult hydroxyl decomposition into H_2. Our findings agree with experiments that a smaller amount of H_2 is produced from reduced CeO_2(100) between 450 and 730 K compared to the (111) facet.[30] Therefore, the mapping of the TOF for the WSR on the (110), (111) and (100) facets of ceria provides an improved understanding of the electrocatalytic WSR on ceria and its facet-dependent behavior.

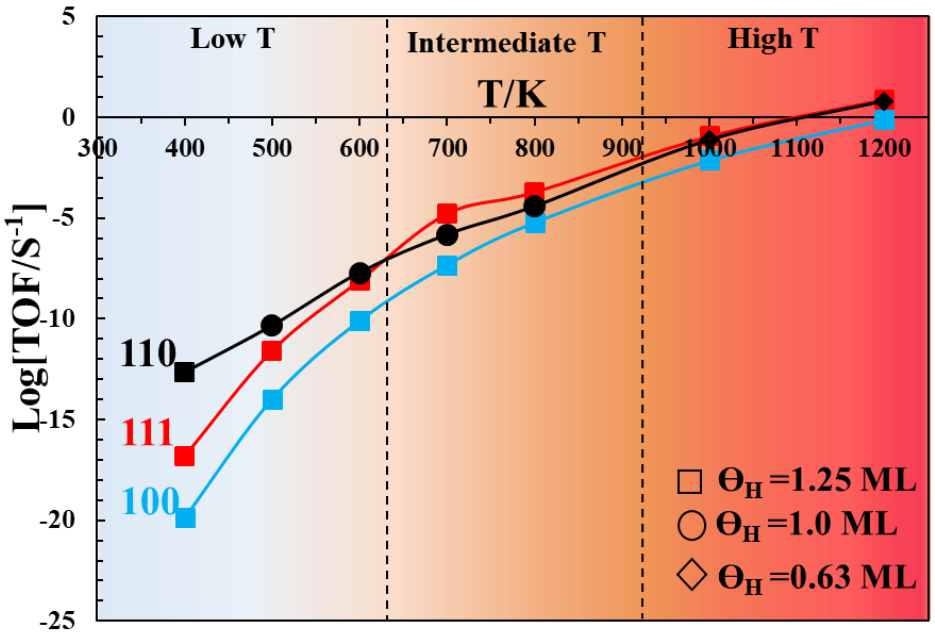

Figure 5-10. Mapping of the TOF of the most efficient reaction pathway (with specific hydrogen coverage) on CeO_2(100), CeO_2(110) and CeO_2(111), respectively, at $400 \leq T \leq 1200$ K.

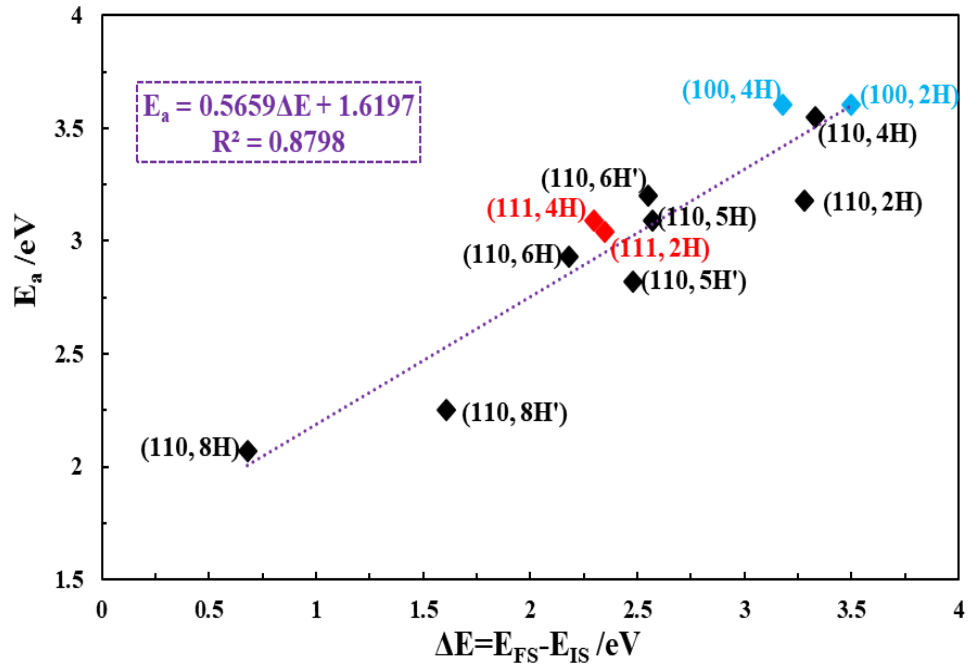

Figure 5-11. The BEP relation between the activation barriers of the hydroxyl (the initial state, IS) decomposition into H_2 (the final state, FS) on the hydroxylated CeO_2(110), CeO_2(100) and CeO_2(111) surfaces, and the reaction energy (E_f=E_{FS}-E_{IS}).

5.4 Chapter Conclusions

After investigating the formation of the reaction intermediates and reaction kinetics of the WSR on ceria exposed with (110) and (100) facets which is compared to the WSR on the (111) facet of ceria, the WSR on ceria is found to be strongly facet-dependent. Compared with the (100) and (111) facets, Ce^{3+} distributions on the reduced CeO_2(110) is more sensitive to H adsorption sites and positions of the created V_O. Although varying with different Ce^{3+} distributions, the formation of one oxygen vacancy on the (100) and (110) facets of ceria is found to be more facile than that on the (111) facet. The preferred Ce^{3+} distributions on these facets of ceria vary significantly, having an energy difference between Ce^{3+} distributions on the CeO_2(110) and CeO_2(100) surfaces above 0.95 and 1.21 eV, respectively. However, the energy difference between Ce^{3+} positions of vacancy-hydroxyl mixed phases becomes smaller, with Ce^{3+} preferentially sitting next to hydroxyls while next nearest neighbor to oxygen vacancies. The formation of hydroxyls and vacancy-hydroxyl mixed phase on the (100) facet of ceria is much more stable than on the (110) and (111) facets. The formation of the fully hydroxylated CeO_2(100) and CeO_2(111) is always thermodynamically favored over other hydrogen coverages at different operating temperature. The formation of the fully hydroxylated CeO_2(110) becomes unstable, leading to a relatively low activation barrier for the H_2 production via hydroxyl decomposition. The higher stability of the hydroxyls on CeO_2(100) inhibits hydroxyl decomposition into H_2.

In addition, the most favored reaction pathways on ceria is also facet-dependent, with the WSR preferentially proceeding on the excessively hydroxylated surface on the (100) and (111) facets, while the preferred pathway on the (110) facet varies with operating temperature. The most favorable pathway on CeO_2(110) proceeds on the fully hydroxylated surfaces at 800 K and shifts on the partially hydroxylated CeO_2(110) at a higher temperature. A mapping of the most favored reaction pathways on these facets at $400 \leq T \leq 1200$ K shows that the WSR on ceria is strongly facet-dependent for $T <$ 950 K. This strong facet-dependence of the WSR on ceria diminishes at a higher temperature. These findings suggest that the facet-dependence of the WSR on ceria is temperature sensitive.

Chapter 6. Conclusions and Outlook

6.1 Conclusions

By using the DFT+*U* method, the fundamental reaction mechanism for the WSR on low index facets of ceria as well as the effect of strain and doping are systemically investigated in this thesis. Several effective ways are found to improve the reactivity of ceria for the WSR as follows.

(1) The incorporation of Gd in ceria plays an important role in stabilizing the intermediates and transition states for hydroxyl decomposition, enhancing the performance of ceria for the WSR. A dopant that stabilizes the reduced ceria surface and has strong binding to hydrogen is capable of effectively improving the reaction activity of ceria for sustainable hydrogen production in a SOEC.

(2) It is found that strain effectively engineers the formation of intermediates during the WSR, as well as adjusts the reaction pathway of the WSR. CeO_2(111) compressed by more than 3.0% strain has high activity for the WSR. Incorporating ceria with carefully selected dopants, covered by a thin CeO_2 shell to form core-shell particles is a possible way to achieve compressed ceria surface. Thus, it is predicted that a strained, doped ceria can have great potential for facilitating H_2 production via the WSR.

(3) After investigating the formation of the reaction intermediates and reaction kinetics of the WSR on ceria exposed with the (110), (100) and (111) facets of ceria, the WSR on ceria is found to be strongly facet-dependent. The formation of intermediates like oxygen vacancies, hydroxyls and vacancy-hydroxyl mixed phase on the (100) facet of ceria are much more facile than that on the (110) and (111) facets. The strong stability of intermediates on the (100) facets inhibits H_2 production via the WSR. Overall, the WSR on the CeO_2(111) and CeO_2(110) is faster than that on CeO_2(100). In addition, the effect of facets at various temperature was also evaluated, revealing that while the WSR on ceria exposed with the (110) or (111) facets is faster than exposed with the (100) facet at intermediate operating temperature, the strong facet-dependence of the WSR on ceria is reduced significantly at high temperature. Thus, it suggests that the catalysis on ceria is sensitive to the exposed facets at intermediate operating temperature.

6.2 Outlook

As shown from the computational studies in this thesis, Gd doped ceria, compressively strained ceria as well as ceria exposed with the (110) and (111) facets used as hydrogen electrode in a SOEC is capable of improving the reactivity of ceria for sustainable hydrogen production. However, the total energetic span required for the H_2 production on GDC is only 0.25 eV lower than that on the pure CeO_2(111). In addition, the operating temperature of the WSR on the GDC, strained (111) facet of ceria, and the (110) facet of ceria is higher than 1000 K. More DFT calculations may therefore be performed in the future to improve kinetics of H_2 production on ceria and further to extend the operation at intermediate temperature (T < 1000 K). Inspired by previous findings in this thesis, doping and co-doping combined with strain technologies holds great potential for improving the catalysis on ceria in several ways as follows.

(1) The preliminary simulations show that incorporating CeO_2(111) with Pd, Pr, and Ga is able to stabilize the formation of the excessively hydroxylated CeO_2(111), which is predicted to improve the WSR on ceria. Instead of doping ceria by replacing cerium atoms with dopants, it is possible to carry out computational investigations on single atom catalyst or clusters like Au, Pd single atom or clusters supported on CeO_2(111) that have high reactivity during many catalytic processes like CH_4 activation and CO oxidation.[116-118]

(2) As presented in Chapter 4, the incorporation of Ga into CeO_2(111) leads to the ceria lattice compressed by 2%. After performing preliminary calculations on the Ga doped CeO_2(111), the formation of intermediates like the excessively hydroxylated (5H) CeO_2(111) becomes much more facile as compared to that on the pure CeO_2(111) compressed by 2% strain, as shown in **Figure 6-1**. In addition, the energetic span for the H_2 production on the Ga doped ceria is about 0.5 eV lower than that on the pure ceria. By contrast, the energetic span for H_2 production on GDC is only 0.25 eV lower in comparison with the pure CeO_2(111), as shown in Chapter 3. Thus, Ga doping may prove more effective for improving the WSR on ceria than Gd doping. Combined with strain technology by tuning the lattice of the Ga doped ceria being slightly compressed is more likely to enhance the activity of ceria. Therefore, the WSR on strained doped (111) facet of ceria is predicted to have improved reactivity.

(3) All above investigations on CeO_2(111) can be further extended to the (110) facet of ceria since the reactivity of the WSR on CeO_2(110) in Chapter 5 is found to be as high as that on CeO_2(111). In addition to the WSR, more investigations can be carried out on other catalytic processes like CO oxidation[116-118] and NO reduction[119, 120] on ceria-based catalysts.

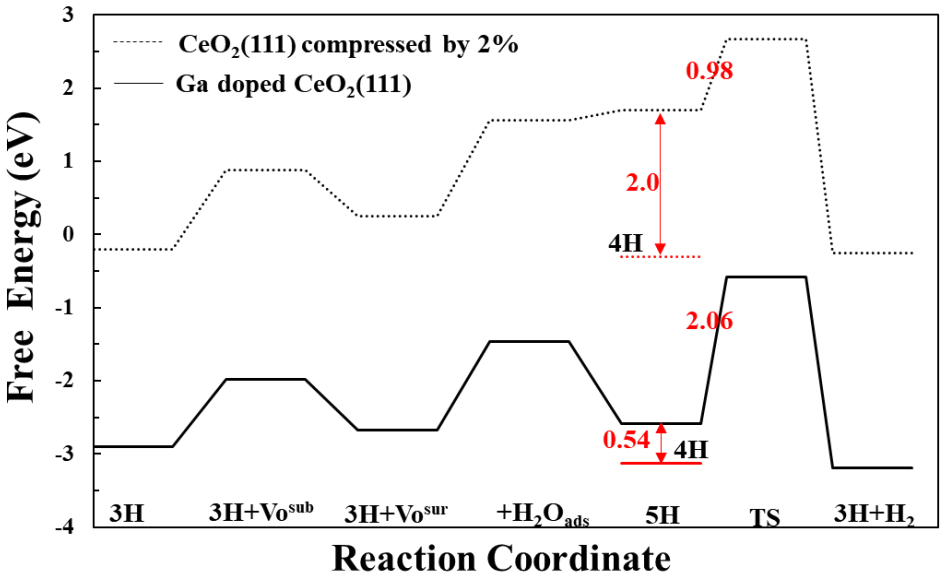

Figure 6-1. Reaction pathways at 1200 K for the WSR on the Ga doped CeO_2(111) and the pure CeO_2(111) compressed by 2% strain.

References

(1) Turner, J. A. Sustainable Hydrogen Production Processes. *Science* **2004**, *305*, 972–975.

(2) Holladay, J. D.; Hu, J.; King, D. L.; Wang, Y. An Overview of Hydrogen Production Technologies. *Catal. Today* **2009**, *139*, 244–260.

(3) Ball, M.; Wietschel, M. The Future of Hydrogen–Opportunities and Challenges. *Hydrog. Econ. Oppor. Challenges* **2009**, *34*, 615–627.

(4) Sapountzi, F. M.; Gracia, J. M.; Weststrate, C. J.; Fredriksson, H. O. A.; Niemantsverdriet, J. W. Electrocatalysts for the Generation of Hydrogen, Oxygen and Synthesis Gas. *Prog. Energy Combust. Sci.* **2017**, *58*, 1–35.

(5) Ibrahim, H.; Ilinca, A.; Perron, J. Energy Storage Systems–Characteristics and Comparisons. *Renew. Sustain. Energy Rev.* **2008**, *12*, 1221–1250.

(6) Feng, Z. A.; El Gabaly, F.; Ye, X.; Shen, Z.-X.; Chueh, W. C. Fast Vacancy-Mediated Oxygen Ion Incorporation across the Ceria-Gas Electrochemical Interface. *Nat. Commun.* **2014**, *5*, 4374.

(7) Irvine, J. T. S.; Neagu, D.; Verbraeken, M. C.; Chatzichristodoulou, C.; Graves, C.; Mogensen, M. B. Evolution of the Electrochemical Interface in High-Temperature Fuel Cells and Electrolysers. *Nat. Energy* **2016**, *1*, 15014.

(8) Li, Q.; Zheng, Y.; Guan, W.; Jin, L.; Xu, C.; Wang, W. G. Achieving High-Efficiency Hydrogen Production Using Planar Solid-Oxide Electrolysis Stacks. *Int. J. Hydrogen Energy* **2014**, *39*, 10833–10842.

(9) Penchini, D.; Cinti, G.; Discepoli, G.; Desideri, U. Theoretical Study and Performance Evaluation of Hydrogen Production by 200 W Solid Oxide Electrolyzer Stack. *Int. J. Hydrogen Energy* **2014**, *39*, 9457–9466.

(10) Hauch, A.; Mogensen, M.; Hagen, A. Ni/YSZ Electrode Degradation Studied by Impedance Spectroscopy–Effect of p(H_2O). *Solid State Ionics* **2011**, *192*, 547–551.

(11) Jen, H.-W.; Graham, G. W.; Chun, W.; McCabe, R. W.; Cuif, J.-P.; Deutsch, S. E.; Touret, O. Characterization of Model Automotive Exhaust Catalysts: Pd on Ceria and Ceria-Zirconia Supports. *Catal. Today* **1999**, *50*, 309–328.

(12) Oh, S. H.; Hoflund, G. B. Chemical State Study of Palladium Powder and Ceria-Supported Palladium during Low-Temperature CO Oxidation. *J. Phys. Chem. A* **2006**, *110*, 7609–7613.

(13) Di Monte, R.; Kašpar, J. On the Role of Oxygen Storage in Three-Way Catalysis. *Top. Catal.* **2004**, *28*, 47–57.

(14) Liu, X.; Zhou, K.; Wang, L.; Wang, B.; Li, Y. Oxygen Vacancy Clusters Promoting Reducibility and Activity of Ceria Nanorods. *J. Am. Chem. Soc.* **2009**, *131*, 3140–3141.

(15) Song, Y.-L.; Yin, L.-L.; Zhang, J.; Hu, P.; Gong, X.-Q.; Lu, G. A DFT+*U* Study of CO Oxidation at CeO_2 (110) and (111) Surfaces with Oxygen Vacancies. *Surf. Sci.* **2013**, *618*, 140–147.

(16) Bunluesin, T.; Gorte, R. J.; Graham, G. W. Studies of the Water-Gas-Shift Reaction on Ceria-Supported Pt, Pd, and Rh: Implications for Oxygen-Storage Properties. *Appl. Catal. B Environ.* **1998**, *15*, 107–114.

(17) Fu, Q.; Saltsburg, H.; Flytzani-Stephanopoulos, M. Active Nonmetallic Au and Pt Species on Ceria-Based Water-Gas Shift Catalysts. *Science* **2003**, *301*, 935–938.

(18) Hilaire, S.; Wang, X.; Luo, T.; Gorte, R. J.; Wagner, J. A Comparative Study of Water-Gas-Shift Reaction over Ceria-Supported Metallic Catalysts. *Appl. Catal. A Gen.* **2001**, *215*, 271–278.

(19) Otsuka, K.; Hatano, M.; Morikawa, A. Hydrogen from Water by Reduced Cerium Oxide. *J. Catal.* **1983**, *79*, 493–496.

(20) Abanades, S.; Legal, A.; Cordier, A.; Peraudeau, G.; Flamant, G.; Julbe, A. Investigation of Reactive Cerium-Based Oxides for H_2 Production by Thermochemical Two-Step Water-Splitting. *J. Mater. Sci.* **2010**, *45*, 4163–4173.

(21) Hansen, H. A.; Wolverton, C. Kinetics and Thermodynamics of H_2O Dissociation on Reduced CeO_2(111). *J. Phys. Chem. C* **2014**, *118*, 27402–27414.

(22) Paier, J.; Penschke, C.; Sauer, J. Oxygen Defects and Surface Chemistry of Ceria: Quantum Chemical Studies Compared to Experiment. *Chem. Rev.* **2013**, *113*, 3949–3985.

(23) Chueh, W. C.; Hao, Y.; Jung, W.; Haile, S. M. High Electrochemical Activity of the Oxide Phase in Model Ceria-Pt and Ceria-Ni Composite Anodes. *Nat. Mater.* **2012**, *11*, 155–161.

(24) Zhang, C.; Grass, M. E.; McDaniel, A. H.; Decaluwe, S. C.; Gabaly, F. E.; Liu, Z.; McCarty, K. F.; Farrow, R. L.; Linne, M. A.; Hussain, Z.; Jackson, G. S.; Bluhm, H.; Eichhorn, B. W. Measuring Fundamental Properties in Operating Solid Oxide Electrochemical Cells by Using in Situ X-Ray Photoelectron Spectroscopy. *Nat. Mater.* **2010**, *9*, 944–949.

(25) Su, Y. Q.; Filot, I. A. W.; Liu, J. X.; Tranca, I.; Hensen, E. J. M. Charge Transport over the Defective CeO_2(111) Surface. *Chem. Mater.* **2016**, *28*, 5652–

5658.

(26) Ganduglia-Pirovano, M. V.; Da Silva, J. L. F.; Sauer, J. Density-Functional Calculations of the Structure of near-Surface Oxygen Vacancies and Electron Localization on CeO_2(111). *Phys. Rev. Lett.* **2009**, *102*, 026101.

(27) Castleton, C. W. M.; Kullgren, J.; Hermansson, K. Tuning LDA+*U* for Electron Localization and Structure at Oxygen Vacancies in Ceria. *J. Chem. Phys.* **2007**, *127*, 244704.

(28) Li, H.-Y.; Wang, H.-F.; Guo, Y.-L.; Lu, G.-Z.; Hu, P. Exchange between Sub-Surface and Surface Oxygen Vacancies on CeO_2(111): A New Surface Diffusion Mechanism. *Chem. Commun.* **2011**, *47*, 6105–6107.

(29) Zhang, D.; Han, Z.-K.; Murgida, G. E.; Ganduglia-Pirovano, M. V.; Gao, Y. Oxygen-Vacancy Dynamics and Entanglement with Polaron Hopping at the Reduced CeO_2 (111) Surface. *Phys. Rev. Lett.* **2019**, *122*, 096101.

(30) Mullins, D. R.; Albrecht, P. M.; Chen, T.-L.; Calaza, F. C.; Biegalski, M. D.; Christen, H. M.; Overbury, S. H. Water Dissociation on CeO_2(100) and CeO_2(111) Thin Films. *J. Phys. Chem. C* **2012**, *116*, 19419–19428.

(31) Molinari, M.; Parker, S. C.; Sayle, D. C.; Islam, M. S. Water Adsorption and Its Effect on the Stability of Low Index Stoichiometric and Reduced Surfaces of Ceria. *J. Phys. Chem. C* **2012**, *116*, 7073–7082.

(32) Yang, Z.; Wang, Q.; Wei, S.; Ma, D.; Sun, Q. The Effect of Environment on the Reaction of Water on the Ceria (111) Surface : A DFT+*U* Study. *J. Phys. Chem. C* **2010**, *114*, 14891–14899.

(33) Dvořák, F.; Szabová, L.; Johánek, V.; Farnesi Camellone, M.; Stetsovych, V.; Vorokhta, M.; Tovt, A.; Skála, T.; Matolínová, I.; Tateyama, Y.; Mysliveček, J.; Fabris, S.; Matolín, V. Bulk Hydroxylation and Effective Water Splitting by Highly Reduced Cerium Oxide: The Role of O Vacancy Coordination. *ACS Catal.* **2018**, *8*, 4354–4363.

(34) Lykhach, Y.; Johánek, V.; Aleksandrov, H. A.; Kozlov, S. M.; Happel, M.; Skála, T.; Petkov, P. S.; Tsud, N.; Vayssilov, G. N.; Prince, K. C.; Neyman, K. M.; Matolín, V.; Libuda, J. Water Chemistry on Model Ceria and Pt/Ceria Catalysts. *J. Phys. Chem. C* **2012**, *116*, 12103–12113.

(35) Henderson, M. A.; Perkins, C. L.; Engelhard, M. H.; Thevuthasan, S.; Peden, C. H. F. Redox Properties of Water on the Oxidized and Reduced Surfaces of CeO_2 (111). *Surf. Sci.* **2003**, *526*, 1–18.

(36) Wang, H.; Chroneos, A.; Schwingenschlögl, U. Impact of Doping on the Ionic Conductivity of Ceria: A Comprehensive Model. *J. Chem. Phys.* **2013**, *138*, 224705.

(37) Rushton, M. J. D.; Chroneos, A. Impact of Uniaxial Strain and Doping on Oxygen Diffusion in CeO_2. *Sci. Rep.* **2014**, *4*, 6068.

(38) Kitchin, J. R.; Nørskov, J. K.; Barteau, M. A.; Chen, J. G. Modification of the Surface Electronic and Chemical Properties of Pt(111) by Subsurface 3*d* Transition Metals. *J. Chem. Phys.* **2004**, *120*, 10240–10246.

(39) Sayle, T. X. T.; Cantoni, M.; Bhatta, U. M.; Parker, S. C.; Hall, S. R.; Möbus, G.; Molinari, M.; Reid, D.; Seal, S.; Sayle, D. C. Strain and Architecture-Tuned Reactivity in Ceria Nanostructures; Enhanced Catalytic Oxidation of CO to CO_2. *Chem. Mater.* **2012**, *24*, 1811–1821.

(40) Logadottir, A.; Rod, T. H.; Nørskov, J. K.; Hammer, B.; Dahl, S.; Jacobsen, C. J. H. The Brønsted-Evans-Polanyi Relation and the Volcano Plot for Ammonia Synthesis over Transition Metal Catalysts. *J. Catal.* **2001**, *197*, 229–231.

(41) Byskov, L. S.; Nørskov, J. K.; Clausen, B. S.; Topsøe, H. DFT Calculations of Unpromoted and Promoted MoS_2-Based Hydrodesulfurization Catalysts. *J. Catal.* **1999**, *187*, 109–122.

(42) Ferrin, P.; Kandoi, S.; Nilekar, A. U.; Mavrikakis, M. Hydrogen Adsorption, Absorption and Diffusion on and in Transition Metal Surfaces: A DFT Study. *Surf. Sci.* **2012**, *606*, 679–689.

(43) Himo, F.; Lovell, T.; Hilgraf, R.; Rostovtsev, V. V.; Noodleman, L.; Sharpless, K. B.; Fokin, V. V. Copper(I)-Catalyzed Synthesis of Azoles. DFT Study Predicts Unprecedented Reactivity and Intermediates. *J. Am. Chem. Soc.* **2005**, *127*, 210–216.

(44) Schrödinger, E. An Undulatory Theory of the Mechanics of Atoms and Molecules. *Phys. Rev.* **1926**, *28*, 1049–1070.

(45) Koch, W.; Holthausen, M. C. A Chemist's Guide to Density Functional Theory. **2001**. ISBNs: 3-527-60004-3.

(46) Sherif, S. A.; Stefanakos, E. K. S.; Steinfeld, A. Handbook of Hydrogen Energy. ISBNs: 978-1-4200-5450-7

(47) Kohn, W. Nobel Lecture: Electronic Structure of Matter-Wave Functions and Density Functionals. *Rev. Mod. Phys.* **1999**, *71*, 1253–1266.

(48) P. Hohernberg, W. K. Inhomogeneous Electron Gas. *Phys. Rev.* **1964**, *136*, B864–B871.

(49) Sham, W. and; Kohn, L. J. Self-Consistent Equations Including Exchange and Correlation Effects. *Phys. Chem. Chem. Phys.* **1965**, *140*, A1133–A1138.

(50) Perdew, J. P.; Schmidt, K. Jacob's Ladder of Density Functional Approximations for the Exchange-Correlation Energy. *AIP Conf. Proc.* **2001**,

577.

(51) Perdew, J. P.; Burke, K.; Ernzerhof, M. Generalized Gradient Approximation Made Simple. *Phys. Rev. Lett.* **1996**, *77*, 3865–3868.

(52) Loschen, C.; Carrasco, J.; Neyman, K. M.; Illas, F. First-Principles LDA+*U* and GGA+*U* Study of Cerium Oxides: Dependence on the Effective *U* Parameter. *Phys. Rev. B* **2007**, *75*, 035115.

(53) Graciani, J.; Márquez, A. M.; Plata, J. J.; Ortega, Y.; Hernández, N. C.; Meyer, A.; Zicovich-Wilson, C. M.; Sanz, J. F. Comparative Study on the Performance of Hybrid DFT Functionals in Highly Correlated Oxides: The Case of CeO_2 and Ce_2O_3. *J. Chem. Theory Comput.* **2011**, *7*, 56–65.

(54) Heyd, J.; Scuseria, G. E.; Ernzerhof, M. Hybrid Functionals Based on a Screened Coulomb Potential. *J. Chem. Phys.* **2003**, *118*, 8207–8215.

(55) Dudarev, S. L.; Botton, G. A.; Savrasov, S. Y.; Humphreys, C. J.; Sutton, A. P. Electron-Energy-Loss Spectra and the Structural Stability of Nickel Oxide: An LSDA+*U* Study. *Phys. Rev. B* **1998**, *57*, 1505–1509.

(56) Kresse, G.; Furthmüller, J. Efficient Iterative Schemes for Ab Initio Total-Energy Calculations Using a Plane-Wave Basis Set. *Phys. Rev. B* **1996**, *54*, 11169–11186.

(57) Kresse, G.; Hafner, J. Ab Initio Molecular Dynamics for Open-Shell Transition Metals. *Phys. Rev. B* **1993**, *48*, 13115–13118.

(58) Blöchl, P. E. Projector Augmented-Wave Method. *Phys. Rev. B* **1994**, *50*, 17953–17979.

(59) Gopal, C. B.; García-Melchor, M.; Lee, S. C.; Shi, Y.; Shavorskiy, A.; Monti, M.; Guan, Z.; Sinclair, R.; Bluhm, H.; Vojvodic, A.; Chueh, W. C. Equilibrium Oxygen Storage Capacity of Ultrathin $CeO_{2-\delta}$ Depends Non-Monotonically on Large Biaxial Strain. *Nat. Commun.* **2017**, *8*, 15360.

(60) Capdevila-Cortada, M.; López, N. Descriptor Analysis in Methanol Conversion on Doped CeO_2(111): Guidelines for Selectivity Tuning. *ACS Catal.* **2015**, *5*, 6473–6480.

(61) Aparicio-Anglès, X.; Roldan, A.; De Leeuw, N. H. Gadolinium-Vacancy Clusters in the (111) Surface of Gadolinium-Doped Ceria: A Density Functional Theory Study. *Chem. Mater.* **2015**, *27*, 7910–7917.

(62) Gerward, L.; Olsen, J. S.; Petit, L.; Vaitheeswaran, G.; Kanchana, V.; Svane, A. Bulk Modulus of CeO_2 and PrO_2—An Experimental and Theoretical Study. *J. Alloys Compd.* **2005**, *400*, 56–61.

(63) Henkelman, G.; Uberuaga, B. P.; Jónsson, H. Climbing Image Nudged Elastic

Band Method for Finding Saddle Points and Minimum Energy Paths. *J. Chem. Phys.* **2000**, *113*, 9901–9904.

(64) Bligaard, T.; Nørskov, J. K.; Dahl, S.; Matthiesen, J.; Christensen, C. H.; Sehested, J. The Brønsted-Evans-Polanyi Relation and the Volcano Curve in Heterogeneous Catalysis. *J. Catal.* **2004**, *224*, 206–217.

(65) Huang, M.; Fabris, S. CO Adsorption and Oxidation on Ceria Surfaces from DFT+*U* Calculations. *J. Phys. Chem. C* **2008**, *112*, 8643.

(66) Da Silva, J. L. F.; Ganduglia-Pirovano, M. V.; Sauer, J.; Bayer, V.; Kresse, G. Hybrid Functionals Applied to Rare-Earth Oxides: The Example of Ceria. *Phys. Rev. B* **2007**, *75*, 045121.

(67) Fabris, S.; Gironcoli, S. D.; Baroni, S.; Vicario, G.; Balducci, G. Reply to Comment on "Taming Multiple Valency with Density Functionals: A Case Study of Defective Ceria." *Phys. Rev. B* **2005**, *72*, 237102.

(68) Farra, R.; García-Melchor, M.; Eichelbaum, M.; Hashagen, M.; Frandsen, W.; Allan, J.; Girgsdies, F.; Szentmiklósi, L.; López, N.; Teschner, D. Promoted Ceria: A Structural, Catalytic, and Computational Study. *ACS Catal.* **2013**, *3*, 2256–2268.

(69) Capdevila-Cortada, M.; García-Melchor, M.; López, N. Unraveling the Structure Sensitivity in Methanol Conversion on CeO_2: A DFT+*U* Study. *J. Catal.* **2015**, *327*, 58–64.

(70) Fernández-Torre, D.; Carrasco, J.; Ganduglia-Pirovano, M. V.; Pérez, R. Hydrogen Activation, Diffusion, and Clustering on CeO_2(111): A DFT+*U* Study. *J. Chem. Phys.* **2014**, *141*, 014703.

(71) Chase, M. W.; Curnutt, J. L.; Downey, J. R.; Mcdonald, R. A.; Syverud, A. N.; Valenzuela, E. A. JANAF Thermochemical Tables, 1982 Supplement. *J. Phys. Chem. Ref. Data* **1982**, *11*, 695–940.

(72) Inaba, H.; Sagawa, R.; Hayashi, H.; Kawamura, K. Molecular Dynamics Simulation of Gadolinia-Doped Ceria. *Solid State Ionics* **1999**, *122*, 95–103.

(73) Ni, M.; Leung, M. K. H.; Leung, D. Y. C. Technological Development of Hydrogen Production by Solid Oxide Electrolyzer Cell (SOEC). *Int. J. Hydrogen Energy* **2008**, *33*, 2337–2354.

(74) Zhang, C.; Li, C.-J.; Zhang, G.; Ning, X.-J.; Li, C.-X.; Liao, H.; Coddet, C. Ionic Conductivity and Its Temperature Dependence of Atmospheric Plasma-Sprayed Yttria Stabilized Zirconia Electrolyte. *Mater. Sci. Eng. B* **2007**, *137*, 24–30.

(75) Dholabhai, P. P.; Adams, J. B.; Crozier, P.; Sharma, R. A Density Functional Study of Defect Migration in Gadolinium Doped Ceria. *Phys. Chem. Chem.*

Phys. **2010**, *12*, 7904–7910.

(76) Grieshammer, S.; Grope, B. O. H.; Koettgen, J.; Martin, M. A Combined DFT + *U* and Monte Carlo Study on Rare Earth Doped Ceria. *Phys. Chem. Chem. Phys.* **2014**, *16*, 9974–9986.

(77) Minervini, L.; Zacate, M. O.; Grimes, R. W. Defect Cluster Formation in M_2O_3-Doped CeO_2. *Solid State Ionics* **1999**, *116*, 339–349.

(78) Vanpoucke, D. E. P.; Bultinck, P.; Cottenier, S.; Van Speybroeck, V.; Van Driessche, I. Aliovalent Doping of CeO_2: DFT Study of Oxidation State and Vacancy Effects. *J. Mater. Chem. A* **2014**, *2*, 13723–13737.

(79) Li, H.-Y.; Wang, H.-F.; Gong, X.-Q.; Guo, Y.-L.; Guo, Y.; Lu, G.; Hu, P. Multiple Configurations of the Two Excess 4*f* Electrons on Defective CeO_2(111): Origin and Implications. *Phys. Rev. B* **2009**, *79*, 193401.

(80) Tang, Y.; Zhang, H.; Cui, L.; Ouyang, C.; Shi, S.; Tang, W.; Li, H.; Lee, J.-S.; Chen, L. First-Principles Investigation on Redox Properties of M-Doped CeO_2 (M=Mn, Pr, Sn, Zr). *Phys. Rev. B* **2010**, *82*, 125104.

(81) Chen, H.-T.; Chang, J.-G.; Chen, H.-L.; Ju, S.-P. Identifying the O_2 Diffusion and Reduction Mechanisms on CeO_2 Electrolyte in Solid Oxide Fuel Cells: A DFT+*U* Study. *J. Comput. Chem.* **2009**, *30*, 2433–2442.

(82) García-Melchor, M.; López, N. Homolytic Products from Heterolytic Paths in H_2 Dissociation on Metal Oxides: The Example of CeO_2. *J. Phys. Chem. C* **2014**, *118*, 10921–10926.

(83) Mavrikakis, M.; Hammer, B.; Nørskov, J. K. Effect of Strain on the Reactivity of Metal Surfaces. *Phys. Rev. Lett.* **1998**, *81*, 2819–2822.

(84) Tripkovic, V.; Zheng, J.; Rizzi, G. A.; Marega, C.; Durante, C.; Rossmeisl, J.; Granozzi, G. Comparison between the Oxygen Reduction Reaction Activity of Pd_5Ce and Pt_5Ce: The Importance of Crystal Structure. *ACS Catal.* **2015**, *5*, 6032–6040.

(85) Clark, E. L.; Hahn, C.; Jaramillo, T. F.; Bell, A. T. Electrochemical CO_2 Reduction over Compressively Strained CuAg Surface Alloys with Enhanced Multi-Carbon Oxygenate Selectivity. *J. Am. Chem. Soc.* **2017**, *139*, 15848–15857.

(86) Ling, T.; Yan, D.-Y.; Wang, H.; Jiao, Y.; Hu, Z.; Zheng, Y.; Zheng, L.; Mao, J.; Liu, H.; Du, X.-W.; Jaroniec, M.; Qiao, S.-Z. Activating Cobalt(II) Oxide Nanorods for Efficient Electrocatalysis by Strain Engineering. *Nat. Commun.* **2017**, *8*, 1509.

(87) Ma, D.; Lu, Z.; Tang, Y.; Li, T.; Tang, Z.; Yang, Z. Effect of Lattice Strain on the Oxygen Vacancy Formation and Hydrogen Adsorption at CeO_2(111)

Surface. *Phys. Lett. A* **2014**, *378*, 2570–2575.

(88) Ahn, J.; Choi, S.; Yoon, K. J.; Son, J. W.; Kim, B. K.; Lee, J. H.; Jang, H. W.; Kim, H. Strain-Induced Tailoring of Oxygen-Ion Transport in Highly Doped CeO_2 Electrolyte: Effects of Biaxial Extrinsic and Local Lattice Strain. *ACS Appl. Mater. Interfaces* **2017**, *9*, 42415–42419.

(89) Rushton, M. J. D.; Chroneos, A.; Skinner, S. J.; Kilner, J. A.; Grimes, R. W. Effect of Strain on the Oxygen Diffusion in Yttria and Gadolinia Co-Doped Ceria. *Solid State Ionics* **2013**, *230*, 37–42.

(90) Kushima, A.; Yildiz, B. Oxygen Ion Diffusivity in Strained Yttria Stabilized Zirconia: Where Is the Fastest Strain? *J. Mater. Chem.* **2010**, *20*, 4809–4819.

(91) De Souza, R. A.; Ramadan, A.; Hörner, S. Modifying the Barriers for Oxygen-Vacancy Migration in Fluorite-Structured CeO_2 Electrolytes through Strain: A Computer Simulation Study. *Energy Environ. Sci.* **2012**, *5*, 5445–5453.

(92) Naghavi, S. S.; Emery, A. A.; Hansen, H. A.; Zhou, F.; Ozolins, V.; Wolverton, C. Giant Onsite Electronic Entropy Enhances the Performance of Ceria for Water Splitting. *Nat. Commun.* **2017**, *8*, 285.

(93) Matz, O.; Calatayud, M. Breaking H_2 with CeO_2: Effect of Surface Termination. *ACS Omega* **2018**, *3*, 16063–16073.

(94) Dholabhai, P. P.; Adams, J. B.; Crozier, P.; Sharma, R. Oxygen Vacancy Migration in Ceria and Pr-Doped Ceria: A DFT+*U* Study. *J. Chem. Phys.* **2010**, *132*, 094104.

(95) Carrasco, J.; López-Durán, D.; Liu, Z.; Duchoň, T.; Evans, J.; Senanayake, S. D.; Crumlin, E. J.; Matolín, V.; Rodríguez, J. A.; Ganduglia-Pirovano, M. V. In Situ and Theoretical Studies for the Dissociation of Water on an Active Ni/CeO_2 Catalyst: Importance of Strong Metal–Support Interactions for the Cleavage of O–H Bonds. *Angew. Chem. Int. Ed.* **2015**, *54*, 3917–3921.

(96) Werner, K.; Weng, X.; Calaza, F.; Sterrer, M.; Kropp, T.; Paier, J.; Sauer, J.; Wilde, M.; Fukutani, K.; Shaikhutdinov, S. Toward an Understanding of Selective Alkyne Hydrogenation on Ceria: On the Impact of O Vacancies on H_2 Interaction with CeO_2(111). *J. Am. Chem. Soc.* **2017**, *139*, 17608–17616.

(97) Kozuch, S.; Shaik, S. How to Conceptualize Catalytic Cycles? The Energetic Span Model. *Acc. Chem. Res.* **2011**, *44*, 101–110.

(98) Kozuch, S. A Refinement of Everyday Thinking: The Energetic Span Model for Kinetic Assessment of Catalytic Cycles. *Wiley Interdiscip. Rev. Comput. Mol. Sci.* **2012**, *2*, 795–815.

(99) Shannon, R. D. Revised Effective Ionic Radii and Systematic Studies of Interatomic Distances in Halides and Chalcogenides. *Acta Cryst.* **1976**, *A32*,

751–767.

(100) Yang, N.; Orgiani, P.; Di Bartolomeo, E.; Foglietti, V.; Torelli, P.; Ievlev, A. V.; Rossi, G.; Licoccia, S.; Balestrino, G.; Kalinin, S. V.; Aruta, C. Effects of Dopant Ionic Radius on Cerium Reduction in Epitaxial Cerium Oxide Thin Films. *J. Phys. Chem. C* **2017**, *121*, 8841–8849.

(101) Hong, S. J.; Virkar, A. V. Lattice Parameters and Densities of Rare-Earth Oxide Doped Ceria Electrolytes. *J. Am. Ceram. Soc.* **1995**, *78*, 433–439.

(102) Aneggi, E.; Wiater, D.; Leitenburg, C. D.; Llorca, J.; Trovarelli, A. Shape-Dependent Activity of Ceria in Soot Combustion. *ACS Catal.* **2014**, *4*, 172–181.

(103) Yang, C.; Yu, X.; Heißler, S.; Nefedov, A.; Colussi, S.; Llorca, J.; Trovarelli, A.; Wang, Y.; Wöll, C. Surface Faceting and Reconstruction of Ceria Nanoparticles. *Angew. Chem. Int. Ed.* **2017**, *56*, 375–379.

(104) Pan, Y.; Nilius, N.; Stiehler, C.; Freund, H. J.; Goniakowski, J.; Noguera, C. Ceria Nanocrystals Exposing Wide (100) Facets: Structure and Polarity Compensation. *Adv. Mater. Interfaces* **2014**, *1*, 1400404.

(105) Jiang, Y.; Adams, J. B.; Van Schilfgaarde, M. Density-Functional Calculation of CeO_2 Surfaces and Prediction of Effects of Oxygen Partial Pressure and Temperature on Stabilities. *J. Chem. Phys.* **2005**, *123*, 064701.

(106) Wang, D.; Kang, Y.; Doan-Nguyen, V.; Chen, J.; Küngas, R.; Wieder, N. L.; Bakhmutsky, K.; Gorte, R. J.; Murray, C. B. Synthesis and Oxygen Storage Capacity of Two-Dimensional Ceria Nanocrystals. *Angew. Chem. Int. Ed.* **2011**, *50*, 4378–4381.

(107) Conesa, J. C. Computer Modeling of Surfaces and Defects on Cerium Dioxide. *Surf. Sci.* **1995**, *339*, 337–352.

(108) Sayle, D. C.; Maicaneanu, S. A.; Watson, G. W. Atomistic Models for CeO_2(111), (110), and (100) Nanoparticles, Supported on Yttrium-Stabilized Zirconia. *J. Am. Chem. Soc.* **2002**, *124*, 11429–11439.

(109) Vilé, G.; Colussi, S.; Krumeich, F.; Trovarelli, A.; Pérez-Ramírez, J. Opposite Face Sensitivity of CeO_2 in Hydrogenation and Oxidation Catalysis Angewandte. *Angew. Chem. Int. Ed.* **2014**, *53*, 12069–12072.

(110) Spezzati, G.; Benavidez, A. D.; Delariva, A. T.; Su, Y.; Hofmann, J. P.; Asahina, S.; Olivier, E. J.; Neethling, J. H.; Miller, T.; Datye, A. K. CO Oxidation by Pd Supported on CeO_2(100) and CeO_2(111) Facets. *Appl. Catal. B Environ.* **2019**, *243*, 36–46.

(111) Herman, G. S. Surface Structure Determination of CeO_2(001) by Angle-Resolved Mass Spectroscopy of Recoiled Ions. *Phys. Rev. B* **1999**, *59*, 14899–14902.

(112) Kropp, T.; Paier, J.; Sauer, J. Interactions of Water with the (111) and (100) Surfaces of Ceria. *J. Phys. Chem. C* **2017**, *121*, 21571–21578.

(113) Beste, A.; Overbury, S. H. Pathways for Ethanol Dehydrogenation and Dehydration Catalyzed by Ceria (111) and (100) Surfaces. *J. Phys. Chem. C* **2015**, *119*, 2447–2455.

(114) Capdevila-Cortada, M.; López, N. Entropic Contributions Enhance Polarity Compensation for CeO_2(100) Surfaces. *Nat. Mater.* **2017**, *16*, 328–334.

(115) Kropp, T.; Paier, J. Activity versus Selectivity of the Methanol Oxidation at Ceria Surfaces: A Comparative First-Principles Study. *J. Phys. Chem. C* **2015**, *119*, 23021–23031.

(116) Liu, J.-X; Su, Y. Filot, I. A.; Hensen, E. J. M. A Linear Scaling Relation for CO Oxidation on CeO_2-Supported Pd. *J. Am. Chem. Soc.* **2018**, *140*, 4580-4587.

(117) Su, Y.; Filot, I. A. W.; Liu. J.-X.; Hensen, E. J. M. Stable Pd-Doped Ceria Structures for CH_4 Activation and CO Oxidation. *ACS Catal.* **2018**, *8*, 75-80.

(118) Kim, H. Y.; Lee, H. M.; Henkelman, G. CO Oxidation Mechanism on CeO_2-Supported Au Nanoparticles. *J. Am. Chem. Soc.* **2012**, *134*, 1560-1570.

(119) Wang, Y.; Makkee, M. The influence of CO_2 on NO reduction into N_2 over reduced Ceria-based catalyst. *Appl. Catal. B Environ.* **2018**, *221*, 196-205.

(120) Bera, P.; Patil, K. C.; Jayaram, V.; Subbanna, G. N.; Hegde, M. S. Ionic Dispersion of Pt and Pd on CeO_2 by Combustion Method: Effect of Metal-Ceria Interaction on Catalytic Activities for NO Reduction and CO and Hydrocarbon Oxidation. *J. Catal.* **2000**, *196*, 293-301.

Appendix A

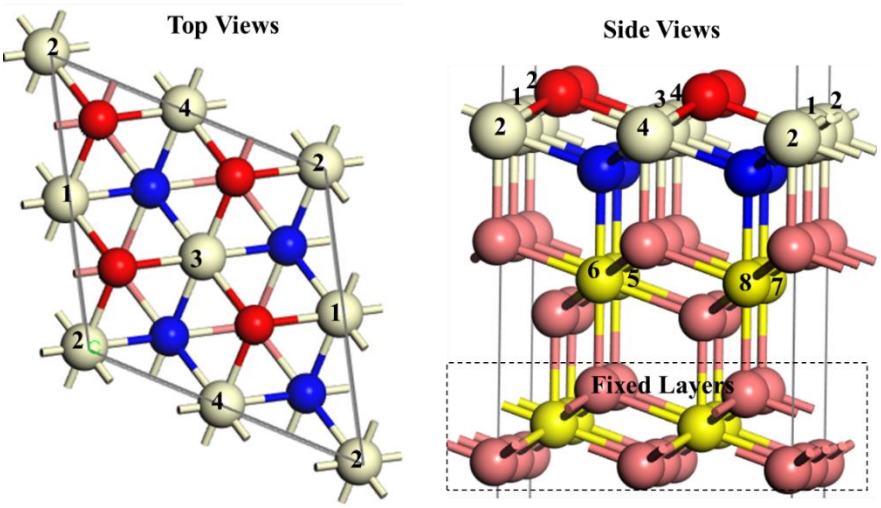

Figure A-1. The top and side views of labelled cerium atoms on the top and subsurface cerium layers of CeO_2(111). Color legend is the same as shown in **Figure 4-1**.

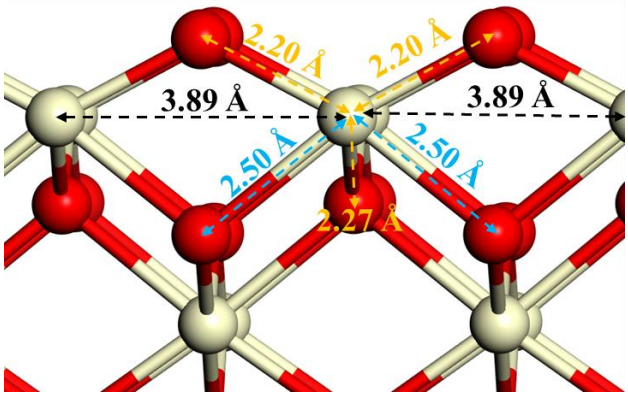

Figure A-2. Configuration of the converged CeO_2(100) surface with selected bond lengths indicated.

Appendix B

List of the Included Publications:

B.1 Paper 1

Mechanism of Water Splitting on Gadolinium Doped CeO_2(111): A DFT+*U* Study

Tiantian Wu, Qingming Deng, Heine Anton Hansen, Tejs Vegge

The Journal of Physical Chemistry C 2019, 123, 5507−5517

B.2 Paper 2

Improved Electrocatalytic Water Splitting Reaction on CeO_2(111) by Strain Engineering: A DFT+*U* Study

Tiantian Wu, Tejs Vegge, Heine Anton Hansen

ACS Catalysis 2019, 9, 4853−4861

B.3 Paper 3

Facet-Dependent Electrocatalytic Water Splitting Reaction on CeO_2: A DFT+*U* Study

Tiantian Wu, Núria López, Tejs Vegge, Heine Anton Hansen

Submitted

B.1 Paper 1

Mechanism of Water Splitting on Gadolinium Doped CeO_2(111): A DFT+*U* Study

Tiantian Wu, Qingming Deng, Heine Anton Hansen, Tejs Vegge

The Journal of Physical Chemistry C 2019, 123, 5507−5517

THE JOURNAL OF PHYSICAL CHEMISTRY C

Article

Cite This: J. Phys. Chem. C 2019, 123, 5507−5517

pubs.acs.org/JPCC

Mechanism of Water Splitting on Gadolinium-Doped CeO_2(111): A DFT + *U* Study

Tiantian Wu, Qingming Deng, Heine Anton Hansen,* and Tejs Vegge*

Department of Energy Conversion and Storage, Technical University of Denmark, Fysikvej, 2800 Kongens Lyngby, Denmark

Supporting Information

ABSTRACT: Ceria-based materials have attracted considerable interest due to their potential applications in the electrocatalytic splitting of water for hydrogen production. In this work, the reaction mechanism of water splitting on gadolinium-doped ceria (GDC) is investigated using DFT + *U* calculations. We found that H_2 evolution preferentially proceeds on the overly hydroxylated surfaces of pure ceria and GDC via the formation of Ce−H and Gd−H intermediates, respectively, which is much more efficient than the H_2 evolution over their partially hydroxylated surfaces. Notably, GDC is more easily and strongly reduced through formation of oxygen vacancies and hydroxyls compared to pure ceria. Thus, the facile formation of the overly hydroxylated states by the incorporation of Gd leads to the improved electrocatalytic activity of water splitting on ceria. These results indicate that a dopant that stabilizes the reduced ceria and favors the formation of metal-H moiety is capable of effectively improving the reaction activity of ceria for water splitting.

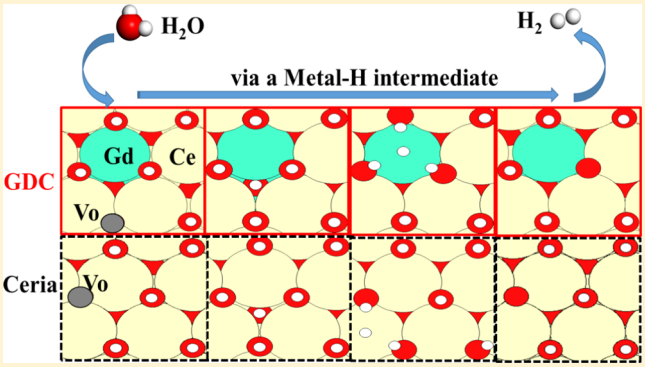

INTRODUCTION

Ceria is widely used in many catalytic processes not only as a support but also as an efficient catalyst in redox reactions due to its particular redox cycle between Ce^{4+} and Ce^{3+}. Ceria can be used to store oxygen in three-way catalysts[1−3] and in the water−gas shift reaction.[4−6] It also provides a sustainable alternative to fuel production using solar thermochemical cycles with high conversion efficiencies.[7,8] As a good ionic or mixed ionic and electronic conductor, doped ceria is a promising material for oxygen ion-conducting solid electrolytes in solid oxide fuel cells[9,10] and solid oxide electrolyzer cells (SOEC).[11,12]

SOEC is a highly efficient technology for hydrogen production through the water splitting reaction at high temperature. By utilization of waste heat at high temperature, an SOEC can produce hydrogen with smaller overpotential losses than low-temperature electrolysis cells.[13] There is, however, pronounced degradation at the electrochemical interfaces (gas/electrode/electrolyte boundaries) in SOEC during high operating temperature, which results from oxygen incorporation into the oxygen conductor, eventually weakening and cracking the reaction interface.[13,14] The hydrogen evolution reaction (HER) usually takes place at triple phase boundaries (TPB) between the gas channels, electronic, and ionic conductors. The efficiency of the HER is significantly restricted by the degradation.[13,14] Replacing the traditional yttria-stabilized zirconia ionic conductor with ceria will extend the TPB reaction zones to a double-phase boundary, where HER proceeds readily at the ceria−gas interface.[15,16] Computational studies have shown that water dissociation for hydrogen production at the ceria−gas interface would be facile once oxygen vacancies can diffuse to the surface.[17] Improved ionic conductivity increases the reaction efficiency of ceria, and doping ceria is a promising approach for improving the ionic conductivity and the electrochemical activity for HER. Gadolinium-doped ceria (GDC) has been demonstrated to have the highest ionic conductivity among ceria-based materials[18] and allows the electrochemical reactions at intermediate temperatures (773−1073 K).[19,20] Therefore, ceria-based materials are promising for hydrogen production through H_2O electrolysis in SOEC.

In the past few decades, the reactions associated with H_2, H_2O, and ceria have been studied extensively, showing that the catalytic behavior of ceria is directly linked to its mixed valence Ce^{3+}/Ce^{4+} redox states and the mobility of oxygen ions.[11,17,21] Recently, the excellent performance of solar thermochemical redox reactions in ceria has been shown to be attributed to the positive entropy contribution associated with the $f^0 \rightarrow f^1$ transition.[22] Electrocatalytic water splitting in ceria includes reaction steps of oxygen vacancy diffusion to the surface, water adsorption on the surface, water reaction with the oxygen vacancy and oxygen ions into hydroxyl ($H_2O_{ads} + 2Ce^{3+} + V_O + O^{2-} \rightarrow 2OH^- + 2Ce^{3+}$), and finally hydroxyl decomposition into H_2 and oxygen ions ($2OH^- + 2Ce^{3+} \rightarrow H_2 + 2Ce^{4+} +$

Received: December 14, 2018
Revised: February 5, 2019
Published: February 7, 2019

DOI: 10.1021/acs.jpcc.8b12037
J. Phys. Chem. C 2019, 123, 5507−5517

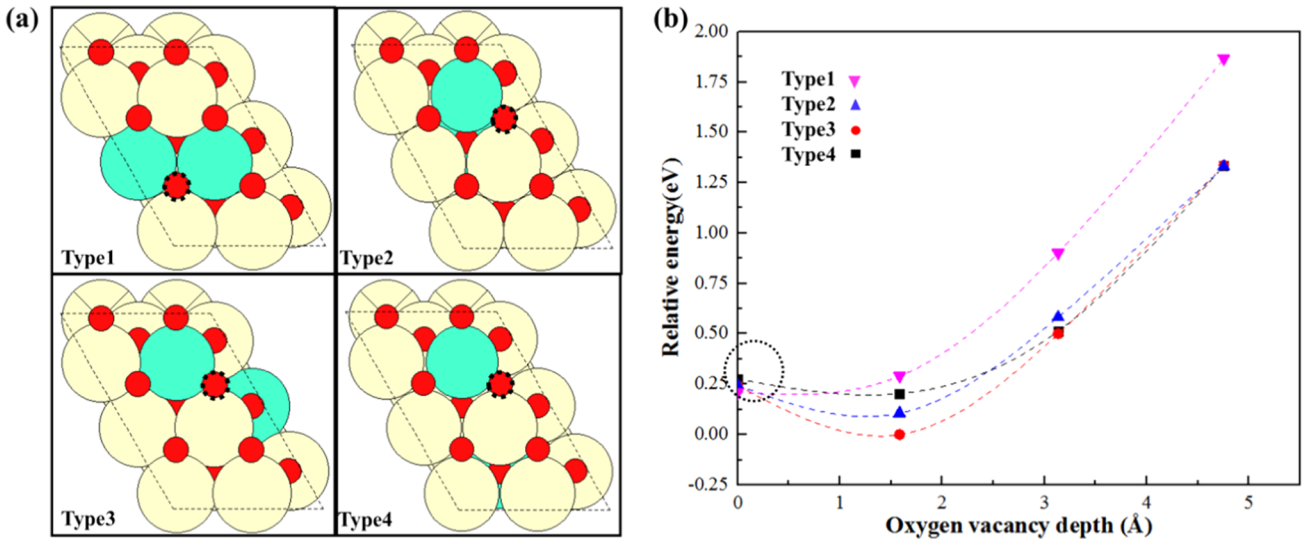

Figure 1. (a) Configurations of the most favorable vacancy in the top surface (depth = 0.0 Å) of the $Gd_2Ce_{16}O_{35}(111)$ with type 1, type 2, type 3, and type 4 Gd distributions. Color legend: yellow for cerium, green for gadolinium, and red for oxygen atoms. The balls with crosses represent the fixed atoms, whereas red balls with a dashed perimeter mark the oxygen vacancy. (b) Relative energy of an oxygen vacancy at different depths in the $Gd_2Ce_{16}O_{35}(111)$ with four types of Gd distribution. The depth is measured from the top of the surface.

$2O^{2-}$). A competing pathway for the water splitting reactions when lattice O^{2-} is unavailable at the ceria surface proceeds through a Ce−H intermediate ($H_2O_{ads} + 2Ce^{3+} + V_O \rightarrow OH^- + Ce^{4+} + Ce^{4+}H^- \rightarrow H_2 + 2Ce^{4+} + O^{2-}$).[17] The localization of the excess electrons after creating an oxygen vacancy varies with different density functional theory (DFT) descriptions of the 4f orbitals on cerium.[17,23,24] Oxygen diffusion to the surface for reaction with adsorbed water and the following step of water dissociation into stable hydroxyls are facile steps, having barriers of 0.65 and 0.06 eV, respectively.[17] Recently, both theoretical and experimental studies indicate that the rate-determining step of the water splitting reaction on ceria involves the charge transfer for H_2 production through hydroxyl decomposition.[11,17] Experimentally, surface hydroxyls can be stabilized up to 400−600 K under ultra-high vacuum conditions.[25,26] Increasing the surface reduction by creating oxygen vacancies or forming hydroxyls can improve the reaction activity for H_2 production.[17,27] Among ceria-based materials, GDC holds great promise to improve the water splitting reaction rate.[18−20] So far, computational studies on GDC have been limited to electronic structures and properties related to oxygen diffusion.[28−30] Therefore, the fundamental understanding of the reaction mechanism for water splitting in SOEC on pure ceria and especially doped ceria remains elusive.

In this work, we present detailed DFT investigations on the formation and diffusion of oxygen vacancies, as well as hydroxyl formation and decomposition on ceria and GDC, respectively. The effect of Gd doping on the stability of the reduced ceria surface by creating oxygen vacancies and formation of hydroxyl groups and the impact of Gd doping on the reaction pathways for water dissociation are discussed to obtain a more clear understanding of the water splitting reaction on the reduced ceria-based materials.

METHODS

Density-functional theory (DFT) calculations are performed using the Vienna Ab initio simulation package (VASP).[31−33] The ionic cores are described by projector augmented wave (PAW) potentials,[34] and the wave functions are expanded in plane waves with an energy cutoff of 550 eV. The exchange and correlation are approximated by the Perdew−Burke−Ernzerhof (PBE) functional,[35] including aspherical gradient corrections within the PAW augmentation spheres. Because of the electron self-interaction error in the Kohn−Sham formalism, the DFT + U approach[36] was used to describe electron localization on the 4f states of Ce^{3+}. We do not include a U correction on gadolinium because the 4f shell of gadolinium is always found to be filled with seven electrons ($4f^7$) and the U contribution on describing the electron localization on the $4f^7$ shell can be negligible.[37] Spin polarization was considered with ferromagnetic ordering because the energy difference between antiferromagnetic and ferromagnetic states is small (<0.01 eV).[38]

The optimal value of the Hubbard U parameter for cerium varies in the range of $0 < U_{eff} < 10$ eV ($U_{eff} = U - J$) depending on the quantity of interest.[36,39−41] PBE + U usually overestimates the lattice constant.[40,41] The reduction energy of ceria is well described already at $U_{eff} \approx 2.0$ eV,[39] whereas the calculated band gap is consistent with experiments for $U_{eff} > 5.5$ eV.[40] We find a strong dependence of the oxygen vacancy formation energy (E_{V_O}) and the barrier for hydroxyl decomposition over the $CeO_2(111)$ on the values of U_{eff}, as shown in Figures S1−S3 in the Supporting Information. As noted in Figure S1, E_{V_O} linearly decreases with increasing U_{eff} when U_{eff} is higher than 3.5 eV. For $U_{eff} < 3.5$ eV, there is a zone of weak electron localization on the 4f orbitals of ceria, which is consistent with the results by Castleton et al. that charge starts to become localized at $U_{eff} \approx 3.0$ eV.[40] The degree of localization reaches a maximum at $U_{eff} \approx 5.5$ eV for the GGA + U method.[40] The calculated barrier for hydroxyl decomposition on the $CeO_2(111)$ increases with U_{eff} because of the higher stability of reduced cerium when using a larger U_{eff} as shown in Figures S2 and S3. Overall, $U_{eff} = 4.5$ eV is often used for investigations on vacancy diffusion and related reactions on ceria, which has been proved to be an appropriate correction to ensure the described chemical properties of

DOI: 10.1021/acs.jpcc.8b12037
J. Phys. Chem. C 2019, 123, 5507−5517

Table 1. Minimum Gd−Gd distance in the Four Types of Gd Distribution in the $Gd_2Ce_{16}O_{36}(111)$ and the Relative Energy Between Them[a]

Gd distribution type	Gd−Gd distance/Å	relative energy/eV	$V_O^{subsurface}$/eV	$V_O^{surface}$/eV
type 1	3.982	0	−0.725	−0.783
type 2	4.014	0.040	−0.927	−0.789
type 3	5.489	0.039	−0.957	−0.787
type 4	6.717	0.065	−0.855	−0.783
$Ce_{18}O_{36}(111)$			1.808	2.184

[a]The formation energy of one oxygen vacancy (V_O) in the uncompensated system to form the $Gd_2Ce_{18}O_{35}(111)$. V_O in the subsurface and in the top surface layer is abbreviated as $V_O^{subsurface}$ and $V_O^{surface}$, respectively.

ceria.[42−45] In addition, the vacancy formation energy and the activation barrier for hydroxyl decomposition on the $CeO_2(111)$ calculated in this work are well consistent with previously reported DFT results.[23,45,46] Thus, U_{eff} = 4.5 eV used in this work is appropriate to describe the electrochemical properties of ceria during the water splitting reaction.

The $CeO_2(111)$ surface is built as a 2 × 3 repeated surface unit cell consisting of nine atomic layers ($Ce_{18}O_{36}$). Three atomic layers in the bottom are fixed as shown in Figure S4 in the Supporting Information. Vacuum with a thickness of 15 Å is added to reduce interaction between the periodic images. The calculated equilibrium lattice constant of bulk ceria is 5.497 Å, which is well consistent with the reported DFT result[28,45] but overestimates the experimental lattice constant of 5.411 Å[47] by 1.6%. The lattice constant has a 1.4% mismatch with the experimental lattice constant of $Ce_{0.8}Gd_{0.2}O_{1.9}$ (5.423 Å).[48] The lattice with the same mismatch has been used by Aparicio-Anglès et al. for investigations of dopant clustering near the GDC(111) surface.[28] The highest ionic conductivity is obtained in ceria with 10% Gd doping.[28,49] In this work, two cerium atoms in $Ce_{18}O_{36}(111)$ are replaced with two gadolinium atoms for a Gd concentration of 11%. The selected system size allows for investigations of compensating oxygen vacancies near the optimal doping level because two Gd^{3+} dopants are expected to induce the formation of one oxygen vacancy. The $Gd_2Ce_{16}O_{35}(111)$ surface was investigated as the GDC model.

Transition states (TS) are identified for oxygen vacancy diffusion, water dissociation into hydroxyls and hydroxyl decompositions, using the climbing image nudged-elastic band method[50] in VASP. Each band is optimized until the maximum force on the band is less than 0.03 eV/Å.

RESULTS AND DISCUSSION

Distribution of Gd and Oxygen Vacancies (V_O) in $Gd_2Ce_{16}O_{35}(111)$. We first investigate the surface without a compensating oxygen vacancy by substituting one Gd atom into the surface layer and another Gd atom into either the surface or subsurface layer. The distribution of the two Gd atoms is labeled from type 1 to type 4 with increasing Gd−Gd distance as shown in Figure 1a. The uncompensated situation was normally investigated for aliovalent dopants in CeO_2.[28,3728,37] Based on the four uncompensated configurations of the $Gd_2Ce_{16}O_{36}(111)$, a compensating oxygen vacancy (V_O) was then introduced into the different oxygen atomic layers, leading to the formation of the $Gd_2Ce_{16}O_{35}(111)$. The V_O formation energy is defined as

$$E_{V_O} = E_{Gd_2Ce_{16}O_{35}} - E_{Gd_2Ce_{16}O_{36}} + \frac{1}{2}E_{O_2}$$

where $E_{Gd_2Ce_{16}O_{35}}$ is the total energy of the system after creating one oxygen vacancy, $E_{Gd_2Ce_{16}O_{36}}$ is the total energy of the uncompensated system, and E_{O_2} is the energy of an oxygen molecule. The formation energies of one oxygen vacancy in the subsurface ($V_O^{subsurface}$) and top surface ($V_O^{surface}$) in the uncompensated system to form $Gd_2Ce_{16}O_{35}(111)$ are listed in Table 1. Creating a $V_O^{subsurface}$ in type 3 is more facile than in other types of Gd distribution, which is taken as a reference. Compared with the $V_O^{subsurface}$ in type 3, the relative energy of the V_O in each oxygen atomic layer in $Gd_2Ce_{16}O_{35}(111)$ with four types of Gd distribution as a function of the distance from the top oxygen layer (depth) is given in Figure 1b. For type 1 GDC, the V_O favors being created in the top surface, in comparison with creating one V_O in the subsurface and deeper layers. However, for type 2, type 3, and type 4 with two gadolinium atoms sitting in two different atomic layers, the most favorable oxygen vacancy sits in the subsurface oxygen layer. The relative energy of the V_O in these GDC model increases when the vacancy is created in the deeper oxygen layers (depth > 1.5 Å), and the two excess electrons remain localized on the two gadolinium atoms. The energy difference between the $V_O^{surface}$ with four types of Gd distribution is lower than 0.006 eV, as displayed in Table 1. Compared to the $V_O^{surface}$, a slightly larger energy difference (within 0.23 eV) between the $V_O^{subsurface}$ is noticed, which is consistent with Aparicio-Anglès's findings (within 0.25 eV).[28] However, the energy difference between the four different types of Gd distribution in $Gd_2Ce_{16}O_{36}$ is within 0.065 eV as presented in Table 1. In addition, we found that the calculated energy difference between the formation energy of $Gd_2Ce_{16}O_{35}(111)$ having one oxygen vacancy in the top surface with four types of Gd distributions is <0.066 eV. With an oxygen vacancy in the subsurface, the energy difference is <0.291 eV (see Table S1 in the Supporting Information). Our results suggest that Gd can distribute freely between the top surface or subsurface of $Gd_2Ce_{16}O_{35}(111)$ at 11% Gd concentration. These results are in line with the previously reported findings.[28]

In addition, the calculated formation energy of an oxygen vacancy in the top surface of the clean $Ce_{18}O_{36}(111)$ is 2.18 eV, which is close to 2.15 eV, calculated by using a p(3 × 3) unit cell and U_{eff} = 4.5 eV.[45] The calculated formation energy for a slightly larger p(3 × 4) unit cell is only 0.16 eV smaller than using a p(2 × 3) unit cell, agreeing well with the report by Li et al.[51] that the interaction with O vacancies in neighboring supercells could be neglected. Because the introduction of a compensating oxygen vacancy into the uncompensated $Gd_2Ce_{16}O_{36}$ system is preferred, the V_O formation energies in $Gd_2Ce_{16}O_{36}$ with four types of Gd distribution are negative.

Reduced GDC and Ceria. Increased surface reduction has been observed to improve the activity for H_2 production.[17,27]

DOI: 10.1021/acs.jpcc.8b12037
J. Phys. Chem. C 2019, 123, 5507−5517

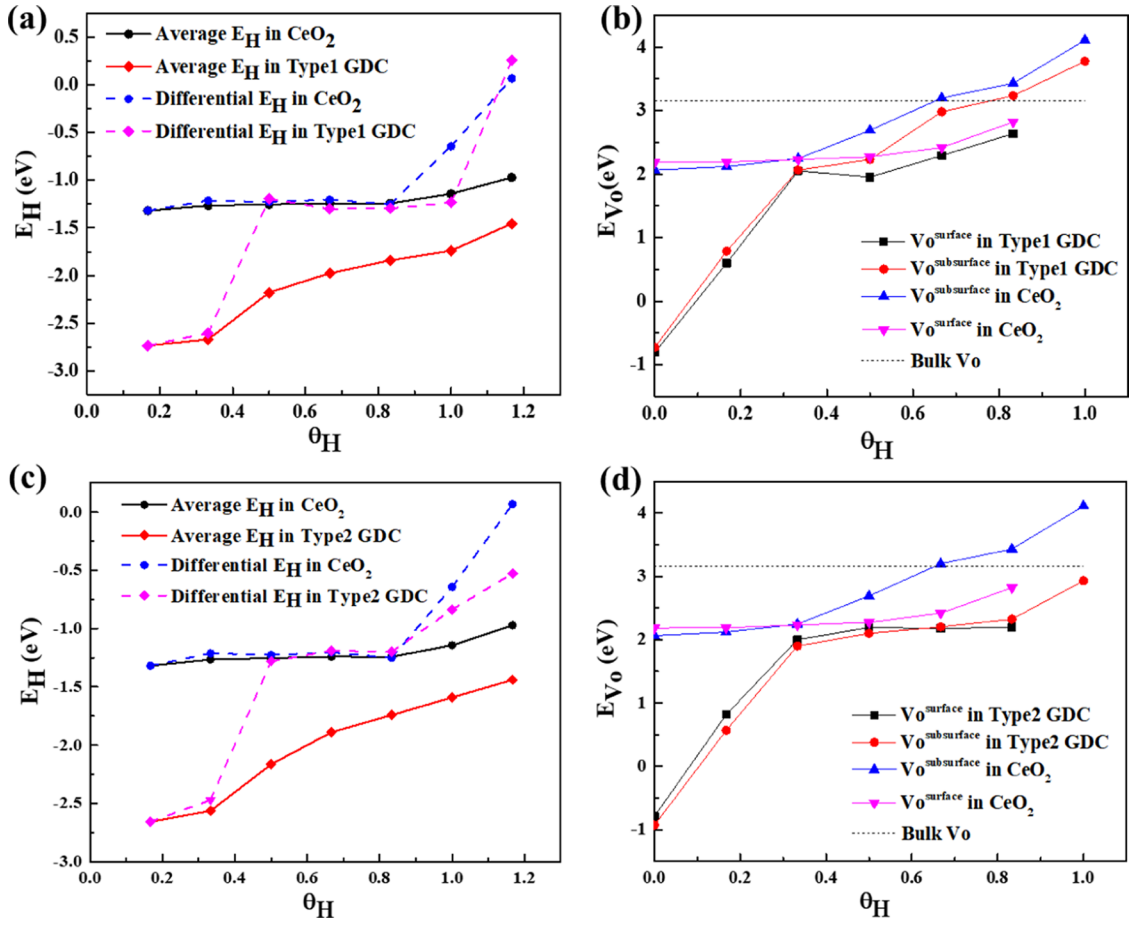

Figure 2. Formation energy of hydroxyl (E_H) as a function of hydroxyl coverage (θ_H) in type 1 GDC (a) and type 2 GDC (c) compared with the E_H in the CeO_2. The formation energy of creating an oxygen vacancy (E_{V_O}) as a function of θ_H in type 1 GDC (b) and type 2 GDC (d) compared with the E_{V_O} in the CeO_2.

In the following, we investigate reduced ceria and GDC with oxygen vacancies (V_O) and hydroxyls formed by water dissociation on lattice oxygen ions. For ceria, the surface reduction reactions can be written as $2Ce^{4+} + O^{2-} \rightarrow 2Ce^{3+} + V_O + \frac{1}{2}O_2$ and $H_2O_{ads} + 2Ce^{3+} + V_O + O^{2-} \rightarrow 2OH^- + 2Ce^{3+}$. The hydroxylated GDC forms via similar reactions. The magnetization of the reduced cerium or gadolinium atoms is labeled and presented in Figures S5−S7 in the Supporting Information. Among the four considered types of Gd distribution, the V_O formation energies in type 2 and type 3 are the lowest. Because the formation energies of oxygen vacancies in type 2 and type 3 are very close, only type 2 is considered for further investigations. Although the subsurface V_O in type 1 is 0.202 eV less stable than the subsurface V_O in type 2, the difference in the formation energy of a V_O in the top surface of type 1 and type 2 is very small (6 meV), which indicates a similar reactivity of the top surface vacancy in GDC regardless of the distribution of the Gd. A comparison of the most favorable configurations of hydroxylated surfaces and mixed hydroxyl-vacancy phases, among type 1, type 2, and ceria, is presented in Figures S5−S7 in the Supporting Information. Here, the hydroxyl coverage $\theta_H = N_H/N$ is used to distinguish surfaces with different degrees of reduction by forming hydroxyls, which is defined as the number of hydroxyls (N_H) divided by the total number of oxygen ($N = 6$) in the top layer. The more reduced surfaces have higher coverage of hydroxyls.

Figure 2 shows the average and differential formation energies of hydroxyls, E_H, and oxygen vacancy formation energies, E_{V_O}, as a function of hydroxyl coverage in type 1 and type 2 GDC compared to ceria. As noticed from Figure 2, the average E_H increases with increasing θ_H. When the GDC surface has one or two hydroxyls, the differential E_H in GDC is about 1.4 eV more negative than in ceria, which again is due to the strong driving force to create Gd^{3+} rather than Ce^{3+}. The magnetization of the reduced cerium or gadolinium atoms is shown in Figures S5−S7 in the Supporting Information. After two hydroxyls form on GDC, Ce^{4+} ions are reduced to Ce^{3+} near these surface hydroxyls because of further reduction, leading to the differential E_H in type 1 and type 2 close to that in ceria as hydroxyl coverage ranging from 0.5 to 0.83. Forming one more hydroxyl at higher θ_H, the differential E_H increases dramatically, which indicates the repulsive interaction between the hydroxyls and the reduced surface. When the hydrogen coverage increases beyond 1.0, the additional hydrogen reacts with subsurface oxygen ions to form one subsurface hydroxyl (subO−H), which is unfavorable compared to surface hydroxyls. The differential energy required for the formation of the subO−H in type 2 GDC is much more negative than that in ceria and type 1 GDC, which means that the formation of the subO−H is relatively favorable in type 2 GDC. Overall,

DOI: 10.1021/acs.jpcc.8b12037
J. Phys. Chem. C 2019, 123, 5507−5517

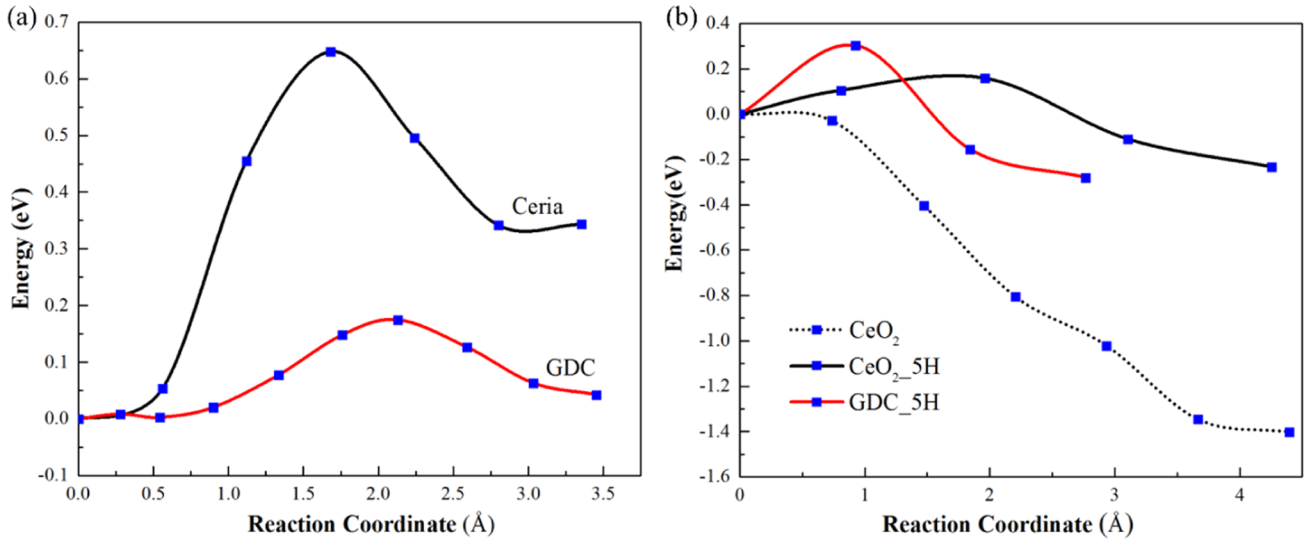

Figure 3. (a) Oxygen vacancy diffusion from the subsurface to the surface in ceria and GDC. (b) Water dissociation into hydroxyl groups over the ceria, the 5H covered ceria, and the 5H covered GDC.

the average E_H in both type 1 and type 2 GDC is much more negative than that in ceria. Therefore, the reduction of ceria via formation of hydroxyls is significantly favored by incorporation of Gd.

At the hydroxylated surfaces, E_{V_O} increases with increasing coverage of hydroxyls. However, E_{V_O} in GDC is more negative than in ceria, which reveals that creating a $V_O^{subsurface}$ or $V_O^{surface}$ in the hydroxylated GDC is much easier than in the hydroxylated ceria. To create one V_O in the hydroxylated ceria surface, $V_O^{subsurface}$ is more favorable than $V_O^{surface}$ at $\theta_H < 0.4$. In type 2, forming a $V_O^{subsurface}$ can be favored until at a high hydroxyl coverage ($\theta_H > 0.8$). By contrast, the $V_O^{surface}$ is always more favorable than the $V_O^{subsurface}$ in type 1 at all hydroxyl coverages. For comparison, the V_O formation energy in the bulk (a $2 \times 2 \times 2$ cubic cell) is 3.16 eV, which is close to the value of 3.10 eV calculated by Tang et al.[52] The V_O in the type 2 GDC surface is more stable than the bulk V_O when the surface is fully hydroxylated. By contrast, the V_O is unstable in the type 1 GDC surface and in ceria at $\theta_H > 0.67$. A more detailed explanation of the relative stabilities of subsurface and surface oxygen vacancies in CeO_2 with and without Gd doping at different H coverages is given in the Supporting Information in Pages S9–S11. Therefore, GDC, especially type 2, can easily be reduced by forming hydroxyls and creating V_O. Since the reduced type 2 is more favorable than reduced type 1, type 2 GDC is used as the GDC model for the following kinetic studies of V_O diffusion, water dissociation, and hydroxyl decomposition.

Reaction Barriers for V_O Diffusion, Water Dissociation, and Hydrogen Formation at Reduced GDC and Reduced Ceria. *Barriers for V_O Diffusion.* Forming the $V_O^{surface}$ in ceria, one Ce^{3+} ion locates in its nearest-neighbored site and the other Ce^{3+} locates in the next-nearest-neighbored (NN–NNN) position. The same local distribution of localized electrons around the most stable $V_O^{surface}$ has been reported by Su et al.[45] and Ganduglia-Pirovano et al.[23] using $U_{eff} = 4.5$ eV. The calculated formation energy of the $V_O^{surface}$ (2.18 eV) is close to the formation energies of 2.15 and 2.34 eV calculated by Su et al. and by Ganduglia-Pirovano et al., respectively. Although the same local configuration is reported by using PBE + U ($U_{eff} = 3.0$ eV),[17] the total formation energy of the $V_O^{surface}$ (2.78 eV) is about 0.6 eV larger than the values calculated using $U_{eff} = 4.5$ eV in this work. This difference is caused by the lower stability of electrons localized in the 4f orbitals of ceria using lower U values, as discussed in the section "Methods".

The most favorable V_O in GDC has electrons localized on two gadolinium atoms (Figure S7). Creating one more V_O, the most favorable configuration has the second V_O in the subsurface, where the two additional compensating electrons are localized on $2Ce^{3+}$ in the NN positions relative to the V_O. The formation energy of creating two V_O in the top surface is very close to creating one V_O in the top surface and the other V_O near the Gd in the subsurface. The most stable configuration with the second V_O in the top surface of GDC has two electrons localized on two Ce^{3+} next to the V_O. We calculate the barriers for oxygen vacancy diffusion from the subsurface configuration to the surface configuration in ceria with one V_O and in GDC with one or two oxygen vacancies. In the one-vacancy system, the diffusion barrier is 0.15 eV in GDC and 0.65 eV in ceria, as shown in Figure 3a. A 0.64 barrier for oxygen vacancy diffusion at the same V_O concentration in ceria has been reported by Chen et al.[53] By contrast, the barrier for vacancy diffusion from the subsurface to the surface increases to 1.5 eV when two vacancies are created in GDC as presented in Figure S8 in the Supporting Information. Although the mobility of oxygen decreases when two vacancies are present in GDC, it is still a facile reaction compared to the hydroxyl decomposition step for breaking the strong O–H bond (having a 2.93 eV activation barrier[17]). The ionic conductivity in ceria is improved significantly by the incorporation of gadolinium in the "one-vacancy" system.

Barriers for Water Dissociation. It is easy for water to adsorb on the ceria or GDC surface after creating an oxygen vacancy. The most stable configuration for adsorption of one water molecule on the $CeO_2(111)$ surface is when water adsorbs at the next-nearest neighbor position to the oxygen vacancy. The water adsorption energy on ceria agrees well with previously reported results as shown in Table S2. On a highly reduced surface having five hydroxyls and an oxygen vacancy, the most stable site for water adsorption is near a cerium or

DOI: 10.1021/acs.jpcc.8b12037
J. Phys. Chem. C 2019, 123, 5507–5517

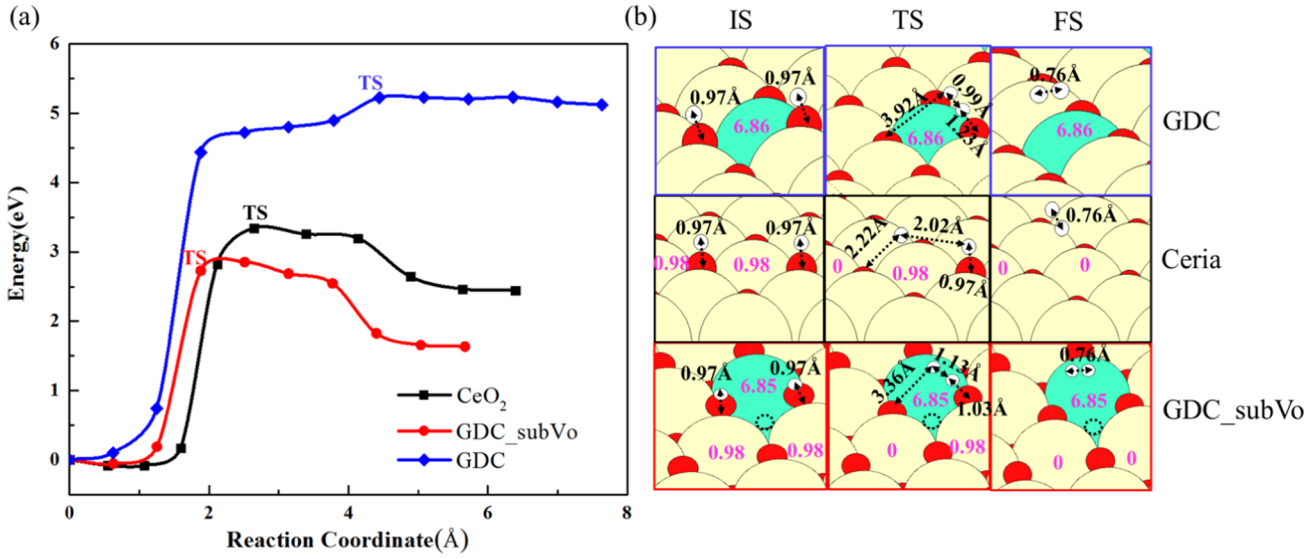

Figure 4. (a) Right panel: Reaction pathways of the hydroxyl decomposition on ceria, GDC, and GDC_subV$_O$ surfaces. Left panel: Configurations of the initial state (IS), transition state (TS), and final state (FS) along each reaction pathway. Bond lengths in surface hydroxyl and H_2, as well as the magnetization (μ_B) of each reaction state, are labeled. The color used for each kind of atom is the same as in Figure 1. The dashed circle indicates oxygen vacancy in the subsurface of GDC.

gadolinium atom next to the $V_O^{surface}$ as shown in Figure S9. The reaction barriers for water dissociation into hydroxyls are calculated and presented in Figure 3b. On the ceria surface having one $V_O^{surface}$ (the dotted line), the water dissociates into two hydroxyls via the reaction of $H_2O_{ads} + 2Ce^{3+} + V_O + O^{2-} \rightarrow 2OH^- + 2Ce^{3+}$. The migration of the V_O from the subsurface to the surface provides a V_O site in the surface and can accommodate one OH coming from H_2O slitting. The other H from H_2O forms a second OH with the nearest-neighbor surface O. The reaction barrier for water dissociation is close to zero and thus it is facile to perform water dissociation at the ceria surface. A similar reaction pathway and a barrier for water dissociation have been demonstrated previously.[17] No reaction path for water dissociation via the reaction of $H_2O_{ads} + 2Gd^{3+} + V_O + O^{2-} \rightarrow 2OH^- + 2Gd^{3+}$ on the GDC with one $V_O^{surface}$ is presented because the activation energy is negligible.

Because of the low barrier for water dissociation into hydroxyls, it is possible to form more hydroxyls on the ceria and GDC surfaces. When the ceria and GDC surfaces are covered by five hydroxyls, we need to create one oxygen vacancy in the surface in order to form more hydroxyls via water dissociation. The water dissociates on such a highly reduced ceria surface via the reaction of $H_2O_{ads} + 7Ce^{3+} + 5OH^- + V_O + O^{2-} \rightarrow 7OH^- + 7Ce^{3+}$, where one OH from H_2O takes the site of the V_O, while the H of H_2O reacts with one subsurface oxygen ion of the ceria to form one subsurface hydroxyl (subO−H). This subO−H is unfavorable compared to other surface hydroxyls as noticed from Figure 2. On the 5OH covered GDC surface, water dissociates into hydroxyls via the reaction $H_2O_{ads} + 2Gd^{3+} + 5Ce^{3+} + 5OH^- + V_O + O^{2-} \rightarrow 7OH^- + 2Gd^{3+} + 5Ce^{3+}$, where one OH from water takes the site of the V_O, while the H of water reacts with the subsurface oxygen that is the nearest neighbor to the Gd. Compared with the facile formation of the 2OH on the surface, the kinetic barriers for water dissociation to form the 7OH on the ceria and GDC increase slightly to 0.2 and 0.3 eV, respectively. Thus, it is easy to form fully and overly hydroxylated ceria and GDC via reactions between water and an oxygen vacancy.

Barriers for Hydroxyl Decomposition. After oxygen vacancies have diffused to the surface and reacted with the adsorbed water to form two hydroxyls on the ceria surfaces, the last step for hydrogen production is hydroxyl decomposition, which is widely reported as the rate-determining step during many hydroxyl-associated reactions.[11,17,44,52] The reaction barriers for hydroxyl decomposition on the ceria ($Ce_{18}O_{36}$), GDC ($Gd_2Ce_{16}O_{36}$), and GDC with a compensating subsurface V_O (GDC_subV$_O$, $Gd_2Ce_{16}O_{35}$) are presented in Figure 4. The hydroxyl decomposition on the ceria surface proceeds via the reaction $2OH^- + 2Ce^{3+} \rightarrow H_2 + 2Ce^{4+} + 2O^{2-}$. The reaction is $2OH^- + 2Gd^{3+} \rightarrow H_2 + 2Gd^{3+} + 2O^{2-} + 2h^+$ on the GDC surface and $2OH^- + 2Gd^{3+} + V_O \rightarrow H_2 + 2Gd^{3+} + V_O + 2O^{2-}$ on the GDC_subV$_O$ surface.

The reaction pathways for hydroxyl decompositions are asymmetric and the transition states appear early when breaking the first O−H bond.[17,46] A vibrational analysis of the transition state for hydroxyl decomposition on these hydroxylated surfaces reveals a single mode with an imaginary frequency. The mode corresponds to a H moving over a Gd/Ce ion while shortening the H−H bond. At the TS for hydroxyl decomposition on the ceria, one O−H bond is broken and one Ce^{3+} is oxidized to Ce^{4+}, where the total magnetization of the ceria decreases from 1.96 to 0.98 μ_B, as shown in Figure 4b. The breaking of an O−H bond and an H−H bond length of 2.02 Å in the transition state agrees well with previous literature reports.[17,54] After the transition state, breaking the second O−H bond is downhill in energy as shown in Figure 4a, which finally leads to the formation of one hydrogen molecule. This asymmetric reaction pathway leads to a 3.4 eV barrier for hydroxyl decomposition over the ceria surface.

Similarly, the asymmetric reaction pathway is found for hydrogen formation on the GDC and GDC_subV$_O$, which, respectively, leads to a 5.2 eV activation barrier and a 2.8 eV barrier. The barrier decreases dramatically for hydrogen formation over the GDC reduced by creating one $V_O^{subsurface}$

DOI: 10.1021/acs.jpcc.8b12037
J. Phys. Chem. C 2019, 123, 5507−5517

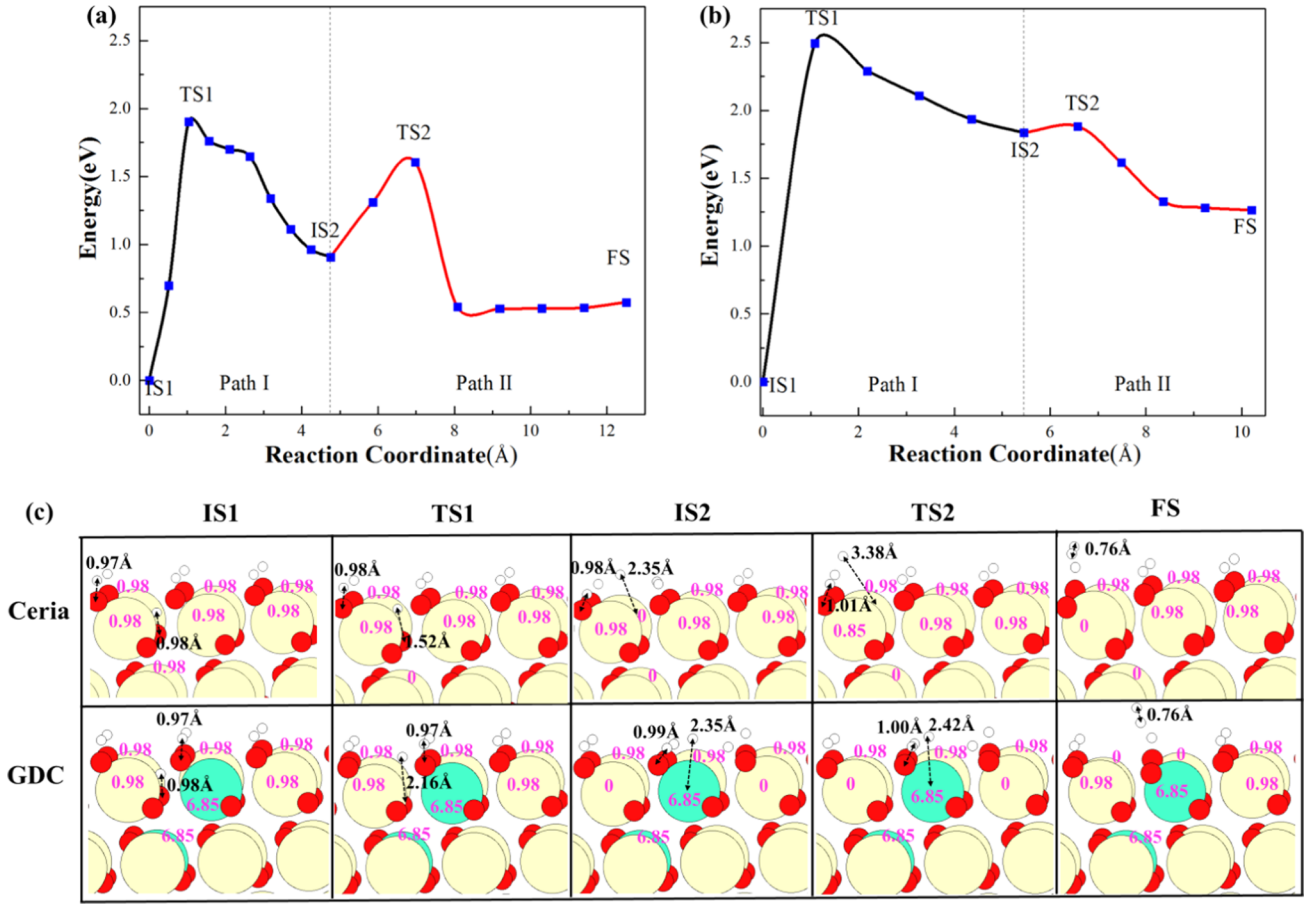

Figure 5. Energy diagrams for hydroxyl decomposition into H_2 on the overly hydroxylated CeO_2 (7H) surface (a) and on the overly hydroxylated GDC (7H) surface (b). (c) Side views of the optimized structures for each intermediate and transition state (top views are given in Figure S10 in the Supporting Information). The bond lengths of O−H, Ce−H, and Gd−H involved in the reactions are labeled. In addition, the magnetization (μ_B) of each reaction state is marked in pink.

and forming two hydroxyls compared with the partially hydroxylated (2H) GDC. This is because the final formation of the GDC_subV$_O$ ($Gd_2Ce_{16}O_{35}$) after the hydroxyl decomposition is more favored than the formation of the uncompensated GDC ($Gd_2Ce_{16}O_{36}$) surface as discussed in the section "Distribution of Gd and Oxygen Vacancies (V_O) in $Gd_2Ce_{16}O_{35}$(111)". Therefore, our results indicate that the hydroxyl decomposition may proceed more easily over the highly hydroxylated GDC surface by creating oxygen vacancy and formation of hydroxyls. It has not been possible to identify Ce(Gd)−H as a stable intermediate structure on the 2H* surface because it easily relaxes into H_2 or 2OH.

The reaction barriers for hydrogen formation on the overly hydroxylated ceria and GDC are presented in Figure 5. As discussed in the section "Barriers for Water Dissociation", the water dissociates into hydroxyls on the 5OH covered ceria surface via the reaction $H_2O_{ads} + 7Ce^{3+} + 5OH^- + V_O + O^{2-} \rightarrow 7OH^- + 7Ce^{3+}$, where the H of water reacts with one subsurface oxygen ion of the ceria to form one subsurface hydroxyl (subO−H). This reaction is competed by $H_2O_{ads} + 5OH^- + 7Ce^{3+} + V_O \rightarrow 6OH^- + Ce^{4+} + Ce^{4+}H^- + 5Ce^{3+}$, where the H from water binds to the metal ions and thus forms a Ce−H moiety on the surface. Two electrons from the 4f shell of $2Ce^{3+}$ contribute to the formation of the $Ce^{4+}H^-$ and one Ce^{4+} (i.e., oxidation of ceria). In this Ce−H system, there are a total of $5Ce^{3+}$ and total magnetization of the system is 5.0 μ_B as presented in Figure 5c. For water dissociation in the GDC system, the Gd−H moiety forms via the reaction $H_2O_{ads} + 5OH^- + 5Ce^{3+} + 2Gd^{3+} + V_O \rightarrow 6OH^- + 2Ce^{4+} + Gd^{3+}H^- + 3Ce^{3+} + Gd^{3+}$. The $4f^1$ of $2Ce^{3+}$ donates two electrons, which contributes to the formation of the $Gd^{3+}H^-$. In the Gd−H system, the magnetization of each Gd^{3+} is 7.0 μ_B and there are $3Ce^{3+}$ with the magnetization of 1.0 μ_B for each, as shown in Figure 5c.

The binding of H to Ce in the surface is about 0.9 eV weaker than the binding to an oxygen in the subsurface as shown in Figure 5a. However, the Ce−H bond is 0.28 and 1.15 eV weaker than the O−H bond when using U_{eff} values of 3.0 and 5.0 eV, respectively, which indicates that these bindings are strongly dependent on the values of U_{eff} corrections. The sensitivity to the choice of U_{eff} arises from the fact that there are $5Ce^{3+}$ ions in the surface with formation of one Ce−H and six O−H, whereas the surface with formation of seven O−H has $7Ce^{3+}$ ions. In the overly hydroxylated GDC, the binding between H and the oxygen next to the Gd in the subsurface is 1.9 eV stronger than the binding between H and Gd in the surface as presented in Figure 5b. Because of the strong binding between H and oxygen in the subsurface, the direct breaking of the O−H bond for H_2 formation is difficult. Herein, for hydroxyl decomposition on such overly hydroxylated surfaces, the reaction pathways are split into two independent paths via Ce−H and Gd−H intermediates, respectively, on the overly hydroxylated ceria and GDC surfaces. Path I involves the breaking of the O−H bond in the

DOI: 10.1021/acs.jpcc.8b12037
J. Phys. Chem. C 2019, 123, 5507−5517

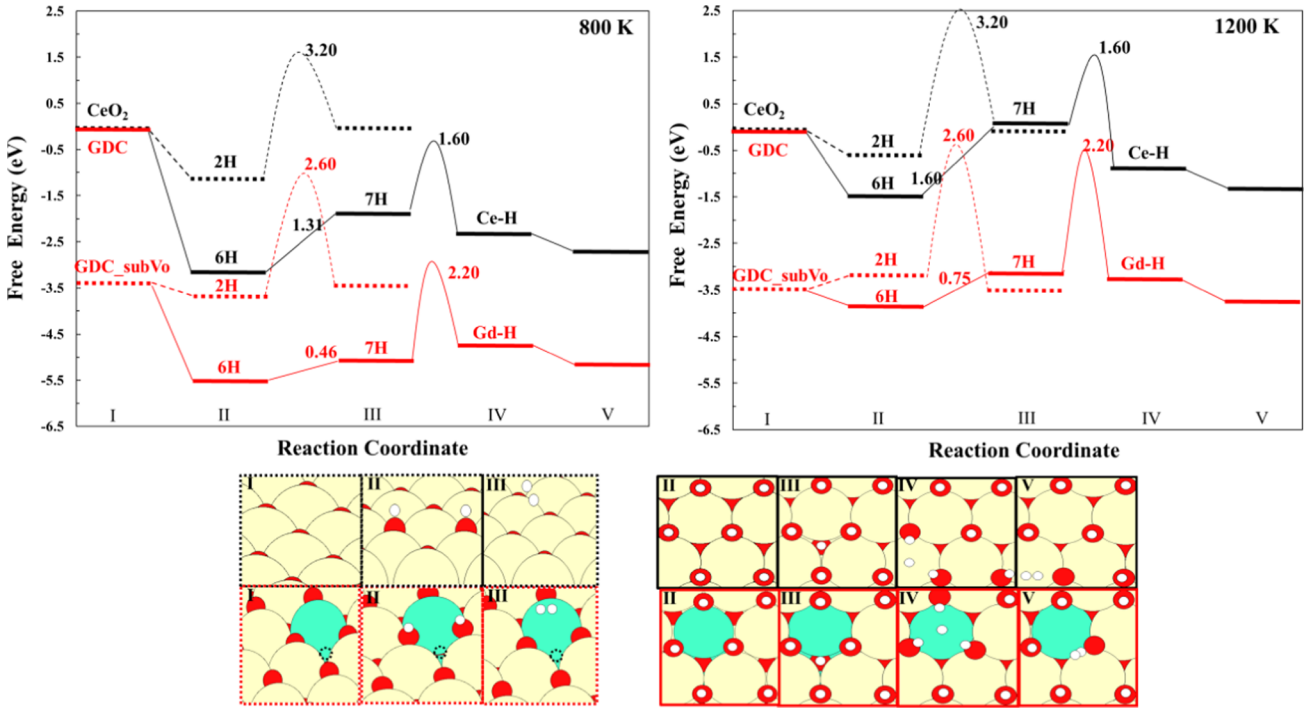

Figure 6. Top panel: Free energy of the intermediates during the hydrogen evolution reaction on the partially (2H) and overly (7H) hydroxylated GDC and CeO_2 at 800 and 1200 K, respectively. Bottom panel: Atomic configurations of reaction intermediates over the four different surfaces. The color used for each kind of atom is the same as in Figure 4. The dashed circle stands for an oxygen vacancy.

subsurface to form Me−H (Gd−H or Ce−H) intermediates. Path II involves the reaction between the Me-H and the nearby O−H, finally leading to the formation of H_2. The reaction along path I is $OH_{subsurface}^{-} + 2Ce^{3+} + Gd^{3+} \rightarrow 2Ce^{4+} + Gd^{3+}H^{-} + O_{subsurface}^{2-}$ on the GDC surface and $OH_{subsurface}^{-} + 2Ce^{3+} \rightarrow Ce^{4+} + Ce^{4+}H^{-} + O_{subsurface}^{2-}$ on the ceria surface. The reaction along path II is $OH_{surface}^{-} + Gd^{3+}H^{-} \rightarrow Gd^{3+} + H_2 + O_{surface}^{2-}$ on the GDC surface and $OH_{surface}^{-} + Ce^{4+}H^{-} \rightarrow Ce^{4+} + H_2 + O_{surface}^{2-}$ on the ceria surface.

For the reaction along path I on ceria, breaking the O−H bond in the subsurface of the overly hydroxylated ceria is difficult, leading to a 2.0 eV activation barrier. At the transition state (TS1), the Ce^{3+} in the subsurface is oxidized to Ce^{4+}, which is followed by the oxidation of the second Ce^{3+} in the top surface to form the Ce−H. For the reaction along path I over the overly hydroxylated GDC, the barrier is 2.5 eV, where the O−H bond of TS1 is broken but the total magnetization remains unchanged (i.e., no Ce^{3+} or Gd^{3+} is oxidized). The higher barrier in the GDC system arises from the higher stability of the overly hydroxylated GDC as discussed in the part of E_H (presented in Figure 2). However, the HER proceeds easily along path II, having 0.7 and 0.05 eV barriers on the overly hydroxylated ceria and GDC, respectively. By comparing path I and path II, it is noticed that breaking the O−H bond in the subsurface in path I is the most difficult step. This indicates that if the formation of the Me−H moiety becomes more favorable by adding a substitutional dopant, the reaction along path I can proceed with a lower activation barrier for H_2 formation.

Reaction Pathways for Hydrogen Production at Reduced GDC and Ceria. Based on the previous discussions on the configurations of the reduced surface and the kinetic barriers of each reaction step at the reduced surface, the free energy of the intermediates at each reaction step during the water splitting reaction (WSR) is calculated. Because the operation during electrochemical reactions over GDC is at temperatures 773−1073 K,[19,20] the free energy diagram at 800 K is investigated, and a higher temperature (1200 K) is investigated for comparison. The simplified free energy diagrams of HER on the ceria and GDC are shown in Figure 6. To calculate the relative free energy of the reduced surfaces at each reaction step, the surface without any vacancies or hydroxyl groups in ceria and GDC is chosen as the reference surface. The reduced surfaces are formed via the reaction between vacancies, oxygen, and water at the reference surface. On the basis of this reaction, the free energies for each reduced surface are calculated (see more details in Pages S11 and S12 in the Supporting Information). The formation of the fully hydroxylated (covered by 6H) GDC and ceria is more favorable than the other H coverage at 400 K < T < 1200 K, as presented in Figure S11. Besides, it is easier to form the overly hydroxylated (7H) GDC than ceria at 400 K < T < 1200 K.

At 800 K, 3.20 and 2.60 eV enthalpy barriers are required for hydrogen formation over the partially hydroxylated ceria and GDC surfaces, respectively, as shown in Figure 6. Here, the transition state occurs with the first O−H bond breaking in hydroxyl coupled with electron transfer from Ce^{3+} as discussed in the section "Barriers for Hydroxyl Decomposition". Compared to the partially hydroxylated pathways, the HER proceeds more efficiently via the Ce−H and Gd−H intermediates on the overly hydroxylated ceria and GDC surfaces, respectively, where we find 1.60 and 2.20 eV kinetic barriers for H_2 formation, respectively. However, the reaction energy required to form the Ce−H intermediate on fully hydroxylated ceria is 1.31 eV, whereas only 0.46 eV is required for the formation of the Gd−H on the fully hydroxylated GDC because of the stabilization of the reduced states by the incorporation of Gd. Thus, it is more difficult to form overly

DOI: 10.1021/acs.jpcc.8b12037
J. Phys. Chem. C 2019, 123, 5507−5517

hydroxylated ceria, and the overall free energy barrier for the HER on the overly hydroxylated ceria surface is 2.91 eV. By contrast, 2.67 eV is required for the hydrogen production on the overly hydroxylated GDC. These results indicate that the reaction activity of the HER on ceria is significantly improved by the incorporation of gadolinium. In addition, if the formation of the 7H is favorable and the Me-H is stabilized by adding a substitutional dopant in ceria, the total free energy for H_2 formation will decrease.

As temperature increases to 1200 K, the free energies of all intermediates increase mainly due to the loss of gas-phase entropy upon adsorption.[17] A significant increase is found for the reaction free energy to form the overly hydroxylated surfaces, which increases to 1.60 and 0.75 eV in ceria and GDC, respectively. The formation of the overly reduced ceria competes heavily with the water adsorption/desorption at high temperature (Figure S12), which prevents the formation of the highly reduced states. However, the hydroxyl decomposition remains to be the rate-determining step, which can be seen from the full reaction pathways in Figure S12 in the Supporting Information. At 1200 K, the reaction proceeding via the Gd−H intermediate on the overly hydroxylated GDC has the lowest energy cost. The operating temperature for the HER on GDC should be higher than 800 K to reach the same rate as on Pt at 400 K (Figure S13 in the Supporting Information). The predicted operating temperature is consistent with the experimental operating temperature range (773−1073 K).[19,20] However, temperatures higher than 900 K are required for the HER on ceria. Therefore, the HER is allowed to proceed at lower temperatures on GDC than on undoped ceria. The reactivity of the WSR on ceria is improved by the incorporation of gadolinium.

CONCLUSIONS

Using the DFT + *U* method, we have studied configurations of reduced ceria and reduced GDC via creating vacancies and forming hydroxyls. We find that Gd can distribute freely between the top surface or subsurface of the $Gd_2Ce_{16}O_{35}(111)$ surface at 11% Gd concentration. The vacancy and hydroxyl formation energy in GDC were more negative than in pure ceria. Thus, it is much easier to form highly reduced GDC than to form highly reduced ceria via creating vacancies and forming hydroxyls. Then, the mechanism of water splitting on the GDC surface compared to pure ceria was revealed by the kinetic investigations. We observed that one vacancy diffusion in the GDC surface was faster than in the ceria surface. The following step for the water dissociation on both GDC and ceria surfaces was facile even at very high hydrogen coverage. However, there is a large barrier for hydroxyl decomposition on the partially hydroxylated ceria and GDC. The reaction activity for the HER was improved significantly via the Gd−H intermediate on the overly hydroxylated GDC surface under the operating temperature (800 and 1200 K), which is attributed to the much favorable formation of the Gd−H than Ce−H intermediate.

In conclusion, the incorporation of Gd plays an important role in stabilizing the intermediates and transition states for hydroxyl decomposition and further enhancing performance of ceria for water splitting. Therefore, a dopant that stabilizes the reduced ceria surface and has strong binding to hydrogen is capable of effectively improving the reaction activity of ceria for renewable hydrogen production in SOEC. Our findings give insight into the mechanism of water splitting in GDC and ceria, which help in the design of ceria-based electrocatalysts for renewable hydrogen production via water splitting reaction.

ASSOCIATED CONTENT

Supporting Information

The Supporting Information is available free of charge on the ACS Publications website at DOI: 10.1021/acs.jpcc.8b12037.

Configurations of the $Ce_{18}O_{36}(111)$, reduced ceria, and GDC surfaces via forming one oxygen vacancy or hydroxyl and also the most stable configurations of water adsorption, overly hydroxylated surface, and hydrogen desorption on ceria and GDC; barriers for hydroxyl decomposition into H_2 and V_O formation energies as a function of the *U* correction on Ce 4f states; pathway for vacancy diffusion in a two-vacancy system of GDC; free energy of the H covered ceria and GDC as a function of hydroxyl coverage; free energy diagrams for water splitting at 800 and 1200 K; views of the optimized structures for each intermediate and transition state during hydroxyl decomposition into H_2; discussions of the relative stability of $V_O^{subsurface}$ and $V_O^{surface}$ in the ceria with and without Gd doping at different hydroxyl coverages; tables of DFT energies for vacancy formation, vacancy diffusion, and water adsorption and dissociation; details of methods for calculating free energies of the reduced surface (PDF)

AUTHOR INFORMATION

Corresponding Authors

*E-mail: heih@dtu.dk. Tel.: +45 46775758 (H.A.H.).
*E-mail: teve@dtu.dk. Tel.: +45 45258201 (T.V.).

ORCID

Qingming Deng: 0000-0002-5293-0256
Heine Anton Hansen: 0000-0001-7551-9470
Tejs Vegge: 0000-0002-1484-0284

Notes

The authors declare no competing financial interest.

ACKNOWLEDGMENTS

This work was supported by the Velux Foundations through the research center V-Sustain (grant number 9455).

REFERENCES

(1) Jen, H.-W.; Graham, G. W.; Chun, W.; McCabe, R. W.; Cuif, J.-P.; Deutsch, S. E.; Touret, O. Characterization of Model Automotive Exhaust Catalysts: Pd on Ceria and Ceria−Zirconia Supports. *Catal. Today* **1999**, *50*, 309−328.

(2) Oh, S. H.; Hoflund, G. B. Chemical State Study of Palladium Powder and Ceria-Supported Palladium during Low-Temperature CO Oxidation. *J. Phys. Chem. A* **2006**, *110*, 7609−7613.

(3) Di Monte, R.; Kašpar, J. On the Role of Oxygen Storage in Three-Way Catalysis. *Top. Catal.* **2004**, *28*, 47−57.

(4) Bunluesin, T.; Gorte, R. J.; Graham, G. W. Studies of the Water-Gas-Shift Reaction on Ceria-Supported Pt, Pd, and Rh: Implications for Oxygen-Storage Properties. *Appl. Catal., B* **1998**, *15*, 107−114.

(5) Fu, Q. Active Nonmetallic Au and Pt Species on Ceria-Based Water-Gas Shift Catalysts. *Science* **2003**, *301*, 935−938.

(6) Hilaire, S.; Wang, X.; Luo, T.; Gorte, R. J.; Wagner, J. A Comparative Study of Water-Gas-Shift Reaction over Ceria-Supported Metallic Catalysts. *Appl. Catal., A* **2004**, *258*, 271−276.

(7) Otsuka, K.; Hatano, M.; Morikawa, A. Hydrogen from Water by Reduced Cerium Oxide. *J. Catal.* **1983**, *79*, 493−496.

DOI: 10.1021/acs.jpcc.8b12037
J. Phys. Chem. C 2019, 123, 5507−5517

(8) Abanades, S.; Legal, A.; Cordier, A.; Peraudeau, G.; Flamant, G.; Julbe, A. Investigation of Reactive Cerium-Based Oxides for H_2 Production by Thermochemical Two-Step Water-Splitting. *J. Mater. Sci.* **2010**, *45*, 4163−4173.
(9) Fergus, J. W. Electrolytes for Solid Oxide Fuel Cells. *J. Power Sources* **2006**, *162*, 30−40.
(10) Shao, Z.; Haile, S. M.; Ahn, J.; Ronney, P. D.; Zhan, Z.; Barnett, S. A. A Thermally Self-Sustained Micro Solid-Oxide Fuel-Cell Stack with High Power Density. *Nature* **2005**, *435*, 795−798.
(11) Feng, Z. A.; El Gabaly, F.; Ye, X.; Shen, Z.-X.; Chueh, W. C. Fast Vacancy-Mediated Oxygen Ion Incorporation across the Ceria−gas Electrochemical Interface. *Nat. Commun.* **2014**, *5*, No. 4374.
(12) Zhang, C.; Yu, Y.; Grass, M. E.; Dejoie, C.; Ding, W.; Gaskell, K.; Jabeen, N.; Hong, Y. P.; Shavorskiy, A.; Bluhm, H.; et al. Mechanistic Studies of Water Electrolysis and Hydrogen Electro-Oxidation on High Temperature Ceria-Based Solid Oxide Electrochemical Cells. *J. Am. Chem. Soc.* **2013**, *135*, 11572−11579.
(13) Irvine, J. T. S.; Neagu, D.; Verbraeken, M. C.; Chatzichristodoulou, C.; Graves, C.; Mogensen, M. B. Evolution of the Electrochemical Interface in High-Temperature Fuel Cells and Electrolysers. *Nat. Energy* **2016**, *1*, 15014.
(14) Hauch, A.; Mogensen, M.; Hagen, A. Ni/YSZ Electrode Degradation Studied by Impedance Spectroscopy - Effect of $p(H_2O)$. *Solid State Ionics* **2011**, *192*, 547−551.
(15) Chueh, W. C.; Hao, Y.; Jung, W.; Haile, S. M. High Electrochemical Activity of the Oxide Phase in Model Ceria−Pt and Ceria−Ni Composite Anodes. *Nat. Mater.* **2012**, *11*, 155−161.
(16) Zhang, C.; Grass, M. E.; McDaniel, A. H.; Decaluwe, S. C.; El Gabaly, F.; Liu, Z.; McCarty, K. F.; Farrow, R. L.; Linne, M. A.; Hussain, Z.; et al. Measuring Fundamental Properties in Operating Solid Oxide Electrochemical Cells by Using in Situ X-Ray Photoelectron Spectroscopy. *Nat. Mater.* **2010**, *9*, 944−949.
(17) Hansen, H. A.; Wolverton, C. Kinetics and Thermodynamics of H_2O Dissociation on Reduced $CeO_2(111)$. *J. Phys. Chem. C* **2014**, *118*, 27402−27414.
(18) Inaba, H.; Sagawa, R.; Hayashi, H.; Kawamura, K. Molecular Dynamics Simulation of Gadolinia-Doped Ceria. *Solid State Ionics* **1999**, *122*, 95−103.
(19) Ni, M.; Leung, M. K. H.; Leung, D. Y. C. Technological Development of Hydrogen Production by Solid Oxide Electrolyzer Cell (SOEC). *Int. J. Hydrogen Energy* **2008**, *33*, 2337−2354.
(20) Zhang, C.; Li, C. J.; Zhang, G.; Ning, X. J.; Li, C. X.; Liao, H.; Coddet, C. Ionic Conductivity and Its Temperature Dependence of Atmospheric Plasma-Sprayed Yttria Stabilized Zirconia Electrolyte. *Mater. Sci. Eng. B* **2007**, *137*, 24−30.
(21) Paier, J.; Penschke, C.; Sauer, J. Oxygen Defects and Surface Chemistry of Ceria: Quantum Chemical Studies Compared to Experiment. *Chem. Rev.* **2013**, *113*, 3949−3985.
(22) Naghavi, S. S.; Emery, A. A.; Hansen, H. A.; Zhou, F.; Ozolins, V.; Wolverton, C. Giant Onsite Electronic Entropy Enhances the Performance of Ceria for Water Splitting. *Nat. Commun.* **2017**, *8*, No. 285.
(23) Ganduglia-Pirovano, M. V.; Da Silva, J. L. F.; Sauer, J. Density-Functional Calculations of the Structure of near-Surface Oxygen Vacancies and Electron Localization on $CeO_2(111)$. *Phys. Rev. Lett.* **2009**, *102*, No. 026101.
(24) Yang, Z.; Wang, Q.; Wei, S.; Ma, D.; Sun, Q. The Effect of Environment on the Reaction of Water on the Ceria (111) Surface: A DFT + U Study. *J. Phys. Chem. C* **2010**, *114*, 14891−14899.
(25) Mullins, D. R.; Albrecht, P. M.; Chen, T. L.; Calaza, F. C.; Biegalski, M. D.; Christen, H. M.; Overbury, S. H. Water Dissociation on $CeO_2(100)$ and $CeO_2(111)$ Thin Films. *J. Phys. Chem. C* **2012**, *116*, 19419−19428.
(26) Lykhach, Y.; Johánek, V.; Aleksandrov, H. A.; Kozlov, S. M.; Happel, M.; Skála, T.; Petkov, P. S.; Tsud, N.; Vayssilov, G. N.; Prince, K. C.; et al. Water Chemistry on Model Ceria and Pt/Ceria Catalysts. *J. Phys. Chem. C* **2012**, *116*, 12103−12113.
(27) Kundakovic, L.; Mullins, D. R.; Overbury, S. H. Adsorption and Reaction of H_2O and CO on Oxidized and Reduced $Rh/CeO_x(111)$ Surfaces. *Surf. Sci.* **2000**, *457*, 51−62.
(28) Aparicio-Anglès, X.; Roldan, A.; De Leeuw, N. H. Gadolinium-Vacancy Clusters in the (111) Surface of Gadolinium-Doped Ceria: A Density Functional Theory Study. *Chem. Mater.* **2015**, *27*, 7910−7917.
(29) Dholabhai, P. P.; Adams, J. B.; Crozier, P.; Sharma, R. A Density Functional Study of Defect Migration in Gadolinium Doped Ceria. *Phys. Chem. Chem. Phys.* **2010**, *12*, 7904.
(30) Grieshammer, S.; Grope, B. O. H.; Koettgen, J.; Martin, M. A Combined DFT + U and Monte Carlo Study on Rare Earth Doped Ceria. *Phys. Chem. Chem. Phys.* **2014**, *16*, 9974.
(31) Kresse, G.; Furthmüller, J. Efficient Iterative Schemes for *Ab Initio* Total-Energy Calculations Using a Plane-Wave Basis Set. *Phys. Rev. B* **1996**, *54*, 11169−11186.
(32) Kresse, G.; Furthmüller, J. Efficiency of Ab-Initio Total Energy Calculations for Metals and Semiconductors Using a Plane-Wave Basis Set. *Comput. Mater. Sci.* **1996**, *6*, 15−50.
(33) Kresse, G.; Hafner, J. Ab Initio Molecular Dynamics for Open-Shell Transition Metals. *Phys. Rev. B* **1993**, *48*, 13115−13118.
(34) Blöchl, P. E. Projector Augmented-Wave Method. *Phys. Rev. B* **1994**, *50*, 17953−17979.
(35) Perdew, J. P.; Burke, K.; Ernzerhof, M. Generalized Gradient Approximation Made Simple. *Phys. Rev. Lett.* **1996**, *77*, 3865−3868.
(36) Loschen, C.; Carrasco, J.; Neyman, K. M.; Illas, F. First-Principles LDA+U and GGA+*U* Study of Cerium Oxides: Dependence on the Effective U Parameter. *Phys. Rev. B* **2007**, *75*, No. 035115.
(37) Vanpoucke, D. E. P.; Bultinck, P.; Cottenier, S.; Van Speybroeck, V.; Van Driessche, I. Aliovalent Doping of CeO_2: DFT Study of Oxidation State and Vacancy Effects. *J. Mater. Chem. A* **2014**, *2*, 13723−13737.
(38) Murgida, G. E.; Ganduglia-Pirovano, M. V. Evidence for Subsurface Ordering of Oxygen Vacancies on the Reduced $CeO_2(111)$ Surface Using Density-Functional and Statistical Calculations. *Phys. Rev. Lett.* **2013**, *110*, 1−5.
(39) Huang, M.; Fabris, S. CO Adsorption and Oxidation on Ceria Surfaces from DFT + U Calculations. *J. Phys. Chem. C* **2008**, *112*, 8643.
(40) Castleton, C. W. M.; Kullgren, J.; Hermansson, K. Tuning LDA +U for Electron Localization and Structure at Oxygen Vacancies in Ceria. *J. Chem. Phys.* **2007**, *127*, No. 244704.
(41) Da Silva, J. L. F.; Ganduglia-Pirovano, M. V.; Sauer, J.; Bayer, V.; Kresse, G. Hybrid Functionals Applied to Rare-Earth Oxides: The Example of Ceria. *Phys. Rev. B* **2007**, *75*, No. 045121.
(42) Kresse, G.; Blaha, P.; Da Silva, J. L. F.; Ganduglia-Pirovano, M. V. Comment on 'Taming Multiple Valency with Density Functionals: A Case Study of Defective Ceria'. *Phys. Rev. B* **2005**, *72*, 1−2.
(43) Farra, R.; García-Melchor, M.; Eichelbaum, M.; Hashagen, M.; Frandsen, W.; Allan, J.; Girgsdies, F.; Szentmiklósi, L.; López, N.; Teschner, D. Promoted Ceria: A Structural, Catalytic, and Computational Study. *ACS Catal.* **2013**, *3*, 2256−2268.
(44) Capdevila-Cortada, M.; García-Melchor, M.; López, N. Unraveling the Structure Sensitivity in Methanol Conversion on CeO_2: A DFT + U Study. *J. Catal.* **2015**, *327*, 58−64.
(45) Su, Y. Q.; Filot, I. A. W.; Liu, J. X.; Tranca, I.; Hensen, E. J. M. Charge Transport over the Defective $CeO_2(111)$ Surface. *Chem. Mater.* **2016**, *28*, 5652−5658.
(46) Fernández-Torre, D.; Carrasco, J.; Ganduglia-Pirovano, M. V.; Pérez, R. Hydrogen Activation, Diffusion, and Clustering on $CeO_2(111)$: A DFT+ U Study. *J. Chem. Phys.* **2014**, *141*, No. 014703.
(47) Gerward, L.; Staun Olsen, J.; Petit, L.; Vaitheeswaran, G.; Kanchana, V.; Svane, A. Bulk Modulus of CeO_2 and PrO_2 - An Experimental and Theoretical Study. *J. Alloys Compd.* **2005**, *400*, 56−61.
(48) Wang, H.; Chroneos, A.; Schwingenschlögl, U. Impact of Doping on the Ionic Conductivity of Ceria: A Comprehensive Model. *J. Chem. Phys.* **2013**, *138*, No. 224705.

DOI: 10.1021/acs.jpcc.8b12037
J. Phys. Chem. C 2019, 123, 5507−5517

(49) Minervini, L. Defect Cluster Formation in M_2O_3-Doped CeO_2. *Solid State Ionics* **1999**, *116*, 339−349.
(50) Henkelman, G.; Uberuaga, B. P.; Jónsson, H. Climbing Image Nudged Elastic Band Method for Finding Saddle Points and Minimum Energy Paths. *J. Chem. Phys.* **2000**, *113*, 9901−9904.
(51) Li, H.-Y.; Wang, H.; Gong, X.; Guo, Y.; Guo, Y.; Lu, G.; Hu, P. Multiple Configurations of the Two Excess 4 f Electrons on Defective CeO_2(111): Origin and Implications. **2009**, *2* 193401. DOI: 10.1103/physrevb.79.193401.
(52) Tang, Y.; Zhang, H.; Cui, L.; Ouyang, C.; Shi, S.; Tang, W.; Li, H.; Lee, J. S.; Chen, L. First-Principles Investigation on Redox Properties of M-Doped CeO_2(M=Mn,Pr,Sn,Zr). *Phys. Rev. B* **2010**, *82*, 1−9.
(53) Chen, H.-T.; Chang, J.-C.; Chen, H.-L.; Ju, S.-P. Identifying the O_2 Diffusion and Reduction Mechanisms on CeO2 Electrolyte in Solid Oxide Fuel Cells: A DFT+*U* Study. *J. Comput. Chem.* **2009**, *30*, 2433−2442.
(54) García-Melchor, M.; López, N. Homolytic Products from Heterolytic Paths in H_2 Dissociation on Metal Oxides: The Example of CeO_2. *J. Phys. Chem. C* **2014**, *118*, 10921−10926.

DOI: 10.1021/acs.jpcc.8b12037
J. Phys. Chem. C 2019, 123, 5507−5517

Supporting Information For "Mechanism of Water Splitting on Gadolinium Doped CeO_2 (111): A DFT+U Study"

Tiantian Wu, Qingming Deng, Heine Anton Hansen* and Tejs Vegge*

Department of Energy Conversion and Storage, Technical University of Denmark, Fysikvej, 2800 Kgs. Lyngby, Denmark.

**Corresponding authors:*

Prof. Dr. Tejs Vegge E-mail: teve@dtu.dk Tel: +45 45258201

Dr. Heine Anton Hansen E-mail: heih@dtu.dk Tel: +45 46775758

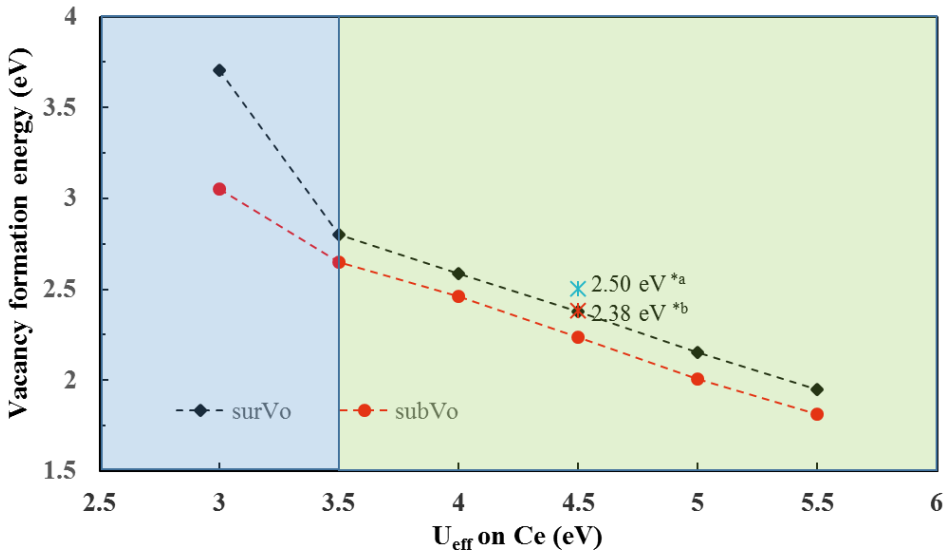

Figure S1. Vacancy formation energy in the CeO_2(111) as a function of values of U_{eff}=U-J (J=0). The CeO_2(111) surface is built as a 2×2 repeated surface unit cell consisting of nine atomic layers ($Ce_{12}O_{24}$). Three atomic layers in the bottom were fixed and a 15 Å vacuum is used to reduce interaction between the periodic images. The calculated equilibrium lattice constant of ceria bulk is 5.497 Å. The formation energy are very close to the value of 2.50[*a] and 2.38[*b] eV calculated by Ganduglia-Pirovano et al[1] and Su et al[2], respectively.

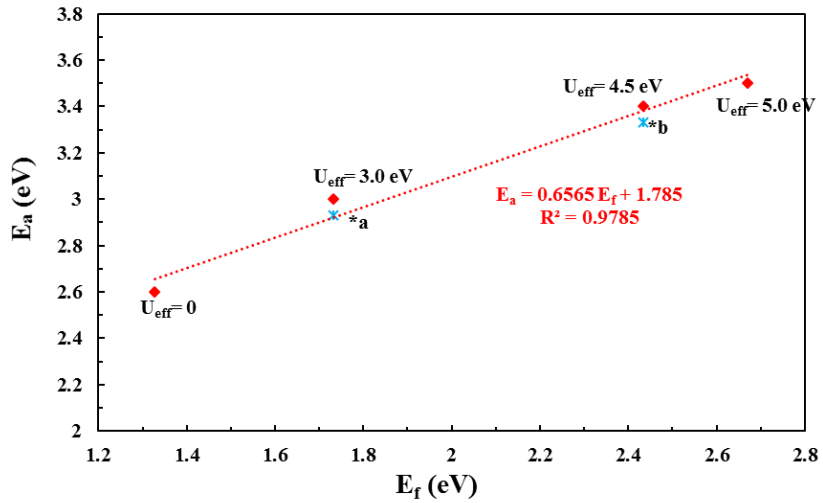

Figure S2. Activation barriers (E_a) for hydroxyl decomposition into H_2 on CeO_2(111) as a function of the hydroxyl formation energy (E_f): *a[3] and *b[4].

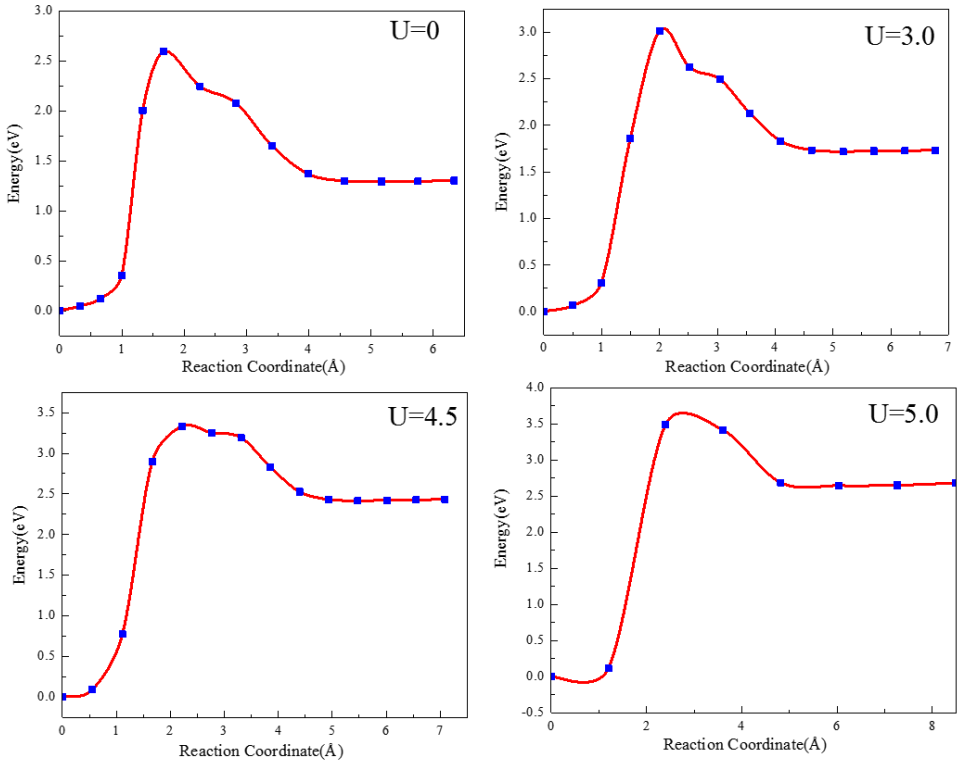

Figure S3. Barriers for hydroxyl decomposition into H_2 on a partially hydroxylated surface (with two hydroxyl groups) calculated using U=0, 3.0, 4.5 and 5.0 eV, respectively.

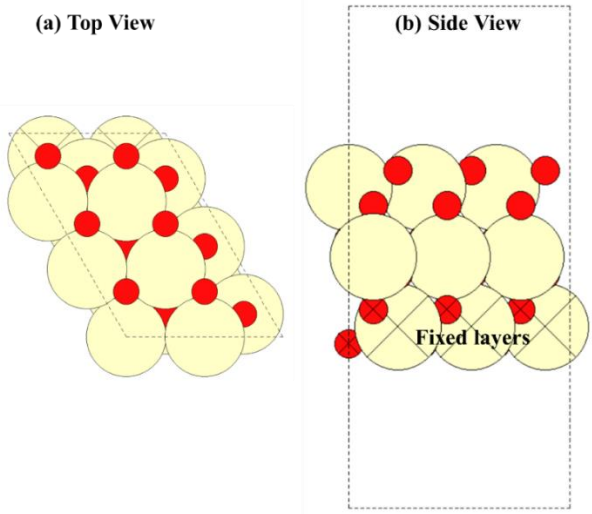

Figure S4. CeO_2(111) surface model ($Ce_{18}O_{36}$): (a) top and (b) side views. Yellow and red balls stand for cerium and oxygen atoms, respectively. The balls with crosses represent fixed atoms.

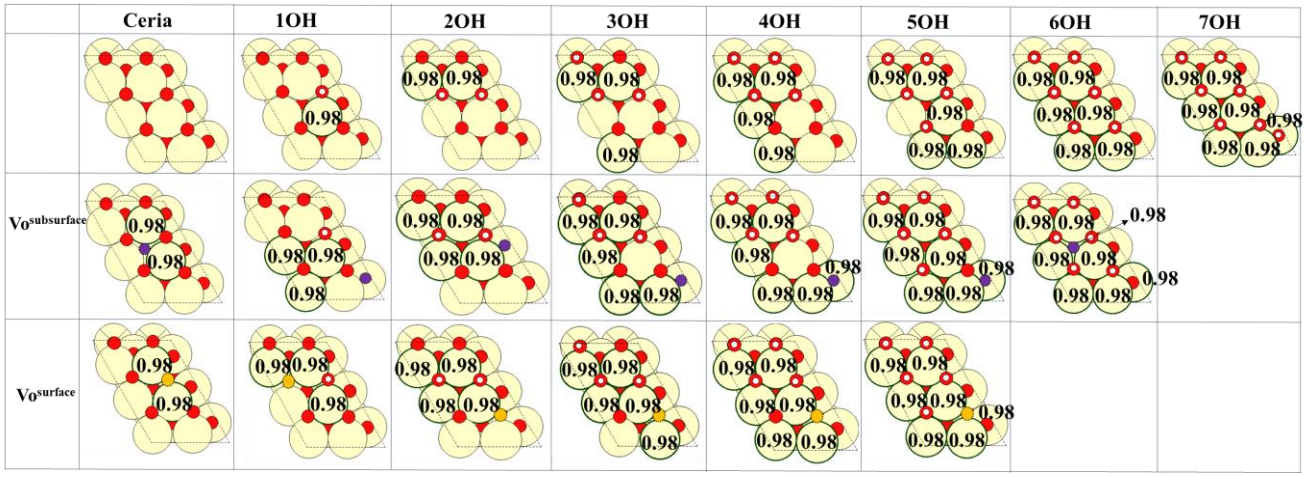

Figure S5. The most stable configurations of the reduced ceria surface via formation of oxygen vacancies, hydroxyls or mixed vacancy-hydroxyl phases. The solid orange and purple balls stand for vacancies in the surface and subsurface, respectively. The magnetization of each reduced cerium atom ($\sim$1.0 μB) is labeled. The O-H bond length of the hydroxyls is 0.97 Å.

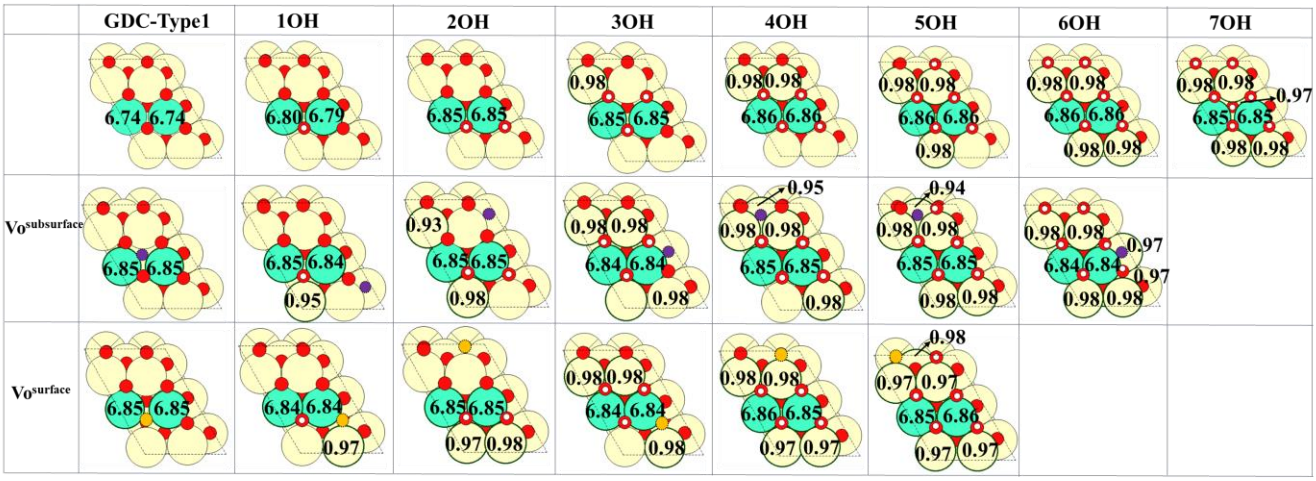

Figure S6. The most stable configurations of the reduced Type1 surface via formation of oxygen vacancies, hydroxyls or mixed vacancy-hydroxyl phases. The atoms and vacancies use the same color as in Figure S4. Blue balls show gadolinium atoms. The magnetization of each reduced cerium atom ($\sim$1.0 μB) and gadolinium atom ($\sim$7.0 μB) is labeled. The O-H bond length of the hydroxyls is 0.97 Å.

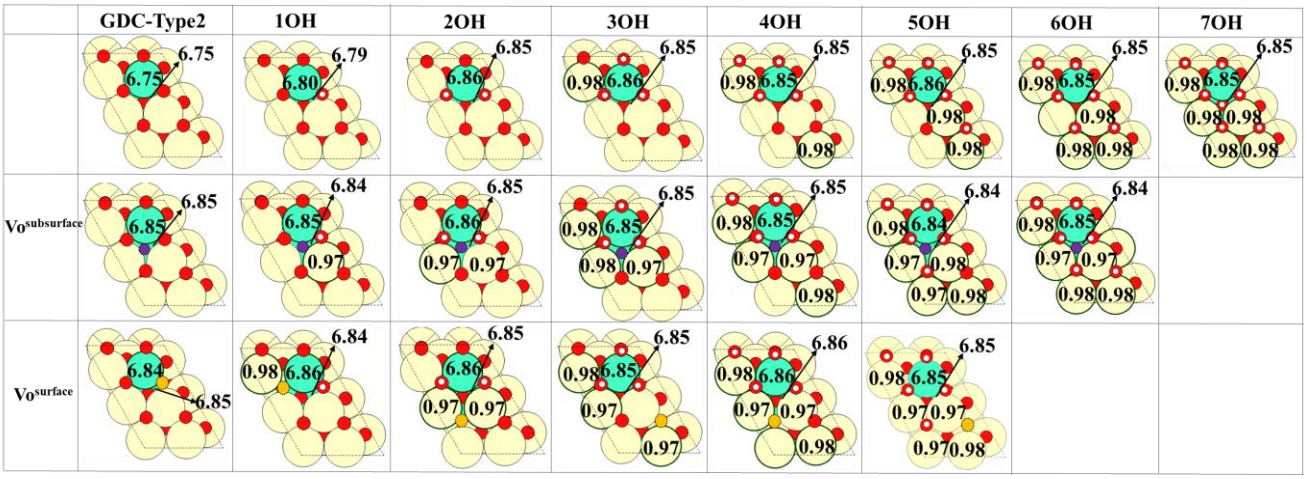

Figure S7. The most stable configurations of reduced Type2 surface via forming oxygen vacancies, hydroxyls or mixed vacancy-hydroxyl phases. The atoms and vacancies use the same color as in Figures S5 and S6. The magnetization of each reduced cerium atom ($\sim$1.0 μB) and gadolinium atom ($\sim$7.0 μB) is labeled. The O-H bond length of the hydroxyls is 0.97 Å.

As noted in Figure S5-S7, the single O-H in the surface is more likely to be next to Gd in both Type1 and Type2, while there is no preferred site to form one O-H in the ceria surface. With increasing θ_H, the additional surface O-H prefers to be as near as possible to Gd, where excess electrons are firstly used to reduce Gd and then on the Ce ions next to OH. For the mixed hydroxyl-vacancy phase in ceria, excess electrons left by creating a Vo in a hydroxylated surface, firstly localize on Ce ions next to the Vo. In Type1 where two Gd atoms are in the top atomic layer, both $Vo^{subsurface}$ and $Vo^{surface}$ are next to cerium atoms at high hydrogen coverage ($\theta_H >$ 0.33), where electrons are easily localized. While in Type2, $Vo^{subsurface}$ is next to the Gd in the subsurface at any hydrogen coverage, where it has the preferred electronic localization.

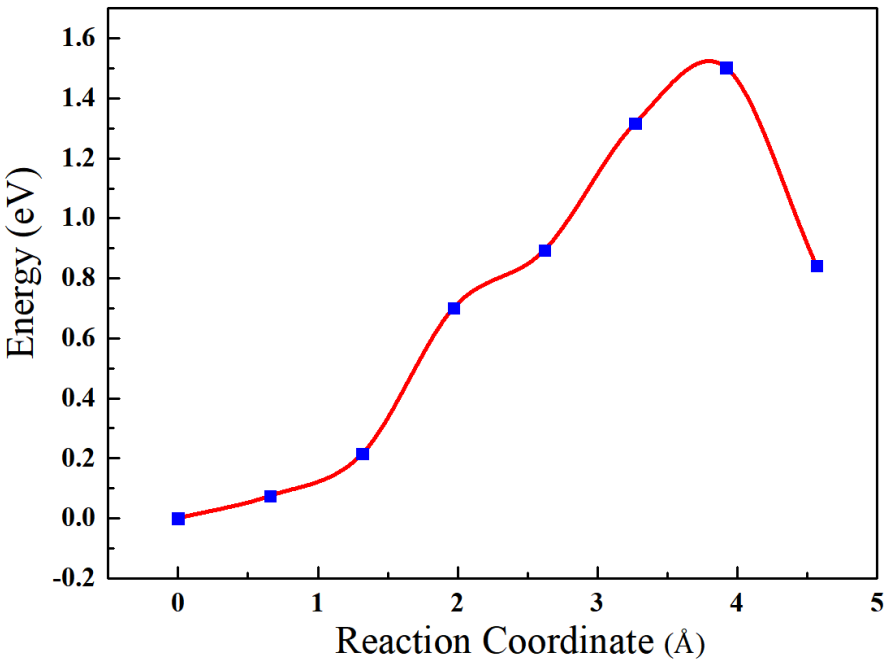

Figure S8. Diffusion of one vacancy from the subsurface to the surface in GDC where the other vacancy remains in the subsurface.

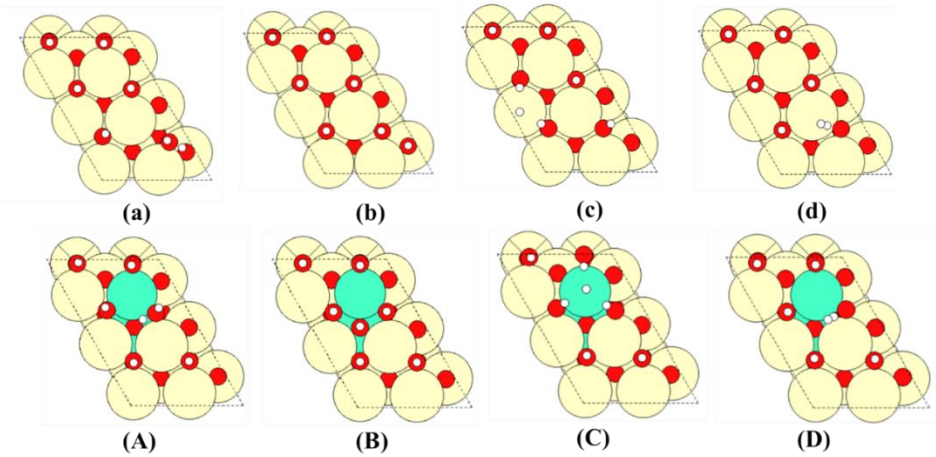

Figure S9. The most stable configurations of adsorbed water (a and A), water dissociated into one O-H in the subsurface (b and B), water dissociated into Me-H moiety in the surface (c and C) and desorbed H_2 near reduced ceria and GDC with 5 hydroxyl groups (d and D, respectively).

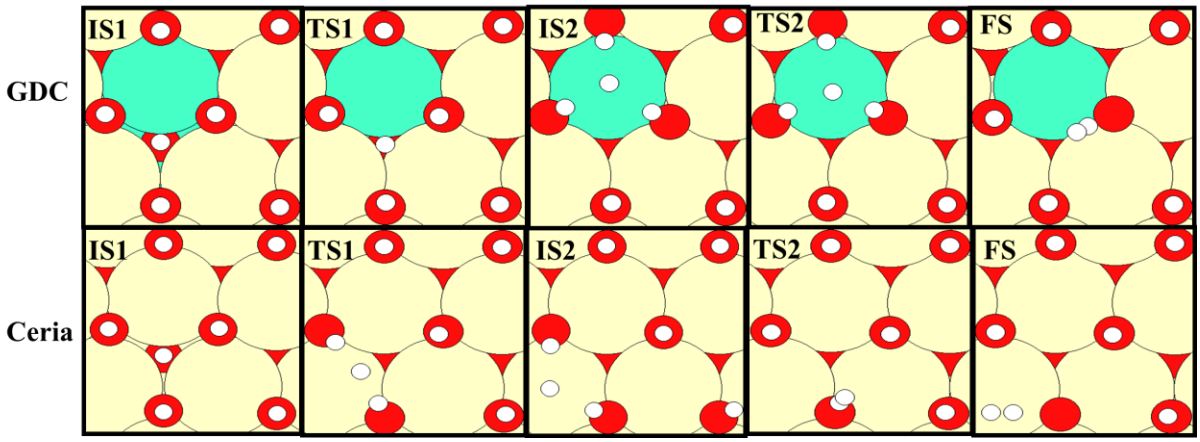

Figure S10. Top views of the optimized structures for each intermediates and transition states during the hydroxyl decomposition into H_2 on the overly hydroxylated (7H) CeO_2 and GDC surface, respectively.

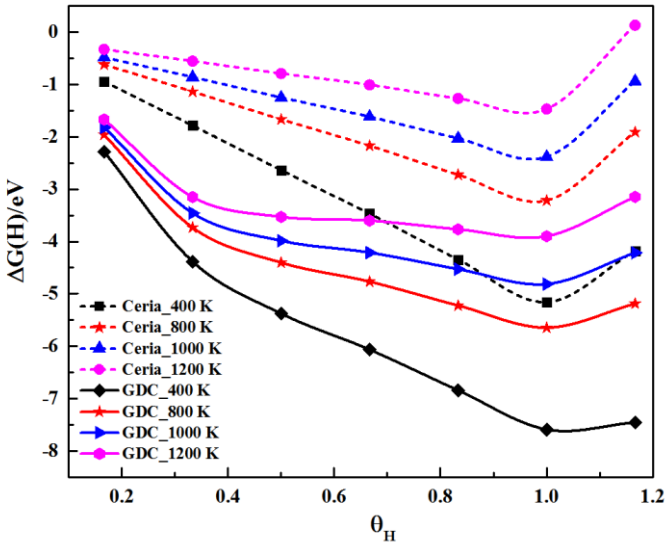

Figure S11. Free energy of hydroxylated ceria and GDC as a function of H coverage (Θ_H), at temperatures of 400, 800, 1000 and 1200 K, respectively.

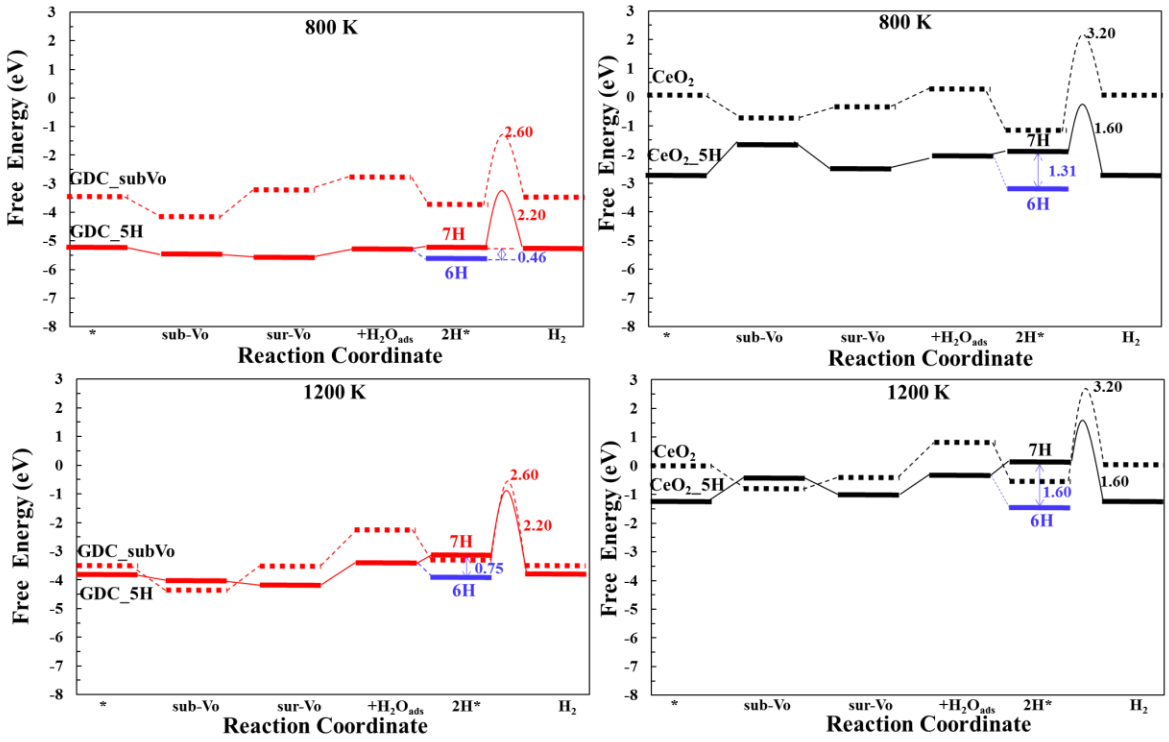

Figure S12. Free energy along different pathways for the water splitting reactions on the reduced GDC and CeO_2, at 800 and 1200 K, respectively.

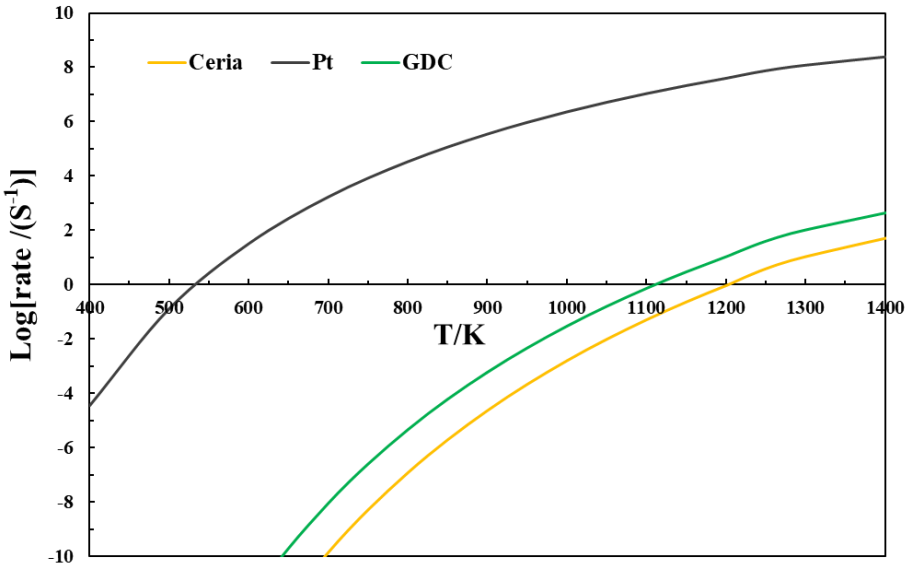

Figure S13. Reaction rates for hydrogen formation on GDC and ceria compared with the HER on Pt (111). The reaction rate on the Pt (111) is calculated as discussed in previous work[3].

Table S1 The formation energy of $Gd_2Ce_{16}O_{35}$ with an oxygen vacancy created in the top or subsurface surface is calculated by the reaction of $Gd_2O_3 + Ce_{18}O_{36} \rightarrow Gd_2Ce_{16}O_{35} + 2CeO_2$. The four different types of Gd distribution are considered.

Gd distribution type	Type4	Type3	Type2	Type1
E_f ($Gd_2Ce_{16}O_{35,}V_o^{surface}$)/eV	-1.712	-1.745	-1.743	-1.778
ΔE/eV	< 0.066			
E_f ($Gd_2Ce_{16}O_{35,}V_o^{subsurface}$)/eV	-1.784	-1.988	-1.881	-1.697
ΔE/eV	< 0.291			

Table S2. DFT energies for vacancy formation, vacancy diffusion, water adsorption and water dissociation. Energies are in eV.

	This work	Hansen et al.[3]	Molinari et al.[5]
XC functional	PBE+U U_{eff}=4.5 eV	PBE+U U_{eff}=3.0 eV	PBE+U U_{eff}=5 eV
Subsurface Vo	1.81	2.42	/
Surface Vo	2.18	2.78	2.01
Vo diffusion barrier	0.65	0.50	/
H_2O adsorption	-0.79	-0.68	-0.82
OH decomposition barrier	3.40	2.93	/
Irreversible water splitting: $H_2O \rightarrow \frac{1}{2}O_2 + H_2$	2.53	2.52	/

Table S3. The average charge on H, O and Ce in different reduced ceria surfaces with oxygen vacancies, hydroxyls or mixed vacancy-hydroxyl.

Atom	slab	$V_O^{subsurface}$	$V_O^{surface}$	2OH	2OH+ $V_O^{subsurface}$	2OH+ $V_O^{surface}$	4OH	4OH+ $V_O^{subsurface}$	4OH+ $V_O^{surface}$
H	/	/	/	-0.23	-0.14	-0.19	-0.22	-0.23	-0.16
O	1.28	1.25	1.26	1.24	1.23	1.24	1.22	1.24	1.23
Ce	-2.50	-2.44	-2.45	-2.45	-2.38	-2.40	-2.40	-2.35	-2.34

Table S4. The average charge on H, O, Ce and Gd in different reduced GDC-Type1 surfaces with oxygen vacancies, hydroxyls or mixed vacancy-hydroxyl.

Atom	slab	$V_O^{subsurface}$	$V_O^{surface}$	2OH	2OH+ $V_O^{subsurface}$	2OH+ $V_O^{surface}$	5OH	5OH+ $V_O^{subsurface}$	5OH+ $V_O^{surface}$
H	/	/	/	-0.19	-0.21	-0.18	-0.17	-0.15	-0.15
O	1.18	1.25	1.24	1.23	1.25	1.24	1.22	1.24	1.23
Ce	-2.44	-2.47	-2.48	-2.50	-2.46	-2.43	-2.48	-2.40	-2.45
Gd	-1.80	-2.03	-1.94	-1.89	-2.01	-2.01	-1.81	-2.04	-1.61

Table S5. The average charge on H, O, Ce and Gd in different reduced GDC-Type2 surfaces with vacancies, hydroxyls or mixed vacancy-hydroxyl.

Atom	slab	$V_O^{subsurface}$	$V_O^{surface}$	2OH	2OH+ $V_O^{subsurface}$	2OH+ $V_O^{surface}$	5OH	5OH+ $V_O^{subsurface}$	5OH+ $V_O^{surface}$
H	/	/	/	-0.25	-0.20	-0.22	-0.18	-0.24	-0.21
O	1.19	1.21	1.23	1.20	1.23	1.23	1.19	1.23	1.20
Ce	-2.42	-2.46	-2.46	-2.42	-2.42	-2.42	-2.39	-2.36	-2.36
Gd	-2.06	-2.02	-2.01	-2.09	-2.04	-2.04	-1.90	-1.83	-1.79

Discussions of the relative stability of $V_O^{subsurface}$ and $V_O^{surface}$ in CeO_2(111) with and without Gd doping at different hydroxyl coverages:

As presented in Figure 2 in the manuscript, at hydroxyl coverage (θ_H) lower than 0.5, the curves for E_{Vo}, the formation energy for $V_O^{subsurface}$ and $V_O^{surface}$ in ceria, Type1 GDC and Type2 GDC, show similar trends. In addition, the difference between $E(V_O^{subsurface})$ and $E(V_O^{surface})$ in ceria, Type1 GDC and Type2 GDC is very low. However, the energy differences between them in ceria and GDC-Type1 become larger at $\theta_H > 0.5$. Vacancies in the surface or subsurface layer are unstable relative to the bulk at these high hydroxyl coverages, because of the strong repulsion between oxygen vacancies and hydroxyls. Increased absolute charges on H, O and Ce ions indicate stronger repulsion between oxygen vacancies and hydroxyls as noticed from **Tables S3-S5**. Therefore, the increased absolute charges on ions indicates the lower stability of the

hydroxyl-vacancy phase, which explains the relative stability of $V_O^{subsurface}$ and $V_O^{surface}$ created in hydroxylated surfaces as shown in Figure 2 in the manuscript.

Take $\theta_H = 0.83$ for example (a surface with 5OH), the formation of $V_o^{surface}$ and $V_o^{subsrface}$ is unfavorable in Type1 GDC, compared to Vo formation in Type2 GDC. This is because increased absolute charge is found on the O, H, Ce and Gd when creating one V_o in the 5OH covered GDC-Type1 compared with creating one V_o in the 5OH covered GDC-Type2 as shown in **Tables S4 and S5**. This indicates stronger repulsion between the hydroxylated GDC-Type1 and the V_o and thus more unfavorable formation of the V_o in the GDC-Type1 at $\theta_H = 0.83$.

For both GDC-Type1 and GDC-Type2, increased absolute charge on ions is found in $V_o^{subsrface}$ than in $V_o^{surface}$ as shown in **Tables S4 and S5**, indicating the relatively instability of the $V_o^{subsrface}$ in the hydroxylated GDC-Type1, compared with the $V_o^{surface}$.

Therefore, the relative stability of the subsurface and surface O vacancy on CeO_2 with and without Gd doping at different hydroxyl coverage can be attributed to the relative repulsion between vacancies and hydroxyls based on the Bader charge analysis.

Methods for Calculation of free energies of the reduced surface:

In order to calculate the free energy of surfaces with different coverage of oxygen vacancies and hydrogen, we assume the surface is in equilibrium with reservoirs of water and oxygen molecules. The same method has been used in our previous work[3]. A surface with N_H excess H atoms and N_{VO} excess oxygen vacancies can be formed via the reaction between H_2O and vacancies at the reference surface "slab(0 H, 0 V_O)" as follows:

$$\text{slab}(0,0) + \frac{N_H}{2} H_2O \leftrightarrow \text{slab}(N_H, N_{Vo}) + (\frac{N_H}{4} + \frac{N_{Vo}}{2}) O_2$$

The free energy of the reduced ceria with two hydroxyl groups (2H) is calculated as follows:

$$\Delta G(2H) = E(2H) - E(0,0) + \frac{1}{2} E(O_2) - E(H_2O) + \Delta\Delta G(2H)$$

Where E(2H), E(0,0), E(O_2) and E(H_2O) are the calculated DFT energies.

$$\Delta\Delta G(2H) = F_{vib}(2,0) - F_{vib}(0,0) + \frac{1}{2}(\mu_{O2}(\rho^0, T) + kB\,T \ln(\rho_{O2}/\rho^0) + ZPE_{O2}) - (\mu_{H2O}(\rho^0, T) + kB\,T \ln(\rho_{H2O}/\rho^0) + ZPE_{H2O})$$

Where $F_{vib} = \sum_i {}^1/_2\, h\nu_i + \sum_i K_B T \ln(1 - \exp(h\nu_i/(K_B T))$ is the vibrational free energy of a slab. It is approximated from the harmonic vibrational frequencies ν_i. $F_{vib}(2,0)$ is the vibrational free energy of a surface with two hydroxyl groups. ZPE is the zero point energy. $\mu_{O2}(\rho^0, T)$ and $\mu_{H2O}(\rho^0, T)$ is the free energy of O_2 and H_2O at temperature T and standard pressure.

The free energy of the reduced ceria with one oxygen vacancy is:

$$\Delta G(\mathrm{Vo}) = \mathrm{E(Vo)} - \mathrm{E}(0,0) + \frac{1}{2}\mathrm{E}(\mathrm{O_2}) + \Delta\Delta\mathrm{G(Vo)}$$

Where $\Delta\Delta G(\mathrm{Vo}) = F_{vib}(0,1) - F_{vib}(0,0) + \frac{1}{2}(\,\mu_{O2}(\rho^0, T) + \mathrm{kB\ T\ ln}\,(\rho_{O2}/\rho^0) + \mathrm{ZPE_{O2}})$

For any (N_H, N_{Vo}) surface, the formation free energy $\Delta G(\mathrm{N_{H,}\ N_{V_o}})$ can be expressed based on $\Delta\Delta G(Vo)$ and $\Delta\Delta G(2H)$:

$$\Delta G(\mathrm{N_{H,}\ N_{V_o}}) = \Delta E(\mathrm{N_{H,}\ N_{V_o}}) + \Delta\Delta G(\mathrm{N_{H,}\ N_{V_o}})$$

Where $\Delta\Delta G(N_H,N_{VO}) = F_{vib}(N_H, N_{VO}) - F_{vib}(0,0) + ½\,(N_{VO} + ½\,N_H)(\,\mu_{O2}(p^0, T) + k_B T \ln\,(p_{O2}/p^0) + ZPE_{O2}) - ½\,NH\,(\mu_{H2O}(p^0,T) + k_B T \ln(p_{H2O}/p^0) + ZPE_{H2O})$

$$= \frac{1}{2}\,\mathrm{N_H}\,(\,\mathrm{F_{vib}}(2,0) - \mathrm{F_{vib}}(0,0)\,) + \mathrm{N_{Vo}}\,(\,\mathrm{F_{vib}}(0,1) - \mathrm{Fvib}(0,0)\,) + \mathrm{F_{vib}}(0,0) - \mathrm{F_{vib}}(0,0)$$
$$+ \frac{1}{2}(\mathrm{N_{Vo}} + 1/2\mathrm{N_H})(\mu_{O2}(\rho^0, T) + \mathrm{kB\ T\ ln}\,(\rho_{O2}/\rho^0) - 1/2\mathrm{N_H}(\mu_{H2O}(\rho^0, T)$$
$$+ \mathrm{kB\ T\ ln}\,(\rho_{H2O}/\rho^0) + \mathrm{ZPE_{H2O}})$$

$$= \frac{1}{2}N_H\left[\mathrm{F_{vib}}(2,0) - \mathrm{F_{vib}}(0,0) + \frac{1}{2}(\mu_{O2}(\rho^0, T) + \mathrm{kB\ T\ ln}\,(\rho_{O2}/\rho^0)\right.$$
$$\left. - (\mu_{H2O}(\rho^0, T) + \mathrm{kB\ T\ ln}\,(\rho_{H2O}/\rho^0\,)\right]$$
$$+ \mathrm{N_{Vo}}\left[\mathrm{F_{vib}}(\mathrm{Vo}) - \mathrm{F_{vib}}(0,0) + \frac{1}{2}(\mu_{O2}(\rho^0, T) + \mathrm{kB\ T\ ln}\,(\rho_{O2}/\rho^0)\right]$$

$$= \frac{1}{2}\mathrm{N_H}\Delta\Delta\mathrm{G(2H)} + \mathrm{N_{Vo}}\Delta\Delta\mathrm{G(Vo)}$$

Then, any $\Delta G(\mathrm{N_{H,}\ N_{V_o}})$ can be calculated by using $\Delta\Delta\mathrm{G(2H)}$ and $\Delta\Delta\mathrm{G(Vo)}$ terms:

$$\Delta G(N_{H,}\ N_{V_o}) = \Delta E(N_{H,}\ N_{V_o}) + \Delta\Delta G(N_{H,}\ N_{V_o})$$
$$= \Delta E(\mathrm{N_{H,}\ N_{V_o}}) + \frac{1}{2}\mathrm{N_H}\Delta\Delta\mathrm{G(2H)} + \mathrm{N_{Vo}}\Delta\Delta\mathrm{G(Vo)}$$

The value of $\Delta\Delta\mathrm{G(2H)}$ and $\Delta\Delta\mathrm{G(Vo)}$ at different temperature is obtained from the previous works[3] as shown in **Table S6**.

Table S6. Free energy corrections for 2H and Vo at different temperature and standard pressure

Temperature/K	400	700	800	1000	1200
$\Delta\Delta G(2H)$/eV	0.30	0.60	0.70	0.85	1.03
$\Delta\Delta\mathrm{G(subVo)/eV}$	-0.30	-0.60	-0.70	-0.85	-1.03

References

(1) Ganduglia-Pirovano, M. V.; Da Silva, J. L. F.; Sauer, J. Density-Functional Calculations of the Structure of near-Surface Oxygen Vacancies and Electron Localization on CeO_2(111). *Phys. Rev. Lett.* **2009**, *102* (2), 1–4.

(2) Su, Y. Q.; Filot, I. A. W.; Liu, J. X.; Tranca, I.; Hensen, E. J. M. Charge Transport over the Defective CeO_2(111) Surface. *Chem. Mater.* **2016**, *28* (16), 5652–5658.

(3) Hansen, H. A.; Wolverton, C. Kinetics and Thermodynamics of H_2O Dissociation on Reduced CeO_2(111). *J. Phys. Chem. C* **2014**, *118* (47), 27402–27414.

(4) Fernández-Torre, D.; Carrasco, J.; Ganduglia-Pirovano, M. V.; Pérez, R. Hydrogen Activation, Diffusion, and Clustering on CeO_2(111): A DFT+ U Study. *J. Chem. Phys.* **2014**, *141* (1).

(5) Molinari, M.; Parker, S. C.; Sayle, D. C.; Islam, M. S. Water Adsorption and Its Effect on the Stability of Low Index Stoichiometric and Reduced Surfaces of Ceria. *J. Phys. Chem. C* **2012**, *116* (12), 7073–7082.

B.2 Paper 2

Improved Electrocatalytic Water Splitting Reaction on CeO_2(111) by Strain Engineering: A DFT+*U* Study

Tiantian Wu, Tejs Vegge, Heine Anton Hansen

ACS Catalysis 2019, 9, 4853−4861

ACS Catalysis

Research Article

Cite This: ACS Catal. 2019, 9, 4853−4861

pubs.acs.org/acscatalysis

Improved Electrocatalytic Water Splitting Reaction on CeO_2(111) by Strain Engineering: A DFT+*U* Study

Tiantian Wu, Tejs Vegge, and Heine Anton Hansen*

Department of Energy Conversion and Storage, Technical University of Denmark, Fysikvej, 2800 Kgs. Lyngby, Denmark

Supporting Information

ABSTRACT: Ceria is a promising cathode material in solid oxide electrolysis cells (SOECs) because ceria can become a mixed electronic and ionic conductor through doping, which enables a high surface area for electrocatalysis. Here, we systemically investigate the effect of strain on the electrocatalytic water splitting reaction (WSR) for renewable hydrogen production on CeO_2(111) by using density functional theory corrected for on-site Coulomb interactions (DFT+*U*). We find that tensile strain stabilizes the reduced states of ceria such as oxygen vacancies and surface hydroxyls, while compressive strain destabilizes the reduced states. These trends are explained by a downshift of the Ce 4f orbital energy under tensile strain and agree with the larger size of the Ce^{3+} ion in comparison to the Ce^{4+} ion. Our results show that hydroxyl decomposition into H_2 has the highest activation energy along the WSR pathway (E_a) and that the free energy of hydroxyl formation (ΔG_H) prior to hydroxyl decomposition can act as a thermodynamic barrier to the WSR. Compressive strain (<−3.0%) correlates strongly with increased WSR activity on CeO_2(111) because it reduces the total barrier ($\Delta G_H + E_a$). Strain also effectively engineers the reaction pathway of the WSR at T > 1000 K. By a comparison of the total reaction barrier on different hydroxylated surfaces, the WSR is found to proceed readily via a Ce−H intermediate on excessively hydroxylated CeO_2(111) under tensile strain because of the lower barrier, while the WSR proceeds preferentially and readily on the partially or fully hydroxylated CeO_2(111) under compressive strain. In addition, a direct mapping between the most efficient WSR pathway and strain at different operating temperatures provides a better understanding of the efficient WSR on the CeO_2(111) facet by strain engineering, which sheds light on electrocatalysis on oxide catalysts.

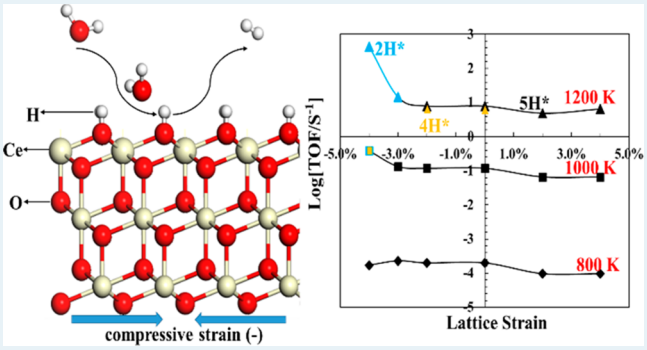

KEYWORDS: *sustainable hydrogen production, ceria, strain effect, DFT simulations, descriptor analysis*

INTRODUCTION

Production of clean fuel with zero carbon emissions can be facilitated by sustainable production of hydrogen.[1,2] The electrocatalysis of the WSR powered by renewable energy (such as wind energy and solar energy) provides a promising approach to achieve this goal.[1,2] In comparison to low-temperature electrolysis cells, SOECs may efficiently reduce water to hydrogen at low overpotentials by utilization of waste heat at higher temperatures.[3−5] However, electrodes in SOECs are mechanically unstable because of cracking at the triple-phase boundaries (TPBs) among the gas channels, the solid electrolyte, and the electrode.[4,6] The important scientific challenge for achieving renewable hydrogen production in SOECs is to develop an earth-abundant, stable, and active catalyst, which can extend the WSR from the limiting TPBs to a two-phase boundary with a much wider surface area and promote the WSR.

As a good mixed ionic and electronic conductor, ceria (CeO_2) has been widely used in many catalytic processes not only as a support but also as an efficient active component in redox reactions such as oxygen storage in three-way catalysts,[7−9] the water-gas shift reaction,[10−12] and production of fuels using solar thermochemical cycles.[13,14] Ceria has also attracted significant interest among the identified materials for electrocatalysis of the WSR in SOECs due to several superior properties: (i) the ceria/gas interface is accessible to both ionic and electronic carriers as well as gas molecules, which can extend the reaction zones from the TPBs to a two-phase (ceria/gas) boundary[15,16] and (ii) the fast ionic conductivity facilitates the reaction activity of ceria. The reactions associated with H_2 production and H_2O splitting on ceria have been studied extensively, demonstrating that the catalytic behavior of ceria can be influenced by its mixed-valence Ce^{3+}/Ce^{4+} redox states, the mobility of oxygen ions (oxygen vacancy diffusion),[3,17,18] and the positive entropy contribution that is associated with the $f^0 \rightarrow f^1$ transition.[19]

Electrocatalysis of the WSR on ceria includes several steps:[3] oxygen vacancy diffusion to the surface, water adsorption near the oxygen vacancy (V_O), water dissociation into hydroxyls

Received: January 16, 2019
Revised: April 2, 2019
Published: April 18, 2019

DOI: 10.1021/acscatal.9b00203
ACS Catal. 2019, 9, 4853−4861

($H_2O_{ads} + 2Ce^{3+} + V_O + O^{2-} \rightarrow 2OH^- + 2Ce^{3+}$), and finally hydroxyl decomposition to release hydrogen ($2OH^- + 2Ce^{3+} \rightarrow H_2 + 2Ce^{4+} + 2O^{2-}$). On excessively hydroxylated ceria, however, water dissociation and release of H_2 might involve the formation of a Ce−H intermediate ($H_2O_{ads} + 2Ce^{3+} + V_O \rightarrow OH^- + Ce^{4+} + Ce^{4+}H^- \rightarrow H_2 + 2Ce^{4+} + O^{2-}$).[17] Both theoretical and experimental studies have found OH species[17,20] play an important role in limiting the WSR activity in ceria-based catalysis and demonstrated that the rate-determining step (RDS) of the WSR on ceria is associated with the oxidation of Ce^{3+} to Ce^{4+} during hydroxyl decomposition into H_2.[3,17]

To overcome the limitations of hydroxyl decomposition, strain engineering is a promising approach due to its significant influence on the local atomic structure and chemical reactivity.[21−26] Because the variation of strain is an unavoidable consequence during the fabrication of nanostructured ceria and ionic incorporation into ceria, the strain effect on ceria has been widely reported,[25−33] although the focus has mostly been on oxygen formation and oxygen ionic transport.[27−33] Even though impressive progress has been made in understanding reaction pathways and the reaction mechanism for the WSR on ceria,[17,19,20] a fundamental understanding of the effect of strain on the reaction kinetics and the formation of intermediates (such as oxygen vacancies, hydroxyls, and their mixed phase) that determines the reaction pathways remains unclear. Here, the effect of strain on the formation of oxygen vacancies, hydroxyls, and oxygen−hydroxyl mixed phases on $CeO_2(111)$ as well as the effect on the activation barriers for oxygen vacancy diffusion, water dissociation into hydroxyls, and the following hydroxyl decomposition is systematically investigated by performing DFT+U calculations. In addition, we provide a direct mapping between the most efficient WSR pathway and strain at operating temperature. Our investigations provide insights into the strain effect on the thermodynamics of WSR intermediates and reaction kinetics.

METHODS

Spin-polarized DFT calculations were performed using the Vienna ab initio simulation package (VASP),[34,35] with the Perdew−Burke−Ernzerhof (PBE) functional.[36] The ionic cores are described by the projector augmented wave method (PAW),[37] and the wave functions are expended in plane waves with an energy cutoff of 550 eV. The exchange and correlation are approximated including aspherical gradient corrections within the PAW augmentation spheres (using standard PAW potentials). We use the DFT+U approach[38] to describe electron localization on the 4f states of the reduced cerium atoms. The value of the effective Hubbard U term used in this work is 4.5 eV, which has been an appropriate correction to ensure electron localization on Ce^{3+}.[39−44] On the other hand, lower values of U appear to be required to match experimental reduction and CO adsorption energies.[45,46]

Using a dense Γ-centered 8 × 8 × 8 k-point mesh, the calculated bulk equilibrium lattice constant of ceria is 5.497 Å, which is quite consistent with both theoretical (5.497 Å[26,27,42,47]) and experimental values (5.411 Å[48]). The Γ-centered 8 × 8 × 8 k-point mesh is also used to calculate lattice constants of doped ceria, Ce_3MO_8, where M = Al, Ga, Ni, Pb, Pr, Gd, La. The $CeO_2(111)$ surface ($Ce_{12}O_{24}$) is built as a 2 × 2 repeating surface unit cell consisting of three O−Ce−O atomic layers, as shown in Figure 1. The O−Ce−O atomic layer at the bottom is kept fixed in the bulk geometry. We introduce a vacuum layer with a thickness of 15 Å to reduce interaction between periodic images. Both compressive (−) and tensile (+) lattice strains are applied in the $CeO_2(111)$ plane. The Ce−O bond lengths of strained and unstrained $CeO_2(111)$ agree well with values reported by Capdevila-Cortada et al.,[26] as shown in Table S1 in the Supporting Information. A Γ-centered 3 × 3 × 1 k-point mesh was used for optimization of all surfaces. Densities of states were recalculated using a Γ-centered 13 × 13 × 1 k-point mesh.

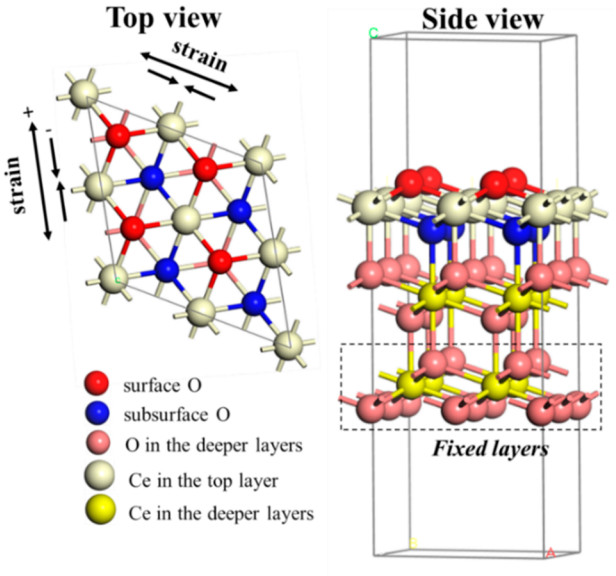

Figure 1. Atomic structure of the $CeO_2(111)$ model slab.

For the identification of transition states and activation energies for oxygen vacancy diffusion, water dissociation into hydroxyls, and hydroxyl decomposition releasing H_2, we use the climbing image nudged-elastic band method as implemented in VASP[49] with a tolerance of 0.03 eV /Å.

RESULTS AND DISCUSSION

The reaction among water, oxygen vacancies, and lattice oxygen is strongly exothermic on unstrained ceria[17,43,50,51]

$$H_2O_{ads} + 2Ce^{3+} + V_O + O^{2-} \rightarrow 2OH^- + 2Ce^{3+}$$

while the hydroxyl decomposition to H_2 has a high kinetic barrier[17]

$$2OH^- + 2Ce^{3+} \rightarrow H_2 + 2Ce^{4+} + 2O^{2-}$$

However, on excessively hydroxylated ceria (above 1 monolayer of H*), surface oxygen anions (O^{2-}) are unavailable and H_2O molecules dissociating on oxygen vacancies react with either subsurface O^{2-} or surface Ce, through e.g.[17]

$$H_2O_{ads} + 2Ce^{3+} + V_O \rightarrow OH^- + Ce^{4+} + Ce^{4+}H^-$$

which is expected to significantly alter the thermodynamics of the WSR. We therefore consider the WSR on partially (2H*), fully (4H*, 1 monolayer of H*), and excessively (5H*, above 1 monolayer of H*) hydroxylated $CeO_2(111)$ under strain in the following.

Strain Effect on the Formation of Reduced $CeO_2(111)$. The most likely reaction pathways via 2H*, 4H*, or 5H* surface structures include creating one oxygen vacancy in the subsurface (V_O^{sub}), which then moves to the surface (V_O^{sur}), followed by water adsorption, hydroxyl formation, and hydrogen desorption through pathways presented in Figure 2. Along these reaction

DOI: 10.1021/acscatal.9b00203
ACS Catal. 2019, 9, 4853−4861

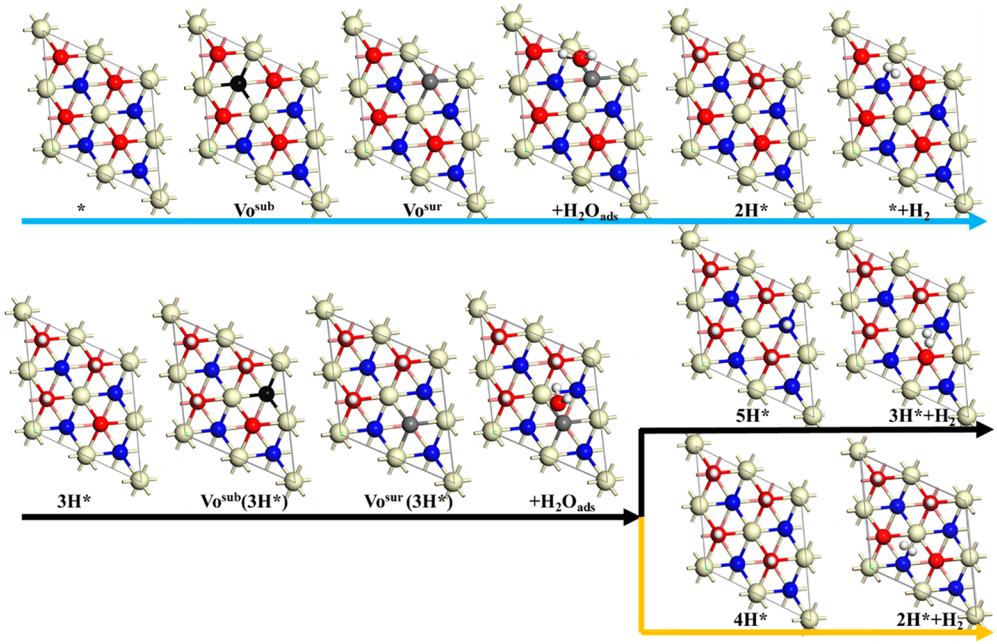

Figure 2. Schematic illustration of the hydrogen formation on the partially (2H*), fully (4H*), and excessively (5H*) hydroxylated $CeO_2(111)$. 3H* represents that the surface is reduced by three hydroxyls (3/4 monolayer hydroxyl). $V_O^{sub}(3H^*)$ and $V_O^{sur}(3H^*)$ represent one oxygen vacancy in the subsurface and in the top surface of the 3H* surface, respectively. Black and gray spheres show the oxygen vacancies in the subsurface and top surface, respectively.

pathways, the ability to create an oxygen vacancy plays an important role in the further formation of the reduced $CeO_2(111)$ for electrocatalysis of the WSR. As noted in Figure S1 (the locations of Ce^{3+} in defected ceria are presented in Figure S2 and Table S2 in the Supporting Information), creating an oxygen vacancy in the top surface and in the subsurface of pure $CeO_2(111)$ is facile in comparison to creating vacancies in hydroxylated $CeO_2(111)$. When the surface is covered by three hydroxyls (3/4 monolayer of hydroxyl), the oxygen vacancies in the subsurface of the expansively strained $CeO_2(111)$ is very unstable in comparison to the oxygen vacancies created in bulk ceria. The formation energy of creating an oxygen vacancy in the unstrained or compressively strained $CeO_2(111)$ follows the order $V_O^{sub} < V_O^{sur} < V_O^{sur}(3H^*) < V_O^{sub}(3H^*)$. In addition, the formation energy of these oxygen vacancies decreases gradually as the lattice strain is increased, consistent with the findings of Ma et al.[28] Under tensile strain, creating one oxygen vacancy becomes much easier in hydroxylated $CeO_2(111)$ in comparison to that under compressive strain. These findings indicate that, due to the difficult formation of the oxygen vacancy−hydroxyl mixed phases, the formation of fully and excessively hydroxylated $CeO_2(111)$ requires more energy than the formation of partially hydroxylated $CeO_2(111)$.

In Figure 3a, we show the average hydrogen adsorption energy (E_H) at different hydrogen coverages (θ_H) on strained $CeO_2(111)$. For coverages up to one monolayer, hydrogen adsorption results in formation of surface hydroxyl and is exothermic. However, the hydrogen adsorption energy when hydroxyls are formed on $CeO_2(111)$ increases dramatically as the hydrogen coverage increases from 1.0 to 1.25, where the surface model now has either five hydroxyls in total by forming an unstable subsurface hydroxyl or a Ce−H moiety in the surface. In addition, E_H at each hydrogen coverage decreases as the lattice strain increases. When the lattice is expanded by 4.0%, E_H decreases significantly, and the formation of the excessively hydroxylated $CeO_2(111)$ becomes as facile as that of the partially hydroxylated $CeO_2(111)$ under no strain. An analysis of the projected density of states shows a downshift of the Ce 4f band center of $CeO_2(111)$ under tensile strain (Figure S3), which in turn leads to higher stability of electrons localized on Ce 4f orbitals in expansively strained ceria. Thus, it is easier to form reduced ceria by creating oxygen vacancies or formation of hydroxyls as the lattice expands. The easier reduction of ceria under tensile strain also agrees with the larger size of the Ce^{3+} ion in comparison to the Ce^{4+} ion.

In addition, lattice strain effectively modifies the most stable configuration of the excessively hydroxylated $CeO_2(111)$, as shown in Figure 3b. As an important intermediate in the hydrogen production along the highly H covered pathway, the excessively hydroxylated $CeO_2(111)$ has two possible configurations: (i) H binding to a Ce atom in the top surface (Ce−H)[17,52] or (ii) H binding to an oxygen atom in the subsurface (subO−H), as shown in Figure 3c. For unstrained $CeO_2(111)$, the average hydrogen adsorption energy in the subO−H is about 0.16 eV more negative than in the Ce−H. The energy difference between the two configurations increases with an increase in the tensile strain. In contrast, the energy difference between the Ce−H and subO−H becomes smaller with increasing compressive strain. As the surface is compressed by 4.0%, Ce−H rather than subO−H is the most stable configuration of the excessively hydroxylated $CeO_2(111)$, which indicates that Ce−H is a likely intermediate for hydroxyl decomposition on excessively hydroxylated $CeO_2(111)$. The strain effects on the formation of the most stable 5H* may further adjust the hydroxyl decomposition via the Ce−H pathway. Hydrogen formation via a Ce−H intermediate has been reported to have a low reaction barrier and might provide an efficient reaction pathway for the WSR on ceria surfaces.[17] The choice of the *U* value affects the H chemisorption energy on ceria.[53] We recently showed that reducing the *U* value from 4.5 to 3 eV could stabilize Ce−H by

DOI: 10.1021/acscatal.9b00203
ACS Catal. 2019, 9, 4853−4861

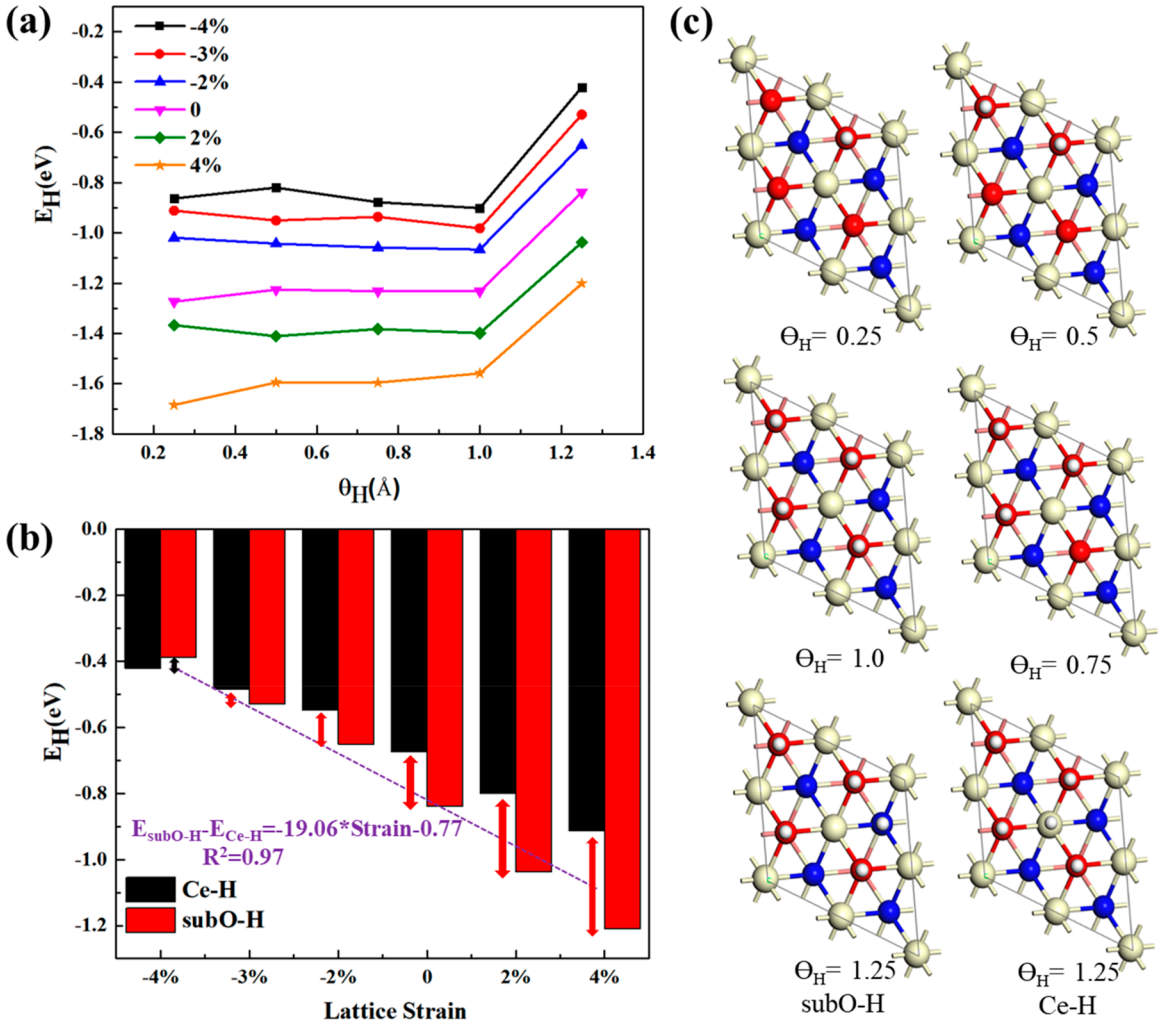

Figure 3. (a) Average hydrogen adsorption energy (E_H) on strained CeO_2(111) as a function of hydrogen coverage Θ_H. (b) Comparison between the E_H values of Ce−H and subsurface hydroxyl (subO-H) at Θ_H = 1.25 under different lattice strains. (c) Top views of the hydroxyls on CeO_2(111) under different hydrogen coverages.

about 0.6 eV relative to subO−H on unstrained CeO_2(111),[43] which indicates that Figure 3b possibly overestimates the strain required for Ce−H to become more stable than subO−H.

Therefore, strain effectively regulates the formation of reduced CeO_2(111) and the most stable intermediates during the WSR, which may influence the kinetics of each reaction step along partially, fully, and highly H covered pathways.

Strain Effect on the Reaction Barriers at Each Reaction Step during the WSR on Reduced CeO_2(111). Using DFT +*U*-based NEB calculations, we determine the activation energy for oxygen vacancy diffusion, water dissociation, and hydroxyl decomposition along partially, fully, and excessively hydroxylated pathways under different lattice strains (the Ce^{3+} locations are presented in Figure S2 and Table S2). There is a strong strain dependence of the barriers for oxygen vacancy diffusion from its most stable subsurface position to the most stable top surface position, as presented in the Figure 4. The diffusion of the oxygen vacancy becomes more facile as the lattice expands, likely because of the larger space available for the diffusing oxygen ion. The efficient strain control of the ionic conductivity in ceria also gives insight into the fast ionic diffusion in doped ceria, where local tensile strain is realized.

The following step of water dissociation on the reduced CeO_2(111) is very facile, with no barrier along the partially[17,43,54] and fully hydroxylated pathways[17,43] and about a 0.25 eV barrier along the excessively hydroxylated pathway under >−3.0% strain. However, the water dissociation has an activation barrier larger than 1.0 eV as the lattice is compressed by more than 3.0% because the hydrogen binding to subsurface O becomes weak (cf. Figure 3b). It has been reported that the oxygen vacancies favor the formation of hydridic H species via H_2 dissociation on ceria, where H^- occupies the vacant O lattice positions.[55] By comparison, we find the presence of an oxygen vacancy in ceria favors the formation of OH via water dissociation, where OH from H_2O is easily accommodated in the vacant O position. Our previous results show that hydroxyl−oxygen mixed configurations like $2H^*+V_O$ or $3H^*+V_O$ are unstable intermediates during the WSR,[17] which easily react with adsorbed H_2O to form 4H* or 5H*, respectively, where H_2O dissociating on oxygen vacancies reacts with either subsurface O^{2-} or surface Ce when the surface is fully hydroxylated.[17,43]

In contrast, the activation barrier for the hydroxyl decomposition, the RDS during the WSR,[3,17] is regulated differently by strain. First, we have compared the different locations of the Ce^{3+} ions around the hydroxyls: e.g., 2H*. We found that the configuration of 2H* with Ce^{3+} as the nearest neighbor to the adsorbed H has the most stable Ce^{3+}

DOI: 10.1021/acscatal.9b00203
ACS Catal. 2019, 9, 4853−4861

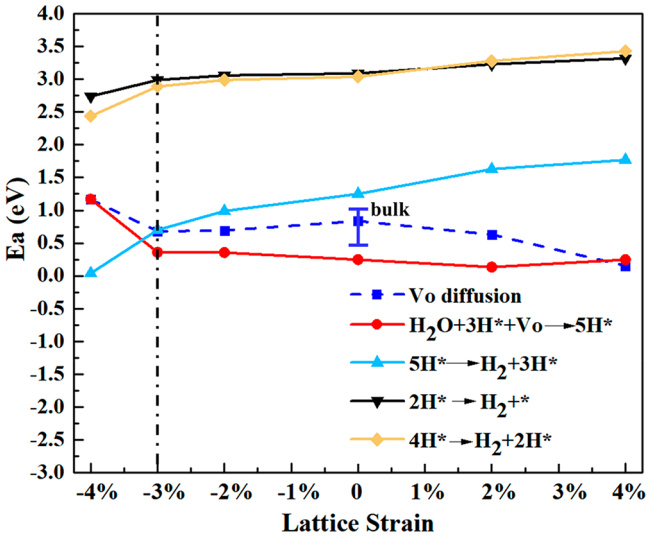

Figure 4. Reaction barriers for oxygen vacancy diffusion from the most stable subsurface position to the most stable top surface position and the formation of 5H* via water dissociation (H_2O_{ads} + 3H* + V_O → 5H*) as well as hydroxyl decomposition on the partially (2H* → H_2 + *), fully (4H* → H_2 + 2H*), and excessively (5H* → H_2 + 3H*) hydroxylated CeO_2(111) under different lattice strains. The calculated diffusion barrier of an oxygen vacancy in unstrained ceria is compared to reported barriers in bulk ceria (0.46−1.08 eV).[57] The water dissociation on the partially and fully hydroxylated CeO_2(111) has negligible activation energy.

configuration, as shown in Table S3 in the Supporting Information. That the relative stability of adsorbed H on ceria strongly depends on the Ce^{3+} locations agrees well with previously reported findings.[53] However, we find the same transition state energy for H_2 formation on the 2H* surfaces with different Ce^{3+} locations, as shown in Figure S4 in the Supporting Information. The highest and lowest energy along the 2H* pathway is therefore independent of the Ce^{3+} locations immediately before the hydroxyl decomposition into H_2. The activation energy for hydroxyl decomposition on the partially, fully, and excessively hydroxylated CeO_2(111) increases as the lattice expands, which arises from the stabilization of hydroxylated CeO_2(111) under tensile strain, as shown in Figure 3. As we can see from Figure 4, the WSR over the fully hydroxylated CeO_2(111) has strong similarities to the hydroxyl formation and decomposition on the partially hydroxylated CeO_2(111).[17] A significant drop in the activation energies for hydroxyl decomposition on the excessively hydroxylated CeO_2(111) when the lattice is compressed by more than 3% is noted from Figure 4, because the most stable intermediate for hydrogen production changes from the subO−H to Ce−H by strain engineering. Our results are consistent with the notion that the activation energy for breaking the Ce−H bond is much easier than that of breaking an O−H bond during hydroxyl decomposition.[17] Therefore, because of the strain effects on the formation of the reduced CeO_2(111) by forming oxygen vacancies, hydroxyl−vacancy phases, or hydroxyls, the activation energies at each reaction step during the WSR on the reduced CeO_2(111) are correspondingly regulated by strain, which gives guidelines on how to reduce the reaction barrier at the RDS and improve the reaction efficiency of the WSR on ceria using strain engineering.

In addition, there exists a Brønsted−Evans−Polanyi (BEP)[56] scaling relationship (shown in Figure S5) between the activation energy of hydrogen formation, E_a, on the different hydroxylated CeO_2(111) surfaces and the reaction energy ($\Delta E = E_{FS} - E_{IS}$, the energy difference between the initial and the final states) because of the similar geometries of the initial and the transition states. As presented in Figures S6 and S7, the calculated E_a value for strained ceria also correlates with the lattice parameter, a, which is an experimentally accessible descriptor for the activation energy of the hydroxyl decomposition.

Strain Engineering of the Thermodynamics of the WSR on Reduced CeO_2(111). To calculate the relative free energy of the reduced CeO_2(111) along each reaction pathway, we use a DFT-based thermodynamics approach described in ref 17. First, the clean CeO_2(111) is chosen as the reference surface. Reduced CeO_2(111) surfaces then form via reactions between oxygen vacancies and water molecules at the referenced surface. In an SOEC, oxygen vacancies are produced at the anode by evolving oxygen. Oxygen vacancies then diffuse through the solid electrolyte to the cathode, where oxygen vacancies react with water to produce hydrogen through the WSR. The net reaction is the splitting of water into H_2 and O_2 driven by an external power source. The chemical potential of oxygen at the ceria cathode is chosen such that H_2O (1 bar) and oxygen vacancies are in equilibrium with H_2 (1 bar), which corresponds to the SOEC being at the equilibrium potential of the net reaction.

Here, we draw simplified free energy diagrams for hydroxyl decomposition on the partially (2H*), fully (4H*), and excessively (5H*) hydroxylated CeO_2(111) under different strains, at 800 (Figure 5), 1000 (Figure S8), and 1200 K (Figure S9). The free energies of intermediates and transition states for the full reaction pathways are given in Tables S4−S6. In addition, the free energies of 2H*, 4H*, and 5H* can be fitted by experimentally measurable descriptors such as temperature (T) and the lattice parameter (a), as shown in Figure S10.

As noted in Figure 5, in the unstrained system at 800 K, the activation barriers for the WSR on the partially, fully, and excessively hydroxylated CeO_2(111) are 3.04, 3.09, and 1.25 eV, respectively. The result shows that, under a certain strain, breaking the H bonding to the CeO_2(111) surface becomes easier as more hydroxyls form on the CeO_2(111) surface. The WSR via a Ce−H intermediate on the excessively hydroxylated CeO_2(111) requires the lowest activation energy, in comparison to the reactions on the partially and fully hydroxylated CeO_2(111). At 800 K, the most stable reduced state is the fully hydroxylated CeO_2(111), in comparison to which the formation of the partially and excessively hydroxylated CeO_2(111) is unfavorable.

To evaluate the turnover frequency (TOF) of the WSR, we use the energetic span model.[58,59] For each reaction path over the 2H*, 4H*, and 5H* surfaces, we identify the TOF-determining intermediate (TDI) and the TOF-determining transition state (TDTS), which are the states along the pathway which maximize the energetic span between the TDI and the TDTS. Consider as an example unstrained CeO_2(111) at 800 K, where the transition state for hydroxyl decomposition to H_2 on the 5H* surface has lower free energy than that on the 2H* and 4H* surfaces, which makes the transition state for the hydroxyl decomposition to H_2 on the 5H* surface the TDTS. On the other hand, the TDI occurs with the 4H* surface. The energetic span can then be approximated by $\delta E = E_a + \Delta G_H$, where E_a is the activation energy for hydroxyl decomposition, and $\Delta G_H = G_H - G^*$, where $G^* = \min(\{G_i\})$ is the free energy of the most stable reduced state of the ceria. In this way, the energetic span

DOI: 10.1021/acscatal.9b00203
ACS Catal. 2019, 9, 4853−4861

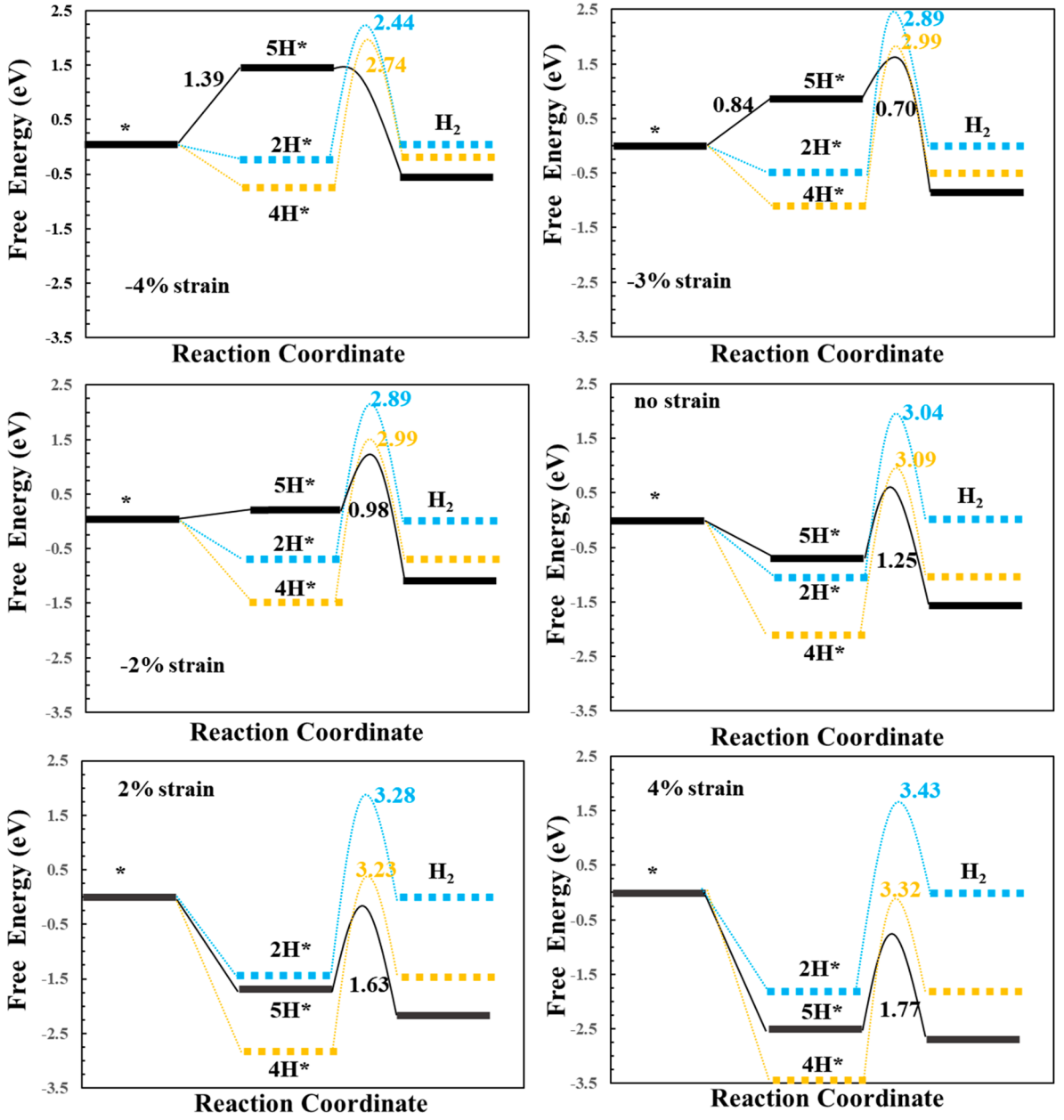

Figure 5. Simplified free energy diagrams for hydroxyl decomposition on the partially (2H*), fully (4H*), and excessively (5H*) hydroxylated $CeO_2(111)$ under different strains, at 800 K. The most efficient reaction pathway under each strain is highlighted by a solid line.

model includes the fact that an excessively hydroxylated surface, which has low activation energy for H_2 formation, is rather unlikely to form due to the low stability in comparison to the fully hydroxylated surface. Transition states for e.g. oxygen vacancy diffusion and water dissociation and reduced states with both oxygen vacancies and hydroxyl are included in the energy span analysis (see Tables S4−S6) but are left out of Figure 5 and Figures S8 and S9 for clarity.

By strain engineering, the activation barrier (E_a) for hydrogen production along each reaction pathway increases with increasing tensile strain, while E_a decreases with increasing compressive strain. The increase in stability of reduced ceria with tensile strain and the BEP relation for hydroxyl decomposition to H_2 explain this trend. The variation of ΔG_H for 2H* with strain follows the same trend as E_a, because formation of the 2H* happens through oxidation of more reduced surfaces such as 4H*. This oxidation becomes increasingly difficult with increasing tensile strain. However, the ΔG_H value of 5H* varies with strain in the opposite way, where ΔG_H decreases with increasing tensile strain and increases with increasing compressive strain (Table S7). The 5H* surface is formed by reduction of less reduced surfaces such as the 4H* surface, which again is facilitated by tensile strain. Thus, when the effect of strain on both E_a and ΔG_H is considered, the WSR proceeds preferentially through the 5H* surface at 800 and 1000 K. At 1200 K, the 5H* surface becomes very unstable, especially under compressive strain, and the formation of the 5H* surface becomes very difficult, leading to hydrogen production preferentially proceeding over the 2H* or 4H* structures under <−3% strain. Therefore, the preferred reaction pathway for the WSR on $CeO_2(111)$ can be controlled by engineering the strain of ceria because the strain affects the formation of hydroxyls.

DOI: 10.1021/acscatal.9b00203
ACS Catal. 2019, 9, 4853−4861

Overall, the fastest WSR is found at −4.0% strain, where it preferentially proceeds through the 5H* structure at 800 K. At 1000 and 1200 K, the reaction, however, proceeds more quickly through the 2H* or 4H* structures, as presented in Figures S8 and S9, respectively. The effect of temperature on the free energies of reduced $CeO_2(111)$ is synergistic with the effects of strain on the activation barriers for the WSR, contributing to the variations of the best pathway for the WSR on the $CeO_2(111)$.

A possible way to achieve compressed ceria surfaces could be through core−shell particles where a thin CeO_2 shell covers a suitably doped ceria core. The lattice constant of doped ceria largely decreases by incorporating ions with a radius smaller than that of Ce^{4+}, as shown in Figure S11, where the dopant ionic radius taken from the database of ionic radii[60] is compared to calculated lattice constants of doped ceria. A decrease in the lattice constant in doped ceria with decreasing dopant ionic radius is confirmed by experiments[61] and can be further decreased when the dopant concentration is increased.[62] Thus, using dopants with an ionic radius smaller than that of Ce^{4+} it is possible to reach <−3% compressive strain, which has great potential to increase the WSR activity on ceria. Doping the particle core with e.g. Ga^{3+} ions might lead to vacancy migration from the core to the particle surface, thereby setting up a dipole layer or space charge region. Although our theoretical model fixes the chemical potential of oxygen vacancies from the H_2−H_2O equilibrium, modifications of intermediate energies in response to the dipole layer are not included in the above treatment. However, vacancy migration from the bulk can be avoided by codoping with small, high-valence ions such as Nb^{5+}. Migration of dopants to the surface can directly influence catalytic activity,[63] and we previously showed that Gd dopants facilitate the formation of oxygen vacancies, hydroxyls, and hydridic H species at the rate-determining step.[43]

A direct mapping between the total free energy required for the WSR ($\Delta G_H + E_a$) and strain at different temperatures gives insights into electrocatalysis of the WSR by strain engineering, as presented in Figures S12 and S13 with corresponding data given in Table S7. The total energy span for the fastest WSR pathway increases (largely) as the strain increases, which on the other hand shows that compressive strain improves the reaction rate. At 800 and 1000 K, the WSR with the lowest free energy span proceeds through the excessively hydroxylated $CeO_2(111)$ surface, as shown in Figure S12. However, a significant drop in the free energy span under −3% strain at 1200 K is noted from Figure S12, where the most efficient reaction proceeds on the partially hydroxylated $CeO_2(111)$ because of a large increase in the required total free energy for the 4H* and 5H* pathways combined with a decrease in the energy span along the 2H* pathway as noted. In addition, Figure 6 shows the forward TOF of the WSR calculated by the energetic span model

$$\mathrm{TOF} = \frac{k_B T}{h} \exp\left(\frac{-\delta E}{k_B T}\right)$$

along the best pathway versus lattice strain at 800, 1000, and 1200 K. The WSR preferentially proceeds on the excessively hydroxylated $CeO_2(111)$ at 800 and 1000 K, while it proceeds readily on the partially or fully hydroxylated $CeO_2(111)$ under compressive strain at higher temperature (>1000 K). At high temperature, strain effectively determines the reaction pathway of the WSR. Our findings provide a direct mapping between experimentally accessible descriptors and kinetic parameters and help explain the WSR pathway under a given strain and operating temperature.

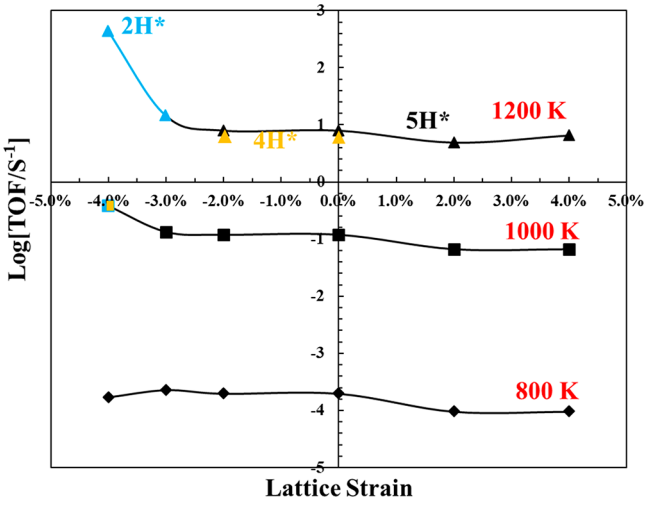

Figure 6. TOF of the WSR along the fastest pathway (the 2H*, 4H*, or 5H* path) versus lattice strain at 800, 1000, and 1200 K.

CONCLUSIONS

By using DFT+U calculations, we investigated the WSR on $CeO_2(111)$ as well as the effect of lattice strain on the formation of the intermediates, reaction barriers, and reaction pathways. It is found that the formation energy of oxygen vacancies, vacancy−hydroxyl phases, and hydroxyls decreases gradually as the lattice strain is increased because of downshifts of the Ce 4f band center, which provides a strong support for the strain engineering on the formation of intermediates during the WSR. Then the activation barriers at each reaction step during the WSR on the reduced $CeO_2(111)$ are correspondingly regulated because of the strain effects on the formation of the reaction intermediates. Strain effectively controls the formation of the Ce−H intermediate along the excessively hydroxylated pathway, which is proved to have a low reaction barrier for hydroxyl decomposition.

By studying the thermodynamics of the WSR on the reduced $CeO_2(111)$, we find that strain effectively adjusts the reaction pathway of the WSR at T > 1000 K. The WSR proceeds via a Ce−H intermediate on the excessively hydroxylated $CeO_2(111)$ under tensile strain. However, it proceeds preferentially and readily on the partially or fully hydroxylated $CeO_2(111)$ under compressive strain. In addition, the free energy of hydroxyl formation (ΔG_H) prior to hydroxyl decomposition can act as a thermodynamic barrier. The sum ($\Delta G_H + E_a$) of the hydroxyl formation energy (ΔG_H) and the activation barrier (E_a) for the hydroxyl decomposition at the RDS during the WSR determines the reaction rate of the hydrogen production on the strained and unstrained $CeO_2(111)$. Our findings show that compressive strain (<−3.0%) correlates strongly with increased WSR activity on $CeO_2(111)$ because of the reduction of $\Delta G_H + E_a$. $CeO_2(111)$ compressively strained by more than 3.0% has high activity for the WSR along the partially or fully hydroxylated pathways at 1200 K. Thus, incorporation of the ceria with carefully selected dopants, which facilitates the formation of excessively hydroxylated ceria (low ΔG_H) and has a stable metal−H intermediate (low E_a for hydrogen formation via a metal−H intermediate), is predicted to significantly improve the reaction efficiency of the WSR on the ceria.

DOI: 10.1021/acscatal.9b00203
ACS Catal. 2019, 9, 4853−4861

Therefore, our findings provide guides on how to improve the reaction efficiency of the WSR on $CeO_2(111)$ by strain engineering, which can be extended to electrocatalysis on other oxide catalysts.

■ ASSOCIATED CONTENT

Supporting Information

The Supporting Information is available free of charge on the ACS Publications website at DOI: 10.1021/acscatal.9b00203.

Formation energy of an oxygen vacancy as a function of lattice strain in comparison to the vacancy formation in bulk ceria, Ce^{3+} locations in reduced ceria, spin-polarized density of states projected on O 2p and Ce 4f orbitals, simplified free energy diagrams for hydroxyl decomposition on the partially, fully, and excessively hydroxylated $CeO_2(111)$ surfaces under different strains, at 1000 and 1200 K, energy span for the most efficient WSR, descriptor fits for the free energy of reduced ceria, BEP scaling relations for the hydroxyl decomposition pathways to form hydrogen on $CeO_2(111)$, and the correlation of E_a against experimentally accessible parameters (PDF)

■ AUTHOR INFORMATION

Corresponding Author

*H.A.H.: e-mail, heih@dtu.dk; tel, +45 45258211.

ORCID

Tejs Vegge: 0000-0002-1484-0284

Heine Anton Hansen: 0000-0001-7551-9470

Notes

The authors declare no competing financial interest.

■ ACKNOWLEDGMENTS

This work was supported by the Velux Foundations through the research center V-Sustain (grant number 9455).

■ REFERENCES

(1) Turner, J. A. Sustainable Hydrogen Production Processes. *Science* **2004**, *305*, 972−974.

(2) Holladay, J. D.; Hu, J.; King, D. L.; Wang, Y. An Overview of Hydrogen Production Technologies. *Catal. Today* **2009**, *139*, 244−260.

(3) Feng, Z. A.; El Gabaly, F.; Ye, X.; Shen, Z.-X.; Chueh, W. C. Fast Vacancy-Mediated Oxygen Ion Incorporation across the Ceria-Gas Electrochemical Interface. *Nat. Commun.* **2014**, *5*, 4374.

(4) Irvine, J. T. S.; Neagu, D.; Verbraeken, M. C.; Chatzichristodoulou, C.; Graves, C.; Mogensen, M. B. Evolution of the Electrochemical Interface in High-Temperature Fuel Cells and Electrolysers. *Nat. Energy* **2016**, *1*, 15014.

(5) Sapountzi, F. M.; Gracia, J. M.; Weststrate, C. J.; Fredriksson, H. O. A.; Niemantsverdriet, J. W. Electrocatalysts for the Generation of Hydrogen, Oxygen and Synthesis Gas. *Prog. Energy Combust. Sci.* **2017**, *58*, 1−35.

(6) Hauch, A.; Mogensen, M.; Hagen, A. Ni/YSZ Electrode Degradation Studied by Impedance Spectroscopy−Effect of $p(H_2O)$. *Solid State Ionics* **2011**, *192*, 547−551.

(7) Jen, H.-W.; Graham, G. W.; Chun, W.; McCabe, R. W.; Cuif, J.-P.; Deutsch, S. E.; Touret, O. Characterization of Model Automotive Exhaust Catalysts: Pd on Ceria and Ceria-Zirconia Supports. *Catal. Today* **1999**, *50*, 309−328.

(8) Oh, S.-H.; Hoflund, G. B. Chemical State Study of Palladium Powder and Ceria-Supported Palladium during Low-Temperature CO Oxidation. *J. Phys. Chem. A* **2006**, *110*, 7609−7613.

(9) Di Monte, R.; Kašpar, J. On the Role of Oxygen Storage in Three-Way Catalysis. *Top. Catal.* **2004**, *28*, 47−57.

(10) Bunluesin, T.; Gorte, R. J.; Graham, G. W. Studies of the Water-Gas-Shift Reaction on Ceria-Supported Pt, Pd, and Rh: Implications for Oxygen-Storage Properties. *Appl. Catal., B* **1998**, *15*, 107−114.

(11) Fu, Q.; Saltsburg, H.; Flytzani-Stephanopoulos, M. Active Nonmetallic Au and Pt Species on Ceria-Based Water-Gas Shift Catalysts. *Science* **2003**, *301*, 935−938.

(12) Hilaire, S.; Wang, X.; Luo, T.; Gorte, R. J.; Wagner, J. A Comparative Study of Water-Gas-Shift Reaction over Ceria-Supported Metallic Catalysts. *Appl. Catal., A* **2001**, *215*, 271−278.

(13) Otsuka, K.; Hatano, M.; Morikawa, A. Hydrogen from Water by Reduced Cerium Oxide. *J. Catal.* **1983**, *79*, 493−496.

(14) Abanades, S.; Legal, A.; Cordier, A.; Peraudeau, G.; Flamant, G.; Julbe, A. Investigation of Reactive Cerium-Based Oxides for H_2 Production by Thermochemical Two-Step Water-Splitting. *J. Mater. Sci.* **2010**, *45*, 4163−4173.

(15) Chueh, W. C.; Hao, Y.; Jung, W.; Haile, S. M. High Electrochemical Activity of the Oxide Phase in Model Ceria-Pt and Ceria-Ni Composite Anodes. *Nat. Mater.* **2012**, *11*, 155−161.

(16) Zhang, C.; Grass, M. E.; McDaniel, A. H.; Decaluwe, S. C.; El Gabaly, F.; Liu, Z.; McCarty, K. F.; Farrow, R. L.; Linne, M. A.; Hussain, Z.; Jackson, G. S.; Bluhm, H.; Eichhorn, B. W. Measuring Fundamental Properties in Operating Solid Oxide Electrochemical Cells by Using in Situ X-Ray Photoelectron Spectroscopy. *Nat. Mater.* **2010**, *9*, 944−949.

(17) Hansen, H. A.; Wolverton, C. Kinetics and Thermodynamics of H_2O Dissociation on Reduced $CeO_2(111)$. *J. Phys. Chem. C* **2014**, *118*, 27402−27414.

(18) Paier, J.; Penschke, C.; Sauer, J. Oxygen Defects and Surface Chemistry of Ceria: Quantum Chemical Studies Compared to Experiment. *Chem. Rev.* **2013**, *113*, 3949−3985.

(19) Naghavi, S. S.; Emery, A. A.; Hansen, H. A.; Zhou, F.; Ozolins, V.; Wolverton, C. Giant Onsite Electronic Entropy Enhances the Performance of Ceria for Water Splitting. *Nat. Commun.* **2017**, *8*, 285.

(20) Dvořák, F.; Szabová, L.; Johánek, V.; Camellone, M. F.; Stetsovych, V.; Vorokhta, M.; Tovt, A.; Skála, T.; Matolínová, I.; Tateyama, Y.; Mysliveček, J.; Fabris, S.; Matolín, V. Bulk Hydroxylation and Effective Water Splitting by Highly Reduced Cerium Oxide: The Role of O Vacancy Coordination. *ACS Catal.* **2018**, *8*, 4354−4363.

(21) Mavrikakis, M.; Hammer, B.; Nørskov, J. K. Effect of Strain on the Reactivity of Metal Surfaces. *Phys. Rev. Lett.* **1998**, *81*, 2819−2822.

(22) Tripkovic, V.; Zheng, J.; Rizzi, G. A.; Marega, C.; Durante, C.; Rossmeisl, J.; Granozzi, G. Comparison between the Oxygen Reduction Reaction Activity of Pd_5Ce and Pt_5Ce: The Importance of Crystal Structure. *ACS Catal.* **2015**, *5*, 6032−6040.

(23) Clark, E. L.; Hahn, C.; Jaramillo, T. F.; Bell, A. T. Electrochemical CO_2 Reduction over Compressively Strained CuAg Surface Alloys with Enhanced Multi-Carbon Oxygenate Selectivity. *J. Am. Chem. Soc.* **2017**, *139*, 15848−15857.

(24) Ling, T.; Yan, D.-Y.; Wang, H.; Jiao, Y.; Hu, Z.; Zheng, Y.; Zheng, L.; Mao, J.; Liu, H.; Du, X.-W.; Jaroniec, M.; Qiao, S.-Z. Activating Cobalt(II) Oxide Nanorods for Efficient Electrocatalysis by Strain Engineering. *Nat. Commun.* **2017**, *8*, 1509.

(25) Sayle, T. X. T.; Cantoni, M.; Bhatta, U. M.; Parker, S. C.; Hall, S. R.; Möbus, G.; Molinari, M.; Reid, D.; Seal, S.; Sayle, D. C. Strain and Architecture-Tuned Reactivity in Ceria Nanostructures; Enhanced Catalytic Oxidation of CO to CO_2. *Chem. Mater.* **2012**, *24*, 1811−1821.

(26) Capdevila-Cortada, M.; López, N. Descriptor Analysis in Methanol Conversion on Doped $CeO_2(111)$: Guidelines for Selectivity Tuning. *ACS Catal.* **2015**, *5*, 6473−6480.

(27) Balaji Gopal, C.; García-Melchor, M.; Lee, S. C.; Shi, Y.; Shavorskiy, A.; Monti, M.; Guan, Z.; Sinclair, R.; Bluhm, H.; Vojvodic, A.; Chueh, W. C. Equilibrium Oxygen Storage Capacity of Ultrathin $CeO_{2-\delta}$ Depends Non-Monotonically on Large Biaxial Strain. *Nat. Commun.* **2017**, *8*, 15360.

(28) Ma, D.; Lu, Z.; Tang, Y.; Li, T.; Tang, Z.; Yang, Z. Effect of Lattice Strain on the Oxygen Vacancy Formation and Hydrogen Adsorption at $CeO_2(111)$ Surface. *Phys. Lett. A* **2014**, *378*, 2570−2575.

(29) Rushton, M. J. D.; Chroneos, A. Impact of Uniaxial Strain and Doping on Oxygen Diffusion in CeO_2. *Sci. Rep.* **2015**, *4*, 6068.

DOI: 10.1021/acscatal.9b00203
ACS Catal. 2019, 9, 4853−4861

(30) Ahn, J.; Choi, S.; Yoon, K. J.; Son, J.-W.; Kim, B.-K.; Lee, J.-H.; Jang, H.-W.; Kim, H. Strain-Induced Tailoring of Oxygen-Ion Transport in Highly Doped CeO_2 Electrolyte: Effects of Biaxial Extrinsic and Local Lattice Strain. *ACS Appl. Mater. Interfaces* **2017**, *9*, 42415−42419.
(31) Rushton, M. J. D.; Chroneos, A.; Skinner, S. J.; Kilner, J. A.; Grimes, R. W. Effect of Strain on the Oxygen Diffusion in Yttria and Gadolinia Co-Doped Ceria. *Solid State Ionics* **2013**, *230*, 37−42.
(32) Kushima, A.; Yildiz, B. Oxygen Ion Diffusivity in Strained Yttria Stabilized Zirconia: Where Is the Fastest Strain? *J. Mater. Chem.* **2010**, *20*, 4809−4819.
(33) De Souza, R. A.; Ramadan, A.; Hörner, S. Modifying the Barriers for Oxygen-Vacancy Migration in Fluorite-Structured CeO_2 Electrolytes through Strain: A Computer Simulation Study. *Energy Environ. Sci.* **2012**, *5*, 5445−5453.
(34) Kresse, G.; Furthmüller, J. Efficient Iterative Schemes for *Ab Initio* Total-Energy Calculations Using a Plane-Wave Basis Set. *Phys. Rev. B: Condens. Matter Mater. Phys.* **1996**, *54*, 11169−11186.
(35) Kresse, G.; Hafner, J. Ab Initio Molecular Dynamics for Open-Shell Transition Metals. *Phys. Rev. B: Condens. Matter Mater. Phys.* **1993**, *48*, 13115−13118.
(36) Perdew, J. P.; Burke, K.; Ernzerhof, M. Generalized Gradient Approximation Made Simple. *Phys. Rev. Lett.* **1996**, *77*, 3865−3868.
(37) Blöchl, P. E. Projector Augmented-Wave Method. *Phys. Rev. B: Condens. Matter Mater. Phys.* **1994**, *50*, 17953−17979.
(38) Dudarev, S. L.; Botton, G. A.; Savrasov, S. Y.; Humphreys, C. J.; Sutton, A. P. Electron-Energy-Loss Spectra and the Structural Stability of Nickel Oxide: An LSDA+U Study. *Phys. Rev. B: Condens. Matter Mater. Phys.* **1998**, *57*, 1505−1509.
(39) Fabris, S.; Gironcoli, S.; Baroni, S.; Vicario, G.; Balducci, G. Reply to ″Comment on 'Taming Multiple Valency with Density Functionals: A Case Study of Defective Ceria. *Phys. Rev. B* **2005**, *72*, 237102.
(40) Farra, R.; García-Melchor, M.; Eichelbaum, M.; Hashagen, M.; Frandsen, W.; Allan, J.; Girgsdies, F.; Szentmiklósi, L.; López, N.; Teschner, D. Promoted Ceria: A Structural, Catalytic, and Computational Study. *ACS Catal.* **2013**, *3*, 2256−2268.
(41) Capdevila-Cortada, M.; García-Melchor, M.; López, N. Unraveling the Structure Sensitivity in Methanol Conversion on CeO_2: A DFT + U Study. *J. Catal.* **2015**, *327*, 58−64.
(42) Su, Y.-Q.; Filot, I. A. W.; Liu, J.-X.; Tranca, I.; Hensen, E. J. M. Charge Transport over the Defective $CeO_2(111)$ Surface. *Chem. Mater.* **2016**, *28*, 5652−5658.
(43) Wu, T.; Deng, Q.; Hansen, H. A.; Vegge, T. Mechanism of Water Splitting on Gadolinium-Doped $CeO_2(111)$: A DFT + *U* Study. *J. Phys. Chem. C* **2019**, *123*, 5507−5517.
(44) Su, Y.-Q.; Liu, J.-X.; Filot, I. A. W.; Zhang, L.; Hensen, E. J. M. Highly Active and Stable CH_4 Oxidation by Substitution of Ce^{4+} by Two Pd^{2+} Ions in $CeO_2(111)$. *ACS Catal.* **2018**, *8*, 6552−6559.
(45) Huang, M.; Fabris, S. CO Adsorption and Oxidation on Ceria Surfaces from DFT + U Calculations. *J. Phys. Chem. C* **2008**, *112*, 8643−8648.
(46) Da Silva, J. L. F.; Ganduglia-Pirovano, M. V.; Sauer, J.; Bayer, V.; Kresse, G. Hybrid Functionals Applied to Rare-Earth Oxides: The Example of Ceria. *Phys. Rev. B: Condens. Matter Mater. Phys.* **2007**, *75*, No. 045121.
(47) Aparicio-Anglès, X.; Roldan, A.; De Leeuw, N. H. Gadolinium-Vacancy Clusters in the (111) Surface of Gadolinium-Doped Ceria: A Density Functional Theory Study. *Chem. Mater.* **2015**, *27*, 7910−7917.
(48) Gerward, L.; Olsen, J. S.; Petit, L.; Vaitheeswaran, G.; Kanchana, V.; Svane, A. Bulk Modulus of CeO_2 and PrO_2−An Experimental and Theoretical Study. *J. Alloys Compd.* **2005**, *400*, 56−61.
(49) Henkelman, G.; Uberuaga, B. P.; Jónsson, H. Climbing Image Nudged Elastic Band Method for Finding Saddle Points and Minimum Energy Paths. *J. Chem. Phys.* **2000**, *113*, 9901−9904.
(50) Molinari, M.; Parker, S. C.; Sayle, D. C.; Islam, M. S. Water Adsorption and Its Effect on the Stability of Low Index Stoichiometric and Reduced Surfaces of Ceria. *J. Phys. Chem. C* **2012**, *116*, 7073−7082.
(51) Yang, Z.; Wang, Q.; Wei, S.; Ma, D.; Sun, Q. The Effect of Environment on the Reaction of Water on the Ceria (111) Surface: A DFT + U Study. *J. Phys. Chem. C* **2010**, *114*, 14891−14899.
(52) Matz, O.; Calatayud, M. Breaking H_2 with CeO_2: Effect of Surface Termination. *ACS Omega* **2018**, *3*, 16063−16073.
(53) Fernández-Torre, D.; Carrasco, J.; Ganduglia-Pirovano, M. V.; Pérez, R. Hydrogen Activation, Diffusion, and Clustering on $CeO_2(111)$: A DFT+ U Study. *J. Chem. Phys.* **2014**, *141*, No. 014703.
(54) Carrasco, J.; López-Durμn, D.; Liu, Z.; Duchoň, T.; Evans, J.; Senanayake, S. D.; Crumlin, E. J.; Matolín, V.; Rodríguez, J. A.; Ganduglia-Pirovano, M. V. In Situ and Theoretical Studies for the Dissociation of Water on an Active Ni/CeO_2 Catalyst: Importance of Strong Metal − Support Interactions for the Cleavage of O-H Bonds. *Angew.Chem. Int. Ed.* **2015**, *54*, 3917−3921.
(55) Werner, K.; Weng, X.; Calaza, F.; Sterrer, M.; Kropp, T.; Paier, J.; Sauer, J.; Wilde, M.; Fukutani, K.; Shaikhutdinov, S.; Freund, H.-J. Toward an Understanding of Selective Alkyne Hydrogenation on Ceria: On the Impact of O Vacancies on H_2 Interaction with $CeO_2(111)$. *J. Am. Chem. Soc.* **2017**, *139*, 17608−17616.
(56) Evans, M. G.; Polanyi, M. Inertia and Driving Force of Chemical. *Trans. Faraday Soc.* **1938**, *34*, 11−24.
(57) Dholabhai, P. P.; Adams, J. B.; Crozier, P.; Sharma, R. Oxygen Vacancy Migration in Ceria and Pr-Doped Ceria: A DFT+U Study. *J. Chem. Phys.* **2010**, *132*, No. 094104.
(58) Kozuch, S.; Shaik, S. How to Conceptualize Catalytic Cycles? The Energetic Span Model. *Acc. Chem. Res.* **2011**, *44*, 101−110.
(59) Kozuch, S. A Refinement of Everyday Thinking: The Energetic Span Model for Kinetic Assessment of Catalytic Cycles. *WIREs Comput. Mol. Sci.* **2012**, *2*, 795−815.
(60) Palmer, J. D.; Livingston, L.; Zusy, F. D. A Persistent Diurnal Rhythm in Photosynthetic Capacity. *Nature* **1964**, *203*, 1087−1088.
(61) Yang, N.; Orgiani, P.; Di Bartolomeo, E.; Foglietti, V.; Torelli, P.; Ievlev, A. V.; Rossi, G.; Licoccia, S.; Balestrino, G.; Kalinin, S. V.; Aruta, C. Effects of Dopant Ionic Radius on Cerium Reduction in Epitaxial Cerium Oxide Thin Films. *J. Phys. Chem. C* **2017**, *121*, 8841−8849.
(62) Hong, S. J.; Virkar, A. V. Lattice Parameters and Densities of Rare-Earth Oxide Doped Ceria Electrolytes. *J. Am. Ceram. Soc.* **1995**, *78*, 433−439.
(63) Fu, Q.; Halck, N. B.; Hansen, H. A.; Lastra, J. M. G.; Vegge, T. Computational Study of Nb-Doped-SnO_2/Pt Interfaces: Dopant Segregation, Electronic Transport, and Catalytic Properties. *Chem. Mater.* **2017**, *29*, 1641−1649.

DOI: 10.1021/acscatal.9b00203
ACS Catal. 2019, 9, 4853−4861

SUPPORTING INFORMATION

Improved Electrocatalytic Water Splitting Reaction on CeO_2(111) by Strain Engineering: A DFT+U Study

Tiantian Wu, Tejs Vegge and Heine Anton Hansen*

Department of Energy Conversion and Storage, Technical University of Denmark, Fysikvej, 2800 Kgs. Lyngby, Denmark.

*Corresponding author:

Assoc. Prof. Dr. Heine Anton Hansen E-mail: heih@dtu.dk Tel: +45 45258211

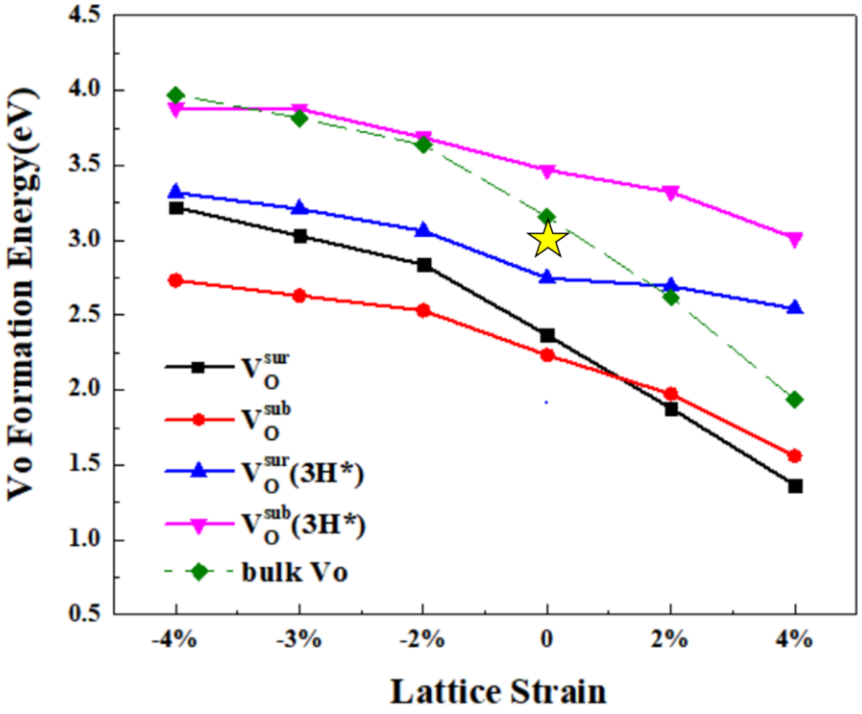

Figure S1. Formation energy of an oxygen vacancy as a function of lattice strain compared to the vacancy formation in bulk ceria. Yellow star represents the vacancy formation energy for unstrained bulk ceria reported by Gopal et al [1]. For creating an oxygen vacancy in unstrained ceria, we have compared the different Ce^{3+} locations in ceria. The most stable configuration of V_O^{sub} has $2Ce^{3+}$ next nearest neighbored to it, which is about 0.5 eV more stable than that $2Ce^{3+}$ locates nearest-neighbored to the V_O^{sub}, as shown in Table S8. For V_O^{sur}, the next nearest neighbored locations of Ce^{3+} is 0.18 eV more favored over the nearest-neighbored locations as shown in Table S9. These findings agree well with the results reported by Ganduglia-Pirovano et al.[2] By comparison, we have investigated the different Ce^{3+} locations at -4%, -3% -2%, 2%, and 4% strain as shown in Tables S8 and S9. The preference of Ce^{3+} locations for both V_O^{sub} and V_O^{sur} is not affected by strain, which is consistent with Ma's findings[3]. For each vacancy formation, the energy difference between different Ce^{3+} locations is below 0.5 eV and the reported polaron hopping between different Ce^{3+} locations is facile[4,5]. In addition, vacancy formation and diffusion is not fundamental step to the discussions on the efficient reaction pathway or TOF as shown in Figure 5 and 6 in the manuscript. Herein, all Ce^{3+} locations are nearest-neighbored to an oxygen vacancy or hydroxyls.

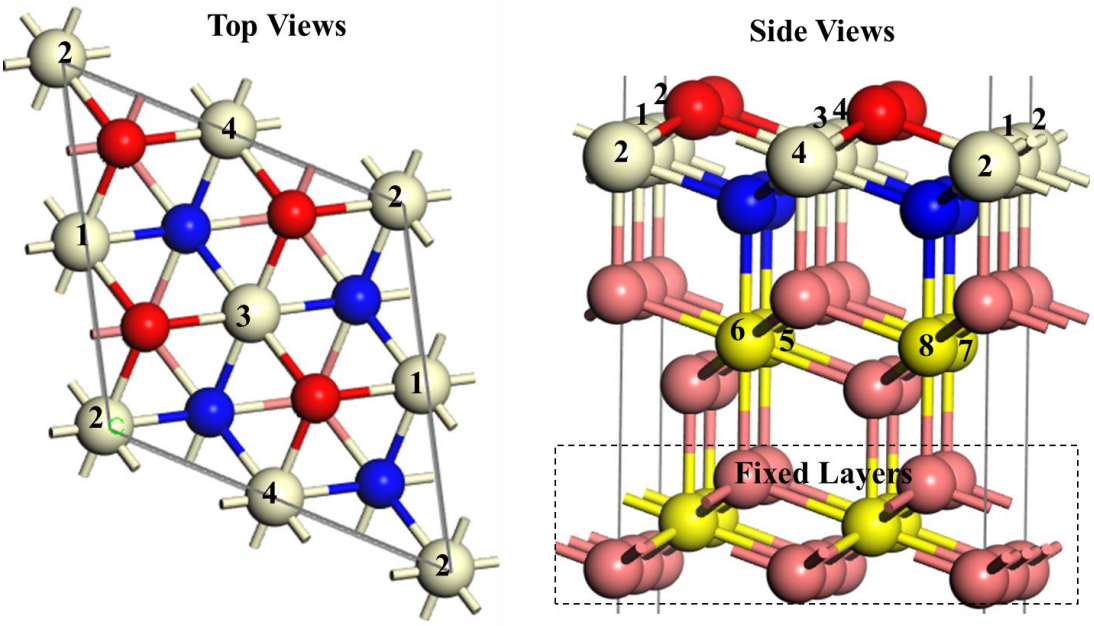

Figure S2. The top and side views of labelled cerium atoms with atom numbers in the top and subsurface layers of CeO_2(111). Color legend is the same as shown in Figure 1.

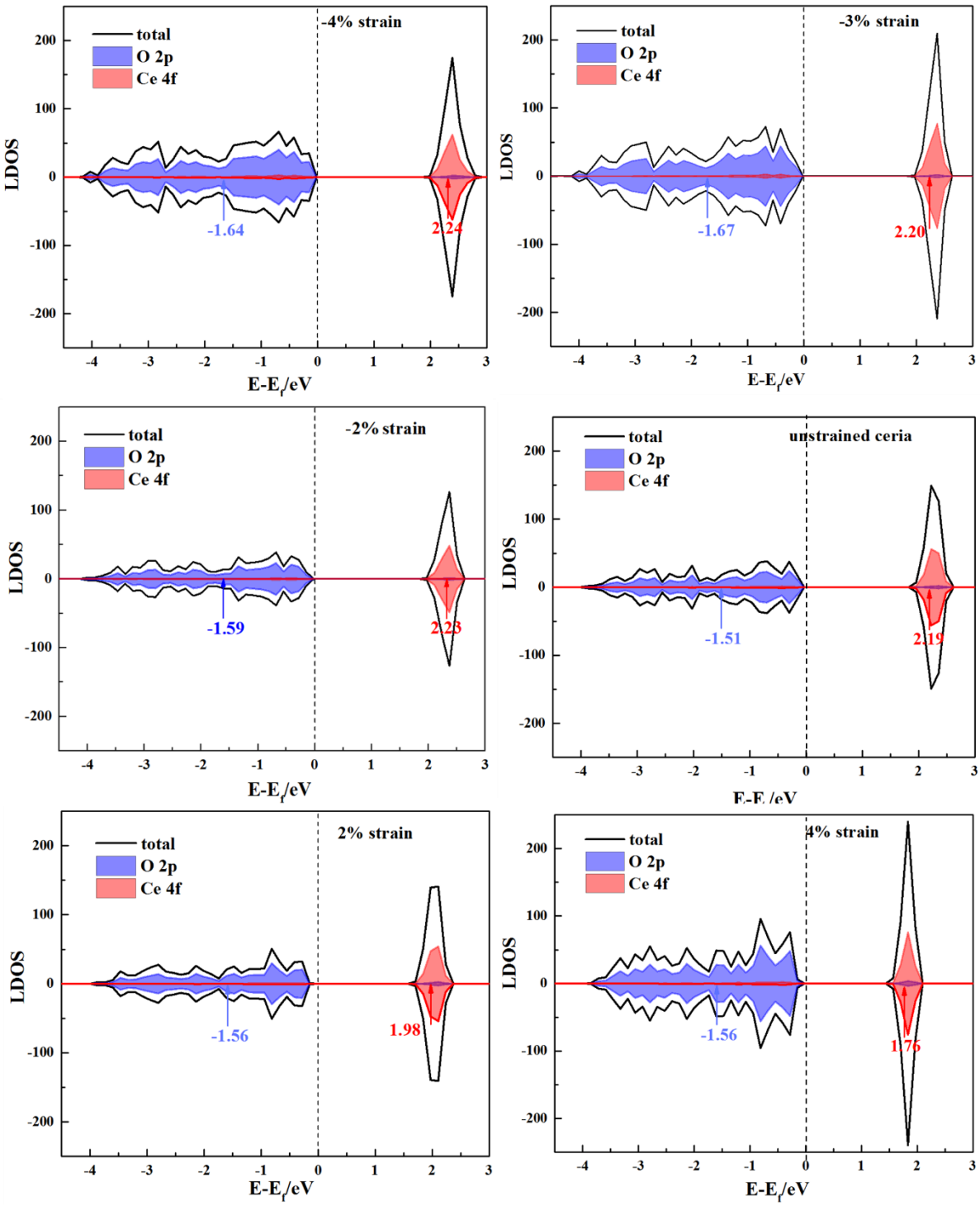

Figure S3. Spin-polarized density of states projected on O 2p and Ce 4f orbitals of strained and unstrained CeO_2(111). The O 2p and Ce 4f band centers are,labeled and marked by blue and red arrows, respectively. The Fermi level is set to zero. The density of states are calculated using a Γ-centered 13×13×1 k-point mesh.

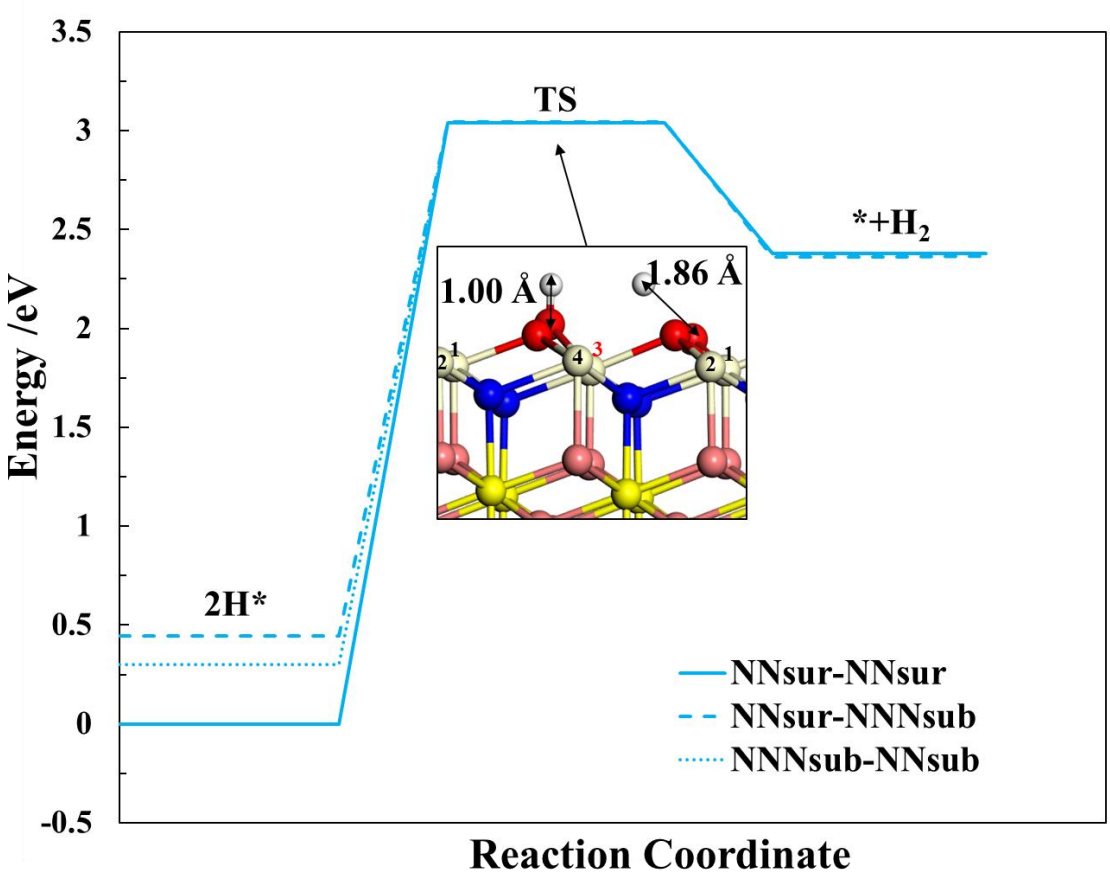

Figure S4. Hydroxyl decomposition into H_2 on the 2H* with the most favorable Ce^{3+} locations of NN_{sur}-NN_{sur}, compared to Ce^{3+} locations of NN_{sur}-NNN_{sub} and NNN_{sub}-NN_{sub}. We found the same transition sate (TS) for H_2 formation on the 2H* with different Ce^{3+} locations, where one H moves close to the other H leading to the breaking of one O-H. At the TS, there is only one Ce^{3+} locating at number 3 cerium as labelled in Figure S4. The configurations of 2H* and *+H_2 are present in Figure 2 in the manuscript. For further description of the Ce^{3+} locations refer to Figure S2 and Table S2.

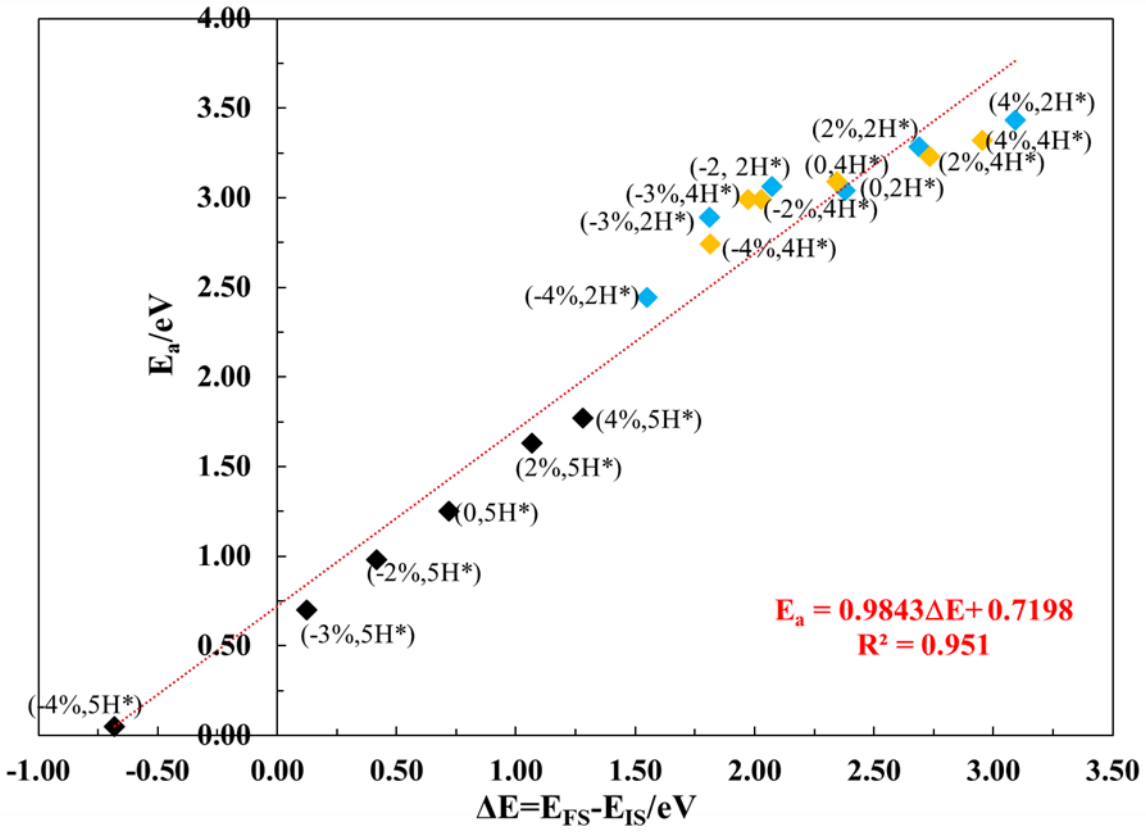

Figure S5. Brønsted-Evans-Polanyi (BEP) scaling relationships for the hydroxyl decomposition to form hydrogen on the different hydroxylated CeO_2(111) surfaces with different strain. The annotation (-4%, 5H*) indicates the activation energy is calculated for a CeO_2(111) surface under -4 % strain and adsorbed with 5H.

Descriptors for E_a

"Seven pillars" describing the geometric and electronic properties, has been proposed to contribute to the selectivity in the heterogeneous oxidation catalysis.[6] Capdevila-Cortada et al. [7] successfully developed the descriptor analysis in methanol conversion on doped CeO_2(111). Inspired by these investigations, we assess the following geometric and electronic descriptors:

(1) Geometric descriptors:

(a) The lattice parameter, a, which is directly affected by strain and can be experimentally measured from the XRD[8].

(b) The Ce-O distance, r_{Ce-O}, turns out ot be linearly dependent on the lattice parameter as shown in Figure S6. Thus, we only consider lattice parameter as the geometric descriptor in this study.

(2) Electronic descriptors:

(a) The basicity of lattice oxygen which is obtained using the O (2p) band center $\varepsilon_{O(2p)}$. In addition, Ce (4f) band center, $\varepsilon_{Ce(4f)}$, is also used to describe the electron localization on Ce 4f states and redox ability of CeO_2(111). The basicity can be experimentally assessed by studying the adsorption of the CO or NH_3 using FTIR spectroscopy[9].

(b) The redox character, E_{red}, which is the energy for reduction of one Ce^{4+} to Ce^{3+}. Temperature-programmed reduction (TPR) or isotopic exchange can directly give information on the redox character[7]. The reduction energy is by the reduction reaction $CeO_2 \rightarrow Ce_2O_3 + {}^1/_2\, O_2$.

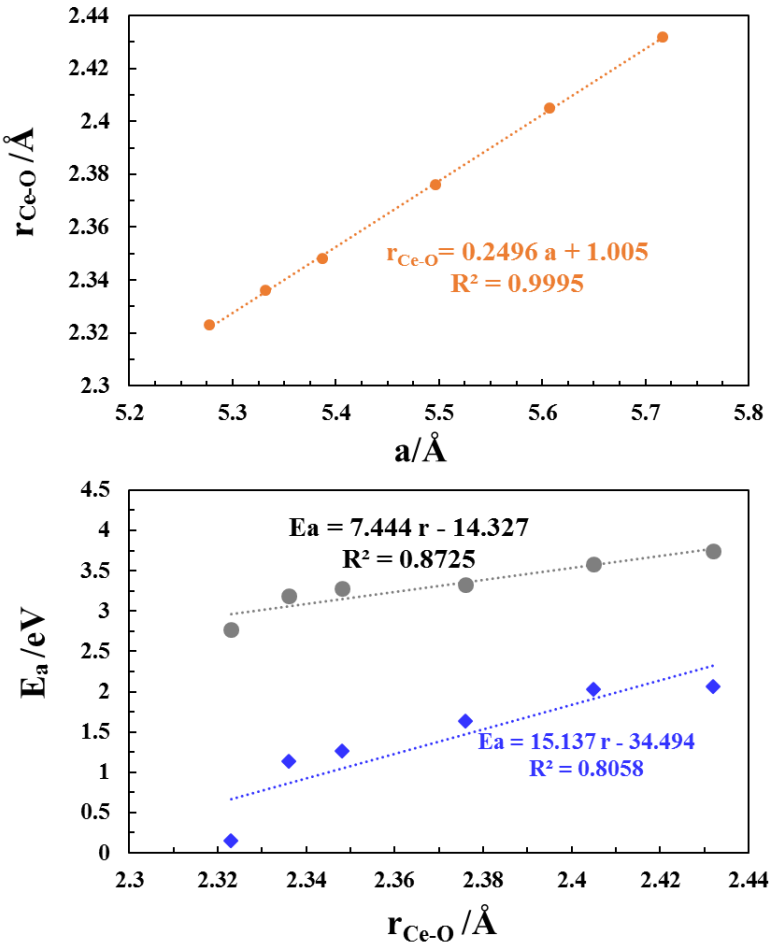

Figure S6. Top: the Ce-O distance, r_{Ce-O}, depends linearly on the bulk lattice parameter, a. Bottom: E_a versus the Ce-O distance for hydroxyl decomposition on the partially (gray spheres) and excessively hydroxylated (blue diamonds) surface.

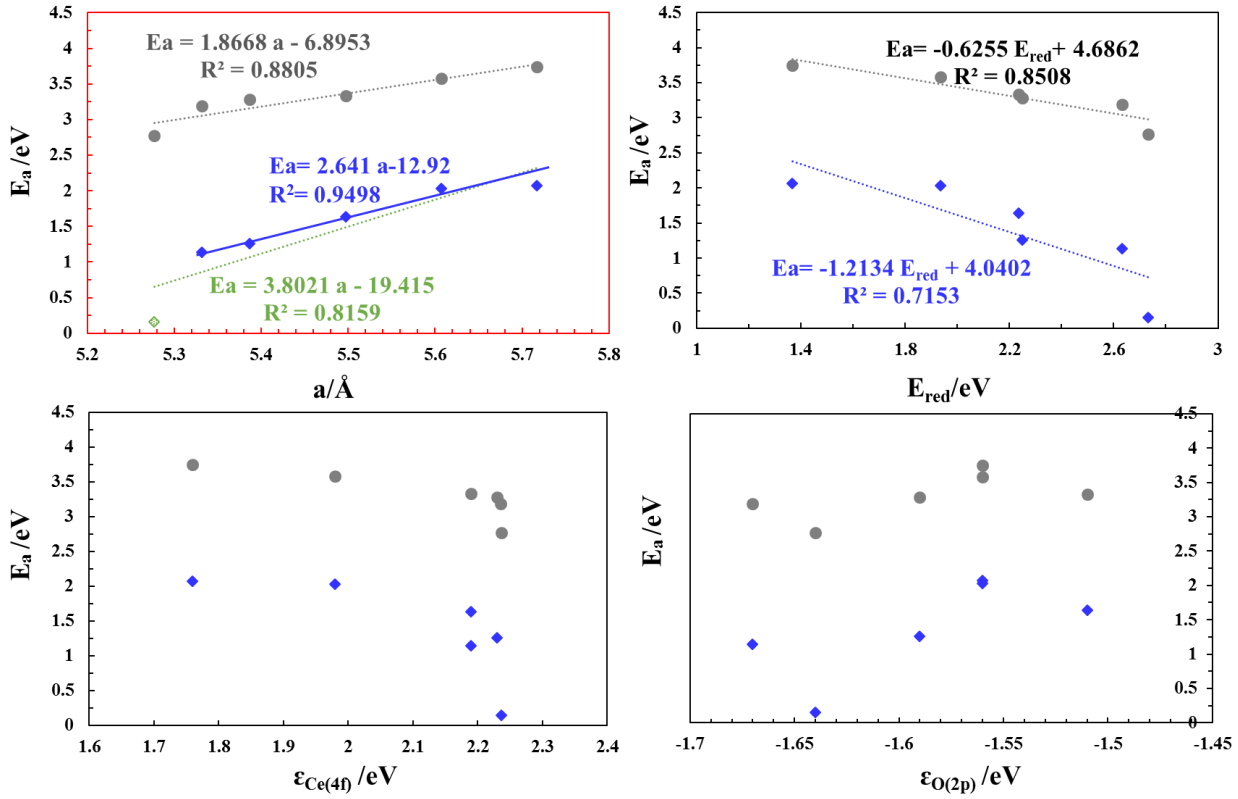

Figure S7. Activation energy for hydroxyl decomposition as a function of the lattice parameter, a, the reduction energy, E_{red}, the Ce 4f band center, $\varepsilon_{Ce(4f)}$, or O 2p band center, $\varepsilon_{O(2p)}$. The reactions on partially and excessively hydroxylated $CeO_2(111)$ are marked, respectively, in grey and blue. The green line shows the scaling between E_a and a (including the data under -4% strain).

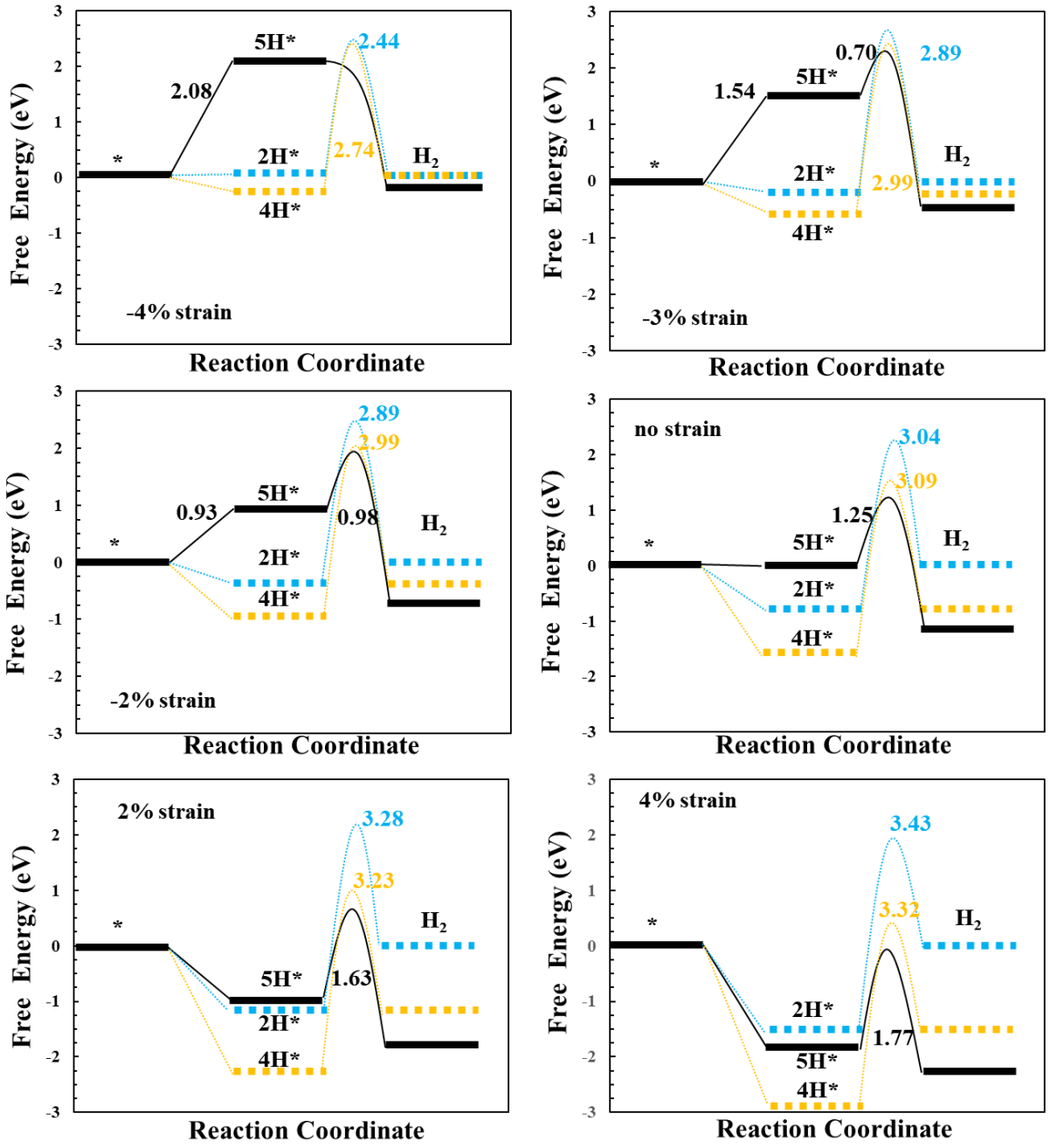

Figure S8. Simplified free energy diagrams for hydroxyl decomposition on the partially (2H*), fully (4H*) and excessively (5H*) hydroxylated CeO_2(111) under different strain at 1000 K. A solid line highlights the most efficient reaction pathway at each lattice strain.

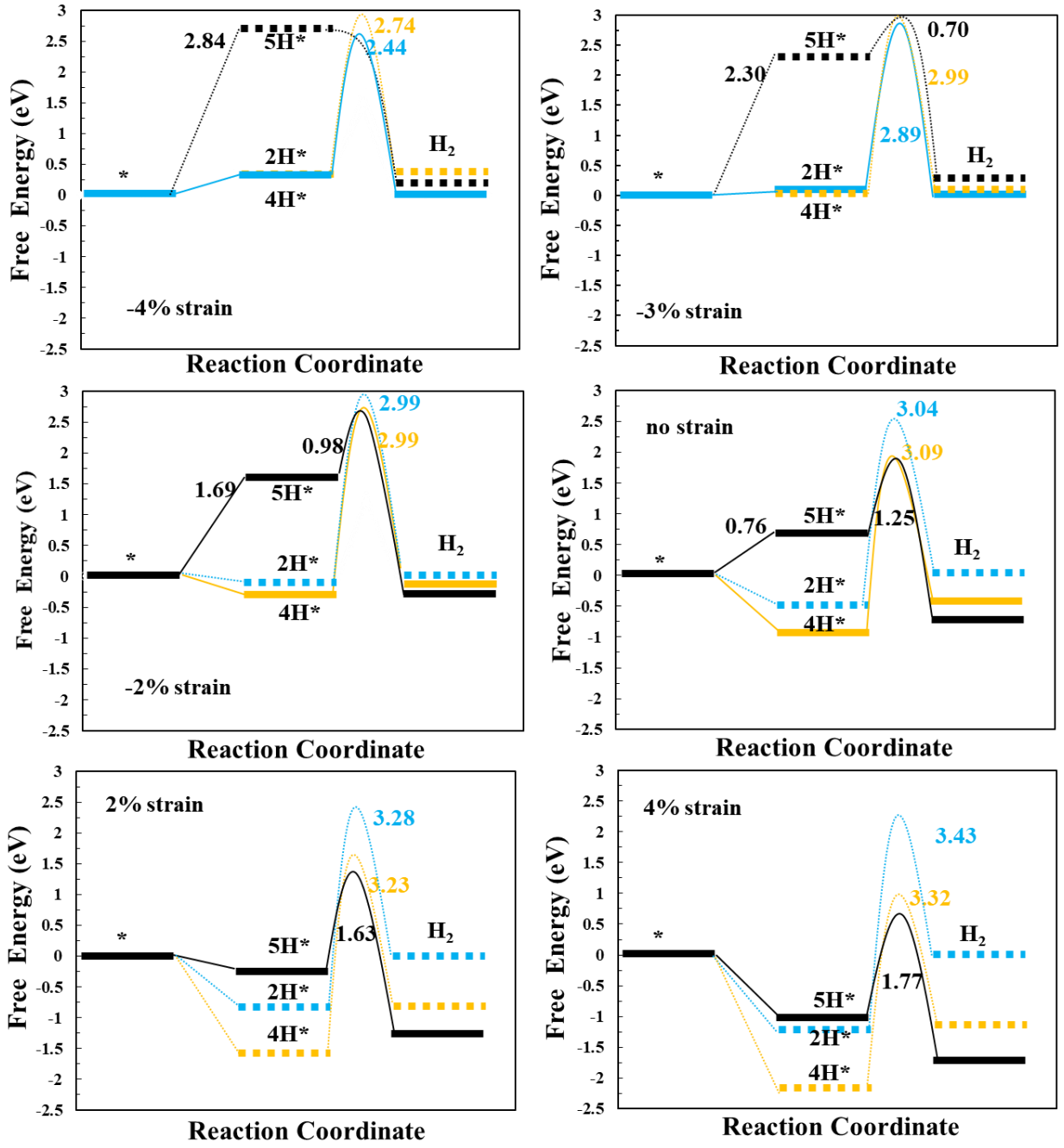

Figure S9. Simplified free energy diagrams for hydroxyl decomposition on partially (2H*), fully (4H*) and highly (5H*) hydroxylated CeO_2(111) under different strain at 1200 K. A solid line highlights the most efficient reaction pathway at each lattice strain.

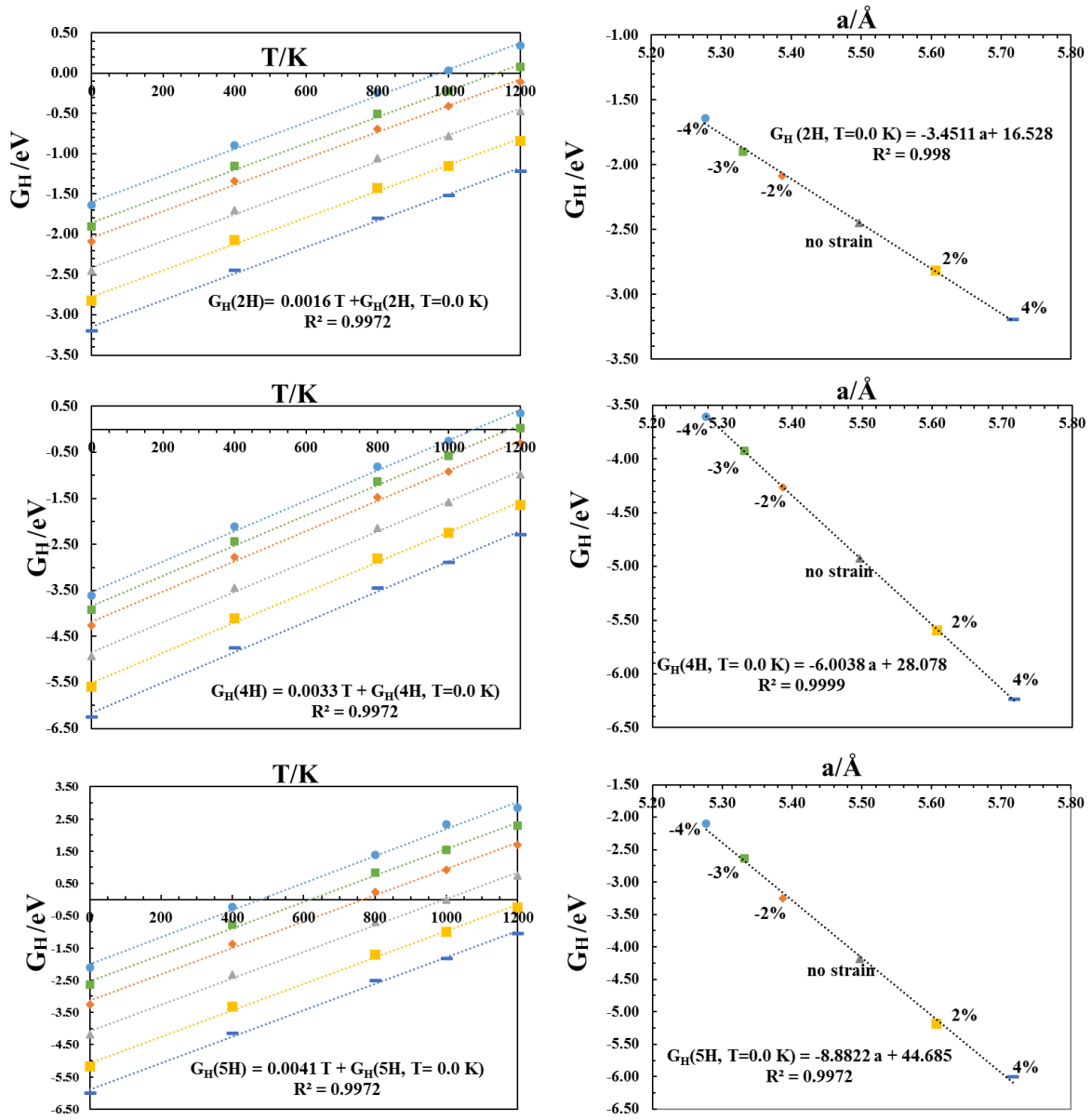

Figure S10. Free energy of partially (2H*), fully (4H*) and excessively (5H*) hydroxylated CeO_2(111) as a function of temperature and lattice parameter. We find a linear scaling between the operating temperature and the free energy of hydroxylated CeO_2(111) surfaces such as 2H*, 4H* and 5H*. The free energy of 2H*, 4H* and 5H* can be fitted by experimentally measurable descriptors such as temperature (T) and the lattice parameter (a) as follows:

$$G_H(2H) = 0.0016T - 3.4511a + 16.5280$$

$$G_H(4H) = 0.0033T - 6.0038a + 28.0780$$

$$G_H(5H) = 0.0041T - 8.8822a + 44.6850$$

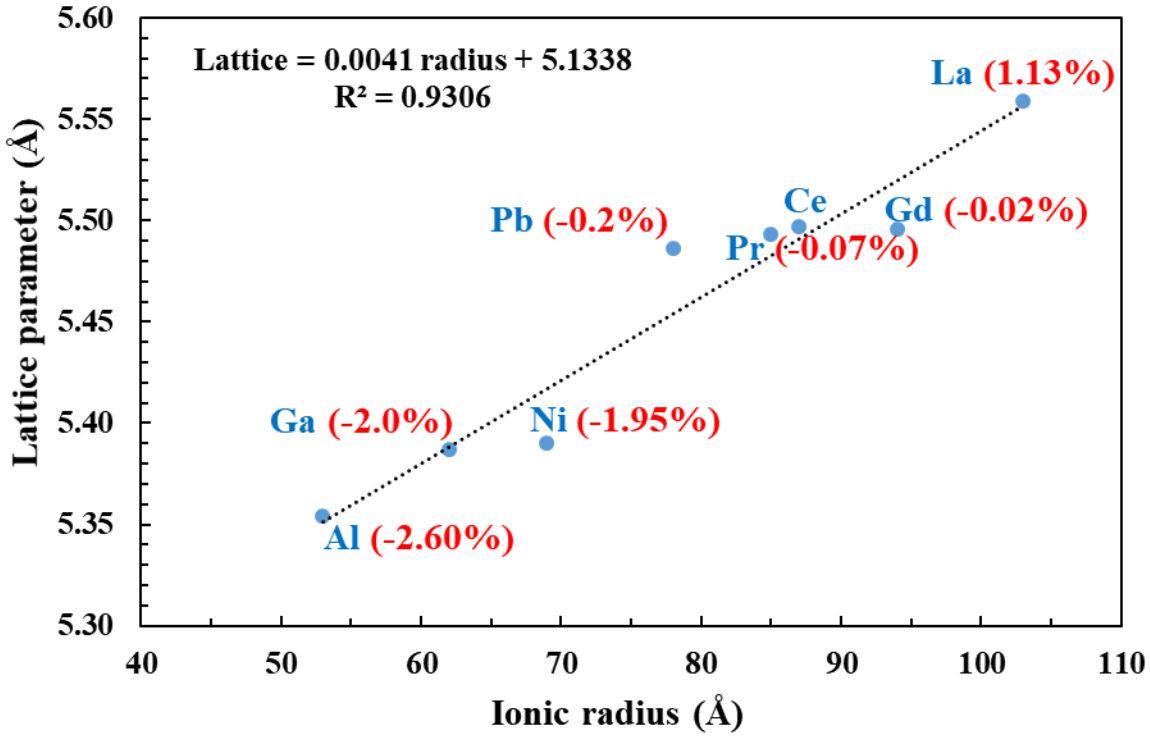

Figure S11. Calculated lattice parameter of doped bulk ceria as a function of the dopant ionic radius. Numbers in parentheses denote the strain of undoped ceria with the same lattice parameter as the doped ceria.

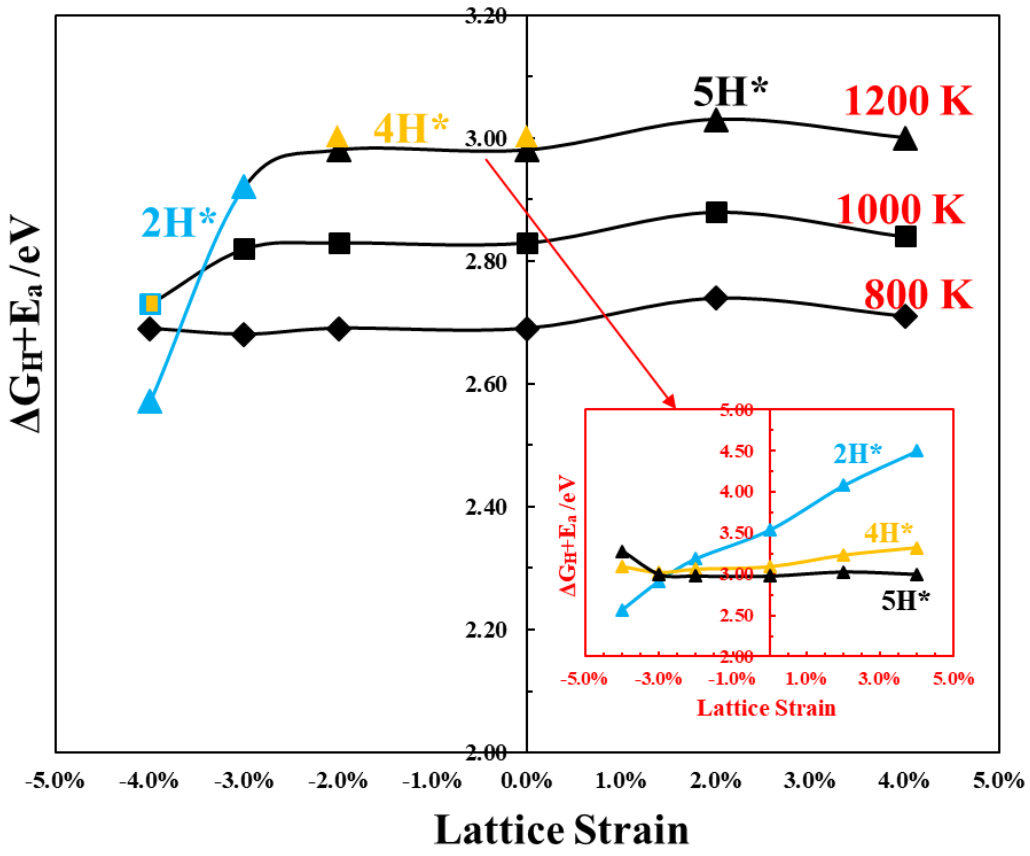

Figure S12. Free energy span, ΔG_H+Ea, for the most efficient WSR pathway versus strain at different temperatures. The free energy span for WSR pathways on the partially (2H*), fully (4H*), and excessively (5H*) hydroxylated CeO_2(111) at 1200 K is shown in the inset.

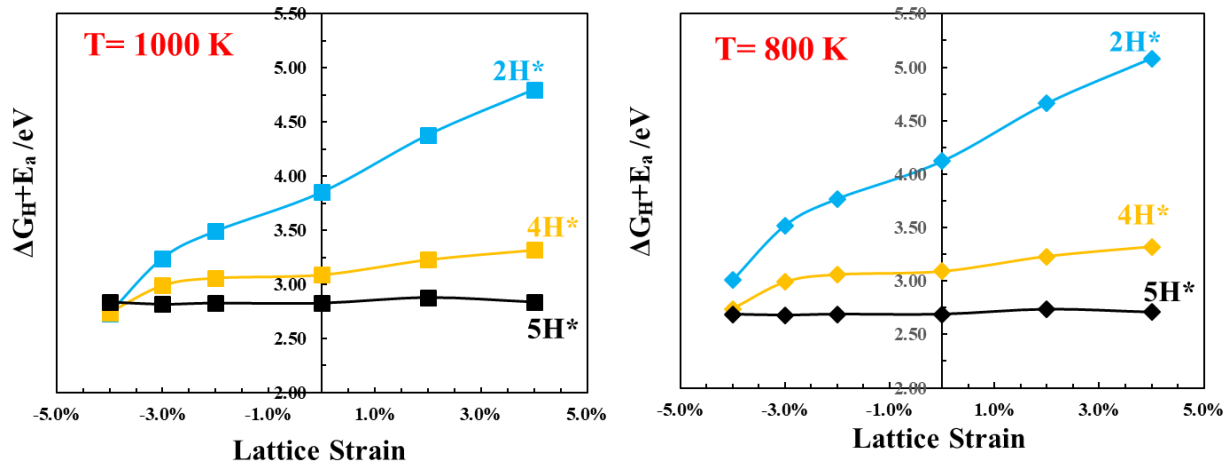

Figure S13. The free energy span for WSR pathways on the partially (2H*), fully (4H*), and excessively (5H*) hydroxylated CeO_2(111) at 800 and 1000 K.

Table S1. Lattice parameter, Ce-O bond length, O 2p $\varepsilon_{O(2p)}$ and Ce 4f $\varepsilon_{Ce(4f)}$ band centers of strained CeO_2(111). The centers of the O 2p and Ce 4f bands are referenced to the Fermi level.

This work	a (Å)	r_{Ce-O} (Å)	$\varepsilon_{O(2p)}$ (eV)	$\varepsilon_{Ce(4f)}$ (eV)
CeO_2	5.497	2.376	-1.51	2.19
+4%	5.717	2.432	-1.56	1.76
+2%	5.607	2.405	-1.56	1.98
-2%	5.387	2.348	-1.59	2.23
-3%	5.332	2.336	-1.67	2.20
-4%	5.277	2.323	-1.64	2.24
Marcel's work[6]	a (Å)	r_{Ce-O} (Å)		
CeO_2	5.497	2.375		
+2%	5.607	2.404		
-2%	5.387	2.348		

Table S2. The locations (atomic numbers) of Ce^{3+} states during pathways for the hydrogen production on ***partially (2H*), fully (4H*)*** and ***excessively (5H*)*** hydroxylated CeO_2(111), under different strain. All Ce^{3+} states are nearest-neighbored to an oxygen vacancy or hydroxyls. Atom numbering refers to Figure S2. The configurations of each intermediates are shown in Figure 2.

Strain	*******	***Vo^{sub}***	***TS1***	***Vo^{sur}***	***$+H_2O_{ads}$***	***TS2***	***2H****	***TS3***	****+H_2***
-4%		(1,3)	(1,3)	(2,4)	(2,4)		(3,4)	(4)	
-3%		(1,3)	(2,4)	(2,4)	(2,4)		(3,4)	(4)	
-2%		(1,3)	(2,4)	(2,4)	(2,4)		(1,2)	(2)	
0%		(1,3)	(1,3)	(2,4)	(2,4)		(2,3)	(3)	
2%		(1,3)	(1,3)	(2,4)	(2.4)		(2,4)	(2)	
4%		(1,3)	(2,4)	(2,4)	(2,4)		(1,2)	(2)	
Strain	***3H****	***3H*+Vo^{sub}***	***TS1'***	***3H*+Vo^{sur}***	***$+H_2O_{ads}$***	***TS2'***	***4H****	***TS3'***	***2H*+H_2***
-4%	(1,3,4)	(1,2,3,4,7)		(1,2,3,4,7)	(1,2,3,4,8)		(1,2,3,4)	(2,3,4)	(3,4)
-3%	(2,3,4)	(1,2,3,4,7)		(1,2,3,4,6)	(1,2,3,4,7)		(1,2,3,4)	(2,3,4)	(3,4)
-2%	(1,2,4)	(1,2,3,4,6)		(1,2,3,4,6)	(1,2,3,4,6)		(1,2,3,4)	(1,3,4)	(1,3)
0%	(1,2,3)	(1,2,3,4,7)		(1,2,3,4,8)	(1,2,3,4,8)		(1,2,3,4)	(1,2,3)	(1,3)
2%	(1,3,4)	(1,2,3,4,6)		(1,2,3,4,6)	(1,2,3,4,6)		(1,2,3,4)	(1,2,4)	(1,2)
4%	(1,2,4)	(1,2,3,4,5)		(1,2,3,4,7)	(1,2,3,4,7)		(1,2,3,4)	(1,2,4)	(1,2)
Strain	***3H****	***3H*+Vo^{sub}***	***TS1'***	***3H*+Vo^{sur}***	***$+H_2O_{ads}$***	***TS2''***	***5H****	***TS3''***	***3H*+H_2***
-4%	(1,3,4)	(1,2,3,4,7)		(1,2,3,4,7)	(1,2,3,4,8)	(1,2,3,4)	(1,2,4)		(1,3,4)
-3%	(2,3,4)	(1,2,3,4,7)		(1,2,3,4,6)	(1,2,3,4,7)		(1,2,3,4,7)	(1,2,3,4)	(2,3,4)
-2%	(1,2,4)	(1,2,3,4,6)		(1,2,3,4,6)	(1,2,3,4,6)		(1,2,3,4,7)	(1,2,3,4)	(1,2,4)
0%	(1,2,3)	(1,2,3,4,7)		(1,2,3,4,8)	(1,2,3,4,8)		(1,2,3,4,7)	(1,2,3,4)	(1,2,3)
2%	(1,3,4)	(1,2,3,4,6)		(1,2,3,4,6)	(1,2,3,4,6)		(1,2,3,4,7)	(1,2,3,4)	(1,2,4)
4%	(1,2,4)	(1,2,3,4,5)		(1,2,3,4,7)	(1,2,3,4,7)		(1,2,3,4,7)	(1,2,3,4)	(2,3,4)

Table S3. Adsorption energy of 2H with different Ce^{3+} locations (atom numbers) on unstrained ceria. Atom numbering refers to Figure S2. NNN and NN represent Ce^{3+} locating next nearest neighbor and nearest neighbor to hydroxyls, respectively. The subscripts of "sur" and "sub" represent Ce^{3+} locating in the top surface and subsurface, respectively.

Ce^{3+} locations to the Vo^{sur}	Atomic number of Ce^{3+}	E(2H)
NN_{sur}-NN_{sur}	(2,3)	-2.45
NNN_{sub}-NN_{sub}	(5,7)	-2.15
NN_{sur}-NNN_{sub}	(2,7)	-2.01

Table S4. Free energies of reduced states during pathways for the hydrogen production on ***partially (2H*), fully (4H*)*** and ***excessively (5H*)*** hydroxylated CeO_2(111), under different strain at 800 K.

Strain	*******	***Vo^{sub}***	***TS1***	***Vo^{sur}***	***$+H_2O_{ads}$***	***TS2***	***2H****	***TS3***	****+H_2***
-4%	0.00	0.20	1.37	0.69	1.06		-0.24	2.20	0.00
-3%	0.00	0.10	0.78	0.50	0.87		-0.50	2.39	0.00
-2%	0.00	0.08	0.77	0.31	0.64		-0.69	2.30	0.00
0%	0.00	-0.29	0.55	-0.16	0.26		-1.06	1.98	0.00
2%	0.00	-0.59	0.03	-0.65	-0.12		-1.43	1.85	0.00
4%	0.00	-0.70	-0.54	-1.16	-0.44		-1.79	1.64	0.00
Strain	***3H****	***3H*+Vo^{sub}***	***TS1'***	***3H*+Vo^{sur}***	***$+H_2O_{ads}$***	***TS2'***	***4H****	***TS3'***	***2H*+H_2***
-4%	-0.54	0.81		0.25	0.88		-0.81	1.93	-0.24
-3%	-0.56	0.37		0.12	0.58		-1.14	1.85	-0.50
-2%	-1.08	0.08		-0.55	0.18		-1.47	1.52	-0.69
0%	-1.60	-0.66		-1.38	-0.53		-2.14	0.95	-1.06
2%	-2.05	-1.26		-1.89	-1.44		-2.80	0.43	-1.43
4%	-2.69	-2.21		-2.68	-2.18		-3.45	-0.13	-1.79
Strain	***3H****	***3H*+Vo^{sub}***	***TS1'***	***3H*+Vo^{sur}***	***$+H_2O_{ads}$***	***TS2''***	***5H****	***TS3''***	***3H*+H_2***
-4%	-0.54	0.81		0.25	0.88	1.88	1.39		-0.59
-3%	-0.56	0.37		0.12	0.58		0.84	1.54	-0.56
-2%	-1.08	0.08		-0.55	0.18		0.24	1.22	-1.08
0%	-1.60	-0.66		-1.38	-0.53		-0.70	0.55	-1.60
2%	-2.05	-1.26		-1.89	-1.44		-1.70	-0.07	-2.05
4%	-2.69	-2.21		-2.68	-2.18		-2.51	-0.74	-2.68

Table S5. Free energies of reduced states during pathways for the hydrogen production on the ***partially (2H*), fully (4H*)*** and ***excessively (5H*)*** hydroxylated CeO_2(111), under different strain at 1000 K.

Strain	*****	***Vo^{sub}***	***TS1***	***Vo^{sur}***	***$+H_2O_{ads}$***	***TS2***	***2H****	***TS3***	****+H_2***
-4%	0.00	0.18	1.35	0.67	1.14		0.03	2.47	0.00
-3%	0.00	0.08	0.76	0.48	0.95		-0.23	2.66	0.00
-2%	0.00	0.06	0.75	0.29	0.72		-0.41	2.58	0.00
0%	0.00	-0.31	0.53	-0.19	0.34		-0.78	2.26	0.00
2%	0.00	-0.62	0.01	-0.67	-0.04		-1.15	2.13	0.00
4%	0.00	-0.72	-0.56	-1.19	-0.36		-1.52	1.91	0.00
Strain	***3H****	***3H*+Vo^{sub}***	***TS1'***	***3H*+Vo^{sur}***	***$+H_2O_{ads}$***	***TS2'***	***4H****	***TS3'***	***2H*+H_2***
-4%	-0.12	1.21		0.64	1.38		-0.26	2.48	0.03
-3%	-0.14	0.77		0.52	1.08		-0.58	2.41	-0.23
-2%	-0.67	0.47		-0.16	0.68		-0.92	2.07	-0.41
0%	-1.19	-0.27		-0.99	-0.04		-1.58	1.51	-0.78
2%	-1.64	-0.87		-1.50	-0.95		-2.25	0.98	-1.15
4%	-2.28	-1.81		-2.29	-1.68		-2.89	0.43	-1.52
Strain	***3H****	***3H*+Vo^{sub}***	***TS1'***	***3H*+Vo^{sur}***	***$+H_2O_{ads}$***	***TS2''***	***5H****	***TS3''***	***3H*+H_2***
-4%	-0.12	1.21		0.64	1.38	2.38	2.08		-0.12
-3%	-0.14	0.77		0.52	1.08		1.54	2.24	-0.14
-2%	-0.67	0.47		-0.16	0.68		0.93	1.91	-0.71
0%	-1.19	-0.27		-0.99	-0.04		-0.01	1.24	-1.19
2%	-1.64	-0.87		-1.50	-0.95		-1.00	0.63	-1.64
4%	-2.28	-1.81		-2.29	-1.68		-1.82	-0.05	-2.26

Table S6. Free energies of reduced states during pathways for the hydrogen production on the ***partially (2H*), fully (4H*)*** and ***excessively (5H*)*** hydroxylated CeO_2(111), under different strain at 1200 K.

Strain	*******	***Vo^{sub}***	***TS1***	***Vo^{sur}***	***$+H_2O_{ads}$***	***TS2***	***2H****	***TS3***	****+H_2***
-4%	0.00	0.13	1.30	0.62	1.58		0.34	2.78	0.00
-3%	0.00	0.03	0.71	0.43	1.39		0.08	2.97	0.00
-2%	0.00	0.01	0.70	0.24	1.16		-0.11	2.88	0.00
0%	0.00	-0.36	0.48	-0.23	0.78		-0.47	2.57	0.00
2%	0.00	-0.67	-0.04	-0.72	0.40		-0.84	2.44	0.00
4%	0.00	-0.77	-0.61	-1.23	-2.92		-1.21	2.22	0.00
Strain	***3H****	***3H*+Vo^{sub}***	***TS1'***	***3H*+Vo^{sur}***	***$+H_2O_{ads}$***	***TS2'***	***4H****	***TS3'***	***2H*+H_2***
-4%	0.33	1.62		1.05	2.28		0.35	3.09	0.34
-3%	0.32	1.17		0.92	1.98		0.03	3.02	0.08
-2%	-0.21	0.88		0.25	1.58		-0.31	2.68	-0.11
0%	-0.73	0.14		-0.58	0.86		-0.97	2.12	-0.47
2%	-1.18	-0.46		-1.09	-0.05		-1.64	1.59	-0.84
4%	-1.82	-1.41		-1.88	-0.79		-2.28	1.04	-1.21
Strain	***3H****	***3H*+Vo^{sub}***	***TS1'***	***3H*+Vo^{sur}***	***$+H_2O_{ads}$***	***TS2''***	***5H****	***TS3''***	***3H*+H_2***
-4%	0.33	1.62		1.05	2.28	3.28	2.84		0.33
-3%	0.32	1.17		0.92	1.98		2.30	3.00	0.32
-2%	-0.21	0.88		0.25	1.58		1.69	2.67	-0.21
0%	-0.73	0.14		-0.58	0.86		0.76	2.01	-0.73
2%	-1.18	-0.46		-1.09	-0.05		-0.24	1.39	-1.18
4%	-1.82	-1.41		-1.88	-0.79		-1.05	0.72	-1.81

Table S7. ΔG_H, E_a and the free energy span required for the WSR on ***partially (2H*), fully (4H*)*** and ***excessively (5H*)*** hydroxylated $CeO_2(111)$, respectively, at 800, 1000 and 1200 K.

T=800 K	**2H***			**4H***			**5H***		
Strain	ΔG_H	E_a	E_{total}	ΔG_H	E_a	E_{total}	ΔG_H	E_a	E_{total}
-4%	0.57	2.44	3.01	0	2.74	2.74	2.69	0	***2.69***
-3%	0.63	2.89	3.52	0	2.99	2.99	1.98	0.70	***2.68***
-2%	0.78	2.99	3.77	0	2.99	2.99	1.71	0.98	***2.69***
0	1.08	3.04	4.12	0	3.09	3.09	1.44	1.25	***2.69***
2%	1.38	3.28	4.66	0	3.23	3.23	1.11	1.63	***2.74***
4%	1.65	3.43	5.08	0	3.32	3.32	0.94	1.77	***2.71***
T=1000 K	**2H***			**4H***			**5H***		
Strain	ΔG_H	E_a	E_{total}	ΔG_H	E_a	E_{total}	ΔG_H	E_a	E_{total}
-4%	0.29	2.44	***2.73***	0	2.74	2.74	2.84	0	2.84
-3%	0.35	2.89	3.24	0	2.99	2.99	2.12	0.70	***2.82***
-2%	0.50	2.99	3.49	0	2.99	2.99	1.85	0.98	***2.83***
0	0.81	3.04	3.85	0	3.09	3.09	1.58	1.25	***2.83***
2%	1.10	3.28	4.38	0	3.23	3.23	1.25	1.63	***2.88***
4%	1.37	3.43	4.80	0	3.32	3.32	1.07	1.77	***2.84***
T=1200 K	**2H***			**4H***			**5H***		
Strain	ΔG_H	E_a	E_{total}	ΔG_H	E_a	E_{total}	ΔG_H	E_a	E_{total}
-4%	0.13	2.44	***2.57***	0.35	2.74	3.09	3.28	0	3.28
-3%	0.03	2.89	***2.92***	0.03	2.99	***3.02***	2.30	0.70	***3.00***
-2%	0.20	2.99	3.19	0	2.99	2.99	2.00	0.98	***2.98***
0	0.50	3.04	3.54	0	3.09	3.09	1.73	1.25	***2.98***
2%	0.80	3.28	4.08	0	3.23	3.23	1.40	1.63	***3.03***
4%	1.07	3.43	4.50	0	3.32	3.32	1.23	1.77	***3.00***

Table S8. Formation energy of creating one oxygen vacancy in the subsurface $E(V_O^{sub})$ of $CeO_2(111)$, at -4%, -3%, -2%, 0, 2%, and 4% strain with different locations of Ce^{3+}. Atom numbering refers to Figure S2. NNN and NN represent Ce^{3+} locating next nearest neighbor and nearest neighbor, respectively. The subscripts of "sur" and "sub" represent Ce^{3+} locating in the top surface and subsurface, respectively.

Ce^{3+} locations to the Vo^{sub}	Atomic number of Ce^{3+}	-4%	-3%	-2%	0	2%	4%
NNN_{sur}-NNN_{sub}	(2,6)	2.51	2.32	2.14	1.75	1.41	1.01
NNN_{sur}-NN_{sur}	(1,2)	2.71	2.48	2.25	1.90	1.49	1.08
NNN_{sur}-NN_{sub}	(2,5)	2.84	2.62	2.42	1.95	1.56	1.05
NN_{sur}-NNN_{sub}	(1,6)	2.75	2.33	2.40	2.20	1.69	1.25
NN_{sur}-NN_{sur}	(1,3)	2.73	2.70	2.53	2.23	1.97	1.56
NN_{sur}-NN_{sub}	(1,5)	3.04	2.88	2.68	2.29	2.10	

Table S9. Formation energy of creating one oxygen vacancy in the top surface $E(V_O^{sur})$ of $CeO_2(111)$, at -4%, -3%, -2%, 0, 2%, and 4% strain with different locations of Ce^{3+}. Atom numbering refers to Figure S2.

Ce^{3+} locations to the Vo^{sur}	Atomic number of Ce^{3+}	-4%	-3%	-2%	0	2%	4%
NNN_{sub}-NNN_{sub}	(5,7)	3.22	2.94	2.64	2.11	1.60	
NN_{sur}-NNN_{sur}	(1,2)	3.19	2.95	2.70	2.19	1.68	1.15
NN_{sur}-NN_{sur}	(2,4)	3.22	3.03	2.84	2.37	1.88	1.37
NN_{sur}-NNN_{sub}	(2,7)	3.49	3.19	2.94	2.46	1.93	1.46

REFERENCES

(1) Gopal, C. B.; García-Melchor, M.; Lee, S. C.; Shi, Y.; Shavorskiy, A.; Monti, M.; Guan, Z.; Sinclair, R.; Bluhm, H.; Vojvodic, A.; Chueh, W. C. Equilibrium Oxygen Storage Capacity of Ultrathin $CeO_{2-\delta}$ Depends Non-Monotonically on Large Biaxial Strain. *Nat. Commun.* **2017**, *8*, 15360.

(2) Ganduglia-Pirovano, M. V.; Da Silva, J. L. F.; Sauer, J. Density-Functional Calculations of the Structure of near-Surface Oxygen Vacancies and Electron Localization on $CeO_2(111)$. *Phys. Rev. Lett.* **2009**, *102*, 026101.

(3) Ma, D.; Lu, Z.; Tang, Y.; Li, T.; Tang, Z.; Yang, Z. Effect of Lattice Strain on the Oxygen Vacancy Formation and Hydrogen Adsorption at CeO_2(111) Surface. *Phys. Lett. A* **2014**, *378*, 2570–2575.

(4) Su, Y.-Q.; Filot, I. A. W.; Liu, J.-X.; Tranca, I.; Hensen, E. J. M. Charge Transport over the Defective CeO_2(111) Surface. *Chem. Mater.* **2016**, *28*, 5652–5658.

(5) Li, H.-Y.; Wang, H.-F.; Guo, Y.-L.; Lu, G.-Z.; Hu, P. Exchange between Sub-Surface and Surface Oxygen Vacancies on CeO_2(111): A New Surface Diffusion Mechanism W. *Chem. Comm.* **2011**, *21*, 6105–6107.

(6) Grasselli, R. K. Fundamental Principles of Selective Heterogeneous Oxidation Atalysis. *Top. Catal.* **2002**, *21*, 79–88.

(7) Capdevila-Cortada, M.; López, N. Descriptor Analysis in Methanol Conversion on Doped CeO_2(111): Guidelines for Selectivity Tuning. *ACS Catal.* **2015**, *5*, 6473–6480.

(8) Deshpande, S.; Patil, S.; Kuchibhatla, S. V.; Seal, S. Size Dependency Variation in Lattice Parameter and Valency States in Nanocrystalline Cerium Oxide. *Appl. Phys. Lett.* **2005**, *87*, 133113.

(9) Farra, R.; Wrabetz, S.; Schuster, M. E.; Stotz, E.; Hamilton, N. G.; Amrute, A. P.; Pérez-Ramírez, J.; López, N.; Teschner, D. Understanding CeO_2 as a Deacon Catalyst by Probe Molecule Adsorption and in Situ Infrared Characterisations. *Phys. Chem. Chem. Phys.* **2013**, *15*, 3454–3465.

B.3 Paper 3

Facet-Dependent Electrocatalytic Water Splitting Reaction on CeO_2: A DFT+*U* Study

Tiantian Wu, Núria López, Tejs Vegge, Heine Anton Hansen

Submitted

Facet-Dependent Electrocatalytic Water Splitting Reaction on CeO_2: A DFT+*U* Study

Tiantian Wu, [a] Núria López, [b,*] Tejs Vegge, [a] Heine Anton Hansen [a,*]

[a] Department of Energy Conversion and Storage, Technical University of Denmark, Fysikvej, 2800 Kgs. Lyngby, Denmark.

[b] Institute of Chemical Research of Catalonia (ICIQ), The Barcelona Institute of Science and Technology, Tarragona, Spain

*Corresponding author:

Núria López E-mail: nlopez@iciq.es

Heine Anton Hansen E-mail: heih@dtu.dk

ABSTRACT

Ceria has attracted considerable interest for electrocatalytic water splitting reaction (WSR) in solid oxide electrolysis cells (SOECs) due to the high efficiency and high stability for sustainable hydrogen production. The mechanism of the WSR on the (111) facet of ceria has been studied extensively, while it remains unclear on other exposed low-index surfaces like the (110) and (100) facets. By using density functional theory corrected for on-site Coulomb interactions (DFT+*U*), we compare the catalytic activity of the WSR on the (110), (100) and (111) facets of ceria. The formation of reaction intermediates like oxygen vacancies, hydroxyls and vacancy-hydroxyl mixed phase on CeO_2(100) is found to be more stable than that on CeO_2(110) and CeO_2(111). The higher stability of hydroxyls on CeO_2(100) inhibits hydroxyl decomposition into H_2, as compared to the reaction on the (110) and (111) facets, leading to the WSR on CeO_2(110) and CeO_2(111) 10~100 times faster than the reaction on CeO_2(100) at temperature (T) < 950 K. However, the strong facet-dependence of the WSR on ceria diminishes at higher temperature, demonstrating that the facet-dependence of the WSR on ceria is strongly sensitive to temperature.

KEYWORDS: Sustainable Hydrogen Production, Ce^{3+} Distributions, Hydrogen Coverages, Facet Dependence, Temperature Sensitivity, Computational Simulation

INTRODUCTION

Being a highly efficient and economically attractive solid oxide catalyst, ceria (CeO_2) has been widely used in many catalytic processes such as oxygen storage in three-way catalysts,[1–3] CO oxidation,[4,5] the water-gas shift reaction,[6–8] and other complex processes[9,10] because of the easy redox cycle between Ce^{4+} and Ce^{3+} states.[11–13] Recently, ceria has also been proposed for the electrocatalytic WSR in SOECs, due to the highly improved efficiency for sustainable hydrogen production by utilization of waste heat at high temperatures.[11,14–17] In addition, the ceria/gas interface is accessible to both ionic and electronic carriers, and molecules and can block cracking and polarization at traditional gas/catalyst/electrolyte boundaries,[18,19] which significantly enhance the stability of the SOECs.

The most stable low-index terminations of ceria are the (110), (100), and (111) facets. Specific morphologies of ceria nanocrystals can expose these low-index surfaces. The (110) and (100) facets are mostly exposed in ceria nanorods and nanocubes, respectively.[20] However, Yang et al.[21] found that rod-shaped ceria nanoparticles are likely to expose the (111) facet. The ceria particles are reported to have more (100) terminations after undergoing a distinct shape evolution with increasing temperature.[22] The (111) facet of ceria is reported to have the lowest free energy under a wide range of oxygen partial pressures up to 1 atm at 300 K and thus becomes the most stable low-index surface of ceria, followed by the (110) and (100) facets.[23] Both experiments[24] and atomistic modelling[25,26] have shown that less energy is required for oxygen vacancy formation on the (100) and (110) facets than that on the (111) facet of ceria. Therefore, the (100) and (110) facets of ceria are predicted to be more catalytically active than the (111) facet.[24-26]

However, facet dependence of catalytic processes on CeO_2 is widely reported.[20,27–30] Vilé et al.[27] found that among the (111), (110), and (100) facets, the CeO_2(100) surface is optimal for CO oxidation, whereas the (111) facet of ceria is more active for the C_2H_2 hydrogenation. Aneggi et al. reported that ceria exposed with the (100) and (110) terminations are more active in soot oxidation.[20] For the WSR on ceria, a smaller amount of H_2 is produced from reduced CeO_2(100) between 450 and 730 K than on CeO_2(111).[30] Recently, a number of computational investigations of water-associated reactions on ceria for H_2 productions have been reported, largely focusing on the most often observed (111) termination.[12,16,17,31,32] The rate-determining step for H_2 production via the WSR on CeO_2(111) is found to be hydroxyl decomposition via

a Ce-H intermediate.[11,12,16,17] Our previous studies have shown that the reaction efficiency of ceria for the WSR can be improved significantly by controlling the formation of Ce-H using strain engineering.[17] In addition, the preference of Ce^{3+} locations on the reduced CeO_2(111) like oxygen vacancies, hydroxyls and vacancy-hydroxyl mixed phases have been found to be sensitive to the position of the created oxygen vacancy, and hydrogen adsorption on CeO_2(111).[33–35] However, the fundamental understanding of the formation of important intermediates like oxygen vacancies, hydroxyls and vacancy-hydroxyl mixed phases during the WSR, as well as the preferred Ce^{3+} locations, and the reaction kinetics on CeO_2(100) and CeO_2(110) remain unclear. In addition, more comparisons among CeO_2(110), CeO_2(100), and CeO_2(111) as reaction surfaces for H_2 productions via the WSR are desired. In this work, we investigate the formation of reaction intermediates as well as the reaction pathways for the WSR on CeO_2(110) and CeO_2(100) by performing DFT+*U* calculations. The effect of hydrogen coverage and operating temperature on the WSR on the (110) and (100) facets are compared to our previous work on CeO_2(111).[17] In addition, a direct mapping of the most efficient WSR pathway on CeO_2(110), CeO_2(100) and CeO_2(111) at different operating temperature gives better understanding on the WSR on ceria exposed with (110), (100) and (111) facets.

COMPUTATIONAL MODELLING AND METHODS

Computational models:

We use 5.497 Å as the bulk equilibrium lattice constant of ceria as in our previous work.[16] This value is quite closed to both theoretical (5.497 Å)[36–39] and experimental values (5.411 Å)[40]. The CeO_2(110) surface is built as a 2×2 surface unit cell consisting of five O-Ce-O atomic layers as shown in **Figure 1(a)**. The CeO_2(100) surface is built as a 2×2 surface unit cell consisting of seven atomic layers as shown in **Figure 1(b)**. The CeO_2(100) surface with O termination is created following suggestions from both experiments[41] and DFT calculations.[28,29,42,43] In addition, half of the oxygen monolayer on the outmost layer of the CeO_2(100) surface is transferred to the bottom in a checkerboard way. Herein, the exposed oxygen and cerium of the CeO_2(100) surface are two-fold and six-fold coordinated, respectively. By contrast, the coordination number of the exposed oxygen and cerium of the CeO_2(110) surface is three and six, respectively. For all DFT calculations in this work, the two O-Ce-O atomic layers at the bottom of the CeO_2(110) surface are kept fixed in the bulk

geometry, while the four outermost atomic layers of CeO_2(100) are allowed to relax as suggested by Capdevila-Cortada et al.[28,44] A 15 Å vacuum gap is applied to block interaction between periodic units of both CeO_2(110) and CeO_2(100). In **Figure 1**, we have enumerated the relaxed cerium atoms in both CeO_2(110) and CeO_2(100) to distinguish their locations and enable labeling of various distributions of Ce^{3+} ions with reduced phases containing oxygen vacancies or hydroxyls.

Computational methods:

To simulate the electrocatalytic WSR on ceria exposed with different facets, we performed spin−polarized DFT calculations by using the Vienna ab initio simulation package (VASP)[45,46] with the Perdew-Burke-Ernzerhof (PBE) functional[47]. Using projector augmented wave method (PAW),[48] the interaction between the ions and the electrons are described by expanding wave functions in plane waves using an energy cutoff of 550 eV. The Ce (4*f*, 5*s*, 5*p*, 5*d*, 6*s*) and O (2*s*, 2*p*) electrons are treated as valence states. In addition, a Hubbard term is added to the PBE functional to describe electron localizations on the 4f orbital of Ce^{3+} states. The value of effective Hubbard *U* term (U_{eff}=*U-J, J=0*) used in this work is 4.5 eV, as reported widely in previous DFT work to ensure electron localizations on the 4*f* orbitals of Ce.[28,38,49–51] Different electron distributions are analyzed for the reduced ceria.[34,52] For the Brillouin zone integration, a Γ-centered 3×3×1 k-point mesh is used for optimization of all CeO_2 surfaces. The climbing image nudged-elastic band method as implemented in VASP [53] with a force tolerance of 0.03 eV /Å is applied for searching transition states and activation energies. In this work, VASP runs by calling a VASP calculator in the Atomic Simulation Environment (version 3.13.0).[54]

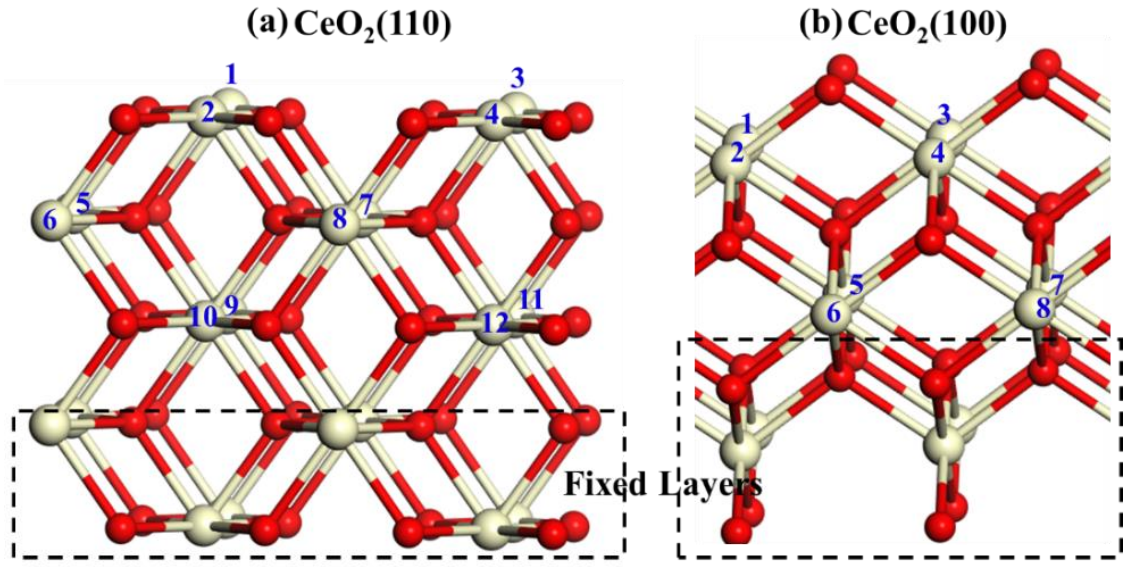

Figure 1. Side views of configurations of: (a) CeO_2(110) and (b) CeO_2(100). The relaxed cerium atoms are enumerated to distinguish their locations. Cerium atoms are light yellow and oxygen atoms red.

RESULTS AND DISCUSSIONS

The electrocatalytic WSR on CeO_2 usually includes several reaction steps as follows.[11,12,16,17]

$$2Ce^{4+} \rightarrow 2Ce^{3+} + V_O + O^{2-} \quad (1)$$

$$H_2O_{ads} + 2Ce^{3+} + V_O + O^{2-} \rightarrow 2OH^- + 2Ce^{3+} \quad (2)$$

$$2OH^- + 2Ce^{3+} \rightarrow H_2 + 2Ce^{4+} + 2O^{2-} \quad (3)$$

During reaction (1), an oxygen vacancy (V_O) is created by removing one lattice oxygen, where two excess electrons are localized on two cerium atoms somewhere in the cerium layers, leading to the reduction of $2Ce^{4+}$ to $2Ce^{3+}$. The distributions of the excess electrons on different facets of ceria at each reaction step will be discussed in detail in the following sections. In a SOEC, the formation of oxygen vacancies is associated with the formation of O_2 at the anode and O^{2-} transport through the electrolyte. Water adsorbs near V_O and easily dissociates into hydroxyls via reaction (2), where OH from H_2O is accommodated in the oxygen vacancy, while the other H binds with a lattice O neighbor to the oxygen vacancy, leading to the formation of two hydroxyls on ceria. After reaction (2), the surface is partially hydroxylated and H_2 then forms via hydroxyl decomposition in step (3), where $2OH^-$ release two lattice O^{2-} and $2Ce^{3+}$ are oxidized to $2Ce^{4+}$. Among steps of (1)-(3), the WSR on ceria undergoes a

$Ce^{4+} \rightarrow Ce^{3+} \rightarrow Ce^{4+}$ redox cycle. H_2 can form via the above reaction steps when the surface is partially hydroxylated and up to the limit where the surface is fully covered by hydroxyls after step (2). However, when CeO_2 is fully hydroxylated and there is no more lattice oxygen available for binding with one more H, reaction (2) is prohibited, and the WSR can instead proceed through

$$2Ce^{3+} + V_O + H_2O_{ads} \rightarrow OH^- + Ce^{4+} + Ce^{4+}H^- \rightarrow H_2 + 2Ce^{4+} + O^{2-} \quad (4)$$

where one lattice Ce^{4+} binds with the adsorbed H forming $Ce^{4+}H^-$ (Ce-H), which is an important intermediate during the WSR.[12,17] We refer to surfaces covering more than one monolayer H like Ce-H as excessively hydroxylated. In this work, the WSR including above reaction steps is investigated on the partially, fully and excessively hydroxylated $CeO_2(110)$ and $CeO_2(100)$, which is compared with the reactions on $CeO_2(111)$. For the WSR on the partially hydroxylated $CeO_2(110)$, the surfaces covered by 2H, 4H, 5H, and 6H are investigated. The $CeO_2(110)$ surface is covered by 8H when it is fully hydroxylated. Total 9H adsorb on $CeO_2(110)$, forming the excessively hydroxylated $CeO_2(110)$. 2H, 4H, and 5H adsorbed on the $CeO_2(100)$ surface is chosen as the partially, fully, and excessively hydroxylated $CeO_2(100)$ surface, respectively.

Creating an oxygen vacancy on $CeO_2(110)$ and $CeO_2(100)$. As discussed in our previous work,[17] the most stable Ce^{3+} locations after creating one oxygen vacancy in the subsurface (V_O^{sub}) and top surface (V_O^{sur}) of $CeO_2(111)$ is that $2Ce^{3+}$ are next-nearest neighbor to the V_O. The oxygen formation energy varies with the Ce^{3+} distribution with a difference below 0.5 eV.

When creating one subsurface V_O in $CeO_2(110)$, $2Ce^{3+}$ prefer to sit nearest neighbor to V_O^{sub} and locate in the deeper cerium atomic layers of $CeO_2(110)$, which is 0.95 eV more stable than the second most stable Ce^{3+} configuration as shown in **Table S1**. When creating one surface V_O in $CeO_2(110)$, an energy difference below 0.63 eV is found among all studied Ce^{3+} distributions in the V_O^{sur}, as shown in **Table S2**. The preferred Ce^{3+} distribution has $2Ce^{3+}$ located in the top cerium atomic layer, where one Ce^{3+} is nearest neighbor to the V_O^{sur} while the other Ce^{3+} is next-nearest neighbor to the V_O^{sur}. Summarizing, Ce^{3+} on the (110) facet of ceria is more likely to sit on the deeper cerium layer and next to the V_O^{sub}, while it favors to locate in the top cerium layer and next to the V_O when creating one V_O^{sur}.

When creating one subsurface V_O in $CeO_2(100)$, we have considered two oxygen vacancy sites for the formation of one V_O^{sub} because there are two different Ce-O bond lengths as

illustrated in **Figure S1**. The most stable configuration of the V_O^{sub} on CeO_2(100) has one Ce^{3+} nearest neighbor and one Ce^{3+} next-nearest neighbor, as shown in **Table S3**. This most favored Ce^{3+} distribution around V_O^{sub} is 1.2 eV more stable than the second most stable Ce^{3+} distribution, indicating a highly unfavorable formation of other Ce^{3+} distribution. Overall, when creating one V_O^{sur} on CeO_2(100), the most favorable Ce^{3+} locations are the same as that for V_O^{sub}, see **Table S4**. In addition to the similar preference for Ce^{3+} locations, the formation energy of the most stable V_O^{sur} (1.62 eV) is also quite close to that of the V_O^{sub} (1.67 eV) on CeO_2(100). Thus, as compared to CeO_2(100), the preferred Ce^{3+} locations on CeO_2(110) are more sensitive to the position of the created V_O.

Finally, we summarize the oxygen formation energy of the most stable V_O^{sub} and V_O^{sur} on the (110), (100), and (111) facets of ceria in **Table 1,** with their preferred Ce^{3+} locations presented in **Figure 2 .** The formation energy of the V_O^{sur} on CeO_2(100) is 0.34 eV larger than that of the relaxed CeO_2(100) surface reported by Kropp et al.[55] The V_O^{sub} in CeO_2(110) is 0.18 eV more stable than the reported configuration.[5] Our previous work has shown that creating one oxygen vacancy in the subsurface of CeO_2(111) is 0.36 eV easier than creating one on the top surface.[17] By contrast, creating one V_O^{sur} on CeO_2(110) becomes 0.34 eV more facile than creating one V_O^{sub}. While the energy difference of the formation energy between V_O^{sur} and V_O^{sub} in CeO_2(100) is only 0.05 eV, indicating that the formation of V_O^{sur} is as facile as that of V_O^{sub} in CeO_2(100). Our results show that creating one V_O^{sur} becomes favorable compared to V_O^{sub} in CeO_2(110) and CeO_2(100). In addition, the formation energy of one oxygen vacancy is much lower on the (110) and (100) facets than that on the (111) facet, well consistent with previously reported findings.[24–26] Our findings show that the (110) and (100) facets are more reducible than the (111) facet by creating oxygen vacancies.

Table 1. Formation energy of one oxygen vacancy in the subsurface (V_O^{sub}) and top surface (V_O^{sur}) of CeO_2(110) and CeO_2(100), compared with CeO_2(111). The data for CeO_2(111) is taken from our previous work.[17]

	(110)	(100)	(111)
$E(V_O^{sub})$/eV	1.48	1.67	1.75
$E(V_O^{sur})$/eV	1.14	1.62	2.11

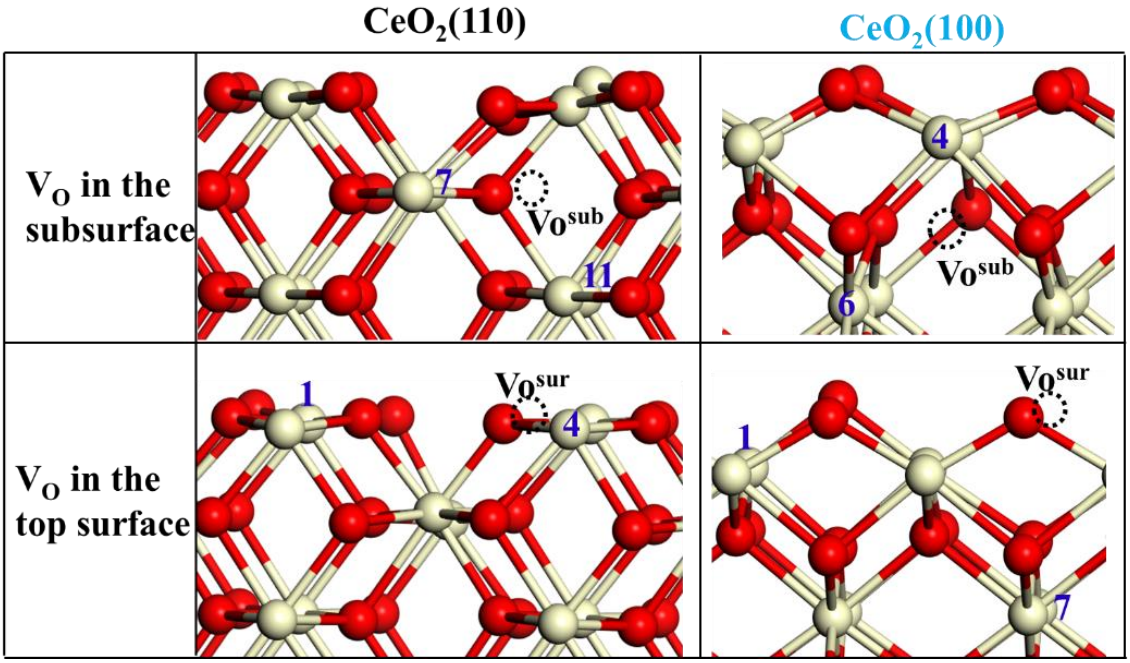

Figure 2. The most stable Ce^{3+} positions for the formation of one oxygen vacancy in the subsurface and top surface of CeO_2(110) and CeO_2(100). The numbering of Ce^{3+} positions corresponds to **Figure 1**.

Hydroxyl formation on CeO_2(110) and CeO_2(100). During the WSR, hydroxyls form via the water dissociation at reaction step (2). Ce^{3+} sitting next to hydroxyls is always the most favored location on CeO_2(111) with different hydrogen coverages.[17] In the following, we investigate hydroxyls formed by hydrogen adsorption on lattice oxygen in CeO_2(110) and CeO_2(100) and compare Ce^{3+} distributions at different hydrogen coverages.

For 1H adsorption on CeO_2(110), the most stable configuration is presented in **Figure 3(a)**, where one Ce^{3+} sits in the outmost layer and is nearest neighbor to the adsorbed H. The energy difference between different Ce^{3+} positions for 1H adsorption is below 0.38 eV, as shown in **Table S5**. For the formation of two hydroxyls on the (110) facet of ceria, the two hydroxyls can locate in one CeO_2 row (2H) or in the two different rows (2H') as shown in **Figure 3(b)** and **3(c)**, respectively. After comparing Ce^{3+} positions in different relaxed cerium layers for the 2H and 2H' structure as listed in **Table S5**, it is found that the most stable configuration of 2H is that one Ce^{3+} is nearest neighbor to the hydroxyls, while the other Ce^{3+} sits in the other row and far away from hydroxyls, as noted in **Figure 3(b)**. The energy difference among different Ce^{3+} positions in 2H is below 0.86 eV. However, $2Ce^{3+}$ are nearest neighbor to 2H', as shown in **Figure 3(c)** and the energy difference among different Ce^{3+} positions is smaller than 0.33 eV. Overall, the formation energy of 2H with the most stable Ce^{3+} positions is 0.43 eV lower than that of 2H' with the most stable Ce^{3+} positions, suggesting that the Ce^{3+} locations on CeO_2(110) is sensitive to the H adsorption site. For the formation of more hydroxyls on CeO_2(110), Ce^{3+} favors sitting next to hydroxyls, as shown in **Figure 3(d)** and **Table S6**. By contrast, the H adsorption sites on the (100) facet of ceria are symmetric. Ce^{3+} always prefers being nearest neighbor to hydroxyls as shown in **Table S7**, which has also been found on the (111) facet.[17]

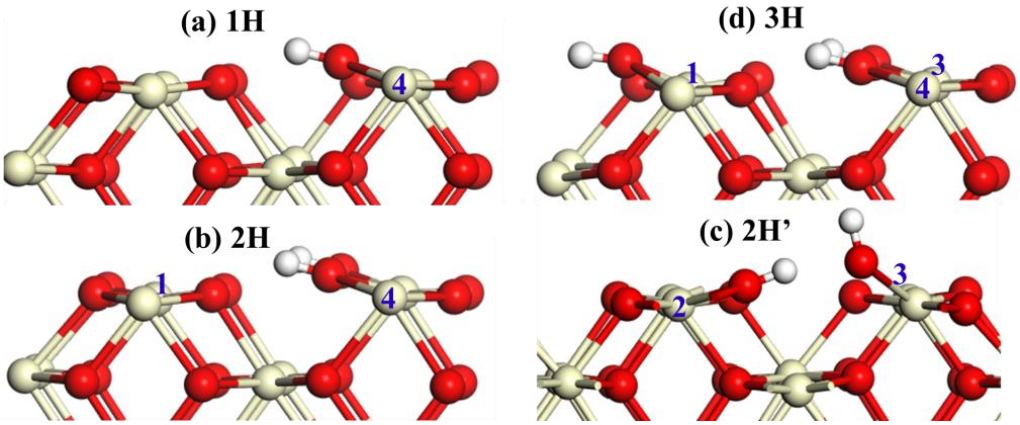

Figure 3. Hydrogen adsorption on the (110) facet with the most stable Ce^{3+} position at different hydrogen coverages. The numbering of Ce^{3+} positions corresponds to **Figure 1.**

Average hydrogen adsorption energy (E_H) diagrams of the most stable hydroxylated CeO_2(110) and CeO_2(100) as a function of hydrogen coverage (Θ_H) are presented in **Figure 4**. The data for CeO_2(111) is taken from reference 17. The definition of Θ_H ($\Theta_H = N_H/N$) is similar

to our previous work,[12,16,17] where it is the number of adsorbed H (N_H) divided by the total number of oxygen (N) in the outmost layer. The most stable configurations of hydroxylated ceria exposed with different facets are shown in **Figures S2** and **S3**. On the CeO_2(100) surface, E_H is around -1.7 eV at Θ_H <1. As the hydrogen coverage increases beyond one monolayer, E_H increases dramatically to -1.2 eV, suggesting that more than one monolayer coverage is unstable compared to a lower hydrogen coverage on the CeO_2(100) surface. In contrast, E_H on CeO_2(110) increases significantly for hydrogen coverages above half a monolayer. As seen from **Figure 4**, hydrogen adsorbs strongest on the (100) facet followed by the (110) and (111) facets at low coverage. The formation of one monolayer hydrogen coverage, is however favored in the order of (100), (111) and (110). **Figure 4** reveals that the hydroxylated CeO_2(100) is much more stable than the hydroxylated CeO_2(110). These results are well consistent with the experimental findings that hydroxyls are much more stable on the (100) than on the (111) facet.[30] The more stable formation of hydroxyls on ceria is expected to inhibit hydroxyl decomposition for H_2 productions on ceria.[12,16,17]

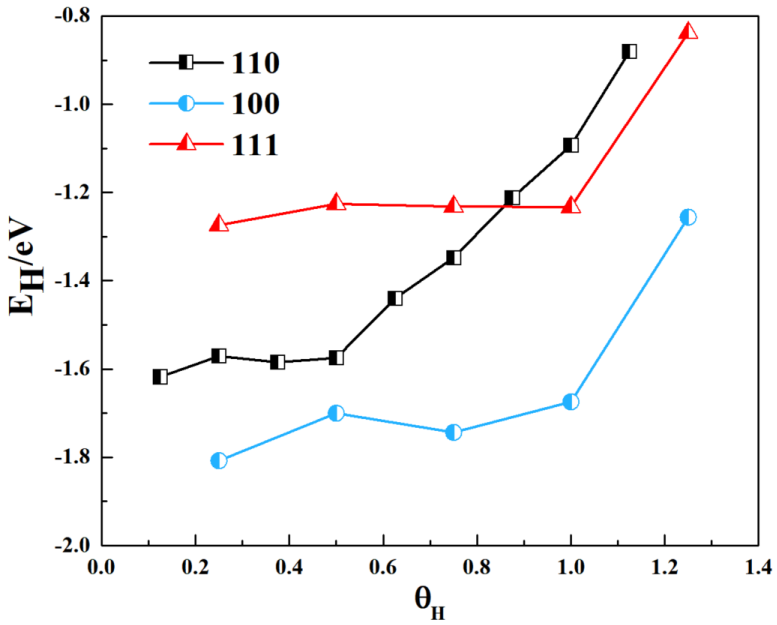

Figure 4. Average hydrogen adsorption energy (E_H) on the (110), (100), and (111) facets of ceria, at different hydrogen coverages (Θ_H).

Formation of vacancy-hydroxyl mixed phases on CeO_2(110) and CeO_2(100). Along the reaction pathways of the H_2 production on the partially (i.e. 2H, 4H, 5H, and 6H), fully (8H), and excessively (9H) hydroxylated CeO_2(110), ceria surfaces form vacancy-hydroxyl mixed

phases when creating one V_O in the 3H, 4H, 6H, and 7H covered CeO_2(110). During the WSR on the partially (2H), fully (4H), and excessively (5H) hydroxylated CeO_2(100), the vacancy-hydroxyl mixed phase on CeO_2(100) forms when creating one V_O on the 3H covered CeO_2(100). We have investigated various Ce^{3+} distributions on these vacancy-hydroxyl mixed phases, as shown in **Tables S8 and S9**. The top cerium atomic layer accommodates $3Ce^{3+}$ for the 3H covered CeO_2(110). When creating one V_O in it, one Ce^{3+} firstly sits on the top cerium layer (making all cerium atoms in this layer Ce^{3+}) while the other Ce^{3+} locates in the third cerium layer, next to the V_O^{sub}. However, when creating one V_O^{sur}, the other Ce^{3+} sits in the second cerium layer and is next-nearest neighbor to V_O^{sur}. Creating one V_O on the 4H covered CeO_2(110), where all Ce^{4+} ions on the top cerium layer have been reduced to Ce^{3+} ions because of hydrogen adsorptions, $2Ce^{3+}$ prefer to sit in the second cerium layer and nearest to the V_O^{sub}. When creating one V_O^{sur} on the 4H covered CeO_2(110), one Ce^{3+} sits in the second cerium layer and next to the vacancy, while the other Ce^{3+} sits in the third cerium layer as next-nearest neighbor to the vacancy. When creating one V_O in the 6H or 7H covered CeO_2(110) surface, the next-nearest neighbor positions to the V_O become unfavorable, leading to $2Ce^{3+}$ located next to the vacancy. The energy difference between different Ce^{3+} locations in the vacancy-hydroxyl mixed phase on CeO_2(110) is below 0.82 eV, which is lower than oxygen vacancy in CeO_2(110) without hydroxyls. In contrast, the energy difference between different Ce^{3+} locations in vacancy-hydroxyl mixed phases on CeO_2(100) is below 0.16 eV. Therefore, there is no obviously favored Ce^{3+} distributions when creating one V_O in the hydroxylated CeO_2(100), while Ce^{3+} prefers to sit next to V_O on hydroxylated CeO_2(110).

In addition, the formation energy of V_O in the CeO_2(110) and CeO_2(111) surfaces increases with increasing Θ_H. Oxygen vacancies in the surface or subsurface becomes unstable compared to the formation of one oxygen vacancy in a cubic bulk ($Ce_{32}O_{64}$), when the surface is covered by more than one monolayer hydrogen, as shown in **Figure S4**. In contrast, the formation of one oxygen vacancy in the hydroxylated CeO_2(100) with Θ_H = 0.5 and Θ_H = 0.75 is 1.0 and 0.5 eV, respectively, more stable than creating one V_O in the hydroxylated CeO_2(110) and CeO_2(111).

The most efficient reaction pathways on CeO_2(110) and CeO_2(100). After investigating the formation of oxygen vacancies, hydroxyls and vacancy-hydroxyl mixed phases, we calculate the free energies of these reaction intermediates relative to a clean stoichiometric ceria surface

by using the method described in our previous works,[12,16,17] where the reduced CeO_2(111) surfaces form via reactions between oxygen vacancies and water (1 bar) at the reference surface. Then we draw the free energy diagrams of the H_2 production on the partially, fully, and excessively hydroxylated ceria, as presented in **Figures 5, 6, and S5-S9**. In addition, the magnetizations at each reaction step are also list in **Tables S10-S16**.

The reaction pathways of the WSR on the partially (2H, 4H, 5H, and 6H), fully (8H), and excessively (9H) hydroxylated CeO_2(110) are shown in **Figures 5 and S5-S8**. The activation barrier for the formation of H_2 via 2H from one as well as two different rows is investigated on the 2H, 5H, 6H, and 8H covered CeO_2(110), where we use the annotations like 8H and 8H' to represent the H_2 production via 2H from one and two rows of the 8H covered CeO_2(110), respectively. For the H_2 production on the 2H covered CeO_2(110) surface as presented in **Figure S5**, the reactions including oxygen vacancy formation and diffusion, as well as water adsorption and dissociation are facile compared to the hydroxyl decomposition into H_2. Although 2H is 0.43 eV more stable than 2H', we find that the energy of the transition state for breaking 2H is close to that for 2H'. Hydroxyl decomposition for H_2 production remains the rate-determining step when more hydroxyls form on CeO_2(110) and the hydrogen coverage is below one monolayer, as seen from **Figure 5**. Similar transition states are found during hydroxyl decompositions on the hydroxylated CeO_2(110) with hydrogen coverage below one monolayer, where one hydrogen moves close to the other with one hydroxyl firstly broken and concomitant oxidation of Ce^{3+} to Ce^{4+}, see the magnetization changes in **Tables S10-S13**. The H_2 production via 2H from two different rows is 0.28 eV more favored over that from one same row when the surface has five hydroxyls, while that transition state for H_2 production via 2H from the same row is 0.26 eV more stable than that from the two different rows when the surface has six hydroxyls. When the surface is fully hydroxylated, the H_2 production via the 8H pathway is 0.18 eV more favorable than the 8H' pathway. The efficient H_2 production via breaking 2H on CeO_2(110) is affected by the hydrogen coverage.

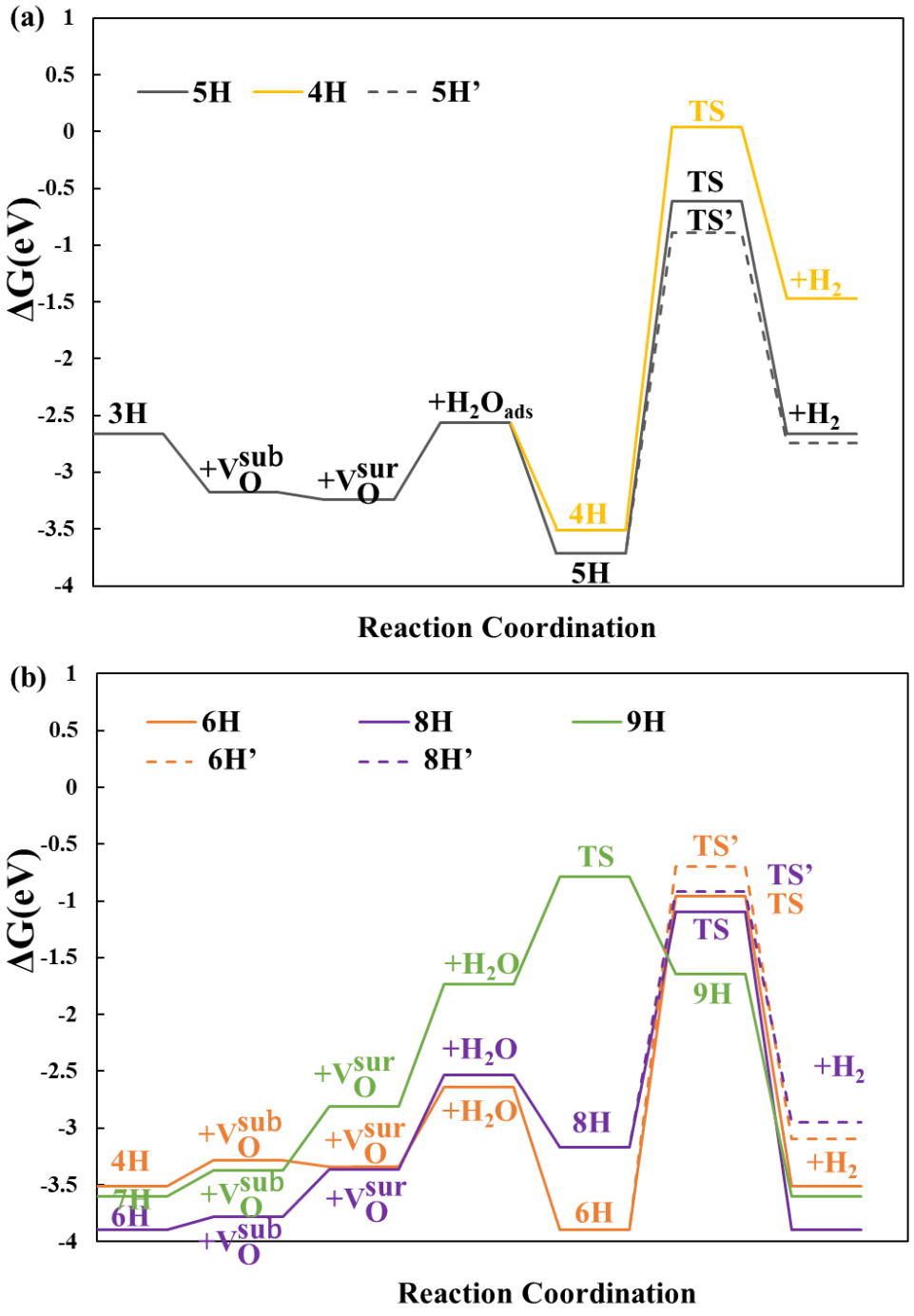

Figure 5. Free energy diagrams at 800 K for the WSR pathways on CeO_2(110) with different hydrogen coverages: (a) 4H, 5H, and 5H'; (b) 6H, 6H', 8H, 8H', and 9H. The configurations of intermediates at each reaction step are presented in **Figures S7 and S8**. The magnetizations of each intermediate are given in **Tables S11-S14**.

By contrast, the hydroxyl decomposition on the excessively hydroxylated CeO_2(110) has no activation barrier, which has also been found for the WSR on CeO_2(111).[12,17] However, an 1.0 eV activation barrier is found for forming the excessively hydroxylated CeO_2(110) via reaction (4), where one H binds with one lattice Ce to form one Ce-H. The rate-determining step during the WSR on the excessively hydroxylated CeO_2(110) becomes the water dissociation into the Ce-H. Although the free energies of each reaction intermediate increase when temperature increases to 1200 K, the rate-determining step along each reaction pathway remains unchanged.

In summary, the most favorable reaction pathway for the WSR on CeO_2(110) at 800 K is the H_2 production on the fully hydroxylated CeO_2(110). As temperature increases to 1200 K, the formation of the fully and excessively hydroxylated CeO_2(110) surface becomes less favorable than the partially hydroxylated CeO_2(110). Therefore, the most efficient hydroxyl decomposition into H_2 at 1200 K proceeds via the partially hydroxylated CeO_2(110) covered by five hydrogens.

Figure 6 presents the reaction pathways of the WSR on the partially (2H), fully (4H), and excessively (5H) hydroxylated CeO_2(100), at 800 K. **Figure S9** compares these reaction pathways at 1200 K. The fully hydroxylated CeO_2(100) surface is more stable than other intermediates at both 800 and 1200 K. Similarly with the WSR on the CeO_2(110) surface, the hydroxyl decomposition into H_2 is the most difficult step during the WSR on the partially and fully hydroxylated CeO_2(100). The identified transition states for hydroxyl decomposition on the partially and fully hydroxylated CeO_2(100) (having a 3.6 eV activation barrier) are similar to that on the (110) and (111) facets, where one H moves close to the neighboring cerium, leading to break apart hydroxyl and oxidize one Ce^{3+} to Ce^{4+}, consistent with the previously reported findings.[28,56] However, the H_2 production on the excessively hydroxylated CeO_2(100) formation where one H binds with one lattice oxygen from the subsurface, only has a 1.8 eV activation barrier. Overall, the fastest reaction on CeO_2(100) proceeds on the excessively hydroxylated surfaces at both 800 and 1200 K.

By comparing the reaction pathways on different facets of ceria, the most favorable reaction pathway on ceria is found to be strongly facet-dependent, with the WSR on the CeO_2(100) and CeO_2(111) facets most efficiently proceeding on the excessively hydroxylated surfaces. However, the fastest hydrogen production via the WSR on CeO_2(110) facet takes

place on the fully hydroxylated surface at 800 K, while it preferentially proceeds on the CeO_2(110) surface with a lower hydrogen coverage at 1200 K.

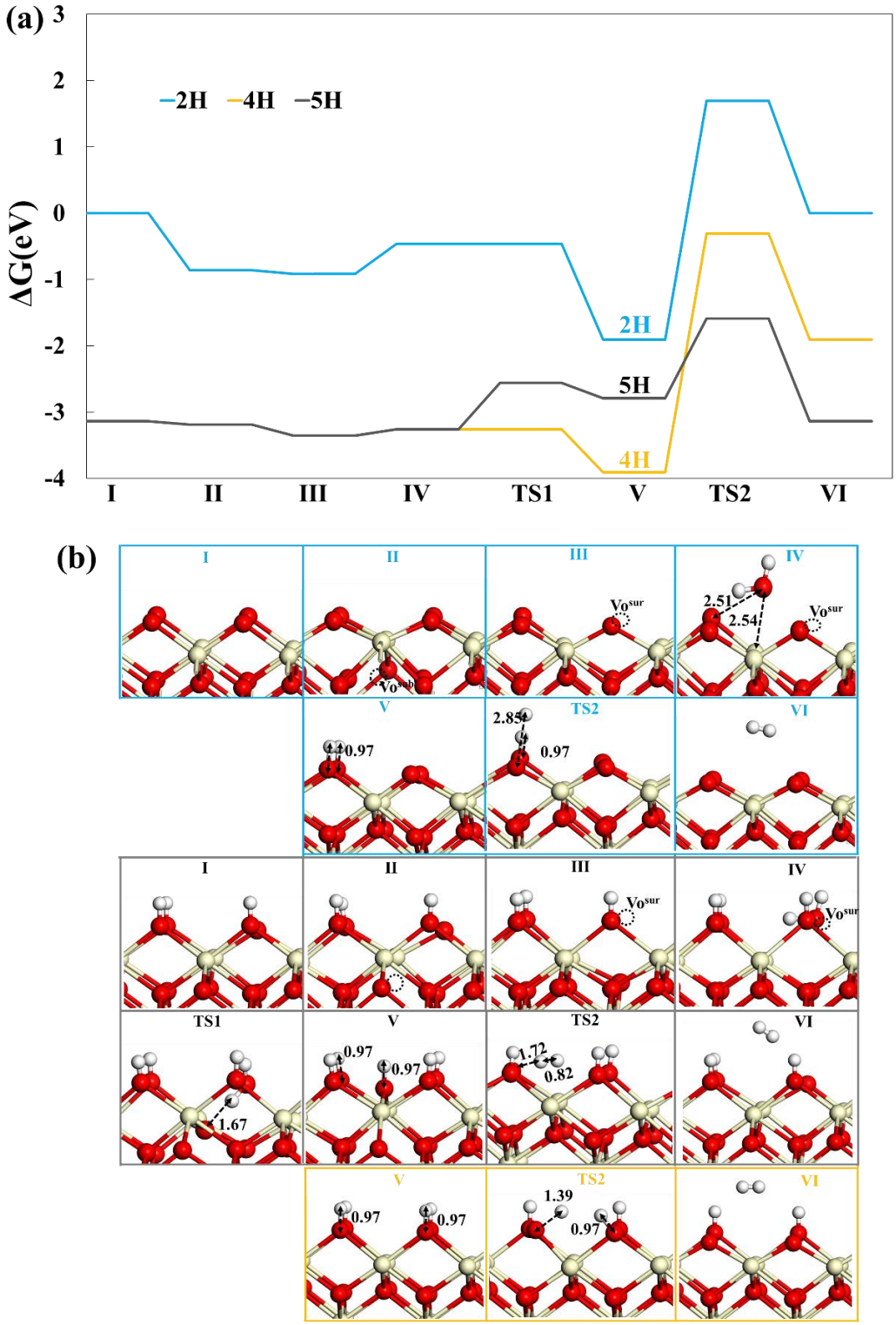

Figure 6. (a) Free energy diagrams at 800 K for the WSR on the hydroxylated CeO_2(100) with different hydrogen coverages. (b) The configurations of intermediates at each reaction step are

shown with selected bond lengths indicated. The magnetizations of each intermediate are given in **Tables S15 and S16**.

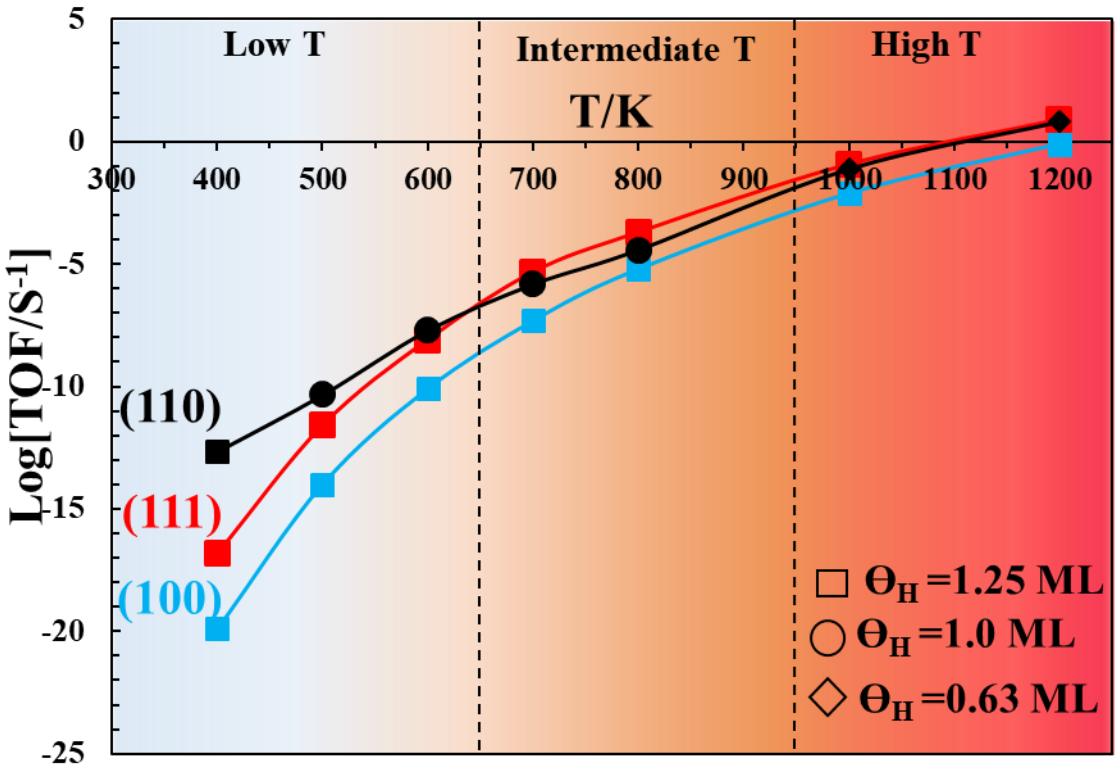

Figure 7. Mapping of the turnover frequency (TOF) of the most efficient reaction pathway (with specific hydrogen coverage) on CeO_2(100), CeO_2(110) and CeO_2(111), respectively, at $400 \leq T \leq 1200$ K.

To give a better understanding of the facet-dependence of the electrocatalytic WSR on ceria, we map the most favored reaction pathways on these facets of ceria at $400 \leq T \leq 1200$ K, which is divided into three temperature regions, as shown in **Figure 7**. The turnover frequency (TOF) for the WSR on the (110) and (100) facets of ceria is calculated by using energetic span between TOF determining intermediate and TOF determining transition state, see the energetic span analysis on the (111) facet of ceria for details.[17] The TOF for the WSR on CeO_2(111) is calculated by using data from our previous simulations.[17] In the low-T region (T< 650 K), the reaction on the hydroxylated ceria with Θ_H=1.25 ML is predicted to be favored on the (110), (111), and (100) facets of ceria. In the intermediate-T region (650 < T < 950 K), the fastest reaction pathway remains on the overly hydroxylated (111) and (100) facets of ceria, while the reaction on the surface with Θ_H=1.0 ML becomes favored on the (110) facet of ceria. In the high-T region (T > 950 K), the most efficient reaction pathway on the (110) facet of ceria shifts

to the reaction on the partially hydroxylated surface with Θ_H=0.63 ML. Thus, the most favored reaction pathway on CeO_2(110) is more sensitive to the operating temperature, as compared to CeO_2(100) and CeO_2(111). This is because the formation of hydroxyls and vacancy-hydroxyl mixed phase on CeO_2(110) is very dependent on the hydrogen coverages and adsorption sites as described in the previous section. The most active hydroxylated surface is affected by the operating temperature, as shown in **Figure 7**. The formation of more than 2H coverage on each facet improves the activity by orders of magnitude for the WSR for each facet at any operating temperature, as seen from **Figure S10.**

In summary, the WSR is most efficient on the (110) facet, followed by the (111) and (100) facets in the low-T region. However, the WSR is fastest on the (111) facet at 650 < T < 950 K. At a higher T, the TOF of the WSR on CeO_2(110) is very closed to that on CeO_2(111), but 10~100 times higher than that on CeO_2(100). Overall, the WSR for H_2 productions on the (111) and (110) facets of ceria is 10~100 times faster than on the (100) facet of ceria at T < 950 K. Thus, the WSR on ceria is strongly facet-dependent at low and intermediate temperature. The Brønsted-Evans-Polanyi (BEP) relation[57] for hydroxyl decomposition on different facets of ceria is established, and shown in **Figure S11**. The BEP relation clearly shows that the H_2 production via hydroxyl decompositions on the hydroxylated CeO_2(100) is more difficult than that on the hydroxylated CeO_2(111) and CeO_2(110), which is consistent with the finding that the higher stability of the hydroxyls on the CeO_2(100) surface leads to more difficult hydroxyl decomposition into H_2 as discussed **Figure 4**. Our findings agree with experiments that a smaller amount of H_2 is produced from reduced CeO_2(100) between 450 and 730 K compared to the (111) facet.[30] Therefore, our studies on the mapping of the TOF for the WSR on the (110), (111) and (100) facets of ceria provides an improved understanding of the electrocatalytic WSR on ceria and its facet-dependent behavior.

CONCLUSIONS

After investigating the formation of the reaction intermediates and reaction kinetics of the WSR on ceria exposed with (110) and (100) facets which is compared to the WSR on the (111) facet of ceria, we find the WSR on ceria is strongly facet-dependent. Compared with the (100) and (111) facets, Ce^{3+} distribution on the reduced CeO_2(110) is more sensitive to H adsorption sites and positions of the created V_O. Although varying with different Ce^{3+} distributions, the formation of one oxygen vacancy on the (100) and (110) facets of ceria is found to be more

facile than that on the (111) facet. The preferred Ce^{3+} distributions on these facets of ceria vary significantly, having an energy difference between Ce^{3+} distributions on the CeO_2(110) and CeO_2(100) surfaces above 0.95 and 1.21 eV, respectively. However, the energy difference between Ce^{3+} positions of vacancy-hydroxyl mixed phases becomes smaller, with Ce^{3+} preferentially sitting next to hydroxyls and next nearest neighbor to oxygen vacancies. The formation of hydroxyls and vacancy-hydroxyl mixed phase on the (100) facet of ceria is much more stable than on the (110) and (111) facets. The formation of the fully hydroxylated CeO_2(100) and CeO_2(111) is always thermodynamically favored over other hydrogen coverages at different operating temperature. The formation of the fully hydroxylated CeO_2(110) becomes unstable, leading to a relatively low activation barrier for the H_2 production via hydroxyl decomposition. The high stability of the hydroxyls on CeO_2(100) inhibits hydroxyl decomposition into H_2.

In addition, the most favored reaction pathways on ceria is also facet-dependent, with the WSR preferentially proceeding on the excessively hydroxylated surface on the (100) and (111) facets, while the preferred pathway on the (110) facet varies with operating temperature. The most favorable pathway on the CeO_2(110) facet proceeds on the fully hydroxylated surfaces at 800 K and shifts on the partially hydroxylated CeO_2(110) at a higher temperature. We further give a mapping of the most favored reaction pathways on these facets at $400 \leq T \leq 1200$ K, and we show that the WSR on ceria is strongly facet-dependent for $T < 950$ K. This strong facet-dependence of the WSR on ceria diminishes above 950 K. These findings suggest that the facet-dependence of the WSR on ceria is temperature sensitive. Therefore, our studies give more understanding of the WSR on the ceria exposed with different low-index facets, which can be further extended to other electrocatalysis like CO oxidation and NO reduction on ceria-based catalysts.

ASSOCIATED CONTENT

Supporting Information:

The supporting information includes the following:

Tables including information of Ce^{3+} locations with V_O, hydroxyls and vacancy-hydroxyl mixed phases. Tables including magnetizations of the reaction intermediates during the WSR. Figures presenting configurations of reaction intermediates during the WSR on CeO_2(110) and CeO_2(100). Figures showing the reaction pathways on CeO_2(110) and CeO_2(100). Figure

presenting BEP relation for the hydroxyl decomposition into H_2 on the CeO_2(110), CeO_2(100) and CeO_2(111) surfaces at different hydrogen coverages. Figure showing formation energy of one oxygen vacancy in hydroxylated (110), (100) and (111) facets of ceria. Figure shows the comparison of TOF between the fastest WSR and the reaction via 2H coverage.

ACKNOWLEDGMENTS

This work was finally supported by the Velux Foundations through the research center V-Sustain (grant number 9455). We also thank Dr. M. Rellán-Piñeiro and N. Daelman for useful discussions.

REFERENCES

(1) Jen, H.-W.; Graham, G. W.; Chun, W.; McCabe, R. W.; Cuif, J.-P.; Deutsch, S. E.; Touret, O. Characterization of Model Automotive Exhaust Catalysts: Pd on Ceria and Ceria–Zirconia Supports. *Catal. Today* **1999**, *50*, 309–328.

(2) Oh, S. H.; Hoflund, G. B. Chemical State Study of Palladium Powder and Ceria-Supported Palladium during Low-Temperature CO Oxidation. *J. Phys. Chem. A* **2006**, *110*, 7609–7613.

(3) Di Monte, R.; Kašpar, J. On the Role of Oxygen Storage in Three-Way Catalysis. *Top. Catal.* **2004**, *28*, 47–57.

(4) Liu, X.; Zhou, K.; Wang, L.; Wang, B.; Li, Y. Oxygen Vacancy Clusters Promoting Reducibility and Activity of Ceria Nanorods. *J. Am. Chem. Soc.* **2009**, *131*, 3140–3141.

(5) Song, Y.-L.; Yin, L.-L.; Zhang, J.; Hu, P.; Gong, X.-Q.; Lu, G. A DFT+*U* Study of CO Oxidation at CeO_2(110) and (111) Surfaces with Oxygen Vacancies. *Surf. Sci.* **2013**, *618*, 140–147.

(6) Bunluesin, T.; Gorte, R. J.; Graham, G. W. Studies of the Water-Gas-Shift Reaction on Ceria-Supported Pt, Pd, and Rh: Implications for Oxygen-Storage Properties. *Appl. Catal. B Environ.* **1998**, *15*, 107–114.

(7) Fu, Q.; Saltsburg, H.; Flytzani-Stephanopoulos, M. Active Nonmetallic Au and Pt Species on Ceria-Based Water-Gas Shift Catalysts. *Science* **2003**, *301*, 935–938.

(8) Hilaire, S.; Wang, X.; Luo, T.; Gorte, R. J.; Wagner, J. A Comparative Study of Water-Gas-Shift Reaction over Ceria-Supported Metallic Catalysts. *Appl. Catal. A Gen.* **2001**, *215*, 271–278.

(9) Puértolas, B.; Rellán-Piñeiro, M.; Núñez-Rico, J. L.; Amrute, A. P.; Vidal-Ferran, A.; López, N.; Pérez-Ramírez, J.; Wershofen, S. Mechanistic Insights into the Ceria-Catalyzed Synthesis

of Carbamates as Polyurethane Precursors. *ACS Catal.* **2019**, *9*, 7708-7720.

(10) Capdevila-Cortada, M.; Vilé, G.; Teschner, D.; Pérez-Ramírez, J.; López, N. Reactivity Descriptors for Ceria in Catalysis. *Appl. Catal. B Environ.* **2016**, *197*, 299–312.

(11) Feng, Z. A.; El Gabaly, F.; Ye, X.; Shen, Z.-X.; Chueh, W. C. Fast Vacancy-Mediated Oxygen Ion Incorporation across the Ceria-Gas Electrochemical Interface. *Nat. Commun.* **2014**, *5*, 4374.

(12) Hansen, H. A.; Wolverton, C. Kinetics and Thermodynamics of H_2O Dissociation on Reduced CeO_2(111). *J. Phys. Chem. C* **2014**, *118*, 27402–27414.

(13) Paier, J.; Penschke, C.; Sauer, J. Oxygen Defects and Surface Chemistry of Ceria: Quantum Chemical Studies Compared to Experiment. *Chem. Rev.* **2013**, *113*, 3949–3985.

(14) Irvine, J. T. S.; Neagu, D.; Verbraeken, M. C.; Chatzichristodoulou, C.; Graves, C.; Mogensen, M. B. Evolution of the Electrochemical Interface in High-Temperature Fuel Cells and Electrolysers. *Nat. Energy* **2016**, *1*, 15014.

(15) Sapountzi, F. M.; Gracia, J. M.; Weststrate, C. J.; Fredriksson, H. O. A.; Niemantsverdriet, J. W. Electrocatalysts for the Generation of Hydrogen, Oxygen and Synthesis Gas. *Prog. Energy Combust. Sci.* **2017**, *58*, 1–35.

(16) Wu, T.; Deng, Q.; Hansen, H. A.; Vegge, T. Mechanism of Water Splitting on Gadolinium-Doped CeO_2(111): A DFT+*U* Study. *J. Phys. Chem. C* **2019**, *123*, 5507–5517.

(17) Wu, T.; Vegge, T.; Hansen, H. A. Improved Electrocatalytic Water Splitting Reaction on CeO_2(111) by Strain Engineering: A DFT+*U* Study. *ACS Catal.* **2019**, *9*, 4853–4861.

(18) Chueh, W. C.; Hao, Y.; Jung, W.; Haile, S. M. High Electrochemical Activity of the Oxide Phase in Model Ceria-Pt and Ceria-Ni Composite Anodes. *Nat. Mater.* **2012**, *11*, 155–161.

(19) Zhang, C.; Grass, M. E.; McDaniel, A. H.; Decaluwe, S. C.; Gabaly, F. E.; Liu, Z.; McCarty, K. F.; Farrow, R. L.; Linne, M. A.; Hussain, Z.; Jackson, G. S.; Bluhm, H.; Eichhorn, B. W. Measuring Fundamental Properties in Operating Solid Oxide Electrochemical Cells by Using in Situ X-Ray Photoelectron Spectroscopy. *Nat. Mater.* **2010**, *9*, 944–949.

(20) Aneggi, E.; Wiater, D.; Leitenburg, C. D.; Llorca, J.; Trovarelli, A. Shape-Dependent Activity of Ceria in Soot Combustion. *ACS Catal.* **2014**, *4*, 172–181.

(21) Yang, C.; Yu, X.; Heißler, S.; Nefedov, A.; Colussi, S.; Llorca, J.; Trovarelli, A.; Wang, Y.; Wöll, C. Surface Faceting and Reconstruction of Ceria Nanoparticles. *Angew. Chem. Int. Ed.* **2017**, *56*, 375–379.

(22) Pan, Y.; Nilius, N.; Stiehler, C.; Freund, H. J.; Goniakowski, J.; Noguera, C. Ceria Nanocrystals Exposing Wide (100) Facets: Structure and Polarity Compensation. *Adv. Mater. Interfaces* **2014**, *1*, 1400404.

(23) Jiang, Y.; Adams, J. B.; Van Schilfgaarde, M. Density-Functional Calculation of CeO_2 Surfaces and Prediction of Effects of Oxygen Partial Pressure and Temperature on Stabilities. *J. Chem. Phys.* **2005**, *123*, 064701.

(24) Wang, D.; Kang, Y.; Doan-Nguyen, V.; Chen, J.; Küngas, R.; Wieder, N. L.; Bakhmutsky, K.; Gorte, R. J.; Murray, C. B. Synthesis and Oxygen Storage Capacity of Two-Dimensional Ceria Nanocrystals. *Angew. Chem. Int. Ed.* **2011**, *50*, 4378–4381.

(25) Conesa, J. C. Computer Modeling of Surfaces and Defects on Cerium Dioxide. *Surf. Sci.* **1995**, *339*, 337–352.

(26) Sayle, D. C.; Maicaneanu, S. A.; Watson, G. W. Atomistic Models for CeO_2(111), (110), and (100) Nanoparticles, Supported on Yttrium-Stabilized Zirconia. *J. Am. Chem. Soc.* **2002**, *124*, 11429–11439.

(27) Vilé, G.; Colussi, S.; Krumeich, F.; Trovarelli, A.; Pérez-Ramírez, J. Opposite Face Sensitivity of CeO_2 in Hydrogenation and Oxidation Catalysis Angewandte. *Angew. Chem. Int. Ed.* **2014**, *53*, 12069–12072.

(28) Capdevila-Cortada, M.; García-Melchor, M.; López, N. Unraveling the Structure Sensitivity in Methanol Conversion on CeO_2: A DFT+*U* Study. *J. Catal.* **2015**, *327*, 58–64.

(29) Spezzati, G.; Benavidez, A. D.; Delariva, A. T.; Su, Y.; Hofmann, J. P.; Asahina, S.; Olivier, E. J.; Neethling, J. H.; Miller, T.; Datye, A. K. CO Oxidation by Pd Supported on CeO_2(100) and CeO_2(111) Facets. *Appl. Catal. B Environ.* **2019**, *243*, 36–46.

(30) Mullins, D. R.; Albrecht, P. M.; Chen, T.-L.; Calaza, F. C.; Biegalski, M. D.; Christen, H. M.; Overbury, S. H. Water Dissociation on CeO_2(100) and CeO_2(111) Thin Films. *J. Phys. Chem. C* **2012**, *116*, 19419–19428.

(31) Molinari, M.; Parker, S. C.; Sayle, D. C.; Islam, M. S. Water Adsorption and Its Effect on the Stability of Low Index Stoichiometric and Reduced Surfaces of Ceria. *J. Phys. Chem. C* **2012**, *116*, 7073–7082.

(32) Yang, Z.; Wang, Q.; Wei, S.; Ma, D.; Sun, Q. The Effect of Environment on the Reaction of Water on the Ceria (111) Surface : A DFT+*U* Study. *J. Phys. Chem. C* **2010**, *114*, 14891–14899.

(33) Fernández-Torre, D.; Carrasco, J.; Ganduglia-Pirovano, M. V.; Pérez, R. Hydrogen Activation,

Diffusion, and Clustering on CeO_2(111): A DFT+*U* Study. *J. Chem. Phys.* **2014**, *141*, 014703.

(34) Ganduglia-Pirovano, M. V.; Da Silva, J. L. F.; Sauer, J. Density-Functional Calculations of the Structure of near-Surface Oxygen Vacancies and Electron Localization on CeO_2(111). *Phys. Rev. Lett.* **2009**, *102*, 026101.

(35) Ma, D.; Lu, Z.; Tang, Y.; Li, T.; Tang, Z.; Yang, Z. Effect of Lattice Strain on the Oxygen Vacancy Formation and Hydrogen Adsorption at CeO_2(111) Surface. *Phys. Lett. A* **2014**, *378*, 2570–2575.

(36) Gopal, C. B.; García-Melchor, M.; Lee, S. C.; Shi, Y.; Shavorskiy, A.; Monti, M.; Guan, Z.; Sinclair, R.; Bluhm, H.; Vojvodic, A.; Chueh, W. C. Equilibrium Oxygen Storage Capacity of Ultrathin $CeO_{2-\delta}$ Depends Non-Monotonically on Large Biaxial Strain. *Nat. Commun.* **2017**, *8*, 15360.

(37) Capdevila-Cortada, M.; López, N. Descriptor Analysis in Methanol Conversion on Doped CeO_2(111): Guidelines for Selectivity Tuning. *ACS Catal.* **2015**, *5*, 6473–6480.

(38) Su, Y. Q.; Filot, I. A. W.; Liu, J. X.; Tranca, I.; Hensen, E. J. M. Charge Transport over the Defective CeO_2(111) Surface. *Chem. Mater.* **2016**, *28*, 5652–5658.

(39) Aparicio-Anglès, X.; Roldan, A.; De Leeuw, N. H. Gadolinium-Vacancy Clusters in the (111) Surface of Gadolinium-Doped Ceria: A Density Functional Theory Study. *Chem. Mater.* **2015**, *27*, 7910–7917.

(40) Gerward, L.; Olsen, J. S.; Petit, L.; Vaitheeswaran, G.; Kanchana, V.; Svane, A. Bulk Modulus of CeO_2 and PrO_2—An Experimental and Theoretical Study. *J. Alloys Compd.* **2005**, *400*, 56–61.

(41) Herman, G. S. Surface Structure Determination of CeO_2(001) by Angle-Resolved Mass Spectroscopy of Recoiled Ions. *Phys. Rev. B* **1999**, *59*, 14899–14902.

(42) Kropp, T.; Paier, J.; Sauer, J. Interactions of Water with the (111) and (100) Surfaces of Ceria. *J. Phys. Chem. C* **2017**, *121*, 21571–21578.

(43) Beste, A.; Overbury, S. H. Pathways for Ethanol Dehydrogenation and Dehydration Catalyzed by Ceria (111) and (100) Surfaces. *J. Phys. Chem. C* **2015**, *119*, 2447–2455.

(44) Capdevila-Cortada, M.; López, N. Entropic Contributions Enhance Polarity Compensation for CeO_2(100) Surfaces. *Nat. Mater.* **2017**, *16*, 328–334.

(45) Kresse, G.; Furthmüller, J. Efficient Iterative Schemes for Ab Initio Total-Energy Calculations Using a Plane-Wave Basis Set. *Phys. Rev. B* **1996**, *54*, 11169–11186.

(46) Kresse, G.; Hafner, J. Ab Initio Molecular Dynamics for Open-Shell Transition Metals. *Phys. Rev. B* **1993**, *48*, 13115–13118.

(47) Perdew, J. P.; Burke, K.; Ernzerhof, M. Generalized Gradient Approximation Made Simple. *Phys. Rev. Lett.* **1996**, *77*, 3865–3868.

(48) Blöchl, P. E. Projector Augmented-Wave Method. *Phys. Rev. B* **1994**, *50*, 17953–17979.

(49) Fabris, S.; Gironcoli, S. D.; Baroni, S.; Vicario, G.; Balducci, G. Reply to Comment on "Taming Multiple Valency with Density Functionals: A Case Study of Defective Ceria." *Phys. Rev. B* **2005**, *72*, 237102.

(50) Farra, R.; García-Melchor, M.; Eichelbaum, M.; Hashagen, M.; Frandsen, W.; Allan, J.; Girgsdies, F.; Szentmiklósi, L.; López, N.; Teschner, D. Promoted Ceria: A Structural, Catalytic, and Computational Study. *ACS Catal.* **2013**, *3*, 2256–2268.

(51) Su, Y.-Q.; Liu, J.-X.; Filot, I. A. W.; Zhang, L.; Hensen, E. J. M. Highly Active and Stable CH_4 Oxidation by Substitution of Ce^{4+} by Two Pd^{2+} Ions in CeO_2(111). *ACS Catal.* **2018**, *8*, 6552–6559.

(52) Daelman, N.; Capdevila-Cortada, M.; López, N. Dynamic Charge and Oxidation State of Pt/CeO_2 Single-Atom Catalysts. **2019** DOI: https://doi.org/10.1038/s41563-019-0444-y.

(53) Henkelman, G.; Uberuaga, B. P.; Jónsson, H. Climbing Image Nudged Elastic Band Method for Finding Saddle Points and Minimum Energy Paths. *J. Chem. Phys.* **2000**, *113*, 9901–9904.

(54) Larsen, A. H.; Mortensen, J. J.; Blomqvist, J.; Castelli, I. E.; Christensen, R.; Dulak, M.; Friis, J.; Groves, M. N.; Hammer, B.; Hargus, C.; et al. The Atomic Simulation Environment—A Python Library for Working with Atoms. *J. Phys. Condens. Matter* **2017**, *29*, 273002.

(55) Kropp, T.; Paier, J. Activity versus Selectivity of the Methanol Oxidation at Ceria Surfaces: A Comparative First-Principles Study. *J. Phys. Chem. C* **2015**, *119*, 23021–23031.

(56) García-Melchor, M.; López, N. Homolytic Products from Heterolytic Paths in H_2 Dissociation on Metal Oxides: The Example of CeO_2. *J. Phys. Chem. C* **2014**, *118*, 10921–10926.

(57) Logadottir, A.; Rod, T. H.; Nørskov, J. K.; Hammer, B.; Dahl, S.; Jacobsen, C. J. H. The Brønsted-Evans-Polanyi Relation and the Volcano Plot for Ammonia Synthesis over Transition Metal Catalysts. *J. Catal.* **2001**, *197*, 229–231.

Figure of TOC:

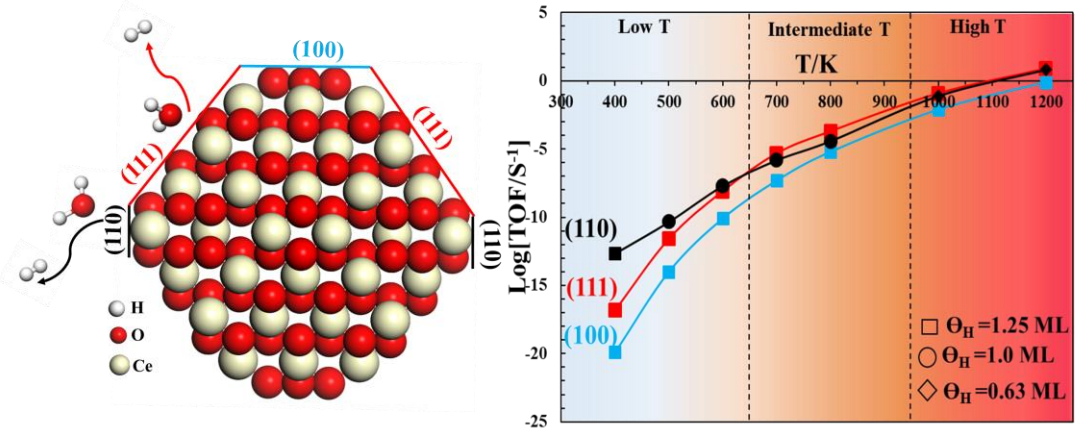

Supporting Information for "Facet-Dependent Electrocatalytic Water Splitting Reaction on CeO_2: A DFT+*U* Study"

Tiantian Wu, [a] Núria López, [b,*] Tejs Vegge,[a] Heine Anton Hansen[a,*]

[a] Department of Energy Conversion and Storage, Technical University of Denmark, Fysikvej, 2800 Kgs. Lyngby, Denmark.

[b] Institute of Chemical Research of Catalonia (ICIQ), The Barcelona Institute of Science and Technology, Tarragona, Spain

*Corresponding author:

Núria López E-mail: nlopez@iciq.es

Heine Anton Hansen E-mail: heih@dtu.dk

Table S1. Formation energy of one oxygen vacancy in the subsurface $E(V_O^{sub})$ of $CeO_2(110)$ with different locations of Ce^{3+}. Atom numbering refers to **Figure 1(a)**. NNN and NN represent Ce^{3+} sitting next-nearest neighbor and nearest neighbor to the V_O, respectively. The subscripts of number 1, 2, and 3 represent Ce^{3+} sitting in the top surface, subsurface, and third cerium layer, respectively.

Ce^{3+} locations to the V_O^{sub}	Atomic number of Ce^{3+}	$E(V_O^{sub})$
NN_2-NN_3	(7,11)	1.48
NNN_1-NN_3	(4,11)	2.43
NNN_1-NN_3	(1,11)	2.47
NN_1-NN_3	(3,11)	2.53
NN_3-NN_3	(11,12)	2.74
NN_2-NN_2	(7,8)	2.93

Table S2. Formation energy of one oxygen vacancy in the top surface $E(V_O^{sur})$ of $CeO_2(110)$ with different locations of Ce^{3+}. Atom numbering refers to **Figure 1(a)**.

Ce^{3+} locations to the V_O^{sur}	Atomic number of Ce^{3+}	$E(V_O^{sur})$
NN_1-NNN_1	(1,4)	1.14
NN_1-NNN_1	(2,4)	1.18
NN_1-NNN_2	(4,8)	1.38
NN_1-NN_2	(4,7)	1.45
NN_2-NN_3	(6,12)	1.46
NN_1-NN_1	(3,4)	1.68
NN_2-NN_2	(7,8)	1.77

Table S3. Formation energy of one oxygen vacancy in the subsurface $E(V_O^{sub})$ of $CeO_2(100)$ with different locations of Ce^{3+}. Atom numbering refers to **Figure 1(b).**

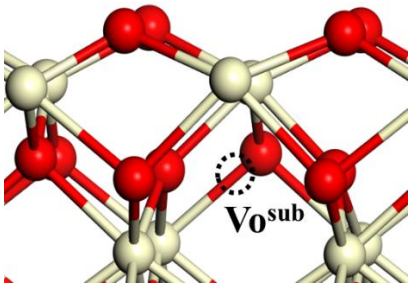

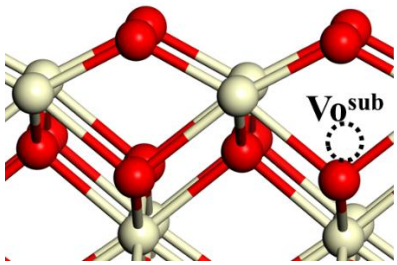

Ce^{3+} locations to the Vo^{sub}	Atomic number of Ce^{3+}	$E(V_O^{sub})$	Ce^{3+} locations to the Vo^{sub}	Atomic number of Ce^{3+}	$E(V_O^{sub})$
NN_1-NNN_2	(4,6)	1.67	NN_2-NNN_2	(7,8)	2.09
NNN_1-NN_1	(1,4)	2.88	NNN_1-NNN_1	(3,4)	2.27
NNN_2-NN_2	(5,7)	3.10	NNN_1-NN_2	(3,7)	2.27
NN_1-NNN_2	(4,5)	3.31	NN_1-NNN_1	(1,3)	2.28
NNN_1-NN_1	(3,4)	3.48	NNN_1-NN_2	(3,5)	2.36
NNN_2-NN_2	(6,8)	4.17	NN_2-NNN_2	(5,6)	2.48

Table S4. Formation energy of one oxygen vacancy in the top surface $E(V_O^{sur})$ of $CeO_2(100)$ with different locations of Ce^{3+}. Atom numbering refers to **Figure 1(b)**.

Ce^{3+} locations to the Vo^{sur}	Atomic number of Ce^{3+}	$E(V_O^{sur})$
NN_1-NNN_2	(1,7)	1.62
NN_1-NN_1	(1,3)	1.72
NNN_2-NNN_2	(7,8)	2.02

Table S5. Adsorption energy of one, two, and three H on CeO_2(110), respectively. Comparisons between different Ce^{3+} distributions.

1H		2H		2H'		3H	
Ce^{3+} locations	E_H	Ce^{3+} locations	E_2H	Ce^{3+} locations	E_2H'	Ce^{3+} locations	E_3H
(4)	-1.62	(1,4)	-3.14	(2,3)	-2.71	(1,3,4)	-4.76
(2)	-1.54	(2,4)	-3.11	(1,3)	-2.69	(2,3,4)	-4.75
(8)	-1.33	(3,4)	-3.02	(3,4)	-2.33	(1,2,3)	-4.61
(11)	-1.24	(1,2)	-2.62	(2,4)	-2.68	(1,3,11)	-4.45
		(4,8)	-2.99	(3,8)	-2.42	(1,2,8)	-4.29
		(4,6)	-2.80	(3,7)	-2.44	(3,4,8)	-4.21
		(4,12)	-2.80	(3,6)	-2.21	(4,7,6)	-4.20
		(4,11)	-2.76	(3,5)	-2.32	(9,3,11)	-3.86
		(4,9)	-2.74	(4,8)	-2.43	(4,7,10)	-4.08
		(1,12)	-2.73	(4,7)	-2.48	(7,3,11)	-4.58
		(2,12)	-2.70	(4,6)	-2.20	(6,7,8)	-3.76
		(2,11)	-2.68	(4,5)	-2.32	(7,8,10)	-4.28
		(4,11)	-2.75	(7,8)	-2.27	(8,10,11)	-4.45
		(2,10)	-2.80	(7,6)	-2.01	(10,11,12)	-3.90
		(3,10)	-2.75	(7,5)	-1.88		
		(7,8)	-2.58	(8,6)	-1.75		
		(5,8)	-2.64	(8,5)	-1.98		
		(5,6)	-2.36	(3,9)	-2.38		
		(8,12)	-2.48				
		(8,10)	-2.28				
		(11,12)	-2.58				

Table S6. The magnetization of the Ce with a specific atom number in the hydroxylated CeO_2(110) at different hydrogen coverages. The configurations are shown in **Figures 3 and Figure S2.** The numbering of Ce (# Ce) refers to **Figure 1(a)** in the manuscript.

# Ce	*	1H	2H	2H'	3H	4H	5H	6H	7H	8H	9H
1	0.0	0.0	1.0	0.0	1.0	1.0	1.0	1.0	1.0	1.0	1.0
2	0.0	0.0	0.0	1.0	0.0	1.0	1.0	1.0	1.0	1.0	1.0
3	0.0	0.0	0.0	1.0	1.0	1.0	1.0	1.0	1.0	1.0	1.0
4	0.0	1.0	1.0	0.0	1.0	1.0	1.0	1.0	1.0	1.0	1.0
5	0.0	0.0	0.0	0.0	0.0	0.0	1.0	1.0	1.0	1.0	0.0
6	0.0	0.0	0.0	0.0	0.0	0.0	0.0	1.0	1.0	1.0	1.0
7	0.0	0.0	0.0	0.0	0.0	0.0	0.0	0.0	0.0	1.0	1.0
8	0.0	0.0	0.0	0.0	0.0	0.0	0.0	0.0	1.0	1.0	1.0
9	0.0	0.0	0.0	0.0	0.0	0.0	0.0	0.0	0.0	0.0	0.0
10	0.0	0.0	0.0	0.0	0.0	0.0	0.0	0.0	0.0	0.0	0.0
11	0.0	0.0	0.0	0.0	0.0	0.0	0.0	0.0	0.0	0.0	0.0
12	0.0	0.0	0.0	0.0	0.0	0.0	0.0	0.0	0.0	0.0	0.0

Table S7. The magnetization of the Ce with a specific atom number in the hydroxylated CeO_2(100) at different hydrogen coverages. The configurations are shown in **Figure S3**. The numbering of Ce (# Ce) refers to **Figure 1(b)** in the manuscript.

# Ce	*	1H	2H	3H	4H	5H
1	0.0	1.0	1.0	1.0	1.0	1.0
2	0.0	0.0	0.0	0.0	1.0	1.0
3	0.0	0.0	1.0	1.0	1.0	1.0
4	0.0	0.0	0.0	1.0	1.0	1.0
5	0.0	0.0	0.0	0.0	0.0	0.0
6	0.0	0.0	0.0	0.0	0.0	1.0
7	0.0	0.0	0.0	0.0	0.0	0.0
8	0.0	0.0	0.0	0.0	0.0	0.0

Table S8. Formation energy of one oxygen vacancy in the top surface E(V_O^{sur}) and subsurface E(V_O^{sub}) of the hydroxylated CeO_2(110) with different Ce^{3+} locations. Configurations are given in **Figures S7 and S8**. Atom numbering refers to **Figure 1(a)**.

H coverage	V_O^{sub}		V_O^{sur}	
	Atomic number of Ce^{3+}	E(V_O^{sub})	Atomic number of Ce^{3+}	E(V_O^{sur})
3H	(1,2,3,4,10)	2.56	(1,2,3,4,6)	1.95
	(1,2,3,4,9)	2.57	(1,2,3,4,5)	1.99
	(1,2,3,4,6)	2.71	(2,3,4,5,9)	2.20
4H	(1,2,3,4,7,8)	2.75	(1,2,3,4,7,11)	2.69
	(1,2,3,4,6,12)	2.76	(1,2,3,4,7,8)	2.90
	(1,2,3,4,11,12)	2.90		
6H	(1,2,3,4,5,6,8,10)	2.65	(1,2,3,4,5,6,7,9)	3.06
	(1,2,3,4,5,6,7,8)	2.71	(1,2,3,4,5,3,7,8)	3.08
	(1,2,3,4,5,6,9,10)	2.79	(1,2,3,4,5,6,7,12)	3.29
7H	(1,2,3,4,5,6,7,8,11)	2.75	(1,2,3,4,5,7,8,12)	3.32
	(1,2,3,4,5,6,7,8,12)	2.75	(1,2,3,4,5,6,7,8,11)	3.36
	(1,2,3,4,6,7,8,11,12)	2.98	(1,2,3,4,6,7,8,11,12)	4.14

Table S9. Formation energy of one oxygen vacancy in the top surface E(V_O^{sur}) and subsurface E(V_O^{sub}) of the 3H covered CeO_2(100). Atom numbering refers to **Figure 1(a)**.

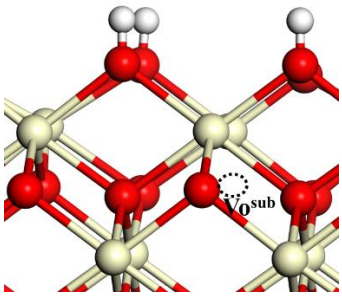		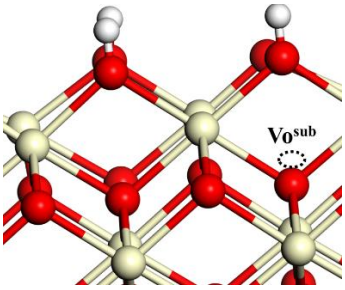		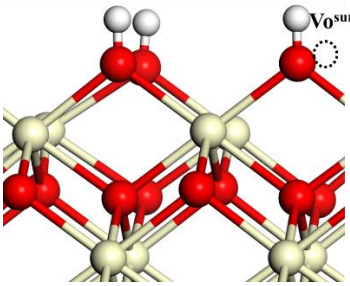	
Atomic number of Ce^{3+}	E(V_O^{sub})	Atomic number of Ce^{3+}	E(V_O^{sub})	Atomic number of Ce^{3+}	E(V_O^{sur})
(1,2,3,4,8)	2.60	(2,3,4,5,7)	2.48	(1.2.3.4.7)	2.31
(2,3,4,5,7)	3.80	(1,2,3,4,7)	2.63	(1,2,3,4,5)	2.35
(1,2,3,4,7)	3.93	(1,2,3,4,5)	2.64	(1,2,4,7,8)	2.31

Table S10. The magnetization of the Ce with a specific atomic number in CeO_2(110) at each reaction step during the H_2 production on the 2H covered CeO_2(110). The numbering of Ce refers to **Figure 1(a)** in the manuscript.

# Ce	*	V_O^{sub}	V_O^{sur}	H_2O_{ads}	2H	TS	H_2	2H'	TS'
1	0.0	0.0	1.0	0.0	1.0	0.0	0.0	0.0	0.0
2	0.0	0.0	0.0	0.0	0.0	0.0	0.0	1.0	0.0
3	0.0	0.0	0.0	1.0	0.0	1.0	0.0	1.0	0.0
4	0.0	0.0	1.0	1.0	1.0	0.0	0.0	0.0	1.0
5	0.0	0.0	0.0	0.0	0.0	0.0	0.0	0.0	0.0
6	0.0	0.0	0.0	0.0	0.0	0.0	0.0	0.0	0.0
7	0.0	1.0	0.0	0.0	0.0	0.0	0.0	0.0	0.0
8	0.0	0.0	0.0	0.0	0.0	0.0	0.0	0.0	0.0
9	0.0	0.0	0.0	0.0	0.0	0.0	0.0	0.0	0.0
10	0.0	0.0	0.0	0.0	0.0	0.0	0.0	0.0	0.0
11	0.0	1.0	0.0	0.0	0.0	0.0	0.0	0.0	0.0
12	0.0	0.0	0.0	0.0	0.0	0.0	0.0	0.0	0.0

Table S11. The magnetization of the Ce with a specific atom number in CeO_2(110) at each reaction step during the H_2 production on the 4H and 5H covered CeO_2(110). The numbering of Ce refers to **Figure 1(a)** in the manuscript.

# Ce	3H	V_O^{sub}	V_O^{sur}	H_2O_{ads}	5H	TS	H_2	TS'	H_2'	4H*	TS	H_2
1	1.0	1.0	1.0	1.0	1.0	0.0	1.0	0.8	0.0	1.0	1.0	0.0
2	0.0	1.0	1.0	1.0	1.0	1.0	0.0	1.0	1.0	1.0	1.0	0.0
3	1.0	1.0	1.0	1.0	1.0	1.0	1.0	1.0	1.0	1.0	0.0	1.0
4	1.0	1.0	1.0	1.0	1.0	1.0	1.0	1.0	1.0	1.0	1.0	1.0
5	0.0	0.0	0.0	1.0	1.0	1.0	0.0	0.8	0.0	0.0	0.0	0.0
6	0.0	0.0	1.0	0.0	0.0	0.0	0.0	0.0	0.0	0.0	0.0	0.0
7	0.0	0.0	0.0	0.0	0.0	0.0	0.0	0.0	0.0	0.0	0.0	0.0
8	0.0	0.0	0.0	0.0	0.0	0.0	0.0	0.0	0.0	0.0	0.0	0.0
9	0.0	1.0	0.0	0.0	0.0	0.0	0.0	0.0	0.0	0.0	0.0	0.0
10	0.0	0.0	0.0	0.0	0.0	0.0	0.0	0.0	0.0	0.0	0.0	0.0
11	0.0	0.0	0.0	0.0	0.0	0.0	0.0	0.0	0.0	0.0	0.0	0.0
12	0.0	0.0	0.0	0.0	0.0	0.0	0.0	0.0	0.0	0.0	0.0	0.0

Table S12. The magnetization of the Ce with a specific atom number in CeO_2(110) at each reaction step during the H_2 production on the 6H covered CeO_2(110). The numbering of Ce refers to **Figure 1(a)** in the manuscript.

# Ce	4H	V_O^{sub}	V_O^{sur}	H_2O_{ads}	6H	TS	H_2	TS'	H_2'
1	1.0	1.0	1.0	1.0	1.0	1.0	1.0	1.0	1.0
2	1.0	1.0	1.0	1.0	1.0	1.0	1.0	0.0	1.0
3	1.0	1.0	1.0	1.0	1.0	1.0	1.0	1.0	1.0
4	1.0	1.0	1.0	1.0	1.0	1.0	1.0	1.0	1.0
5	0.0	0.0	0.0	1.0	1.0	0.0	0.0	1.0	0.0
6	0.0	0.0	0.0	1.0	1.0	0.0	0.0	1.0	0.0
7	0.0	1.0	0.0	0.0	0.0	0.0	0.0	0.0	0.0
8	0.0	1.0	1.0	0.0	0.0	0.0	0.0	0.0	0.0
9	0.0	0.0	0.0	0.0	0.0	0.0	0.0	0.0	0.0
10	0.0	0.0	0.0	0.0	0.0	0.0	0.0	0.0	0.0
11	0.0	0.0	0.0	0.0	0.0	0.0	0.0	0.0	0.0
12	0.0	0.0	1.0	0.0	0.0	0.0	0.0	0.0	0.0

Table S13. The magnetization of the Ce with a specific atom number in CeO_2(110) at each reaction step during the H_2 production on the 8H covered CeO_2(110). The numbering of Ce refers to **Figure 1(a)** in the manuscript.

# Ce	6H	V_O^{sub}	V_O^{sur}	H_2O_{ads}	8H	TS	H_2	TS'	H_2'
1	1.0	1.0	1.0	1.0	1.0	1.0	1.0	1.0	1.0
2	1.0	1.0	1.0	1.0	1.0	1.0	1.0	1.0	1.0
3	1.0	1.0	1.0	1.0	1.0	1.0	1.0	1.0	1.0
4	1.0	1.0	1.0	1.0	1.0	1.0	1.0	1.0	1.0
5	1.0	1.0	1.0	1.0	1.0	1.0	1.0	1.0	1.0
6	1.0	1.0	1.0	1.0	1.0	1.0	1.0	1.0	0.0
7	0.0	1.0	0.0	1.0	1.0	0.0	0.0	1.0	0.0
8	0.0	0.0	1.0	1.0	1.0	1.0	0.0	0.0	1.0
9	0.0	1.0	0.0	0.0	0.0	0.0	0.0	0.0	0.0
10	0.0	0.0	1.0	0.0	0.0	0.0	0.0	0.0	0.0
11	0.0	0.0	0.0	0.0	0.0	0.0	0.0	0.0	0.0
12	0.0	0.0	0.0	0.0	0.0	0.0	0.0	0.0	0.0

Table S14. The magnetization of the Ce with a specific atom number in CeO_2(110) at each reaction step during the H_2 production on the 9H covered CeO_2(110). The numbering of Ce refers to **Figure 1(a)** in the manuscript.

# Ce	7H	V_O^{sub}	V_O^{sur}	H_2O_{ads}	TS	9H	H_2
1	1.0	1.0	1.0	1.0	1.0	1.0	1.0
2	1.0	1.0	1.0	1.0	1.0	1.0	1.0
3	1.0	1.0	1.0	1.0	1.0	1.0	1.0
4	1.0	1.0	1.0	1.0	1.0	1.0	1.0
5	1.0	1.0	1.0	1.0	1.0	1.0	1.0
6	1.0	1.0	1.0	1.0	1.0	1.0	1.0
7	1.0	1.0	1.0	1.0	1.0	1.0	1.0
8	0.0	1.0	1.0	1.0	0.0	0.0	0.0
9	0.0	0.0	1.0	1.0	0.0	0.0	0.0
10	0.0	1.0	0.0	0.0	0.0	0.0	0.0
11	0.0	0.0	0.0	0.0	0.0	0.0	0.0
12	0.0	0.0	0.0	0.0	0.0	0.0	0.0

Table S15. The magnetization of the Ce with a specific atom number in CeO_2(100) at each reaction step during the H_2 production on the 2H covered CeO_2(100). The numbering of Ce refers to **Figure 1(b)** in the manuscript.

# Ce	*	V_O^{sub}	V_O^{sur}	H_2O_{ads}	2H	TS	H_2
1	0.0	0.0	1.0	1.0	1.0	0.0	0.0
2	0.0	0.0	0.0	0.0	0.0	0.0	0.0
3	0.0	0.0	0.0	0.0	1.0	1.0	0.0
4	0.0	1.0	0.0	0.0	0.0	0.0	0.0
5	0.0	0.0	0.0	0.0	0.0	0.0	0.0
6	0.0	1.0	0.0	0.0	0.0	0.0	0.0
7	0.0	0.0	1.0	1.0	0.0	0.0	0.0
8	0.0	0.0	0.0	0.0	0.0	0.0	0.0

Table S16. The magnetization of the Ce with a specific atom number in $CeO_2(100)$ at each reaction step during the H_2 production on the 4H and 5H covered $CeO_2(100)$. The numbering of Ce refers to **Figure 1(b)** in the manuscript.

# Ce	3H	V_O^{sub}	V_O^{sur}	H_2O_{ads}	5H	TS	H_2	4H	TS	H_2
1	1.0	0.0	1.0	1.0	1.0	1.0	1.0	1.0	1.0	1.0
2	0.0	1.0	1.0	1.0	1.0	1.0	1.0	1.0	0.0	0.0
3	1.0	1.0	1.0	1.0	1.0	0.0	0.0	1.0	1.0	1.0
4	1.0	1.0	1.0	1.0	1.0	1.0	1.0	1.0	1.0	0.0
5	0.0	1.0	0.0	0.0	0.0	0.0	0.0	0.0	0.0	0.0
6	0.0	0.0	0.0	0.0	0.0	0.0	0.0	0.0	0.0	0.0
7	0.0	1.0	1.0	1.0	0.0	0.0	0.0	0.0	0.0	0.0
8	0.0	0.0	0.0	0.0	1.0	0.0	0.0	0.0	0.0	0.0

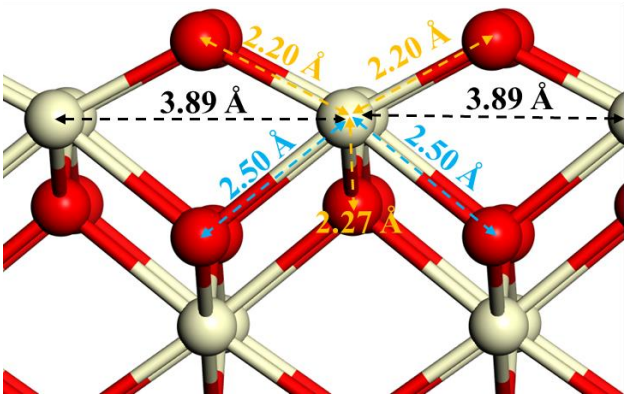

Figure S1. Configuration of the converged $CeO_2(100)$ surface, with selected bond lengths indicated.

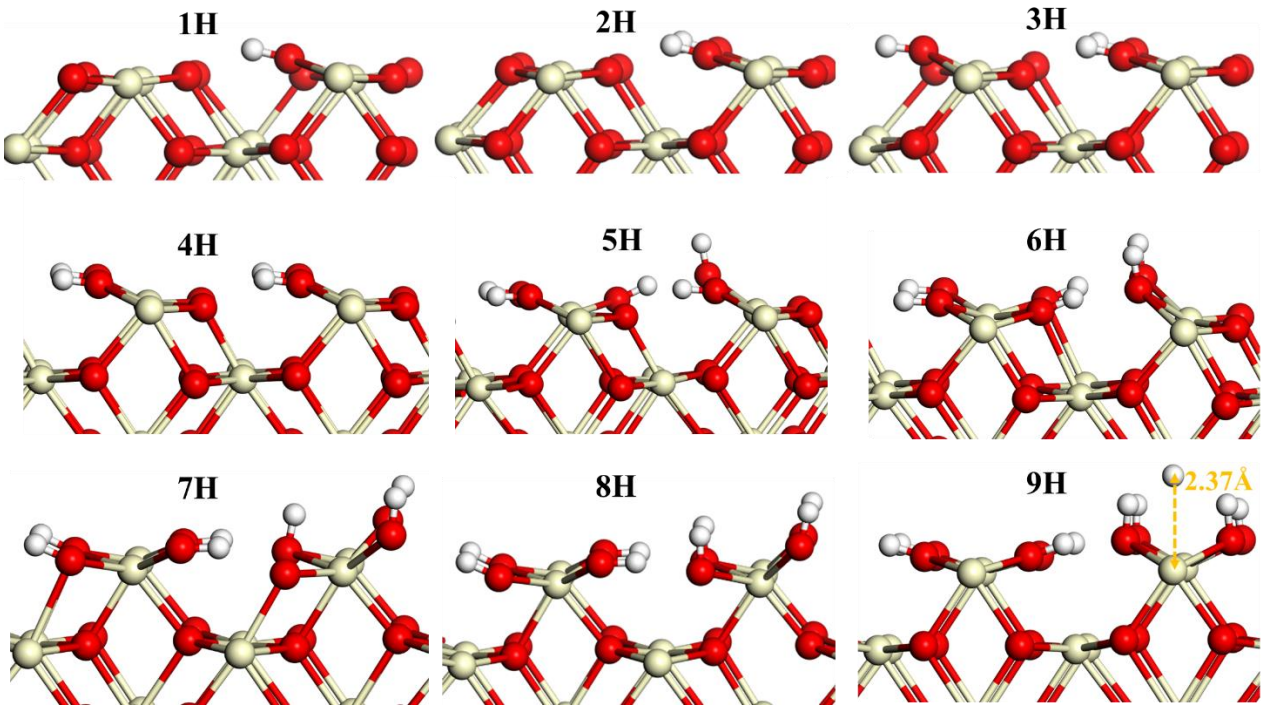

Figure S2. Configurations of the hydroxylated CeO_2(110) with different hydrogen coverages.

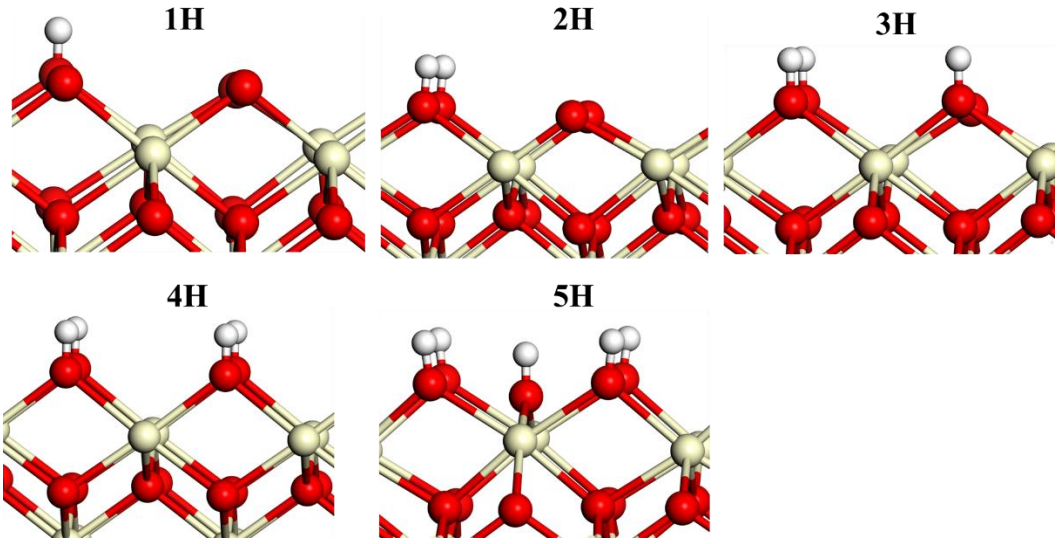

Figure S3. Configurations of the hydroxylated CeO_2(100) with different hydrogen coverages.

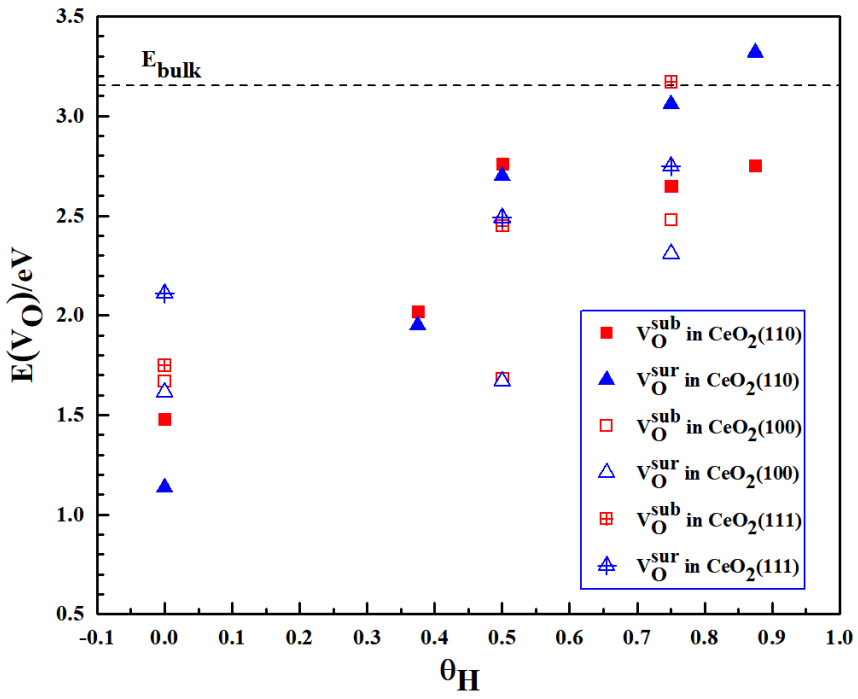

Figure S4. Formation energy of one oxygen vacancy in the hydroxylated (110) and (100) facets of ceria, as compared to the (111) facet. E_{bulk} refers the formation energy of one oxygen vacancy in a bulk ($Ce_{32}O_{64}$) calculated by using Γ-centered 4×4×4 k-point mesh.

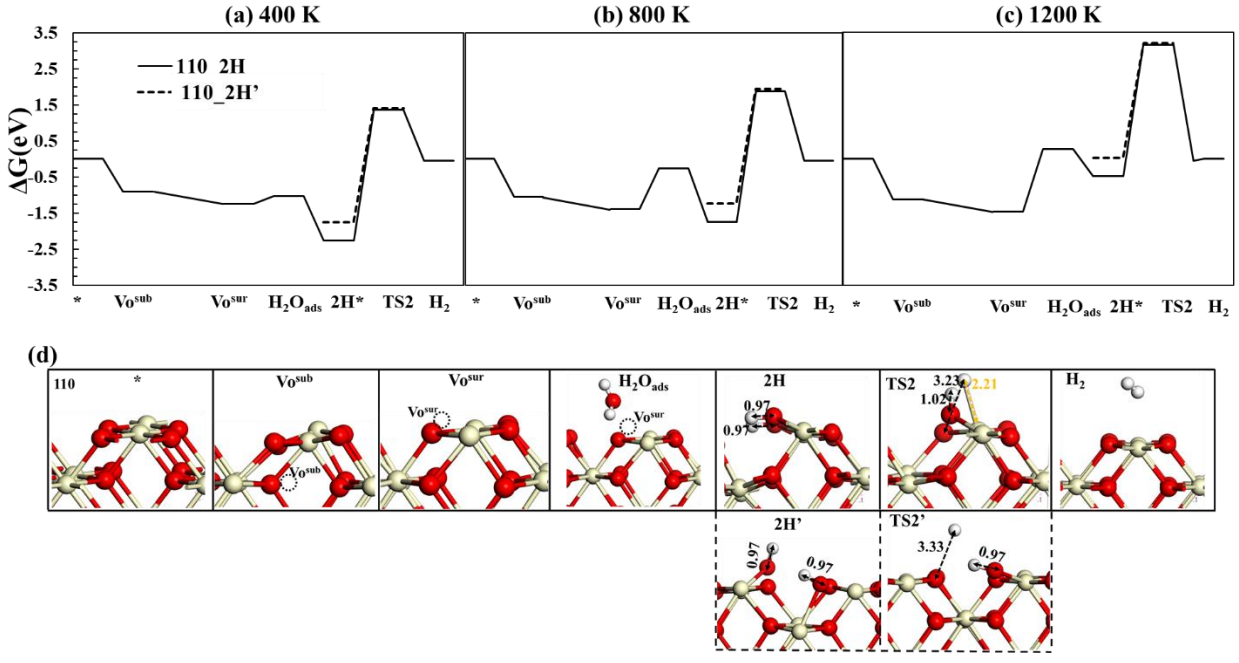

Figure S5. Free energy diagrams for the WSR pathway via the partially hydroxylated (Θ_H=0.25 ML) CeO_2(110) at (a) T= 400 K, (b) T= 800 K, and (c) T= 1200 K. The configurations of intermediates at each reaction step are shown in (d) with selected bond lengths indicated. The magnetizations of each intermediate are given in **Table S10.**

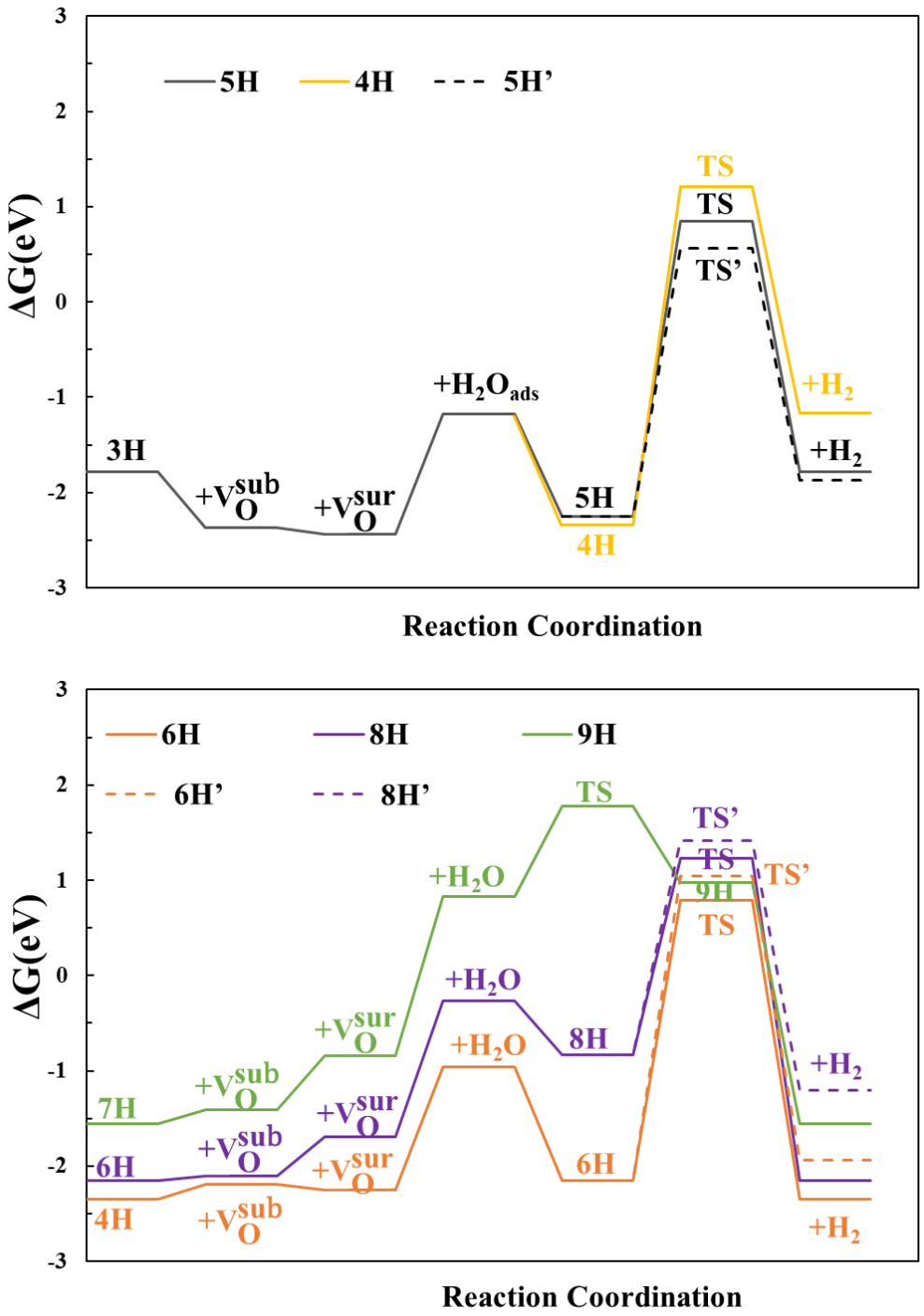

Figure S6. Free energy diagrams at 1200 K for the WSR pathways via the hydroxylated CeO_2(110) with different hydrogen coverages. The configurations of intermediates at each reaction step are shown in **Figure S7** and **S8**. The magnetizations of each intermediate are given in **Tables S11-S14.**

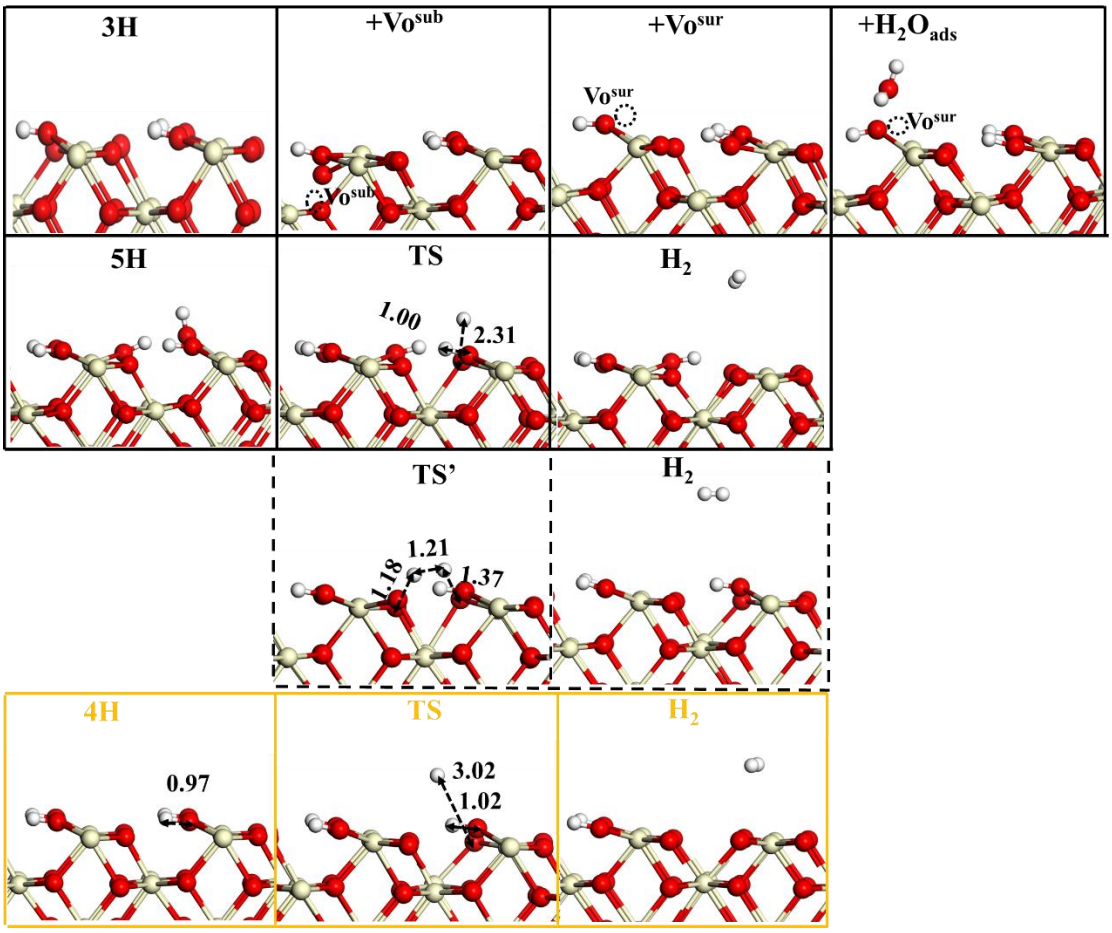

Figure S7. The configurations of intermediates at each reaction step of the WSR via the hydroxylated (5H, 4H, and 5H') CeO_2(110). Selected bond lengths are indicated.

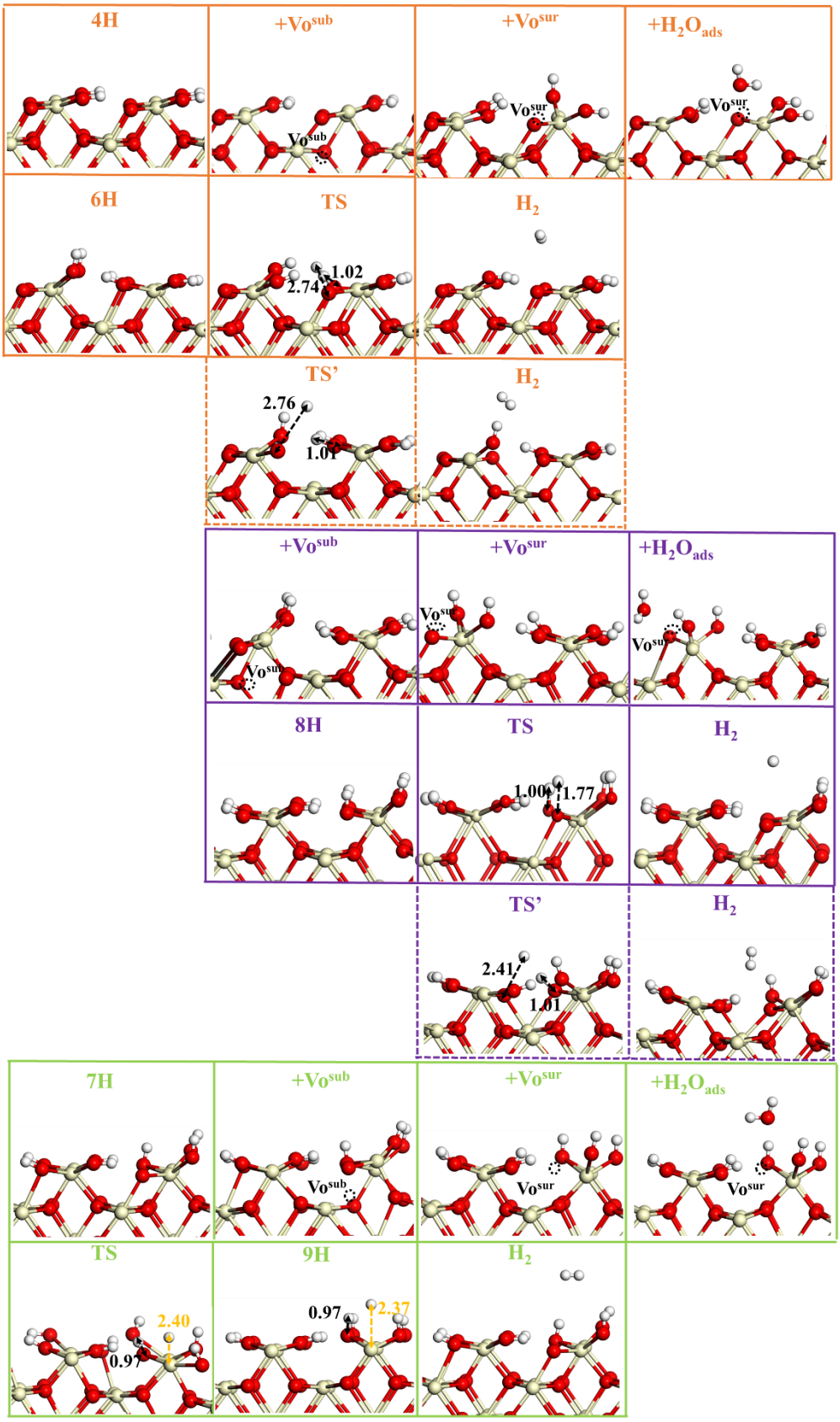

Figure S8. The configurations of intermediates at each reaction step of the WSR via the hydroxylated (6H, 6H', 8H, 8H', and 9H) CeO_2(110). Selected bond lengths are indicated.

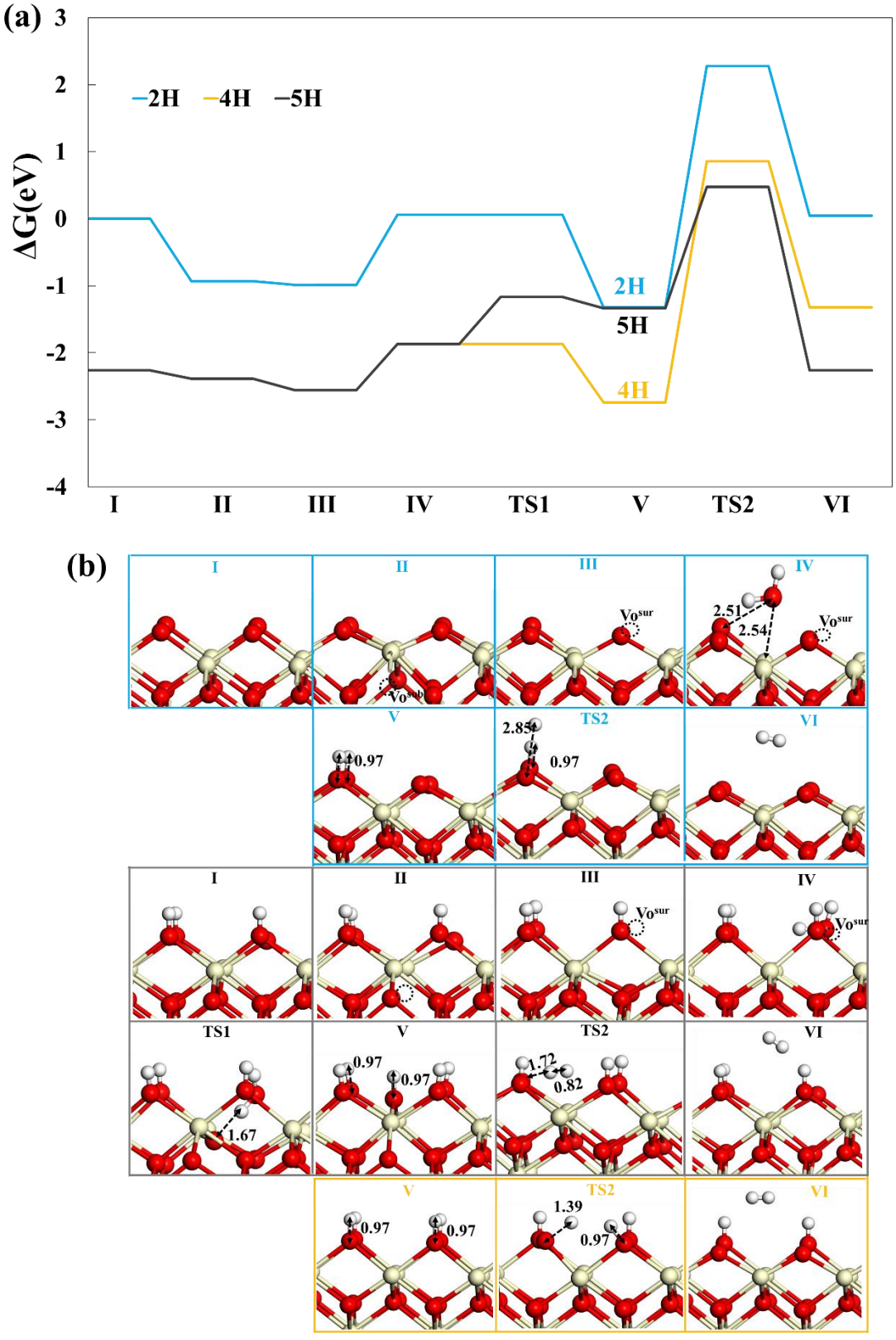

Figure S9. (a) Free energy diagrams at 1200 K for the WSR pathways via the hydroxylated CeO_2(100) with different hydrogen coverages. (b) The configurations of intermediates at each reaction step with selected bond lengths indicated. The magnetizations of each intermediate are given in **Tables S15 and S16**.

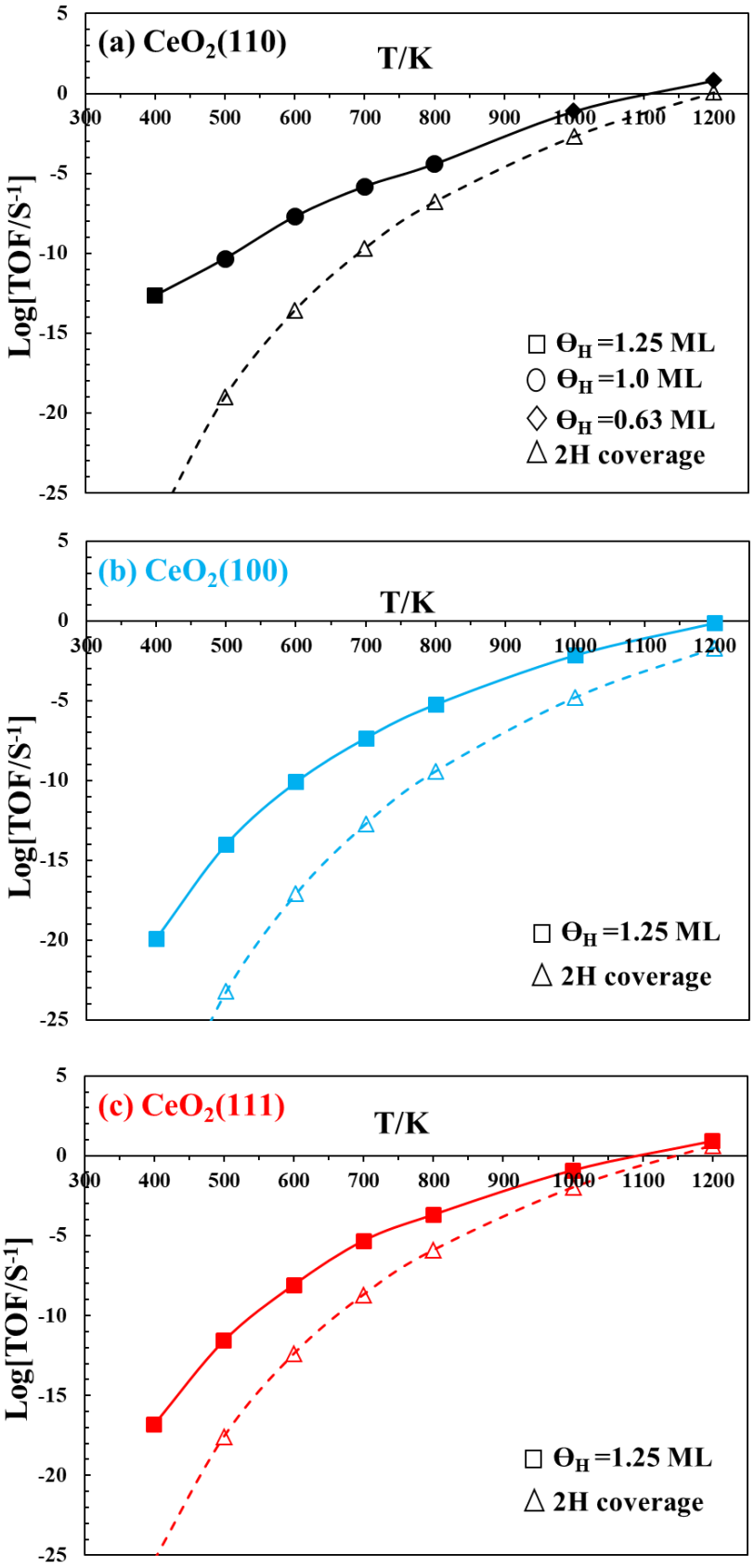

Figure S10. Comparison of TOF between the fastest WSR and the reaction via 2H covered (a) CeO_2(110); (b) CeO_2(100); (c) CeO_2(111).

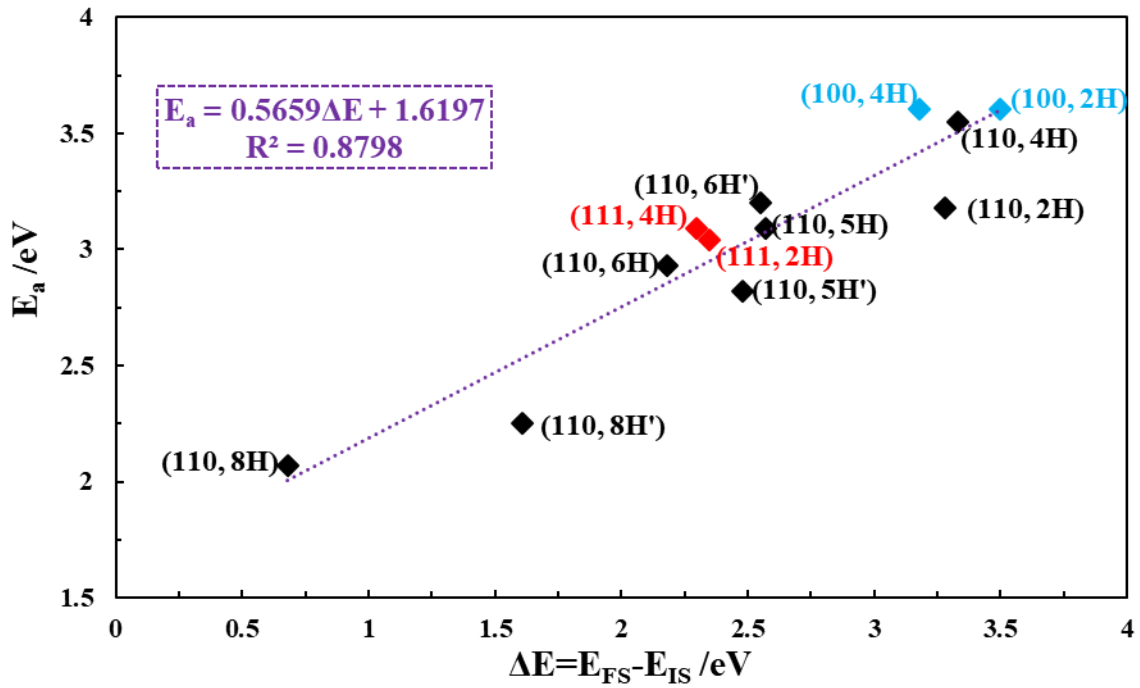

Figure S11. The Brønsted-Evans-Polanyi (BEP) relation between the activation barriers of the hydroxyl (the initial state, IS) decomposition into H_2 (the final state, FS) on the hydroxylated CeO_2(110), CeO_2(100) and CeO_2(111) surfaces, and the reaction energy ($E_f=E_{FS}-E_{IS}$). The annotation (110, 8H) indicates the CeO_2(110) surface is covered by 8H and the activation energy is calculated for forming H_2 via 2H from the same row. The annotation (110, 8H') indicates the activation energy is calculated for forming H_2 via 2H from the two different rows.